Development of an Image Guidance System for Breast Cancer Surgery

By

Rebekah H. Conley Griesenauer

Dissertation

Submitted to the Faculty of the

Graduate School at Vanderbilt University

in partial fulfillment of the requirements

for the degree of

DOCTOR OF PHILOSOPHY

in

Biomedical Engineering

August 11, 2017

Nashville, TN

Approved:

Michael Miga, Ph.D.

Brett Byram, Ph.D.

Ingrid Meszoely, M.D.

Jared A. Weis, Ph.D.

Benoit Dawant, Ph.D.

ACKNOWLEDGMENTS

First, I would like to start by thanking the current and former members of the Biomedical Modeling Laboratory at Vanderbilt, especially Dr. Tom Pheiffer for his guidance and help with the ultrasound data. I would also like to thank Yifei Wu, Jarrod Collins, Saramati Narasimhan, Ma Luo, Jacob Chadwell, Sarah Goodale, Logan Clements, and Jon Heiselman for their helpful discussions and assistance with data acquisition. I also gratefully acknowledge Dr. Lori Arlinghaus-Davis for her crucial help in producing our supine breast images. Without her resilient effort to produce high quality supine magnetic resonance images, many aspects of this thesis would have suffered.

Mostly, I would like to thank my committee members - Dr. Michael Miga, Dr. Brett Byram, Dr. Ingrid Meszoely, Dr. Jared Weis, and Dr. Benoit Dawant for their guidance, encouragement, and sage advice. I would specifically like to acknowledge Dr. Ingrid Meszoely for her encouragement and overall enthusiasm to work with me to obtain breast cancer patient data. I would like to sincerely thank Dr. Jared Weis for his critical role in helping me learn, understand, and implement some of the most technical pieces of this thesis. I would like to extend my gratitude to my thesis adviser, Dr. Miga, for working with me to initialize this project and for providing guidance for without this project would not have succeeded. Furthermore, I would like to graciously thank Dr. Miga for allowing me to pursue all of my outside interests beyond this thesis work during my time as a graduate student in his lab. Dr. Miga not only served as a sound scientific advisor, but also as an excellent mentor for my career and professional aspirations.

I would like to acknowledge the Vanderbilt Initiative in Surgery and Engineering Pilot Award Program for support of this work. This work was supported in part by a National Science Foundation Graduate Research Fellowship. This work was also partially funded by CTSA award No. UL1TR000445 from the National Center for Advancing Translational Sciences. Other financial support came from the NIH through R21EB022380.

I would like to graciously thank all of the women who volunteered to by part of my studies. Finally, I would like to thank my family and friends for their continued support and encouragement throughout this process, especially my husband, Andy.

TABLE OF CONTENTS

LIST OF TABLES

LIST OF FIGURES

SUMMARY

Breast cancer is the most common cancer in women and the second highest cause of cancer related deaths among women in the United States. A woman has a 1-in-8 lifetime risk of developing breast cancer and a 1-in-35 lifetime risk of dying from the disease [14]. Most breast cancers are treated by some form of surgical intervention. Mastectomies remove the entire breast and were the gold standard for breast cancer surgery for almost 100 years. Eventually, surgeons began to gradually remove less and less breast tissue while achieving the same survival rates. Today, many women are eligible for breast conservation therapy, which is meant to preserve breast shape and structure by removing only the tumor and a small margin of surrounding non-cancerous tissue (known as a lumpectomy). An immense amount of evidence shows that there is no difference in overall survival rates between lumpectomy and the much more radical option of mastectomy, provided that complete tumor removal is achieved. A successful lumpectomy, therefore, includes negative margins (meaning that there are no cancer cells at the edges of the excised tissue) and an acceptable cosmetic outcome. Unfortunately, women eligible for breast conservation therapy may elect for a mastectomy due to surgical uncertainties. This is well founded considering a majority of studies report that positive margins occur in 16.5-40% [15, 16] of patients undergoing lumpectomy, resulting in an unacceptable rate of second surgeries and mastectomies. Surgical difficulties arise due to the inability to visualize the tumor in the operating room. Images of the tumor taken before surgery are acquired with the patient lying prone or standing up, while surgery is performed with the patient lying on her back. There can be drastic shape and location changes of the tumor between these two anatomical positions. A recent study published in the New England Journal of Medicine captures this backdrop well referring to breast cancer re-excision rates as "*The Other Breast Cancer Epidemic*"[17]. Reoperations cause patient pain, depression, anxiety, poor cosmetic outcomes, and an overall decrease in quality of life. Furthermore, reoperations are estimated to cost $53.7 million a year in surgical costs alone (Appendix A). This does not include hospital operational costs or outpatient costs.

This thesis addresses the need for improved surgical tools to localize tumors intraoperatively with the ultimate goal of reducing the number of reoperations associated with lumpectomy surgeries. The localization approach developed herein utilizes volumetric images of the breast taken prior to surgery and digitization technology to map patient images to the surgical space. Patient-specific tissue prop-

erties and biomechanical models are incorporated to correct the deformation that occurs between the breast geometry acquired by preoperative imaging and the breast geometry observed in the surgical setup. Once the preoperative images are corrected and co-registered to the patient in the operating room, surgeons can effectively navigate to tumors by using the co-registered preoperative images as patient-specific maps. The development of this image-guidance system for breast cancer surgery is detailed within this thesis, with chapters focusing on relevant background material, important research methods, initial assessment of tools and methods needed for an image guidance system, registration approaches, validation frameworks, the creation and integration of patient specific models, and a look into future studies to be performed.

CHAPTER I

Introduction

Breast cancer is the most frequently diagnosed cancer and the leading cause of cancer related deaths among females worldwide [18]. In the United States, breast cancer is the second most commonly diagnosed cancer among women and a leading cause of cancer related deaths, second only to lung cancer [14]. Approximately 249,260 new cases of invasive breast cancer were diagnosed in the U.S. in the year 2016. In addition, approximately 61,000 new diagnosed cases of in situ breast cancers were estimated to occur in 2016 [14]. Breast cancer is a complex and heterogeneous disease with multi-modal approaches for treatment. Initial treatment of primary breast tumors is usually surgical. Surgical options include mastectomy (total removal of the breast) and breast conservation therapy (BCT). BCT consists of removal of the tumor with a margin of normal tissue combined with radiation therapy. Mastectomy was the procedure of choice for newly diagnosed breast cancer patients until the 1980s when studies revealed that lumpectomy, the far less disfiguring option, was shown to have the same 10 year survival rate as mastectomy [19]. Since this time, breast conservation therapy (BCT) has become the preferred treatment choice for women diagnosed with early stage breast cancer. An investigation into costs and complications of local therapies for early stage breast cancer found that mastectomy followed by breast reconstruction was associated with twice the risk of complications and higher cost when compared to BCT [20]. BCT involves a lumpectomy (removal of the cancerous lesion with a small margin of surrounding healthy tissue) coupled with radiation therapy. A lumpectomy is considered successful when negative margins (no cancer cells on margin of the excised tissue) are obtained along with a favorable cosmetic result.

Unfortunately, the current re-excision rates due to positive margins average 16.5-40% [15, 16, 21]. The European Union of Breast Cancer Specialists (EUSOMA) endorse a minimum standard of 80% and a target of 90% success rate of first time surgeries as a quality of care metric [22]. Second and third operations reported in breast surgery are disproportionately high compared with other general surgery practices [23]. Reoperations cause a host of problems including emotional and financial stress on the patient as well as an increase in the public healthcare burden. The cost of re-excisions was estimated to be $53.7 million per year in surgical costs alone (Appendix A). Other consequences of

failing to achieve negative margins during the initial surgery include delay of postoperative radiation treatment and chemotherapy, increase risk for local recurrence, compromises in the cosmetic outcome, and an overall reduction in the value of BCT over mastectomy plus reconstruction. Thus, reducing the rate of second and third operations for margin re-excision or full mastectomy has benefits that are patient-centered and cost-effective.

Avoiding reoperations due to positive margins can be difficult. The challenge in determining surgical margins intraoperatively is that geometric and spatial cues are quickly lost in the surgical presentation. The inability to accurately locate tumor boundaries intraoperatively is a significant contributor to these high re-excision rates. Several methods have been proposed to improve intraoperative tumor localization including wire-guided localization [24], intraoperative ultrasound [25], radio guided occult lesion localization [26], and various seed localization strategies [27–29]. There has also been extensive work directed at real time identification of residual disease following tumor removal [30–39]. Wire guide localization, the most common approach for clinically occult lesions, has been criticized in the last several years due to the inexact nature of the procedure and high rates of positive margins (38-43%) [21, 40]. While intraoperative ultrasound has shown to improve breast conservation surgeries, ultrasound has a limited capability of only visualizing 50% of non-palpable tumors [41]. Advances and shortcomings of tools developed for intraoperative tumor localization and margin assessment is expanded upon in sections II.3.3 and II.3.2.

Preoperative imaging has limited utility as a surgical guidance tool because images are acquired in significantly different orientations than the typical patient setup for surgery, resulting in anatomical shifts that are no longer representative of the intraoperative breast. Preoperative magnetic resonance imaging (MRI) is performed in the prone position with pendant breasts and mammography is performed in a standing position with the breast compressed between two plates, while surgery is conducted in the supine position. While MRI has superior sensitivity and ability to characterize disease extent when compared with other common breast imaging modalities [42–44], the diagnostic scans are not particularly useful in the context of surgical planning and guidance. Several studies have measured and reported significant displacements in breast tumors between the prone and supine positions on the order of 18-60 mm [45–48]. An example of this challenge is displayed in Figure IV.7, where the breast undergoes significant shape change between the prone and supine positions causing the tumor to deform and change location.

(a) Prone MR image of breast (b) OR presentation (c) supine MR image of breast

Figure I.1: Demonstration of the challenge of using preoperative images for surgical guidance. (a) and (c) are axial slices of T_1-weighted THRIVE sequence MR images in the prone and supine positions with red ovals designating the same tumor in the same axial slice. Changes in patient setup cause the tumor to move, yielding the diagnostic scan in (a) less valuable for locating the tumor in the surgical setup, shown in (b).

These relatively large displacements render diagnostic images sub-optimal for use in surgical planning and navigation, which may contribute to studies finding little to no benefit of preoperative MRI for surgical use. The motivation of this work lies in the need to improve lumpectomy procedures to decrease reoperation rates. Superior ability to localize tumors and delineate borders intraoperatively has the potential to decrease the incidence of positive margins. Currently, the under-utilization of MR data in the operating room (OR) could be remedied by acquiring supine MR images that more closely represent surgical orientation and registering them to patient space. Therefore, the development of an image guidance system using supine MRI to guide lumpectomy procedures could address the need for superior localization strategies. Due to these realizations, preliminary investigations towards the use of supine MRI for surgical guidance have been forthcoming to remedy the under-utilization of MR data in the operating room [49–52]. Exploratory frameworks for image guidance systems in breast cancer surgery [46, 53–55] show qualitative promise towards the use of supine MRI in a surgical guidance system, however, there have been no descriptions of a comprehensive, patient-specific platform nor a robust evaluation of such a platform for image guided breast cancer surgery.

I hypothesize that an image guidance system consisting of preoperative supine MR images, digitization technology, and patient specific biomechanical models can provide an intraoperative localization tool for breast conserving surgeries. Furthermore, I expect that creating a truly patient-specific image guidance system by incorporating patient-specific mechanical properties into the nonrigid registration

procedure can increase the overall accuracy of the system. Towards this end, the specific aims of this thesis are as follows:

- Perform a survey of measurement techniques for image guided breast surgery, quantify deformation that occurs between preoperative imaging and surgery, and create validation tools for the image guidance system.
- Integrate image guidance system components for breast cancer surgery and develop a nonrigid preoperative image correction framework.
- Create a novel framework for the determination of patient-specific mechanical breast tissue properties to be implemented in the image guided breast surgery system.

Reported in the following chapters is the first description of a comprehensive image guidance platform for breast cancer surgeries that has been tested and evaluated under appropriate clinical conditions. The future application of this guidance system will provide superior tumor localization in the operating room, especially for tumors poorly visualized by ultrasound. Ch. II begins with a background of relevant breast anatomy and a brief introduction to breast cancer diagnosis and treatment is provided. Next, details of breast conserving surgery and an introduction to image guided surgery is discussed with a focus on biomechanical breast models and biomechanical properties of breast tissue. In Ch. III, a comprehensive review of the research methods used throughout the dissertation is provided.

Ch. IV contains studies detailing a survey of data collection techniques for IGBS (Image Guided Breast Surgery) to evaluate potential components of the final IGBS system. Included in Ch. IV is an initial integration of the following components for IGBS: optical digitization methods, intraoperative ultrasound, preoperative magnetic resonance images, and biomechanical models. Work performed in Ch. IV established and tested the first comprehensive framework of system components involved in a surgical guidance system for breast cancer surgery, with the following novel components: *a*) use of intraoperative ultrasound to measure subsurface registration accuracy in the context of image guided breast surgery is first reported here, *b*) the use of a novel biomechanical model based nonrigid registration to correct preoperative patient specific models and images to better match the surgical presentation of the breast, and *c*) this work is the first to incorporate the chest wall as a rigid feature to improve alignment. These novel components are presented and validated on human study participants with breast cancer.

Ch. V establishes a novel quantitative breast tissue stiffness estimation framework amenable to clinical workflows associated with interventional/surgical image-guided environments. With this single additional scan, we created an ability to develop patient-specific breast geometric models with appropriate quantitative stiffness estimates for use within novel image guided-breast surgery systems with no specialized equipment and using standard imaging sequences available on traditional clinical MR scanners. The first *in vivo* reproducibility studies of a gravity-based stiffness estimation method are reported here.

Ch. VI works towards incorporating the breast tissue stiffness estimation framework created in Ch. V into IGBS systems by introducing optimization procedures into the methodology. Due to inevitable differences in patient breast size, fibroglandular content, deformation levels, and stiffness values, we opted to test a variety of optimization methods to determine the most appropriate method to use going forward in the context of image-guided breast surgery. Ch. VI contains this investigation work involving the use of various optimization routines to reconstruct the values of patient specific breast tissue stiffness. This chapter is especially important for making the IGBS system truly patient-specific.

In Ch. VII, work towards the creation of validation frameworks is discussed. These validation methods include the development of a mock-phantom setup and MR image volumes that represent preoperative-pseudo-intraoperative datasets. Work on the quantification of breast tissue deformation between preoperative and intraoperative setups is also discussed. Finally, avenues for future work are explored and summarized.

CHAPTER II

Background

In the following sections, relevant clinical background will provide a review on the current management of breast disease and the state of surgical treatment. This begins with a short review on the breast anatomy, highlighting important tissue types and medical terms that will be used throughout the dissertation. Next, a general overview of breast diagnosis with more specific detail directed at breast imaging is discussed. A section on the surgical management of breast cancer will provide a detailed review on the current limitations in breast conserving surgery including margin assessment and intraoperative tumor targeting techniques. Finally, a background in image guided procedures is provided with special detail to image-to-physical space registration methods and biomechanical model deformation correction strategies.

II.1 Relevant Breast Anatomy

The breast is comprised of specialized tissue that produce milk (glandular tissue) as well as fatty tissue (adipose). Connective tissue and ligaments provide support and are responsible for breast shape. Female breast tissue is sensitive to cyclic hormone levels as well as age. Fluctuations in estrogen and progesterone concentrations prior to and following menopause result in atrophic changes to glandular and connective tissue [56]. Therefore, younger women might have denser and less fatty breast tissue than do older women that have gone through menopause. The breast lies on top of the pectoralis major and pectoralis minor muscles. In this text, the pectoralis muscles and intercostal muscles are referred to as the ”chest wall”, which is located beneath the base of the breast. Figure II.1a(right) shows the chest wall and remaining breast structures.

The lymphatic drainage of the breast is of great clinical importance. About 95% of lymph from the breast drains towards the axilla [56]. Patients with invasive breast cancer undergo some form of axillary surgery to assess lymph node involvement. The axilla is a compartment between the arm and chest wall, close to the underarm. Figure II.1a (left) shows the lymphatics throughout the breast.

There are four quadrants of the breast known as the upper outer, lower outer, upper inner, and lower inner. Locations of features within the breast are often described using these quadrants as well as radial

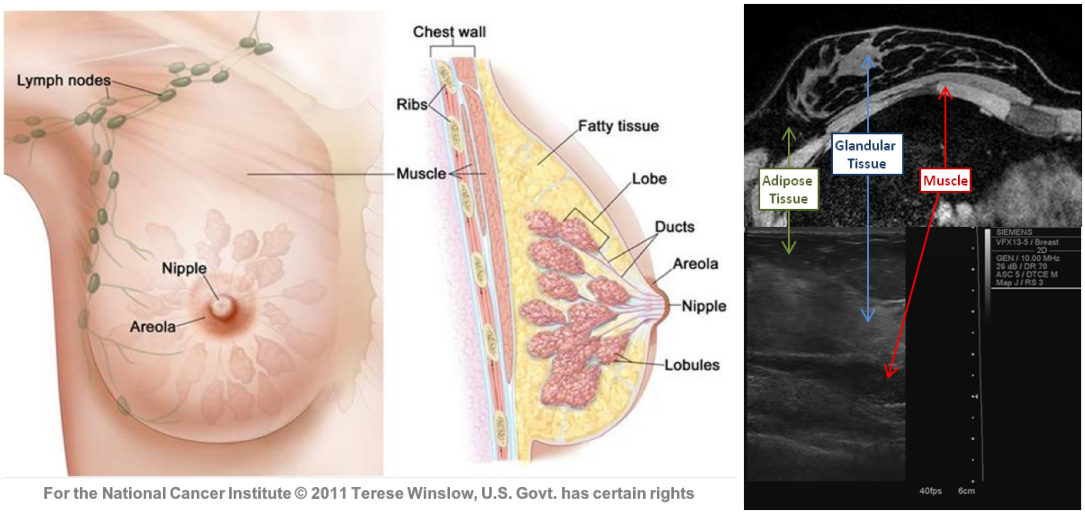

(a) (b)

Figure II.1: (a) Anatomy of the female breast (reprinted with permission from [5]) showing chest wall area as well as lymphatics, lobules, ducts, and fatty tissue. (b) Breast tissue structures as visualized by MRI (top) and b-mode ultrasound (bottom).

clock positions. Figure II.2a shows how the breast is broken up into four quadrants as well as the 12, 3, 6, and 9 o'clock positions. Other anatomical descriptions of the breast and its surrounding tissue include medial, lateral, inferior, and superior. Figure II.2 shows these positions along with a review of the anatomical planes used to describe the body (Figure II.2b).

Numerous imaging modalities are used to view the anatomical structures in the breast. Each modality has a unique contrast mechanism for the various breast structures. The main modalities used in this text are magnetic resonance images and b-mode ultrasound images. Therefore, the ability to identify certain breast structures in these images is important. Figure II.1b (top) is an axial slice of a healthy supine breast produced by magnetic resonance imaging and II.1b (bottom) is a b-mode ultrasound image of a healthy breast. The main tissue types of the breast: muscle, adipose, and glandular are depicted in each modality.

II.2 Breast Cancer Diagnosis

Concern over a possible breast lump and/or a suspicious screening mammogram are the most common presentations of disease at breast clinics [56]. Breast cancer may be treated differently depending on the type of tissue from which the cancer originates. Carcinomas, which consist of tumors that originate in

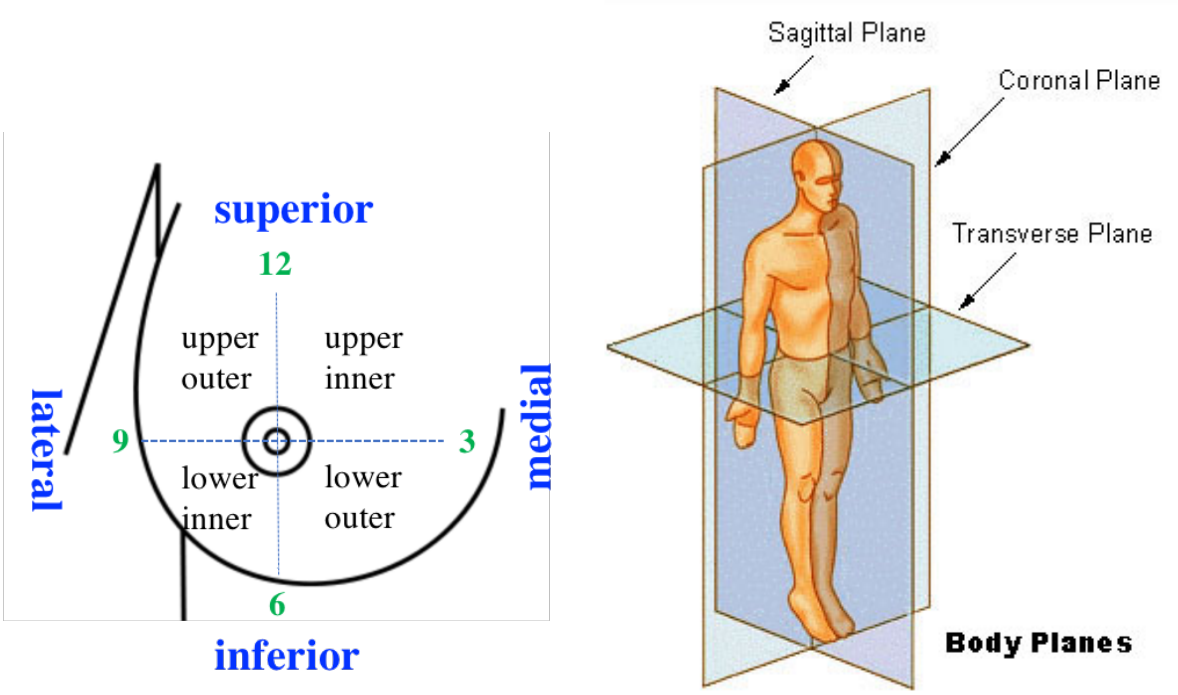

(a) (b)

Figure II.2: (a) Quadrants and anatomical descriptions of the right breast (image redrawn from [6]), (b) anatomical planes (image reprinted from [7])

mammary epithelial cells, represent a majority of breast cancers. Cancers that originate in muscle, fat, or connective tissue are referred to as sarcomas. Carcinomas are classified as non-invasive, commonly called ductal carcinoma in situ (DCIS), when cancerous cells have not invaded through the walls of the ducts into the surrounding tissue. The most commonly diagnosed breast cancer is invasive ductal carcinoma, where cancer cells have invaded through the wall of the duct and infiltrated surrounding tissue. Invasive lobular carcinomas originate in milk producing glands and are more difficult to detect than invasive ductal carcinoma [1].

Traditionally, assessment of the breast involves three key components: clinical exam, imaging, and histology. Histological assessment includes a core needle biopsy and/or fine needle aspiration cytology. The clinical breast exam involves a palpation inspection of the breast, axilla, and chest wall while also considering breast symmetry, nipple inversion, and skin changes. Mammography and ultrasound are recommended for palpable and significant radiological abnormalities. Once a cancer diagnosis has been

[1] Descriptions of cancer types referenced from www.breastcancer.org

confirmed, the extent of the disease is next to be determined. Staging of breast cancer looks at tumor size, lymph node involvement, and the presence of distant metastasis. Multifocality and multicentricity are common descriptors used to characterize breast cancer. Two or more foci of cancer within the *same* breast quadrant are multifocal where two or more foci of cancer in *separate* breast quadrants are defined as multicentric. Further histological assessments and imaging may be performed for staging purposes.

The acquisition methods, strengths, and limitations of each imaging modality used to acquire breast images are of particular importance in this dissertation. The following section provides more detail on the common imaging modalities used in breast cancer screening and diagnosis.

Breast Imaging

Mammography, ultrasound, and magnetic resonance imaging (MRI) are the most commonly used imaging modalities in breast cancer screening, diagnosis and staging. Magnetic resonance imaging has been increasingly used for screening high risk patients, determining tumor extent, identifying contralateral breast cancers, and assessing the response to neoadjuvant chemotherapy.

Mammography uses low energy x-rays to create shadowgrams of the breast to screen for and diagnose breast cancers. Mammographic signals are a result from the different attenuation of x-rays passing through structures in the breast. A mammogram is performed with the patient in a standing position with the breast compressed between two plates and can be uncomfortable for the patient. Figure II.3a shows a typical setup for acquiring a mammographic image and Figure II.3b shows a typical shadowgram of a breast produced by mammography. The American Cancer Society recommends that all women undergo mammographic screening for breast cancer starting at age 45 [57]. This screening exam allows physicians to establish a baseline for further annual screening of the patient breast tissue. Screening mammograms are usually acquired in two views of the breast. Mammography detects mass lesions, areas of parenchyma distortion, and microcalcifications that could be indicators of breast disease. Mammography is generally not performed in patients under the age of 35 because their breasts are more radiographically dense (less fat, more glandular tissue). Diagnostic mammograms are performed when a suspicious lump or mass is palpable or has been identified on the screening mammogram. Diagnostic mammogram exams consist of taking multiple angled images of the breast along with some concentrated imaging on suspicious areas. Mammograms are sometimes used to guide needle biop-

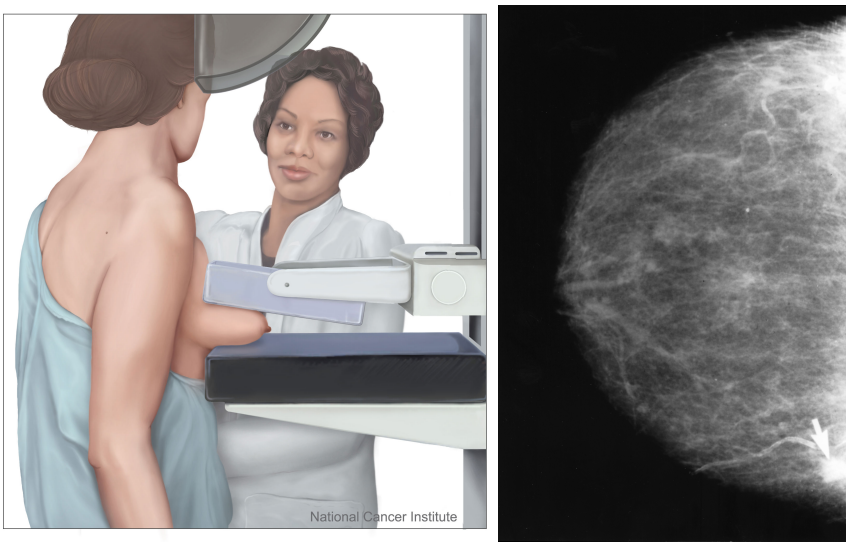

(a) (b)

Figure II.3: (a) Mammogram configuration with breast compressed between two plates (reprinted from [8]), (b) Image of breast produced by mammography (reprinted from [9])

sies and place wire guides for intraoperative tumor localization. Although there are several benefits to mammography, not all cancers can be visualized on screening mammograms.

Ultrasound is usually used to supplement mammography to evaluate high risk patients or women with dense breasts [58]. Ultrasound images are produced using high-frequency sound waves that pass through breast tissue and create acoustic reflections that are detected by an ultrasound transducer. Figure II.4a shows a typical setup for an ultrasound exam and Figure II.4b shows an image produced by b-mode ultrasound containing a breast tumor. Ultrasound is used to assess tumor size, location, and the presence of lymph node metastases. Ultrasound is also used to guide biopsy procedures and has been shown to lower re-excision rates when used intraoperatively during breast conservation therapy [25]. However, ultrasound cannot image most cases of ductal carcinoma in situ (DCIS) [59] and is limited in detecting multifocality, bilateral breast cancers, and intraductal spread characteristics of invasive cancers.

Both ultrasound and mammography tend to underestimate tumor size [60]. Compared with mammography, MRI has a higher sensitivity for the detection of breast cancer and is not limited by breast density [59]. MRI is considered the most accurate imaging modality in the context of breast cancer [61, 62]. However, the limited specificity of MRI provides controversy, with some contending that

(a) (b)

Figure II.4: (a) Ultrasound exam configuration (reprinted from [10]), (b) Image of breast produced by b-mode ultrasound. The spherical dark shadow shows an invasive carcinoma mass.

MRI causes over treatment [63, 64]. The clinical uses of breast MRI include screening of high risk patients (family history, genetic predisposition), screening newly diagnosed patients for contralateral breast cancer, screening women with breast implants, evaluating the extent of disease (multicentricity, multifocality, chest wall invasion), and evaluating treatment response [65]. Figure II.5 shows the typical patient setup for a breast MRI scan.

Attempts to improve MRI specificity are being made that identify imaging parameters that can act as biomarkers to distinguish invasive vs. benign disease. Dynamic Contrast Enhanced (DCE) MRI quantifies the uptake and washout rate of contrast material injected intravenously. The most common parameter extracted from DCE exams is the kinetic curve (time signal intensity curve) [66]. In general, when the uptake of contrast is high in a suspicious region followed by a decrease in enhancement (washout), there is a strong indicator of malignancy with an 87% positive predictive value [66]. Other parameters that can be extracted from DCE imaging and analyzed for cancer detection include enhancement patterns and breast vascularity. Further studies to improve the ability to quantify parameters from MR images to reflect physiological and anatomical information about the lesion are ongoing [67–70]. Pharmacokinetic modeling analyzes contrast enhancement characteristics and patterns of tissue perfusion to enable quantifiable assessments of treatment response in the setting of neoadjuvant chemotherapy [67, 68]. Diffusion weighted imaging (DWI) is another MR technique that has shown

Figure II.5: Patient setup for an MRI scan of the breast with the subject lying in the prone position with free pendant breasts (image reprinted with permission from [11]).

to provide quantifiable differences between benign and malignant breast lesions [71–75]. DWI is sensitive to changes in the diffusion of water in the extracellular and intracellular spaces. Differences between the apparent diffusion coefficient (ADC) can be used to discern malignant and benign lesions as well as provide functional and metabolic information that can be used to assess treatment response of neoadjuvant chemotherapy [73–75].

Breast MRI is commonly used in a clinical setting due to its high sensitivity and accuracy, improved specificity, and emerging functional information that can all be obtained volumetrically without ionizing radiation. Breast MRI is an excellent tool for lesion characterization and assessment of treatment response. However, the use of MRI for presurgical evaluation and guidance has historically been controversial. The use of MRI for surgical navigation will be expanded upon in section II.7. Once a breast cancer patient is diagnosed and staged, a plan for treatment is put into place.

II.3 Surgical Management of Breast Cancer

Treatment of breast cancer is a multimodal platform with a customized approach for each new patient. Standard treatment of breast cancer includes varying types of surgery, with or without radiation therapy, with or without chemotherapy, hormonal therapies, and targeted therapies. These treatment strategies address the following components: *a*) local treatment of the primary breast cancer, *b*) treatment of the draining lymph nodes, and *c*) systemic treatments to eradicate disease outside the breast. Surgical treatment of primary tumors is the focus of this dissertation. Therefore, other types of treatment will not be discussed in depth. Surgical options include mastectomy and breast conservation therapy.

II.3.1 Mastectomy and Breast Conservation Therapy

For decades, radical mastectomy was the gold standard for local breast cancer until 1977, when the National Surgical Adjuvant Breast and Bowel Project (NSABP) trial concluded that there are no appreciable survival differences between radical mastectomy and total mastectomies [76]. A radical mastectomy consists of removal of the breast, overlying skin, pectoral muscle, and axillary lymph nodes [77], whereas a total mastectomy involves removal of the breast only, leaving the chest wall muscles intact. This trial represented a shift in breast cancer treatment towards less radical surgery and a more multimodal approach. In 1984, a randomized prospective study comparing total mastectomies to lumpectomies with axillary lymph node dissection with or without breast radiation in patients with tumors equal to or less than 4 cm revealed that there was no statistical differences in overall survival, disease free survival, and distant disease free survival between the two groups [19]. This trial established the acceptance of breast conservation therapy (breast conservation surgery with radiation) as the preferred treatment for early stage breast cancers [76, 78]. Two 20-year follow-up studies comparing breast conservation therapy to total mastectomy and radical mastectomy had the same outcomes: no difference in survival between the two groups [79, 80]. Further studies concluded that BCT was also a viable option for non invasive cancers [76, 81, 82].

Mass breast cancer screenings with mammography has resulted in women being diagnosed at earlier stages with smaller tumors allowing for a majority of women to be eligible for BCT [83]. Factors affecting patient eligibility for BCT include tumor size to breast volume ratio, location of tumor, multicentricity, ability to achieve negative margins, ability to undergo radiation therapy, and ability to achieve an acceptable cosmetic result [84]. Multicentric tumors, persistent positive margins, diffuse

microcalcifications on preoperative mammogram, and a history of breast radiation are situations not amenable to BCT. Approximately 80% of newly diagnosed breast cancer patients are eligible for BCT [85, 86]. However, there has been an increasing trend in patients choosing mastectomy over BCT despite the equal survival benefit [87]. Studies report that 25-50% [41, 88–90] of eligible BCT patients will choose mastectomy. There have been several suggested explanations for increased mastectomy rates. Adkisson et al. attest that younger patients are more likely to pursue mastectomy compared to older women [91]. Preoperative genetic testing affects surgical decision making with women found to have a higher genetic susceptibility to breast cancer choosing to undergo mastectomy and even bilateral mastectomy to prevent recurrence [92]. Other factors contributing to the recent increase in mastectomy rates include findings during preoperative MRI, patient involvement in the decision, and an increased awareness about breast reconstruction [93, 94]. Another underlying motivator for choosing mastectomy is patient fear of recurrence and perceived survival benefit [88]. Improved surgical techniques for lumpectomy may decrease patient related fears and anxieties. Two complementary approaches to improving lumpectomy techniques with the goal of lowering reoperation rates include accurate tumor localization and real time or near real time margin assessment. Simply put, we want to know where the tumor is and then make sure that it has been completely removed. Current and emerging methods for margin assessment and intraoperative tumor localization are expanded upon in the next sections.

II.3.2 Margin Assessment

A reoperation is necessary when tumor cells are found on the borders of the tissue removed during the lumpectomy procedure. The surgical goal is to remove a volume of tissue that centrally contains the tumor with a small margin of surrounding healthy tissue. In order to confirm a successful lumpectomy, tumor margin assessment must be performed. The most common practice for tumor margin assessment is pathological assessment. Once excised, the specimen is inked using various colors or sutured to designate the anatomical orientation of the specimen and analyzed for positive margin status. If cancer cells are found on the margin, the color of the ink is used to help the surgeon determine the anatomical location that needs further resection. Negative margins, defined as “no tumor on ink”, minimizes the risk of ipsilateral breast tumor recurrence, with wider margin widths not significantly lowering this risk [95]. The American Society of Breast Cancer Surgeons recently came to an agreement that surgeons should be generally satisfied with “no tumor on ink” for invasive cancers and a 2 mm margin for DCIS

[96]. Since the adoption of the "no tumor on ink" standard, the positive margin resection rate has decreased to about 16.5% [16]. Although pathological analysis provides definitive margin status, it is unable to provide real time information on the presence of residual tumor. Therefore, intraoperative margin assessment strategies have been suggested.

Frozen section analysis has been used as an attempt to confirm negative margin status at the time of operation. In this procedure, the specimen is frozen, sliced, and analyzed under a microscope. Frozen section analysis has a reported sensitivity and specificity of 90 and 100% [97]. However, this technique takes on average 30 minutes to complete and is labor intensive, increasing surgical time, which often limits its use. Intraoperative touch prep or imprint cytology is a quicker alternative in which the surfaces of the specimen are touched to a glass slide. The slide is then screened with the assumption that malignant cells will stick to the slides and benign or healthy cells will not. This method has a sensitivity of 63-90.9%, specificity of 98.5-100%, and diagnostic accuracy of 96% [98, 99]. Intraoperative specimen radiology is another method of assessing surgical margins. This technique uses x-ray radiography to look for biopsy clips and microcalcifications close to the edges of the specimen. However, sensitivity and specificity are relatively low (49% and 77%) for this method [100]. One recent, promising approach is the practice of cavity shaving, a technique that resects a portion of the breast parenchyma immediately after the lumpectomy on margin cavities. In [101], a retrospective review of 976 cases showed that the cavity shave margins group (n=812) had 98.2% clear margins where 74.4% of the simple lumpectomy group (n=164) had clear margins. Thus, the cavity shave margins technique was shown to significantly reduce reexcisions when compared to a simple lumpectomy. Future directions in intraoperative margin assessment include optical methods such as Raman spectroscopy, optical coherence tomography, and near-infrared fluorescence optical imaging [34, 36, 38, 39]. While margin assessment techniques are needed to confirm that the tumor has been successfully removed, they are of minimal use in localizing the tumor for resection. In the next section, tumor localization strategies are introduced.

II.3.3 Intraoperative Tumor Localization Strategies

Historically, wire guided localization has been the standard technique for localizing non-palpable or clinically occult breast lesions intraoperatively. Wire guide localization consists of introducing a wire into the tumor under the guidance of mammography, ultrasound, or MRI. The wire consists of an an-

chor located at the distal end to avoid dislodging the wire during the time between wire placement and surgery. This wire then protrudes out from the breast surface until the patient is taken into the operating room. Once there, the surgeon identifies the wire trajectory using the preoperative mammogram or intraoperative ultrasound. A plan is then made to resect tissue along the trajectory of the wire stopping 1-2 cm before the distal end. Once here, the surgeon will change direction to resect around the wire tip while taking care to avoid penetrating into the cancerous lesion. Once excised, the specimen should contain the wire tip, biopsy clip, calcifications, and tumor with a surrounding margin of healthy tissue. Figure II.6a is an example of the guide wire placement protruding from the breast surface and Figure II.6b shows two mammographic views of the wire placement. These images are made available intraoperatively to help guide the surgeon.

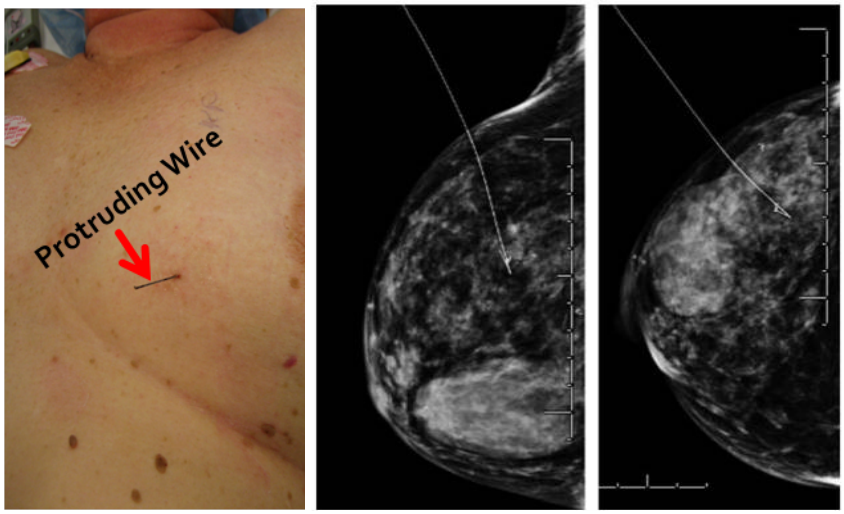

(a) (b)

Figure II.6: (a) Patient in surgical setup showing the protruding wire guide designated by the red arrow. (b) Mammographic images of the wire guide placement.

This technique has been criticized in the last several years due to the inexact nature of the procedure and high rates of positive margins (38-43%) [24, 102]. An obstacle surrounding the use of wire guide localization is that the guide wire does not provide a 3D perspective of the tumor and therefore cannot delineate tumor borders. In some cases, the trajectory of the wire is dictated by mammographic guidance and can represent inefficient surgical routes to the target which would direct the surgeon to navigate through excessive amounts of tissue or require the surgeon to make a visual estimation of a better route, both potentially leading to poor outcomes in regards to cosmesis and a clean excision.

Other problems that occur with wire guide localization include off target placement of the wire and dislodgement/movement of the wire prior to or during the surgical procedure due to specimen manipulation.

Intraoperative ultrasound is commonly used and has shown to improve BCT [25]. However, the use of intraoperative ultrasound is limited by the fact that only 50% of non-palpable tumors are visible by ultrasound in the breast [41]. Radioguided occult lesion localization (ROLL) and radio-guided seed localization (RSL) have shown promise to improve localization of clinically occult lesions. Specifically, ROLL has shown to reduce the incidence of positive margins when compared to wire guide localizations [26]. The ROLL technique injects a radioisotope into the tumor under stereotactic or ultrasound guidance. The location of the tumor can then be found using a hand-held gamma probe. The gamma probe can also be used to locate areas of higher radioactivity following excision of the tumor to identify potential remnant tumor cells. The shortcomings of radio-guided occult lesion localization is that the radioisotope must be accurately placed into the tumor and diffusion of the radiotracer into surrounding tissue decreases accuracy of the tumor location [26]. RSL is similar to ROLL except for a radioactive seed is introduced into the tumor prior to surgery. Similar seed based approaches have also been suggested using ultrasound visible markers (HydroMark,[27]) and using an implantable, infra-red activated electromagnetic wave reflector [28]. RSL and other seed-based approaches cannot provide a 3D delineation of tumor borders. Both ROLL and seed-based methods rely upon accurate injection/placement of the radioisotope under image guidance. While used in many breast cancer centers, seed-based and ROLL techniques have yet to be widely adopted. Therefore, there still exists a need for intraoperative tumor localization techniques. In the next sections, the field of image guided procedures is introduced as a novel strategy to address these localization needs.

II.4 Image Guided Procedures

Image guided surgery (IGS) is performed by placing pre-surgical images into the same 3D coordinate system as the operating room. The fundamental idea for IGS is to track the surgical position and display this location on the preoperative image. Placing preoperative images into the physical space of the operating room is done by an image processing technique known as registration. Corresponding landmarks visible in each space (both in the image and in the operating room) are used to transform images to surgical space by calculating a transformation that includes a rigid displacement and rotation.

The main components necessary for an IGS system include: a 3D physical space localizer to create a 3D coordinate system of the operating room, a preoperative image, a registration technique, and a screen with software to display the image and tracked locations. An example of such a setup is shown in Figure II.7. To initiate an image guidance system for breast cancer surgery, the integration of these components is necessary to begin preliminary testing of feasibility.

Figure II.7: Example of an image guided surgery setup showing an optical tracking system, tracked tools, and preoperative images displayed on a computer screen (image adapted from [12]).

Image guided surgery was first adopted for brain procedures. Registration between image and physical space is more readily facilitated for rigid structures, such as the skull. For procedures involving soft tissue, such as the breast, deformation between the preoperative image and operating room position is inevitable; the preoperative images no longer match the surgical reality. Research in nonrigid image to physical space registration has allowed for image guided procedures to be adapted for soft tissue applications, such as in the brain and abdomen [103–110].

A contribution of this dissertation to the field of image guided procedures involves the creation of novel image-to-physical space registration techniques and creation of a comprehensive guidance

system for breast cancer surgeries with an emphasis in patient specificity. Central to IGS techniques is the process of image-to-physical registration. In following sections, we discuss the foundations of this process. Then, a review the current state of surgical guidance using MRI in breast cancer surgery is provided.

Rigid Registration

Rigid registration can be used to establish a correspondence between the spatial information in the preoperative image volume and the operating room. Features visible in both spaces are used to perform such registrations. Two methods commonly used are point based registration techniques and surface based methods.

In point based registration, corresponding points are identified in the preoperative and intraoperative spaces. Points used for point based registrations include anatomical landmarks or synthetic fiducials adhered to the patient. An optimal translation and rotation is found that minimizes the root mean squared distances between the corresponding points. Closed form solutions for these problems exist that take advantage of singular value decomposition factorization [111]. This method relies on the assumption that for every point in the preoperative space, the exact corresponding point for the intraoperative space is known. These methods are also subjected to fiducial localization errors, or errors due to noise or uncertainty in the identification of fiducial position.

Determining corresponding surfaces rather than corresponding points between preoperative images and the operating room is another approach to calculating rigid transformations. In order to match the surface geometry in the preoperative image to the surface geometry of the patient in physical space, surface based techniques have relied on information from organ surfaces [112, 113], blood vessels [114, 115], and subsurface features extracted from ultrasound images [114, 116, 117]. Most rigid registration methods that rely on surface information are iterative in nature. That is, they search for an optimal transformation matrix that minimizes some disparity function. A method known as the iterative closest point algorithm (ICP) reduces this general nonlinear minimization problem to a series of point-based registration solves [118]. Several variants of the ICP method have been established to improve speed and increase its ability to find a global minimum [119]. The difficulty in finding true correspondence using traditional ICP methods stems from the fact that there is not enough information available to differentiate points within close physical proximity of each other. In order to address this

limitation, other techniques have been proposed. For example, areas of more reliable correspondence can be weighted to improve the registration accuracy [120]. Clements et al. weighted reliably identified salient features higher in their ICP algorithm to improve image-to-physical space registrations in image guided liver surgery [121]. Other image intensity and image texture based registration methods are used for image-to-image registration, but not discussed here as have only sparsely been applied to image-to-physical space registrations.

For procedures involving soft tissue, rigid registrations may not be sufficient due to nonrigid deformations that occur between the preoperative image and the operating room representation. In the next section, mechanics based nonrigid registration methods are introduced followed by a background on the biomechanical breast model used in this thesis.

Mechanics Based Nonrigid Registration

Biomechanical models to simulate this tissue movement have been applied in conjunction with rigid techniques to improve registration accuracy in deformable tissue. These models transform the preoperative images by simulating the physical behavior of the tissue. Data collected intraoperatively can be used to drive and constrain these models. Displacements of the tissue of interest can usually be measured intraoperatively and used to establish boundary conditions.

Biomechanically-assisted nonrigid image registration techniques have been developed for many applications. Methods for soft tissue correction of brain shift caused by changes in intracranial pressure after opening of the dura matter have been proposed to increase the accuracy of image guidance systems for neurosurgery [106–109]. Modeling of tissue retraction and resection has also been employed to update images for IGS [122]. Other avenues of soft tissue IGS application are in abdominal procedures, such as the liver and kidney [103, 105, 123], prostate [124], and in rudimentary breast applications [53]. The next section reviews the biomechanical model used in this dissertation to simulate breast tissue deformation.

II.5 Biomechanical Modeling of the Breast

The set of equations governing linear elastic deformations of the breast is shown here:

$$\nabla \cdot (G\nabla u) + \nabla(\frac{G}{1-2\nu}(\nabla \cdot u)) + \beta = 0 \tag{II.1}$$

where υ is Poisson's ratio, G is the shear modulus of elasticity ($G = E\,/\,2(1+\nu)$), u is the 3D displacement vector, and β is a body force. Solving these Navier-Cauchy equations generates a displacement field for soft tissue deformation correction. The finite element method (FEM), a method used to obtain a numerical solution to these partial differential equations, was employed. Due to the ability of FEM to handle complex geometries, the FEM is often used for applying biomechanical models to the breast and other soft tissue organs. A geometric representation of the domain must first be established in order to apply biomechanical models. This is usually done by segmenting an image volume, designating the organ of interest from surrounding structures or air and also labeling particular tissues of interest within the organ. The next step is discretization (meshing) of the organ into usually many thousands of nodal points and connecting elements that form a volumetric mesh representation of the organ. Note that standard tetrahedral elements were used in this thesis. Then application of a field quantity, such as displacement, can be applied at a node which is then interpolated across the connecting elements using polynomials [125]. A set of equations can then be established for each node and an exact solution to the approximate problem can be obtained.

The discretization process was performed using the Galerkin method of weighted residuals and begins with weighting and volumetric integration of equation II.1:

$$\langle \phi_i \nabla \cdot G \nabla u \rangle + \langle \phi_i \nabla \tfrac{G}{1-2\nu} (\nabla \cdot u) \rangle + \langle \beta \phi_i \rangle = 0 \tag{II.2}$$

where $\langle\rangle$ represents a problem domain integration. Here, ϕ_i is a scalar spatial weighting function at the ith position. After integrating by parts and application of the divergence theorem, equation II.2 becomes:

$$\langle G \nabla u \cdot \nabla \phi_i \rangle + \langle \frac{G}{1-2\nu} (\nabla \cdot u) \nabla \phi_i \rangle + \langle \beta \phi_i \rangle = \oint G \hat{n} \cdot \nabla u \phi_i ds + \oint \frac{G}{1-2\nu} \hat{n} (\nabla \cdot u) \phi_i ds \tag{II.3}$$

In this work, C^0 local Lagrange polynomials were used for the weighting and basis functions. These basis functions are used to expand the unknown displacement vector as follows:

$$u(x,y,z) = \sum_j u_j \phi_j (x,y,z) \tag{II.4}$$

Following weighting, volume integration, and substitution of the basis function, the algebraic system expressed as local coordinates at the ith equation and jth set of displacement coefficients is given by:

$$[K_{i,j}]u_j = b_i \tag{II.5}$$

where $[K_{i,j}] =$

$$\begin{bmatrix} G\langle\frac{2(1-\nu)}{1-2\nu}\partial_{xx}+\partial_{yy}+\partial_{zz}\rangle & G\langle\frac{2\nu}{1-2\nu}\partial_{yx}+\partial_{xy}\rangle & G\langle\frac{2\nu}{1-2\nu}\partial_{zx}+\partial_{xz}\rangle \\ G\langle\frac{2\nu}{1-2\nu}\partial_{xy}+\partial_{yx}\rangle & G\langle\partial_{xx}+\frac{2(1-\nu)}{1-2\nu}\partial_{yy}+\partial_{zz}\rangle & G\langle\frac{2\nu}{1-2\nu}\partial_{zy}+\partial_{yz}\rangle \\ G\langle\frac{2\nu}{1-2\nu}\partial_{xz}+\partial_{zx}\rangle & G\langle\frac{2\nu}{1-2\nu}\partial_{yz}+\partial_{zy}\rangle & G\langle\partial_{xx}+\partial_{yy}+\frac{2(1-\nu)}{1-2\nu}\partial_{zz}\rangle \end{bmatrix}$$

$$u_j = \begin{Bmatrix} u_j \\ v_j \\ w_j \end{Bmatrix}$$

$$b_i = \begin{Bmatrix} -\langle\hat{x}\cdot\beta\phi_i\rangle + \hat{x}\cdot\oint\sigma_s\cdot\hat{n}\phi_i ds \\ -\langle\hat{y}\cdot\beta\phi_i\rangle + \hat{y}\cdot\oint\sigma_s\cdot\hat{n}\phi_i ds \\ -\langle\hat{z}\cdot\beta\phi_i\rangle + \hat{z}\cdot\oint\sigma_s\cdot\hat{n}\phi_i ds \end{Bmatrix}$$

where b contains body force contributions and boundary conditions. A global stiffness matrix, K, is constructed from the contributions of each tetrahedral element. In this thesis, two types of boundary conditions are generally applied. Type I, or Dirichlet boundary conditions specify the displacement vector, u. Type II, or Neumann boundary conditions where stress is specified. The global equation, $[K]u = b$, can then be solved to resolve the unknown displacement coefficients.

Corotational Finite Element Method: In this model, we neglect the quadratic terms in the Green Lagrange strain tensor and use a linear approximation (or small strain). Due to the nature of motion and deformation in our system, strain calculations are compromised by the introduction of large rigid body rotations and translations when neglecting the nonlinear terms of the strain tensor (i.e. the linear approximation to the strain tensor is not invariant to rotation). This introduces ghost forces and distortions into the model solution. Therefore, in these cases, we employ a nonlinear corotational FEM formulation [126], which represents a compromise in terms of computational burden and accuracy between the full nonlinear strain tensor and the linear approximation. Corotational FEM models have been widely used within the soft-tissue large deformation mechanics literature [126–128]. In the coro-

tational model, large local rigid body movements are accounted for and the remaining shape change is handled by linear elastic mechanics. In the tetrahedral mesh, every element has an associated stiffness matrix K_e that is linear with respect to u. In the corotational formulation, each elemental stiffness matrix is rotated ($\tilde{K_e} = R_e K_e R_e^T$) so rigid body motions are eliminated before being deposited into the global stiffness matrix. Here, the elemental deformation gradient ($\nabla u + I$) is used to extract the local element rigid body rotation, R_e. R_e is calculated on each element through a polar decomposition of the deformation gradient, based on an assumption of the deformation field. At zero displacement (the initial assumption), a standard linear system is solved. An iterative approach is then used to solve and refine the displacement field guess. This process continues until the solution stops changing. It should be noted that in this thesis, three forward-solve iterations were used to compute R_e. Further implementation details of a biomechanical model for breast deformation as it relates to this dissertation can be found in Chapter III.

Biomechanical models of the breast employing the use of the finite element method have been developed to predict deformations during biopsy procedures [129], for modeling compression that occurs during x-ray mammography to facilitate registration between mammographic images and MR images [130–132], for reconstructing breast properties in elastography [133, 134], and for prone to supine image registration of MR images [53, 135–140]. Accurate applications of stress-strain relationships of tissue within the breast can improve the accuracy of biomechanical models that attempt to simulate breast movements. In the next section, biomechanical properties of the breast and measurement techniques to estimate these properties are reviewed.

II.6 Biomechanical Properties of Breast Tissue

The state of biological tissue can be represented by defining characteristics such as the material stiffness, compressibility, viscosity, anisotropy, nonlinearity, etc [141]. For linear elastic materials (an assumption commonly made to approximate breast tissue), the important mechanical parameters are the Young's modulus (also called elastic modulus), E, and Poisson's ratio, ν. E describes the material stiffness and ν represents the compressibility of a material. The elastic modulus is sensitive to transformations in tissue structure associated with pathological and physiological changes [141, 142]. Therefore, Young's modulus has been used as a contrast mechanism between healthy and diseased tissue.

Tissue stiffness interrogation is fundamental to breast cancer diagnosis and treatment. Furthermore, the stiffness of a material is an important variable in biomechanical models attempting to simulate soft tissue deformations. Biomechanical breast models have been employed in medical image analysis [143] for computer aided diagnostics [144], nonrigid registration for tumor tracking and data fusion [145, 146], and nonrigid registration for validation purposes[147]. Mechanical models for breast deformation have also been created for needle path and biopsy planning [148, 149], breast augmentation planning and simulation [150–152], radiation therapy targeting [153], and image guidance for breast cancer surgeries and biopsies [140, 154]. Within these applications, various material constitutive models have been used. Breast tissue has been modeled as nonlinear or linear elastic, isotropic or anisotropic, and homogeneous or heterogeneous depending on their applications, deformation magnitude, and desired accuracy. Ultimately, the stiffness of a material must be defined and the accuracy of this estimation directly impacts the overall performance of the model. Therefore, incorporating material properties of breast tissue into cancer diagnosis and biomechanical models can be beneficial. Young's modulus values have been estimated using *ex vivo* samples and *in vivo* elastography measurements for breast tissue, prostate tissue [2], liver [155, 156], muscle [157], bone, brain [158], cardiac tissue [159] and beyond. The range of Young's modulus in biological tissue is quite large, with softer adipose tissue on the order to 10^2 Pa and bone on the order of 10^7 Pa or greater [160].

Specifically within breast tissue, *ex vivo* measurements of Young's modulus vary greatly within the breast itself, especially for cancerous tissue. A recent review of the biomechanical properties of breast tissue [161] reported a large variation in the mechanical properties for glandular, adipose, ductal carcinoma *in situ*, and invasive ductal carcinomas. Variations in reported stiffness properties are mainly due to differences in testing methodologies, continuum assumptions, measurement errors, and natural inter and intra patient differences in tissue elasticity. Measurement methods for *in vivo* and *ex vivo* breast tissue mechanical properties are discussed in further detail below.

Ex Vivo

As illustrated in table II.1, there is a large variation in the reported material properties in *ex vivo* samples for glandular, adipose, DCIS, and invasive ductal carcinomas. *Ex vivo* testing is generally performed using small samples, therefore connective tissue that may play a role in bulk deformability may be ignored. It is also reasonable to expect that these *ex vivo* specimens are heterogeneous and small samples

Table II.1: Ranges of E (in kPa) values for breast tissue determined by *ex vivo* testing [1–4]

Strain (%)	**Study Label**	**Adipose (kPa)**	**Fibroglandular (kPa)**	**Ductal Carcinoma in situ**	**Invasive Ductal Carcinoma**
Unspecified	Samani (2007)	3.25 ± 0.91 N=71	3.24 ± 0.61 N=26	16.38 ± 1.55 N=16	Low-grade: 10.40 ± 2.60 N=12 Intermediate: 19.99 ± 4.2 N=21 High-grade: 42.52 ± 12.47 N=9
1	Wellman (1999)	4.8 ± 2.5 N=26	17.5 ± 8.6 N=7	71.2 ± 0 N=1	47.1 ± 19.8 N=25
5	Krouskop (1998)	19 ± 7 N=8	Glandular: 33 ± 11 N=31 Fibrous: 107 ± 31 N=18	25 ± 4 N=23	93 ± 33 N=32
	Wellman (1999)	6.6 ± 7 N=26	33 ± 12.0 N=7	188.7 ± 0 N=1	115.7 ± 19.8 N=25
10	Wellman (1999)	10.4 ± 7.9 N=26	88.1 ± 66.7 N=7	638.7 ± 0 N=1	384.5 ± 19.8 N=25
15	Wellman (1999)	17.4 ± 8.4 N=26	271.8 ± 167.7 N=7	2162.1 ± 0 N=1	1366.5 ± 348.2 N=25
20	Krouskop (1998)	20 ± 6 N=8	Glandular: 57 ± 19 N=31 Fibrous: 232 ± 60 N=18	301 ± 58 N=23	490 ± 112 N=32
Stress (kPa) 0 - 0.2	Umemoto (2014)	0.69 ± 0.19 N=29	0.79 ± 0.18 N=24	5.25 ± 0.46 N=8	13.82 ± 9.6 N=22
Stress (kPa) 1-1.2	Umemoto (2014)	19.08 ± 4.99 N=29	16.99 ± 4.92 N=24	16.15 ± 4.24 N=8	30.5 ± 11.46 N=22

may not reflect the entire tissue if there is variation. Furthermore, *ex vivo* tissue samples are likely to exhibit different mechanical behaviors than *in vivo* samples due to many factors including tissue hydration, fixation, stress relaxation and hysteresis, and tissue degeneration, among others. Most importantly, breast material properties vary greatly between subjects so generalized applications of material properties in biomechanical models used for clinical guidance is not ideal. Variations in between subject material properties can be attributed to age (more adipose, less glandular tissue [162] and breakdown of connective tissue), genetics, and hormonal changes [163]. Therefore, for procedure planning and guidance purposes, patient specific *in vivo* material property estimation is likely to result in improved accuracy.

In Vivo

In-vivo determination of material properties is generally performed using a technique known as elastography. Elastography methods rely on information gathered in images to determine tissue stiffness by capturing tissue response to a mechanical excitation and reconstructing the material properties responsible for the observed deformation. There are three main components of elastography systems: *a*) method of tissue excitation *b*) method of measuring tissue response *c*) and method of mechanical property estimation. Modalities used to measure the response of tissue to a mechanical excitation source include ultrasound [164], optical imaging [165], magnetic resonance imaging (MRI) [160], and computer tomography (CT) [166]. In general, tissue stimulation can be static/quasi-static or dynamic. Static excitations visualize the displacement induced within tissue under externally applied compressions or other mechanical sources [167, 168]. Dynamic excitations include harmonic and transient elastography methods that visualize the amplitude and phase, axial displacements, or wave velocity [160, 169, 170]. The underlying equations of motion for each approach dictates how the material properties are estimated. The method of mechanical property estimation usually reports values of tissue stiffness expressed as Young's modulus, E, (quantitative) or contrast ratios between tissue types (qualitative). Magnetic resonance elastography (MRE) uses dynamic mechanical excitation by introducing small amplitude shear waves into the tissue. These waves are then visualized by a specialized MR image sequence that has been synchronized to the mechanical excitation. The shear modulus can then be determined using mathematical inversion algorithms based on equations of motion [160]. In MRE, the shear modulus, G, is commonly reported, which for most incompressible tissue is related to Young's

modulus by $E = 3G$.

Ultrasound strain imaging [171], provides relative values of stiffness by estimating the strain through measurements of local displacements by compressing the tissue with the ultrasound transducer. Shear wave ultrasound elastography can provide quantitative elastic property values. Instead of compressing the tissue with the ultrasound probe, shear wave ultrasound techniques use acoustic radiation force impulses (ARFI) to cause localized displacements in the tissue [172]. Conventional b-mode imaging is used to capture the displacement of the tissue that ultimately relates to stiffness. Virtual Touch [173] quantification provides numerical values (shear wave-velocity values) of tissue stiffness. A limitation of ultrasound is that estimation of strain is confined to the ultrasound image plane. Depending on the application, quantitative stiffness values may be desirable. Measuring tumor response to therapy, between subject tissue stiffness comparison, characterization of different tissue types, and finite element biomechanical models that use type II boundary conditions are examples of scenarios which benefit from quantitative stiffness values.

Dynamic stiffnesses (such as determined in shear wave MRE) can be useful in diagnostic contexts as a contrast mechanism between diseased and healthy tissue, but less important for clinical procedures that involve quasi-static loading. Biological tissue properties are known to exhibit complex behavior, especially when different mechanical excitation sources are applied. It has been well documented that large compressive forces and high frequency shear waves result in higher observed stiffness values [161, 174]. While diagnostic imaging is often performed under compression with the patient standing (x-ray mammography) or lying prone with freely hanging breasts (MRI) , a majority of therapeutic interventions are performed in the supine position (tumor removal and breast augmentation surgery, radiation therapy, biopsy, etc). In summary, gravitation loading and compressive forces applied in diagnostic exams are not representative of the surgical patient presentation.

Mechanical property estimations using patient specific biomechanical models with "known" boundary conditions have been previously developed to represent stiffness properties under deformations seen in specific applications (such as mammographic compression or prone-supine registration). These methods rely on creating a patient specific biomechanical model of the breast in one configuration, applying known boundary conditions, and adjusting material parameters until the model deformed data matches the experimentally acquired deformed breast configuration. In this context, loading conditions are either gravity induced or compressive in nature.

In [167, 175], a new approach to elasticity imaging was described using compressive forces, biomechanical modeling, and principles of nonrigid registration. The technique, known as modality independent elastography (MIE), uses image volumes before and after an externally applied deformation. A deformable image registration algorithm [176] is performed to generate a deformation field between the undeformed and deformed breast surfaces. A biomechanical model that makes isotropic and Hookean linear elasticity assumptions is used to simulate breast deformations between the undeformed and deformed image volumes. Displacement boundary conditions are prescribed on the whole breast surface using the displacement map generated in the nonrigid image registration step. A distribution of relative elasticity values is reconstructed by minimizing an image volume similarity metric. The method has been investigated in simulation [166, 167, 177], gel phantoms [178], and murine models [179]. Clinical applications of the approach have been applied in breast [180–182], liver [183], and dermoscopy [184] contexts. In [185], a similar framework to MIE was used to estimate relative breast tissue properties for use in simulating large breast deformations. Due to the use of displacement boundary conditions, MIE and other similar methods result in qualitative stiffness values.

II.7 Breast Cancer Surgical Navigation with Preoperative MRI

The use of preoperative MR images for surgical planning has historically been controversial. Previous studies report that retrospective data and randomized trials have not shown preoperative MRI to reduce re-excisions, lower recurrence rates, or improve survival benefits [186–191]. Many argue that preoperative MRI is associated with an increase in the use of mastectomy, delay in treatment, and an increase in the number of additional biopsies [63, 64, 188] and therefore should not be routinely used for preoperative planning purposes. Alternatively, several studies have disputed these claims arguing that MRI provides invaluable information regarding the extent of disease. A recent prospective, randomized, multicenter study reports a significant decrease in reoperation rates between women who received a preoperative staging MRI vs. women who did not receive an MRI prior to lumpectomy [192]. Sung et al. published a retrospective analysis that concluded that reoperation rates among BCT patients were lower for women who received a preoperative MRI [193]. Several other studies report positive findings for improved preoperative staging using MRI [192–196]. Overall, the argument surrounding the value of preoperative MRI remains inconclusive. However, it is generally agreed upon that MRI provides the most accurate delineation of the size and extent of cancer and offers the highest sensitivity for intraduc-

tal extensions involved in invasive cancers. One confounding factor involved with the use preoperative MRIs are how the images are presented to the surgeon for guidance. As previously discussed, preoperative MR images are acquired in the prone position with pendulous breasts while surgery is performed with the patient lying supine. Several studies have reported significant displacements in breast tumors between the prone and supine positions on the order of 18-60 mm [46–48]. These relatively large displacements render prone MR images sub-optimal for use in surgical planning and navigation, which may contribute to studies finding little to no benefit of preoperative MRI.

Due to these realizations, several groups have investigated the use of preoperative MR images rendered in positions that more closely represent the surgical orientation. Prone-to-supine registration methods of MR images for use in image guided breast surgery have been developed [53, 135–140] . A more direct approach is to use supine MR images to direct surgery, which has been explored by several groups. Tozaki and Fukuda reported that acquiring preoperative supine MR images may be useful for the planning of breast conservation therapy [49]. An approach to breast conserving surgery that uses a projection technique to reproduce an outline of the lesion on the breast surface using the location of the tumor based on the preoperative supine MRI was described in [50]. Yamashiro et al. presented a technique that uses supine MRI to modify resection lines for tumors with unclear margins by ultrasound [51]. Abe et al. made use of a thermoplastic shell to reproduce the preoperative breast shape in the OR to mark the location of the tumor based on the preoperative supine MRI [52]. Intraoperative MRI for breast cancer surgery was evaluated by [197, 198]. However, intraoperative MRI surgical suites are not present in most hospitals across the U.S.

Registration of preoperative supine MR images to physical space in the operating room for MRI navigated breast surgery has been another avenue of development. Frameworks using prone-to-supine registration followed by supine image to physical space registration have been described [53, 138]. Alderliesten et al. used preoperative supine MR images and optical tracking technology to quantify needle tip position uncertainty for radioactive seed localization procedures and demonstrated that using preoperative supine MR to demarcate breast cancer in the operating room is feasible [54]. Alignment of pre-surgical supine MR images to surgically oriented MR images using surface markers has been shown to be feasible [55]. Preoperative supine MR images rigidly registered using surface markers coupled with an intraoperative optical scan of the breast has also demonstrated qualitative alignment value [46]. While developments in image guided surgical systems for breast cancer surgeries have been

encouraging, the integration of supine MR images, optical tracking and digitization technology, patient specific biomechanical models for nonrigid registration, and tracked ultrasound for subsurface feature localization have yet to be realized as a surgical guidance platform for breast conserving surgery.

CHAPTER III

Research Methods

This section outlines the methods used to collect preoperative data and intraoperative measurements. Also detailed here is the generation of patient specific finite element meshes from preoperative images, the processing of ultrasound images, the general approach to rigid registration using adhesive fiducial markers, and the biomechanical model employed in nonrigid deformation correction. Finally, a variety of validation and error metrics is described.

III.1 Preoperative Measurements

Magnetic Resonance Imaging

Magnetic resonance images (MRI) of the breast are typically acquired with a dedicated breast coil with the patient lying in the prone position with freely hanging breasts. However, supine MR images are also desirable because they more closely represent the surgical position. For each orientation, the patient is carefully positioned in a closed bore 3T Achieva MR scanner (Philips, Healthcare, Best, The Netherlands).

Prone MRI

For the prone images, the subject is placed on a MammoTrack table with a 16-channel receive double-breast coil (Philips Healthcare, Best, The Netherlands). A THRIVE (T_1-weighted, **h**igh **r**esolution **i**sotropic **v**olume **e**xcitation) sequence with fat suppression is used to acquire high resolution anatomical scans of the breast. The following MR parameters are typically used with these scans: repetition time (TR) = 6.5 ms, echo time (TE)= 3.4 ms, field of view (FOV)= 192 mm $\times$ 192 mm $\times$ 160 mm, matrix size = 384 x 383, scan time (mm:ss) = 02:48, and number of signal averages (NSA)=1.

Supine MRI

A 16-channel sensitivity encoding torso coil (SENSE XL Torso Coil, Philips Healthcare) is situated carefully as to not deform the breast, and the ipsilateral arm is placed above the patient's head to more closely replicate the surgical presentation. Supine image volumes are acquired with: TR=7.422 ms,

TE=3.91 ms, and flip angle= 10 degrees using SENSE parallel imaging (acceleration factor = 2). High resolution anatomical images are acquired with a T_1-weighted, 3D turbo field echo sequence with fat suppression, a field of view of 200 mm $\times$ 200 mm $\times$ 160 mm, and a reconstructed voxel size of 0.391 mm $\times$ 0.391 mm $\times$ 1 mm. The duration of each image volume acquisition was 120.6 seconds.

To facilitate accurate tumor segmentation when imaging breast cancer patients, contrast enhanced images can be obtained. The basic procedure for obtaining contrast enhanced images include taking a baseline image, injecting an intravenous contrast agent, followed by another image acquisition. More specifically, a catheter placed within an antecubital vein delivers 0.1 mmol/kg of Magnevist at a rate of 2 mL/s after the acquisition of the baseline image. After a 90 second wait period, another image is obtained. The pre and post contrast images are post processed to obtain an objective segmentation of the tumor based on increased signal intensity due to contrast. The enhancement in the tumor region can be quantified as percentage enhancement, calculated as:

$$\frac{SI_{post} - SI_{pre}}{SI_{pre}} \times 100 \tag{III.1}$$

where SI_{pre} is the signal intensity in the region of interest in the pre-contrast enhanced image and SI_{post} is the signal intensity in the region of interest in the post-contrast enhanced image. Figure III.1 shows a preliminary acquisition of a contrast enhanced supine MRI. Figure III.1a shows an axial slice prior to contrast injection. From this image, it is difficult to distinguish between glandular tissue and tumor (both with brighter signal). In the post contrast image (Fig III.1b), the tumor signal is higher than the glandular tissue. Figure III.1c shows an overlay of the enhanced tumor as a hot colormap. Figure III.1d shows the 3D segmentation of the tumor. The percent enhancement in the tumor region for this particular acquisition was 160%.

Building Patient Specific Models from MRI Volumes

Segmentation of the MR volume into breast tissue, tumor, and chest wall is performed using the Insight Registration and Segmentation Toolkit (ITK-SNAP) [199] or Analyze 9.0 (Mayo Clinic Rochester, MN, USA). Figure IV.10c illustrates the segmentation of a preoperative supine MRI of a patient volunteer. In this step, various features of the breast can be designated for use in future registration steps and registration accuracy measurements. The location of the fiducial marker centers in the images are

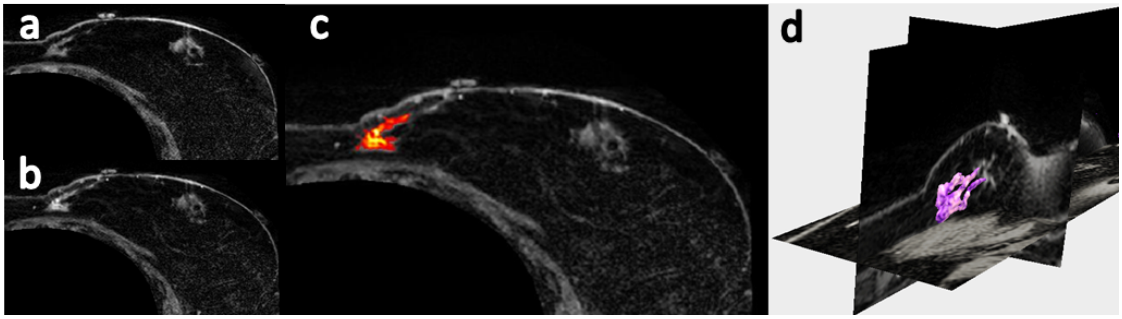

Figure III.1: Axial slices of supine MRI of patient volunteer using ”Supine MRI” imaging parameters from section III.1. (a) pre-contrast anatomical image, (b) post contrast anatomical image, (c) shows an overlay of the enhanced tumor as a hot colormap, and (d) shows a 3D segmentation of the tumor in magenta.

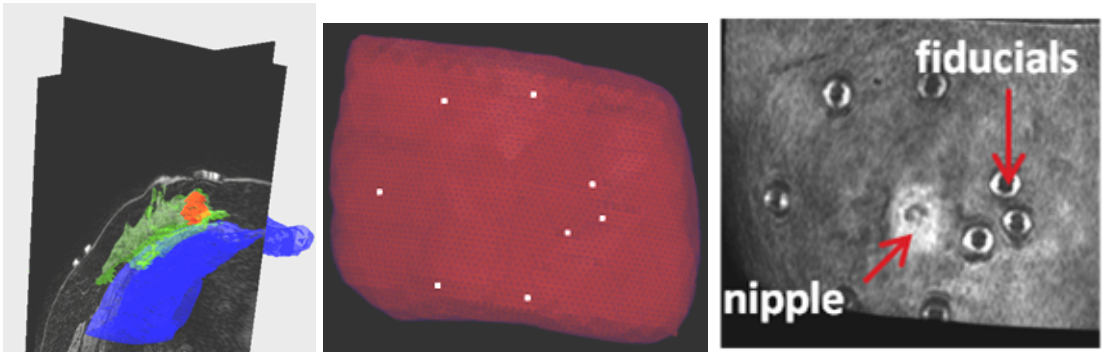

(a) (b) (c)

Figure III.2: Segmentation of preoperative supine MR images: (a) segmentation of glandular tissue in green, chest wall in blue, and tumor in red. (b) is a volume rendering of the supine MR image, and (c) is the preoperative mesh showing locations of fiducial centers in white.

determined manually and recorded. Following segmentation, a binary mask of the whole breast can be used to generate an isosurface using a standard marching cubes algorithm [200]. The marching cubes algorithm has been implemented using the Visualization Toolkit (VTK) [201], a collection of open source c++ libraries. Once a surface has been generated, it is smoothed with a radial basis function using the FastRBF Toolbox (Farfield Technologies, Christchurch, New England). A volumetric finite element mesh is created from this surface using a custom mesh generator [202]. An example mesh is shown in Figure IV.10 with white points representing fiducial marker centers. The adhesive fiducial markers can be seen in the volume render of a supine MR image shown in Fig IV.10b.

III.2 Intraoperative Measurements

Establishing a 3D Coordinate System within the Operating Room

To establish a 3 dimensional coordinate system within the operating room, a spatial localizer that determines the pose (location and orientation) of selected rigid objects is needed. In this work, a passive optical tracking system is used due to its large field of view, high measurement accuracy (0.3 mm RMS [1]), and compatibility with most operating suites. A Polaris Spectra (Northern Digital, Waterloo, ON, Canada) is used to make all geometric measurements. This optical tracking system detects the location of retro-reflective spheres by emitting infrared light and detecting the reflections off of the spheres. Figure III.3a (top) shows a Polaris Spectra and Figure III.3b shows its working volume. Figure III.3a (bottom) shows various tools that can be tracked by localizing the reflective spheres. Varying geometries of the reflective spheres allows tracking of several different objects at once. The limitation of using passive optical tracking is that a direct line of sight is needed to track an object. The interface software used to obtain and save geometric measurements include NDI ToolBox [2], NDI 6D Architect[3], and custom software developed at Vanderbilt by the Biomedical Modeling Lab and Surgical Navigation and Aparatus Research Lab.

Digitization of the Breast Surface

The geometric position of the breast surface in the operating room is likely different than the breast position in the preoperative images. Therefore, robust measurement of the breast surface in the intraoperative state is necessary to facilitate image to physical space registration. Breast surface measurements can drive registration, provide boundary conditions for biomechanical models, and assess surface fit between the preoperative and intraoperative surface following registration. A summary of the surface digitization methods that have been surveyed using phantoms, healthy volunteers, and breast cancer patients is provided. A tracked pen probe (Figure III.4a) can be used to digitize points on the breast surface such as fiducial markers that are used in point based registration. The pen probe can also create a sparse sampling of the breast surface by swabbing the probe over the surface while tracking the probe

[1] More information on Polaris Spectra technology can be obtained at http://www.ndigital.com/medical/products/polaris-family

[2] Northern Digital, Waterloo, ON, Canada. More information on this software can be found at www.ndigital.com/medical/wp-content/uploads/sites/4/2013/09/nditoolbox.pdf

[3] Northern Digital, Waterloo, ON, Canada. More information on this software can be found at www.ndigital.com/medical/wp-content/uploads/sites/4/2013/09/devkit_6da_web.pdf

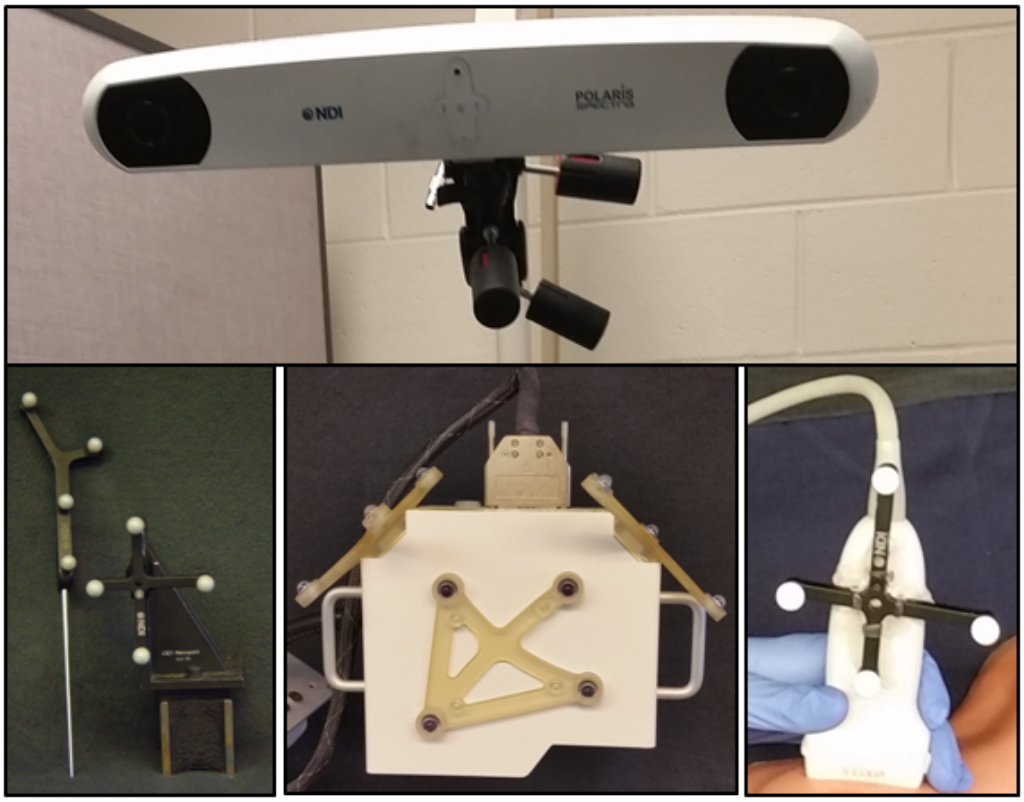

(a) Polaris (Top). Pen probe digitizer, reference body, laser range scanner, ultrasound probe (Bottom- from left to right).

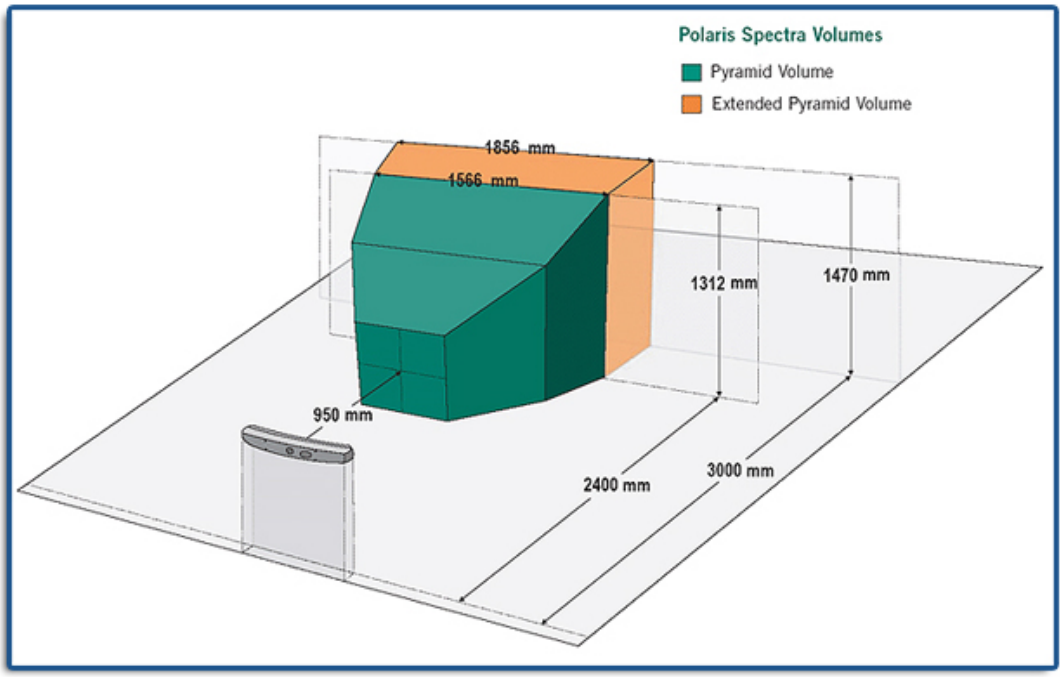

(b) Working volume of Polaris Spectra

Figure III.3: (a) Polaris spectra with examples of tracked tools. (b) Working volume (NDI Medical, www.ndigital.com/medical/products/polaris-family/features/measurement-volume)

location. Fig III.4a (bottom) shows the results of a pen probe swab on a volunteer. A dense 3D point cloud with operating room coordinates and texture information can be obtained using a tracked laser range scanner (LRS). The LRS works by sweeping a laser line over the surface of the breast while a camera captures the shape of the laser line. A textured 3D point cloud is formed by triangulation of the locations of the laser line and mapping color information captured by the camera to each point in the point cloud. The use of a tracked LRS is desirable because it can acquire the breast surface with a relatively fast, dense sampling and without tissue deformation caused by contact. The overall accuracy of our custom built laser range scanner was tested in [203] and was reported to be approximately 2 mm. Figure III.4b shows the LRS and also a textured 3D point cloud that has been registered and overlaid on the transparent breast model built from the preoperative MR volume of a volunteer. Another way to obtain surface shape is by swabbing the breast with a tracked ultrasound transducer. This produces a slightly denser sampling than the pen probe, but is undesirable due to compression of the breast surface by application of the ultrasound transducer. This can be seen in Figure III.4c where the green points show the measurements made by tracked ultrasound and are located slightly below the registered preoperative breast.

Subsurface Digitization

Subsurface features such as tumor, glandular tissue, cysts, and chest wall muscle can be digitized by tracked ultrasound. Figure III.5 shows b-mode ultrasound images of chest wall muscle, tumor, and cyst, and a strain image of a tumor. Ultrasound data is tracked in the operating room by synchronizing the ultrasound video as displayed by the ultrasound machine and tracking data captured by the optical tracking system discussed in section III.2. A passive rigid body with retro-reflective spheres was firmly attached to the ultrasound probe to make pose measurements. The tracked ultrasound was calibrated using a method developed by [204] that takes multiple b-mode ultrasound images of a tracked stylus tip in the imaging plane to develop a rigid transformation between the image plane and physical space. Once calibrated, all pixels in each image have a 3D coordinate and orientation. All ultrasound images were acquired using an Acuson Antares ultrasound machine (Siemens, Munich, Germany) using a VFX13-5 linear array probe set at 10 MHz. Strain images can also be captured using the eSie Touch elasticity software in the ultrasound unit.

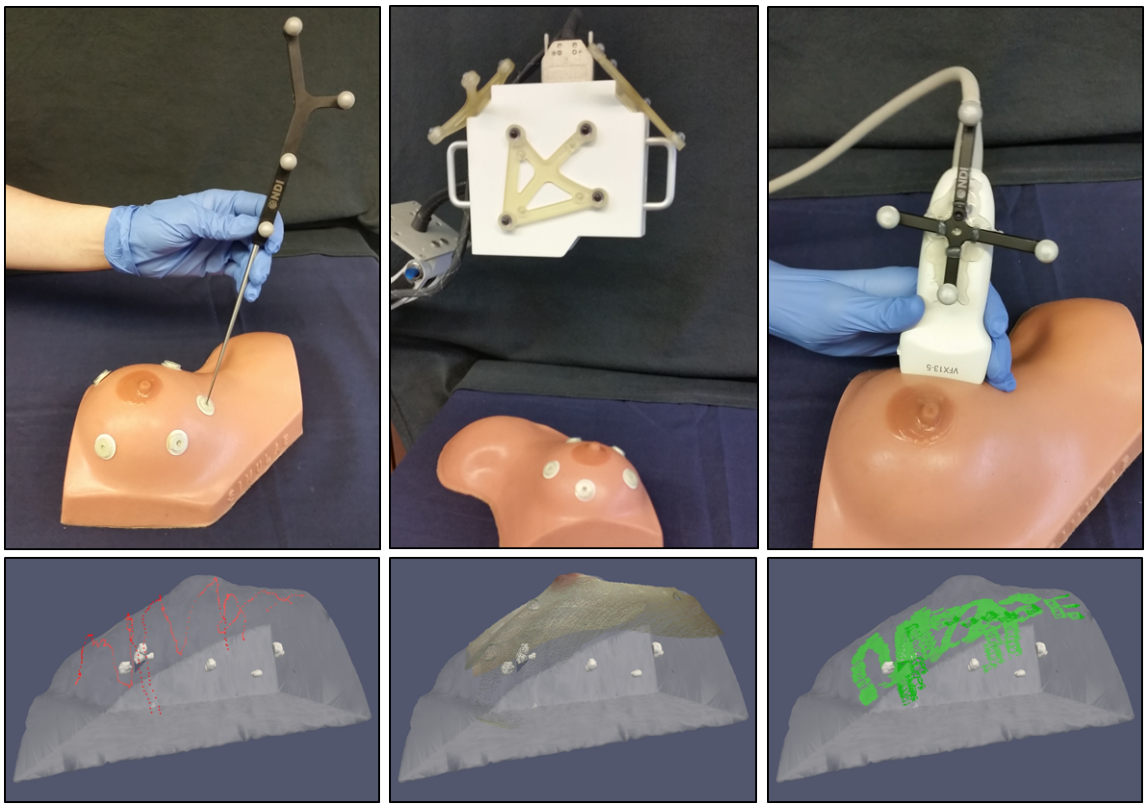

(a) Tracked pen probe (b) Tracked laser range scanner (c) Tracked ultrasound probe

Figure III.4: Surface digitization tools are shown in the top panels. Each tool has a different geometry of retro-reflective spheres for tool differentiation during simultaneous tracking. The lower panels show example points collected from each tool. Each set of points is overlaid onto a co-registered 3D mesh of a volunteer with benign cysts. (a) The top panel shows the tracked pen probe and the lower panel shows the sparse data points (red) that can be collected while swabbing the breast surface with the pen probe. (b) The top panel shows the tracked laser range scanner and the bottom image shows the dense 3D textured point cloud that is obtained by scanning the breast surface with the LRS. (c) The top panel shows the tracked ultrasound probe and the bottom panel shows the points (green) collected from swabbing the surface of the breast with the tracked ultrasound transducer.

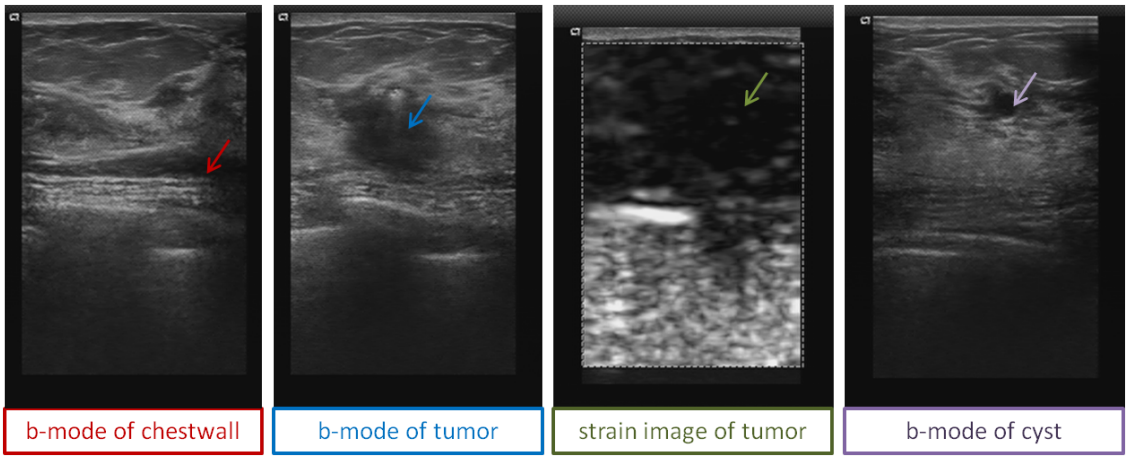

Figure III.5: This figure represents a panel of images that can be collected by our ultrasound machine. Features of interest in this proposal are shown in these images such as: chest wall (red arrow), tumor in b-mode (blue arrow), tumor in a strain image (green arrow), and a benign cyst (purple arrow).

Ultrasound Image Processing

Features in the ultrasound images, such as those shown in Fig III.5, can be segmented to obtain feature contours. Segmentation of ultrasound images is performed by a custom implementation of the Livewire technique [205]. Livewire segmentation is a semi-automatic segmentation method that automatically contours an image based off three or more control points.

Compression of the breast tissue by the ultrasound transducer leads to incorrect measurements of tumor size and location. In this work, a previously developed biomechanical model based correction scheme [206] is implemented to compensate for the compression of the target by the ultrasound transducer. The method utilizes the position of the tracked ultrasound probe to measure 3D displacements to drive a linear elastic model. The relative positions of the probe surface can be used to estimate the displacement of the breast tissue. Once a registration is made between the patient specific MR mesh and physical

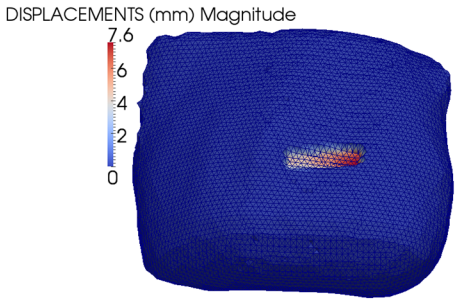

Figure III.6: Example simulation of displacement caused by the ultrasound transducer. The color bar indicates the magnitude of displacement with larger displacements shown in red. An area of larger displacement is shown on the mesh indicating the position of the co-registered ultrasound probe and amount of applied compression.

space, the ultrasound probe is now in the same space as the mesh. The probe surface will be located slightly below the surface of the mesh, depending on the compression of the tissue by the user. The pose of the probe surface provides displacement boundary conditions for a forward linear elastic model that deforms the patient specific mesh to the compressed state exerted by the probe. A deformed mesh showing displacements caused by ultrasound probe compression is shown in Fig III.6. The deformation field generated by this model is then applied in reverse manner to deform/correct the ultrasound slices and the segmented tumor contours such that they are correctly rendered in the uncompressed state associated with the pre-procedural supine MR orientation. Figure III.7 provides a visual overview of

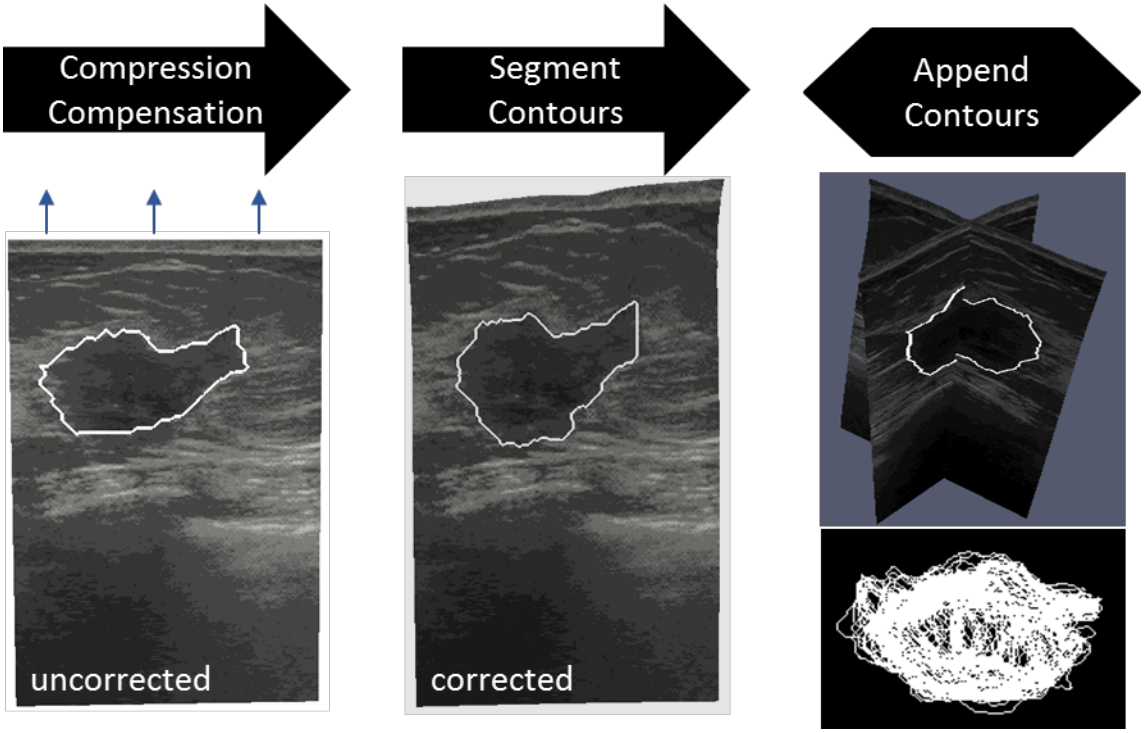

Figure III.7: Steps involved in processing tracked intraoperative ultrasound data. The ultrasound images are first corrected for tissue compression exerted by the ultrasound transducer. The tumor contour is then segmented in each 2D slice. Lastly, all contours are appended to form a 3D representation of the intraoperative tumor.

the processing steps involved in acquiring tracked ultrasound data of an intraoperative tumor volume. Contours of the tumor are created for each 2D b-mode image and are then corrected for probe deformation. All of the corrected contours are then appended to create a 3D representation of the intraoperative tumor geometry as a point cloud set.

III.3 Breast Tissue Stiffness Estimation

In this section, an additional piece of data is added to the IGBS framework. Beyond anatomical image volumes, highly resolved meshes, and contrast enhanced image data, the elastic properties of the patient's breast are quantified and incorporated into the IGBS arsenal. Here, an image-derived computational framework to obtain quantitative, patient specific stiffness properties was developed to incorporate patient specific stiffness parameters into the nonrigid registration framework. The method uses two MR acquisitions of the breast in different supine gravity-loaded configurations to fit mechanical properties to a biomechanical breast model. First, the change in gravitational loading is quantified between a baseline and gravity-induced deformation image. This gravity-induced deformation results from slightly rotating the volunteer along the longitudinal axis of the body by placing a support wedge posterior to the breast being imaged. After the change in gravitational loading is quantified, a biomechanical model is used to deform the gravity-induced image until it matches the baseline image. This can be done through a systematic parameter sweep or using an optimization procedure to minimize the residual error between the model-deformed image and baseline images.

This section outlines the pre-processing steps required to obtain the patient specific stiffness values. The chest wall is assumed to be a reliably rigid structure in relation to breast tissue. Therefore, rigid alignment using chest wall intensity information is performed to extract the relative rotation that occurred between the baseline configuration and the torso rotated image configuration. The following image processing steps were performed to extract the geometric change of the breast relative to the direction of gravity:

1. **Segment the chest wall muscles in each image**:

   The chest wall is semi-automatically segmented in each image using ITK-SNAP's implementation of the Snake's algorithm [207].

2. **Rigidly register the baseline and gravity-induced images**:

   A standard rigid registration [208] is performed using image contrast patterns of the *chest walls* in the two image volumes to transform the baseline image (I_{g1}) into the gravity-induced configuration space (I_{g2}). Fig. III.8 displays a representative result of such a registration. I_{g1} and I_{g2} chest wall image masks are highlighted to show the driving components of the registration (Fig. III.8a,III.8b). The transformation matrix (containing translation, t and rotation, R) is used

to rigidly align the baseline image to the gravity-induced configuration image (Fig. III.8c). An overlay of the gravity-induced (I_{g2}) and registered baseline images ($I_{g1\rightarrow g2}$) are shown in Fig. III.8d and visually confirms that the chest wall muscle beneath the breast rigidly aligns compared to the breast tissue above that has deformed due to the difference in gravitational loading. Once aligned, rigid translational components are accounted for and the remaining tissue dissimilarity is due to rotational components that arise from gravity-induced deformations.

3. **Extract gravity differential vector:**

   The gravity differential vector can be extracted from the rotation matrix using (III.2):

$$\Delta\hat{g} = \hat{g}_1 - R * \hat{g}_1 \tag{III.2}$$

$$\beta = 9.8\frac{m}{s^2}\,\rho\,\Delta\hat{g} \tag{III.3}$$

   where $\hat{g}_1$ is assumed to be unit vector normal to the MR table. In (III.3) , β is subsequently applied as a body force of tissue weight in the biomechanical model (II.1). The tissue density, ρ is assumed to be uniform and approximately equal to water,1000 kg/m^3. The model nodes associated with the chest wall are fixed in the x, y, and z directions, i.e. applied Dirichlet boundary conditions set to zero.

The stiffness estimation process involves generating an eroded binary mask of the torso-rotated image volume for the purpose of designating zones in which to compute an image similarity metric between the model deformed image and the chest wall aligned baseline image. The Youngs modulus values for adipose and fibroglandular tissue are then estimated by either performing an exhaustive search of the parameter space or by using an optimization procedure to minimize the image similarity metric defined by eq. (III.4).

$$S = (1 - CC) \tag{III.4}$$

where S is the similarity metric to be minimized and CC is the image correlation coefficient defined by equation III.9 in the following section. Once completed, a set of patient specific stiffness properties have been obtained prior to surgery. These properties are to be incorporated to increase the accuracy of the mechanics-based nonrigid image-to-physical space algorithm. In the next section, error analysis

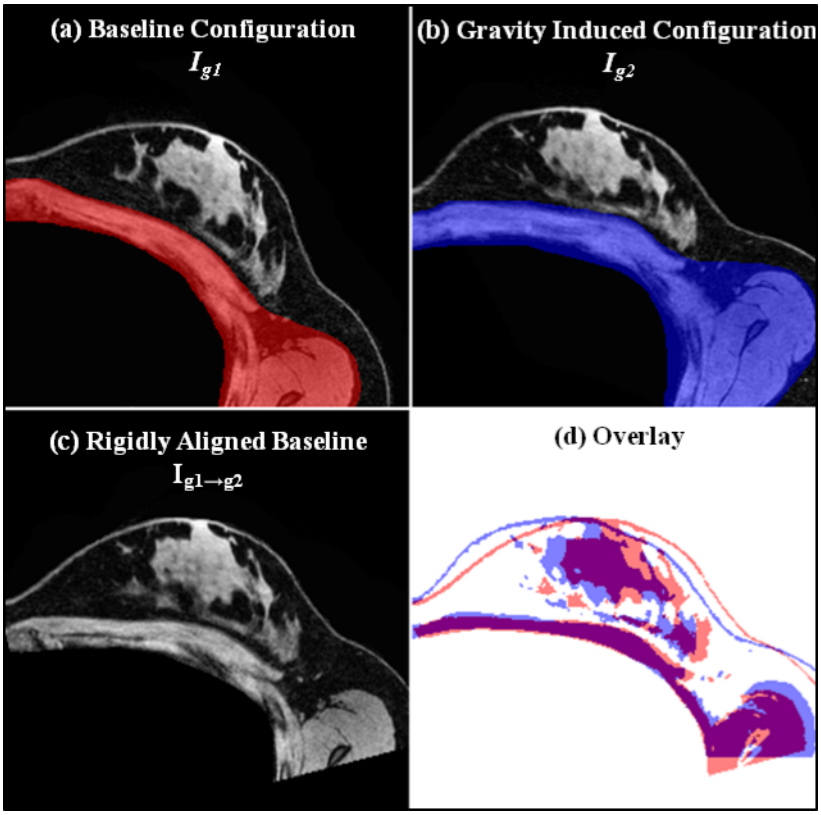

Figure III.8: Representation of the rigid alignment procedure. Central axial slices are shown of the (a) baseline configuration image, and (b) gravity-deformed configuration with overlays of chest wall regions used in initial alignment. The transformation matrix extracted from the rigid registration is used to align the chest walls in the baseline configuration and the gravity-deformed configuration so that the resulting misalignment of breast tissue is due to deformations caused by the change in gravitational loading. In (c), we see the aligned baseline to the gravity-induced reference frame, and (d) contains image masks of the rigidly aligned baseline image ($I_{g1 \rightarrow g2}$) (red) and gravity deformed image (I_{g2}) (blue). It is clear that the chest wall is relatively rigid compared to the mismatch in breast tissue structures due to gravity induced nonrigid deformation.

metrics for quantifying registration accuracy and image volume alignment are discussed.

III.4 Error Metrics

Signed Closest Point Distance Maps

The fit between two co-registered surfaces can be reported as a signed closest point distance map. Positive values indicate areas where the intraoperative surface lies on top of the co-registered patient specific mesh. Negative values represent points that lie beneath the co-registered mesh surface. A colormap representing the signed closest point distances overlaid onto the co-registered mesh can highlight areas

of poor alignment. An example of such a map is shown in Figure III.9.

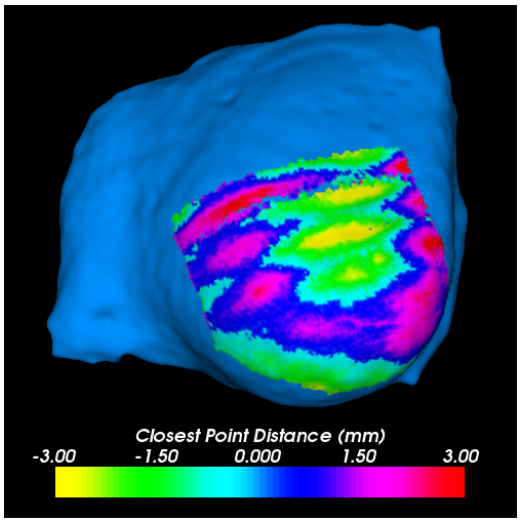

Figure III.9: Example of a signed closest point distance map. The blue surface is a finite element mesh built from a preoperative MR image volume of a patient volunteer. A patch of co-registered intraoperative surface (digitized by the laser range scan) was used to calculate the signed closest point distances between the two surfaces.

Modified Hausdorff Distance (MHD)

The subsurface tumor registration accuracy can be measured by comparing the location of the tumor contour in the compression corrected ultrasound image and the tumor contour in the MR volume. The segmented MR tumor is re-sliced to provide a co-planar MR slice according to the 3D location and orientation of the co-registered ultrasound slice. Measurements made between the MR contour and the US contours are planar (2D). The modified Hausdorff distance (MHD) [209] between the MR tumor contour and the US image contour is defined for two contours, A and B in accordance with equations IV.2 and IV.3.

$$d(A,B) = \frac{1}{N_a} \sum_{a \varepsilon A} min_{b \varepsilon B}(||a-b||) \tag{III.5}$$

$$MHD = max(d(A,B), d(B,A)); \tag{III.6}$$

The mean closest point distance $d(A,B)$ is calculated in the direction from A to B, and then again from B to A. MHD is the maximum mean closest point between the two contours. This method was used in section IV.2.

Centroid Distances

Comparisons between the mapped preoperative and tracked ultrasound digitized intraoperative tumor contours can be made in 2D or 3D. For 2D calculations, the centroid location of a co-planar MR slice tumor contour is compared to the centroid location of the co-registered ultrasound slice tumor contour. Several ultrasound slices can be analyzed in this manor. This method was used in section IV.2. For 3D comparisons, the centroid location of the mapped preoperative segmented tumor is compared to the centroid location of the appended 3D tracked iUS tumor contours (processed as shown in Fig. IV.12). This method was used in section IV.3.

The centroid of a finite number of points is computed as follows:

$$C = [C_x, C_y, C_z] = \frac{\sum_{i=1}^{k} [P_{ix}, P_{iy}, P_{iz}]}{k} \tag{III.7}$$

where k is the number of points in the domain and P_i is a point in space. Using equation IV.7, The Euclidean distance ($l_2 - norm$) between the intraoperative tumor centroid ($C_{intraop}$) and preoperative tumor centroid (C_{preop}) was used to measure target registration error: Centroid Difference= $||C_{intraop} - C_{preop}||$.

Dice Similarity Coefficient (DSC)

The Dice Similarity Coefficient (DSC) [210] is a measurement of region overlap and can be used to measure the agreement between the mapped preoperative tumor location and the intraoperative tumor location. The DSC is defined by the union of two sets of points divided by the average size of the two point sets:

$$DSC = \frac{2N(A \cap B)}{N(A) + N(B)} \tag{III.8}$$

In equation III.8, N represents the number of points enclosed in each set. A and B represent the tumor point sets in the intraoperative space and preoperative space, respectively.

Image Similarity: Correlation Coefficient (CC) and Mutual Information

The image correlation coefficient is a measure of image similarity in which the intensity in I_{1i} and I_{2i}

is assumed to be linearly related.

$$CC = \frac{\sum_i (I_{2i} - \bar{I}_2)(I_{1i} - \bar{I}_1)}{\sqrt{\sum_i (I_{2i} - \bar{I}_2)} \sqrt{\sum_i (I_{1i} - \bar{I}_1)}} \tag{III.9}$$

where I_{2i} and I_{1i} are the intensity values at pixel i for the model deformed and chest wall aligned baseline images, respectively. $\bar{I}_2$ and $\bar{I}_1$ are the mean intensity values of the model deformed and chest wall aligned baseline images. CC has a value of 1 if two images are absolutely identical and a value of zero if completely uncorrelated.

Mutual information (MI) [208] is a measure of dependence between image A and image B with the relationship according to (III.10):

$$MI(A,B) = \sum_{a,b} p_{AB} log \frac{p_{AB}}{p_A \cdot p_B} \tag{III.10}$$

where p_{AB} represents the joint probability distribution, and p_A, p_B are the marginal probability distributions. Maximization of MI is used to register images and is especially useful for registering images of different modalities.

CHAPTER IV

Framework for Image Guided Breast Surgery

IV.1 Summary and Contributions

The intent of this chapter was to survey the data collection techniques that are available for integration into the guidance system and to identify the components that when integrated provide the best overall performance and accuracy. The following sections describe the development of an image guidance system that integrates supine MR images, optical tracking and digitization technology, patient specific biomechanical models for non-rigid registration, tracked ultrasound for subsurface validation, and performs initial validation on breast cancer patient data. The work herein contains the first comprehensive description of system components involved in a surgical guidance system for breast cancer surgery. The extent of available data that can be incorporated into registration frameworks for image guided breast surgery is also reported. The use of intraoperative ultrasound to measure subsurface registration accuracy in the context of image guided breast surgery is also first reported here. Finally, preliminary studies on breast cancer patients under appropriate clinical conditions demonstrating system feasibility are presented.

In section IV.2, a preliminary study was performed on one patient using only rigid registration to judge the feasibility of using supine magnetic resonance images to guide surgical procedures for breast cancer. This study served as an initial attempt to align intraoperative data and preoperative data for breast conserving surgery. A very important methodology for the rest of this thesis work was developed in this study: the novel use of tracked intraoperative ultrasound digitized tumors to measure subsurface registration errors in the context of image guided breast surgery (see Figure IV.6).

In section IV.3, a study that builds upon the work completed in section IV.2 explores the importance of including nonrigid methods into the registration framework. Here we present two patient subjects as an initial investigation towards the realization of a biomechanical model assisted surgical platform. This section employs the use of a novel biomechanical model based nonrigid registration to correct preoperative patient specific models and images to better match the surgical presentation of the breast. The model presented in this chapter was purposefully designed to be work-flow friendly and establish a baseline understanding of the capability of a model-based correction technique. The significance

of this work is that it is the first full description and implementation of a comprehensive system for image guided resection of breast tumors. This work is the first to incorporate the chest wall as a rigid feature to improve alignment. In this study, we identified several areas of future investigation. For example, based off of the two patient cases reported here, significant variances in breast deformation can occur between patients of different breast sizes and of different mechanical properties(see Figure IV.15). Therefore, we identified a need to observe the deformation of the breast as it correlates to breast size, patient age, and breast density. We also found that the next obvious progression of this work is to improve the model approach for nonrigid correction by incorporating patient-specific stiffness properties into the biomechanical model, incorporating more intraoperative measurements, and employing an optimization procedure to reconstruct the displacements or forces responsible for deformation to generalize this model to all patient cases.

IV.2 Image to physical space registration of supine breast MRI for image guided breast surgery

The work in this section appears in:

R. H. Conley, I. M. Meszoely, T. S. Pheiffer, J. A. Weis, T. E. Yankeelov, and M. I. Miga, "Image to physical space registration of supine breast MRI for image guided breast surgery", SPIE 2014 Medical Imaging: Image-guided Procedures, Robotic Interventions, and Modeling Conference, Vol. 9036, San Diego, CA, April 2014

Abstract

Breast conservation therapy (BCT) is a desirable option for many women diagnosed with early stage breast cancer and involves a lumpectomy followed by radiotherapy. However, approximately 50% of eligible women will elect for mastectomy over BCT despite equal survival benefit (provided margins of excised tissue are cancer free). Determining surgical margins intraoperatively is difficult and achieving negative margins is not as robust as it needs to be, resulting in high re-operation rates and often mastectomy. Magnetic resonance images (MRI) can provide detailed information about tumor margin extents, however diagnostic images are acquired in a fundamentally different patient presentation than that used in surgery. Therefore, the high quality diagnostic MRIs taken in the prone position with pendant breasts are not optimal for use in surgical planning/guidance due to the drastic shape change between preoperative images and the common supine surgical position. This work proposes to investigate the value of supine MRI in an effort to localize tumors intraoperatively using image-guidance. Mock intraoperative setups (realistic patient positioning in non-sterile environment) and preoperative imaging data were collected from a patient scheduled for a lumpectomy. The mock intraoperative data included a tracked laser range scan of the patient's breast surface, tracked center points of MR visible fiducials on the patient's breast, and tracked B-mode ultrasound images. The preoperative data included a supine MRI with visible fiducial markers. Fiducial markers localized in the MRI were rigidly registered to their mock intraoperative counterparts using an optically tracked stylus. The root mean square (RMS) fiducial registration error using the tracked markers was 7.5 mm. Following registration, the average closest point distance between the MR generated surface nodes and the LRS point cloud was 1.76 +/- 0.502 mm

IV.2.1 Introduction

Due to mass breast cancer screenings, women are being diagnosed at earlier stages with smaller tumors. Therefore, breast conserving therapy (BCT) is a viable option for many women with early stage breast cancer, provided that negative margins (no cancer cells present on resected specimen) and acceptable cosmetic outcomes can be achieved. Breast conserving therapy involves a lumpectomy (removal of tumor with a margin of surrounding healthy tissue) followed by radiation therapy. For decades, BCT has shown to have the same survival rate as mastectomy (removal of the whole breast) [80, 211, 212] in properly selected patients. However, there is an increasing trend toward choosing mastectomy over BCT due to surgical uncertainties [213], despite recent research showing BCT to have improved disease-specific survival over mastectomy [214].

The hesitation to choose BCT over mastectomy derives from the fact that determining surgical tumor margins intraoperatively is very difficult and negative margins are not always achieved, resulting in the need for a second surgery or salvage mastectomy. Positive margins are often a result of an inability to visualize tumor location. Current techniques to localize breast lesions in the operating room include wire-guide localization and intraoperative ultrasound. Intraoperative ultrasound guidance is often ineffective for non-palpable breast tumors as approximately only half of these tumors can be visualized with ultrasonography [41]. The standard technique for intraoperative tumor localization is wire-guided localization in which a radiologist inserts a wire into the tumor with guidance of ultrasound or mammography prior to entering the operating room. The surgeon will follow the trajectory of the wire to a distance in close proximity to the tumor and then begin circumferential dissection through presumed normal breast tissue. The shortcomings of this approach is that the guide wire does not provide a 3D perspective of the tumor and therefore cannot delineate tumor boundaries, which contributes to an unacceptable high rate of positive margins [215]. In addition, often the trajectory of the wire is dictated by mammographic guidance and can at times represent an inefficient surgical route to the target which would direct the surgeon to navigate through excessive amounts of tissue, or would require the surgeon to make a visual estimation of a better route, both potentially leading to navigational errors.

Magnetic resonance (MR) imaging is the preferred imaging modality for preoperative clinical assessment and planning [215]. However, preoperative planning images are acquired in the prone position with breast pendant, while surgery is performed in the supine position with arm extended. The breast undergoes significant deformation and shape change between the two positions. While prone breast

MR images have superior image quality, they are not particularly valuable for surgical planning. Prone to supine image registration of breast MRI for aid in surgical planning has previously been proposed [53, 137, 138, 216]. Alternatively, in the work presented here, we propose to register supine MR images to physical space for intraoperative tumor localization. This approach has clear advantages: (1) the breast anatomy within the image volume is in a presentation that is representative of the operative setting, (2) tumor volume changes as it deforms under the breast's weight are captured better and should reflect better correlation between pathology reports and intraoperative observations, and (3) image-to-physical registration methods will be facilitated more readily.

Mock intraoperative data and preoperative data were collected from a patient scheduled for lumpectomy. The mock intraoperative data represents the localization of the patient's breast in physical space via multiple digitization methods (optically tracked laser range scan, stylus, and ultrasound imaging). Preoperative data includes MR images of the breast containing the lesion acquired in the supine orientation with MR-visible markers attached. Image to physical space registration was performed using landmarks visible in both the MR images and in physical space. The fiducial registration error (FRE), a measure of overall landmark misalignment, is reported as well as the closest point distance map of the registered preoperative and intraoperative surface. Subsurface registration accuracy was assessed by comparing the registered MR tumor contours to their intraoperative counterparts as digitized by tracked ultrasound.

IV.2.2 Methods

Preoperative data collection and patient specific modeling

In the imaging phase of the experiments, adhesive MR visible fiducial markers (IZI Medical Products, Owing Mills, MD) were distributed across the surface of the breast prior to imaging. The patient was placed in the supine position within a closed bore 3T Philips scanner. T_1-weighted, 3D turbo field echo (TFE) with fat suppression images were acquired using a torso coil carefully placed as to not deform the breast surface. The acquired image volume was 512 mm $\times$ 512 mm $\times$ 160 mm with a reconstructed voxel size of 0.391 mm $\times$ 0.391 mm $\times$ 1 mm. The breast and pectoral muscle were segmented using a semi-automatic active contour technique by ITK-SNAP's [199] implementation of the Snakes [207] algorithm. The tumor was manually segmented and exported as a mesh from ITK-SNAP. A standard marching cubes algorithm [200] was used to create an isosurface of the breast and pectoral muscle and

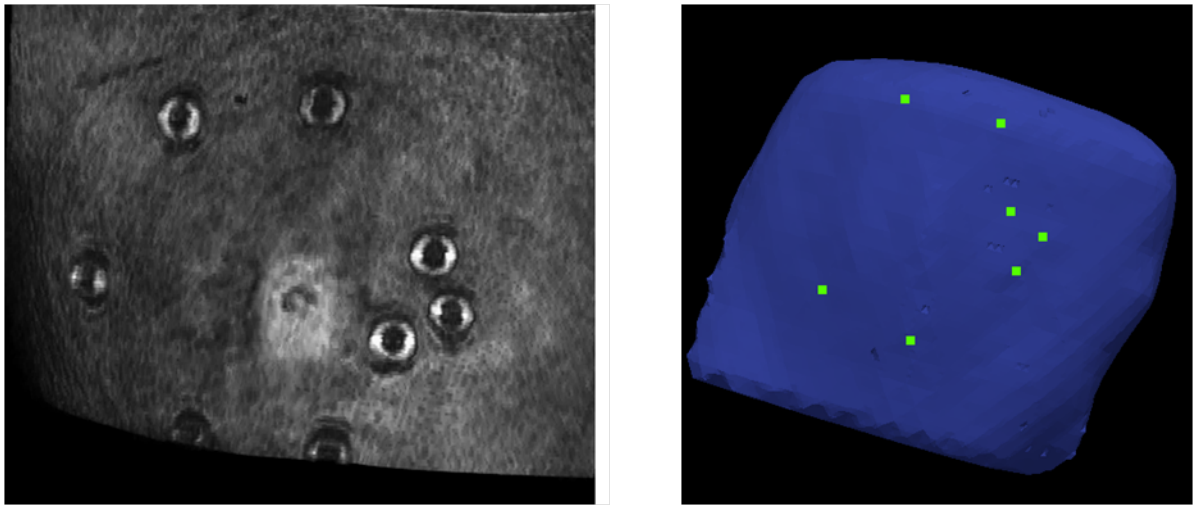

(a) (b)

Figure IV.1: (a) Volume render of supine breast MRI. (b) Patient specific finite element mesh. Green points are manually selected fiducial centers.

was further smoothed using FastRBF Toolbox (Farfield Technologies, Christchurch, New Zealand). From this surface, a tetrahedral mesh was generated using a custom mesh generator [202]. A volume render of the breast surface and the mesh generated by the MR volume is shown in Figure IV.1. The green points in Figure IV.1b indicate the centers of the markers and were manually determined using Analyze 9.0 (Mayo Clinic, Rochester, MN, USA).

Mock intraoperative data collection

In our mock intraoperative setup, the patient was placed in a typical surgical orientation by a surgical oncologist to accurately depict operating room positioning. An optically tracked laser range scanner was used to scan the breast surface, providing a textured point cloud of the breast surface with known 3D coordinates. An optically tracked pen probe was used to collect the location of the centers of each of the fiducial markers. Finally, tracked ultrasound images were collected to provide the physical location of the tumor with respect to the breast surface. In this experiment, ultrasound images were acquired using the Acuson Antares system (Siemens Medical Solutions USA, inc, Mountain View, CA) using a VFX13-5 linear array probe with a depth of 6 cm and frequency of 10 MHz. The ultrasound images were tracked in 3D by collecting synchronized video and tracking data on a host PC with the utilization of software based on the Visualization Toolkit (VTK). The ultrasound images were calibrated

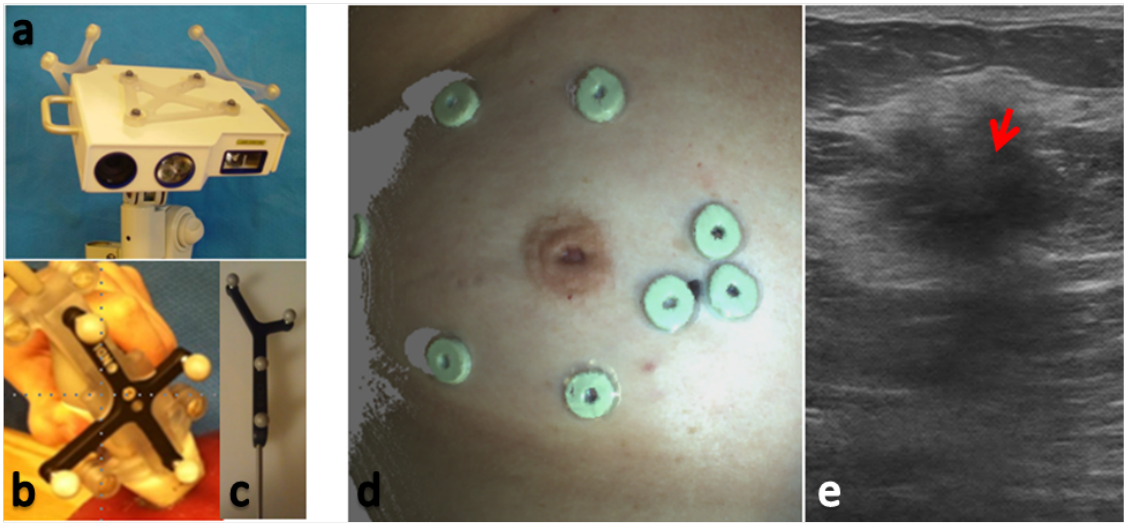

Figure IV.2: (a) Laser range scanner with rigid bodies for tracking. (b) Ultrasound transducer with rigid body for tracking. (c) Tracked pen probe. (d) Textured point cloud produced by tracked laser range scanner with known 3D coordinates. The green rings are MR visible adhesive fiducial markers. (e) Example of a 2D ultrasound slice of a breast tumor (dark shadow shown by red arrow).

to physical space using a method [204] based on the relationship between an optically tracked pointer and an optically tacked ultrasound transducer. Image to physical space registration between points located in the ultrasound image plane and their physical space counterparts determined by the tracked pen probe was performed to transform an ultrasound image into physical space. Following calibration, the compression of tissue caused by the ultrasound transducer was compensated for using a model based correction technique [206].

Registration technique

MR-digitized marker locations were rigidly registered to the mock intraoperative tracked stylus points using a 3D point-based singular value decomposition registration algorithm [217], yielding a 4×4 transformation matrix. The fiducial registration error (FRE), a measure of overall landmark misalignment, is reported according to equation IV.1.

$$FRE = \sqrt{\frac{1}{N}\sum_{i=1}^{N}(R(x_i + \Delta x_i)) + t - (y_i + \Delta y_i)} \tag{IV.1}$$

where x_i and y_i are 3×1 vectors of corresponding points in two spaces, Δx_i and Δy_i are the fiducial localization errors for each point in the two spaces, N is the total number of fiducials, R is a 3×3

rotation matrix and t is a 3×1 vector containing displacements. With respect to surface fit assessment, the closest point distance map between the LRS point cloud and the MR generated mesh is reported.

Subsurface validation and ultrasound image processing

Compression of the breast tissue by the ultrasound transducer leads to incorrect measurements of tumor size and location. In this paper, we utilize a previously developed model based correction scheme developed by Phieffer et al [206] to compensate for the compression of the target by the ultrasound transducer. The method utilizes the position of the tracked ultrasound probe to measure 3D displacements to drive a linear elastic correction model. The relative positions of the probe surface can be used to estimate the displacement of the breast tissue. Once a registration is made between the patient specific MR mesh and physical space, the ultrasound probe is now in the same space as the mesh. The probe surface will be located slightly below the surface of the mesh, depending on the compression of the tissue by the user. The pose of the probe surface provides Dirichlet boundary conditions for a forward linear elastic model that deforms the patient specific mesh to the compressed state exerted by the probe. The deformation field generated by this model is then applied in reverse manner to deform/-correct the ultrasound slices and the segmented tumor contours such that they are correctly rendered in the uncompressed state associated with the pre-procedural supine MR orientation.

The subsurface tumor registration accuracy was measured by comparing the location of the tumor contour in the compression corrected ultrasound image and the tumor contour in the MR volume. The distance between the centroid of the US tumor and the MR tumor is reported. The modified Hausdorff distance (MHD) [209] between the MR tumor contour and the US image contour is reported for seven ultrasound slices. The MHD is defined for two contours, A and B in accordance with equations IV.2 and IV.3.

$$d(A,B) = \frac{1}{N_a}\sum_{a\varepsilon A} min_{b\varepsilon B}(||a-b||) \tag{IV.2}$$

$$MHD = max(d(A,B),d(B,A)); \tag{IV.3}$$

The mean closest point distance $d(A,B)$ is calculated in the direction from A to B, and then again from B to A. MHD is the maximum mean closest point between the two contours.

IV.2.3 Results

The digitized breast surface acquired by the tracked laser range scanner was registered to the patient specific mesh using corresponding landmarks. The digitized breast surface is shown registered to the patient mesh in Figure IV.3a. The fiducial registration error was 7.4 mm. Figure IV.3b shows the

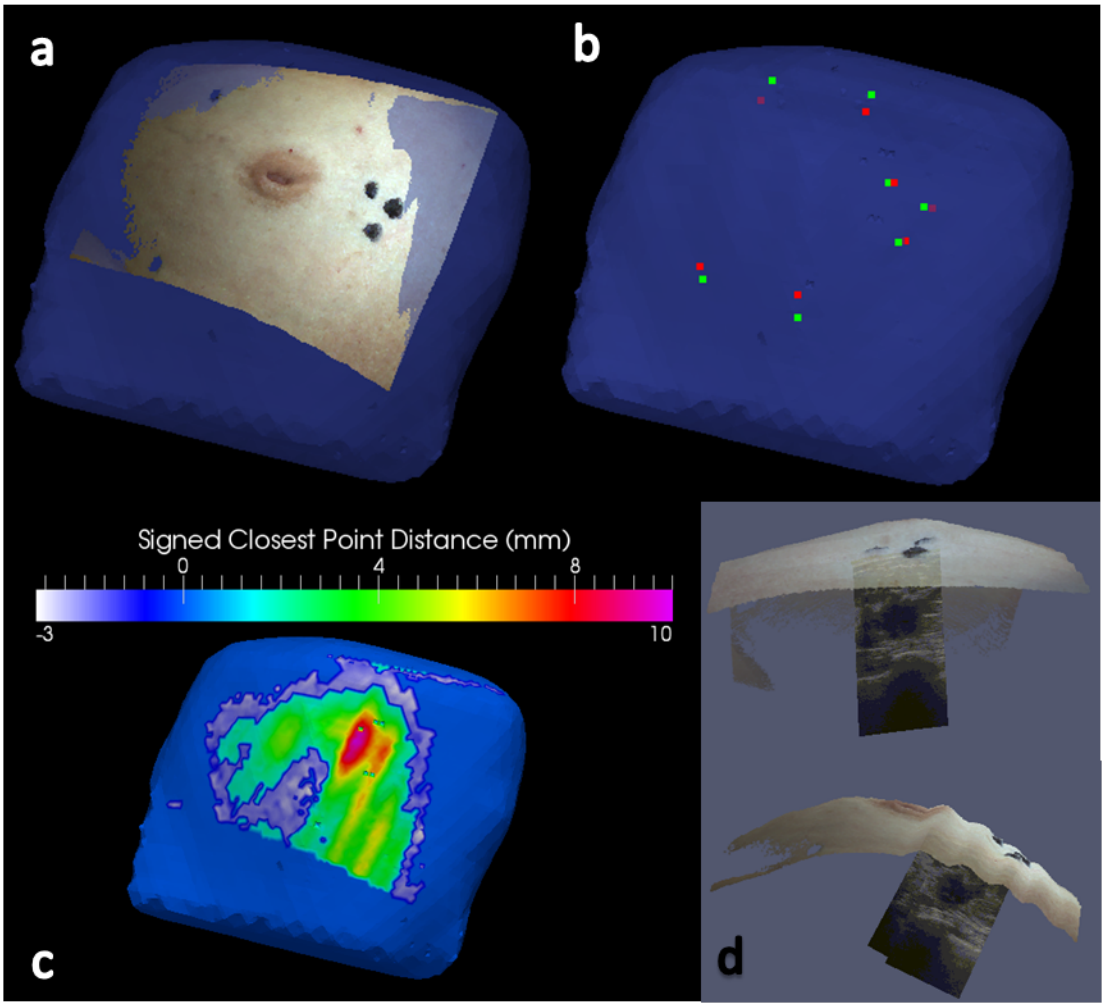

Figure IV.3: (a) Registered digitized breast surface overlaid onto MR generated mesh. (b) MR fiducial center points (green) with registered physical space fiducial center points (red) overlaid onto patient specific mesh surface nodes. (d) Two orthogonal views of a textured point cloud of the breast with calibrated ultrasound slices showing tumor location in physical space.

mesh and MR fiducial center points with the registered physical space fiducial centers. The surface alignment was inspected by calculating the signed closest point distances between the point cloud and mesh surface nodes. The average closest point distance was 1.76+/- 0.502 mm. A signed closest point distance map is shown in Figure IV.3c. Figure IV.3d shows how tumor location can be viewed in respect

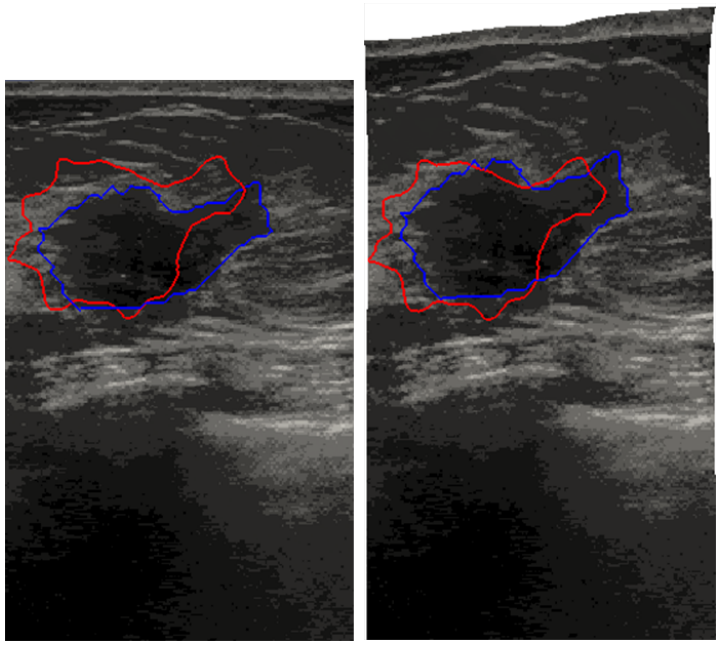

Figure IV.4: Left: Uncorrected ultrasound slice with uncorrected ultrasound tumor contour (blue) and MR contour (red). Right: corrected ultrasound slice with ultrasound tumor contour (blue) and MR contour (red).

to the breast surface by superimposing the LRS point cloud with select ultrasound slices.

Following registration, the ultrasound slices and their corresponding tumor contours are corrected to compensate for the tissue compression applied by the ultrasound transducer. Figure IV.4 shows an uncorrected and a corrected ultrasound slice. The blue outline is the ultrasound tumor contour while the red outline is the registered MR tumor contour. The average MHD value for the seven uncorrected US tumor contours was 2.68 +/- 0.6846 mm. The average MHD value for the seven corrected US tumor contours was 2.0814 +/- 0.4454 mm. The average distance from the centroid of the uncorrected US tumor contour and the MR tumor centroid was 3.93 +/- 1.2795 mm, while the centroid distance from the corrected US contours was 3.212 +/- 0.985 mm. Figure IV.5 shows two plots, one of the MHD values for the corrected and uncorrected tumor contours and the centroid distances for the corrected and uncorrected tumor contours. In each case, the corrected ultrasound contours yielded a smaller average distance than the uncorrected ultrasound contours. Figure IV.6 shows three out of the seven slices processed and show the corrected ultrasound slices overlaid onto their corresponding MR slices. The right hand column of Figure IV.6 shows US (blue) and MR (red) tumor contours as well as the

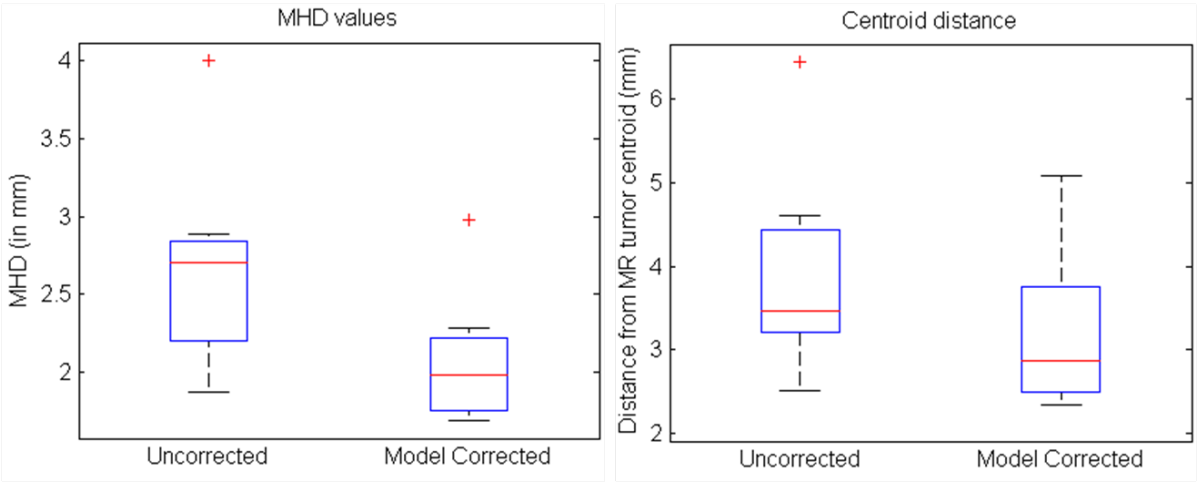

Figure IV.5: Tumor alignment errors for the corrected and uncorrected ultrasound slices. The modified hausdorff distance (MHD) between the co-aligned MR tumor contours and the US tumor contours are reported for the uncorrected and model corrected ultrasound slices. The distance between the MR tumor centroid and the US tumor centroids are also reported. The red line inside the box represent the mean and the edge of the boxes represent the 25th and 75th percentiles, and the lines extend to the most extreme observation points not considered as outliers.

reported MHD value between the two contours.

IV.2.4 Discussion

The results of the overall surface alignment are on average less than 2 mm. However, multiple inspiration and expiration events happen over the 20-40 seconds that it takes for the laser range scanner to pass across the whole surface of the breast. This causes a rippling effect to be present in the point cloud collected by the LRS. This is evident in the bottom image in Fig. IV.3d. The rippling due to respiratory motion increases a mismatch between the point cloud and mesh surface. This is propagated to the closest point distance map shown in Fig. IV.3c where the largest error (10 mm) is at the location of the largest inspiration peak on the point cloud. These respiratory affects can be diminished by using a faster scanner or a different digitization device, such as a stereo vision camera system, where capture of the breast surface occurs at the speed of the camera frame rate (usually $<$1 second).

The model corrected ultrasound slices produced a better average alignment with the MR tumor contours than the uncorrected tumor contours. A Wilcoxon signed rank test was performed to test for differences between the corrected and uncorrected MHD values (significance at p-value < 0.05). There was a significant improvement in tumor alignment when using the model corrected ultrasound

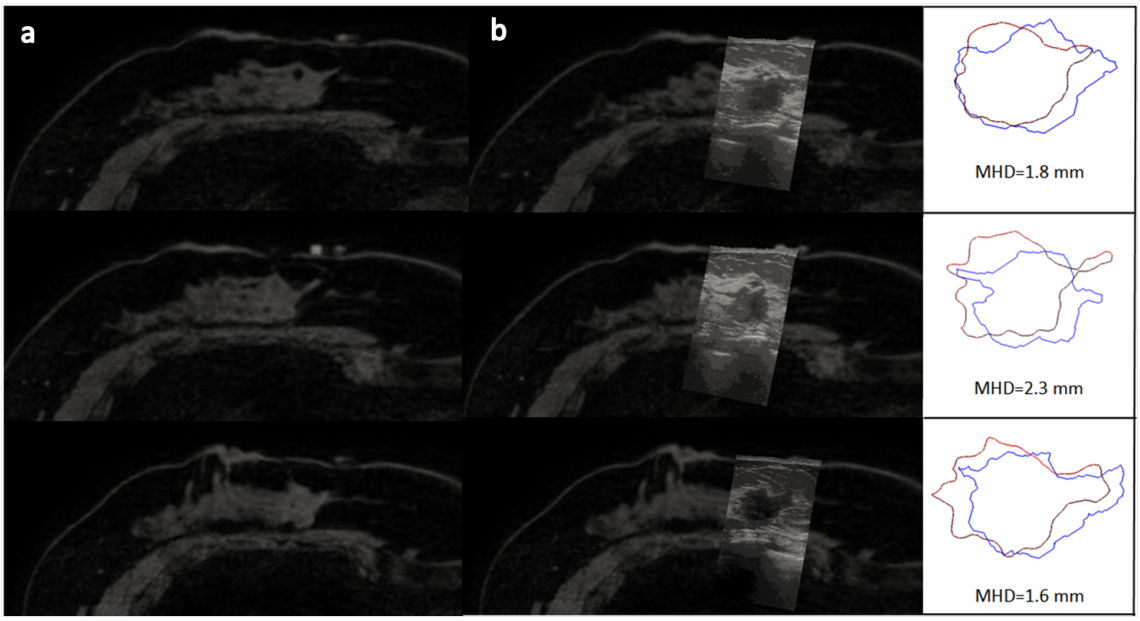

Figure IV.6: column (a) is three supine MR slices, Column (b) shows three different registered ultrasound slices overlaid on the corresponding MR slice. The third column shows MR contours (red) and corrected US contours (blue) as well as the MHD values for the two contours.

slices (p=0.015). There was not a significant difference (p-value=0.078) between the corrected and uncorrected tumor centroid distances, although a trend was identified with lower errors associated with corrected tumor contours. More study is needed to provide a statistically significant result. Sources of variability that may have contributed to the error is the uncertainty of manual segmentation of the tumor borders in the ultrasound and MR images. Ideally, in the future we will acquire pre and post contrast enhanced magnetic resonance images to get a concrete and user independent tumor border in the MR images. It should also be noted that multiple sources of error may have contributed to the final misalignment of the US and MR tumor contours. Errors associated with the optical tracking equipment, tracked ultrasound calibration, and ability to accurately localize the fiducial center points may be related and not necessarily additive leading to an uncertainty of how the noises of the system propagate. This uncertainty is characteristic of any realistic guidance platform.

While we are pleased that the surface of the LRS and the surface of the patient mesh were adequately aligned, our real concern is the accuracy of the subsurface features, particularly the cancerous lesion located within the fibroglandular tissue. Fig. IV.6 shows successful alignment between the ultrasound images to the MR slices, with especially promising correspondence between the pectoral muscle

and fibroglandular tissue in the MR and US images. The average MHD and centroid distance values of the model corrected ultrasound slices and the MR tumors were around 2-3 mm. A surgical oncologist typically aims to remove 5 mm of surrounding healthy tissue, so a 2-3 mm error is acceptable for this surgical domain.

IV.2.5 Conclusion

In this work we present a workflow for the acquisition of data, processing of images, creation of patient specific models, and validation for an image based guidance system for the removal of cancerous breast lesions. We collected preoperative images and mock intraoperative data from a breast cancer patient scheduled for a lumpectomy to survey our ability to register and validate our alignment accuracy. With our subsurface alignment errors being on average less than 5 mm, we are encouraged to further investigate the potential of utilizing the combination of supine magnetic resonance images, patient specific biomechanical models, and intraoperative tracked ultrasound as a framework for an image guidance system for breast conservation surgeries.

IV.3 Realization of a biomechanical model assisted image guidance system for breast cancer surgery using supine MRI

The work in this section appears in:

Conley, R. H., Meszoely, I. M., Weis, J. A., Pheiffer, T. S., Arlinghaus, L. R., Yankeelov, T. E., and Miga, M. I. (2015). "Realization of a biomechanical model-assisted image guidance system for breast cancer surgery using supine MRI. International journal of computer assisted radiology and surgery", 10(12), 1985-1996.

Abstract

Purpose: Unfortunately, the current re-excision rates for breast conserving surgeries due to positive margins average 20-40%. The high re-excision rates arise from difficulty in localizing tumor boundaries intraoperatively and lack of real time information on the presence of residual disease. The work presented here introduces the use of supine magnetic resonance (MR) images, digitization technology, and biomechanical models to investigate the capability of using an image guidance system to localize tumors intraoperatively.

Methods: Preoperative supine MR images were used to create patient specific biomechanical models of the breast tissue, chest wall, and tumor. In a mock intraoperative setup, a laser range scanner was used to digitize the breast surface and tracked ultrasound was used to digitize the chest wall and tumor. Rigid registration combined with a novel nonrigid registration routine was used to align the preoperative and intraoperative patient breast and tumor. The registration framework is driven by breast surface data (laser range scan of visible surface), ultrasound chest wall surface, and MR-visible fiducials. Tumor localizations by tracked ultrasound were *only* used to evaluate the fidelity of aligning preoperative MR tumor contours to physical patient space. The use of tracked ultrasound to digitize subsurface features to constrain our nonrigid registration approach and to assess the fidelity of our framework makes this work unique. Two patient subjects were analyzed as a preliminary investigation towards the realization of this supine image guided approach.

Results: An initial rigid registration was performed using adhesive MR-visible fiducial markers for two patients scheduled for a lumpectomy. For patient 1, the rigid registration resulted in a root mean square fiducial registration error (FRE) of 7.5 mm and the difference between the intraoperative tumor centroid as visualized with tracked ultrasound imaging and the registered preoperative MR counterpart was 6.5

mm. Nonrigid correction resulted in a decrease in FRE to 2.9 mm and tumor centroid difference to 5.5 mm. For patient 2, rigid registration resulted in a FRE of 8.8 mm and a 3D tumor centroid difference of 12.5 mm. Following nonrigid correction for patient 2, the FRE was reduced to 7.4 mm and the 3D tumor centroid difference was reduced to 5.3 mm.

Conclusion: Using our prototype image guided surgery platform, we were able to align intraoperative data with preoperative patient specific models with clinically relevant accuracy; i.e., tumor centroid localizations of approximately 5.3 -5.5 mm.

IV.3.1 Introduction

Breast cancer is the most frequently diagnosed cancer in women and is also the leading cause of cancer related deaths among women worldwide, with 1.7 million new cases being diagnosed and more than 500,000 deaths occurring in 2012 [218]. Breast cancer treatment is dependent upon multimodal therapy with surgery being a primary component, especially for early stage cancers. Mastectomy (total removal of the breast) was the most common procedure choice for newly diagnosed breast cancer patients until the 1980s when studies revealed that lumpectomy, the far less disfiguring option, was shown to have the same 10 year survival rate as mastectomy [19]. Despite this fact, approximately 25-50% of patients eligible for breast conservation therapy (BCT) will choose mastectomy over lumpectomy [219, 220]. A substantial concern of BCT patients is whether or not negative margins will be obtained in the initial surgery. Negative margins are achieved when no cancer cells are present on or near (usually within 5-10 mm) the border of the excised tissue and are considered necessary for a successful lumpectomy. Unfortunately, the current re-excision rates due to positive margins average 20-40% [21]. Failure to achieve negative margins can result in the delay of radiation treatment, increase risk for local recurrence, cause psychological and physical stress on the patient, compromise cosmetic results, and increase cost.

The high re-excision rates arise from the difficulty in localizing tumor boundaries intraoperatively and lack of real time information on the presence of residual disease [215]. The challenge in determining surgical margins intraoperatively is that geometric and spatial cues are quickly lost in the surgical presentation. Equally confounding is that valuable diagnostic images are acquired in a significantly different breast presentation than the typical surgical setup. Diagnostic and biopsy information are driven by mammography and preoperative MR images in which the patient is standing or lying prone with

(a) Prone MR image of breast (b) OR presentation (c) supine MR image of breast

Figure IV.7: Demonstration of the challenge of using preoperative images for surgical guidance. (a) and (c) are axial slices of T_1-weighted THRIVE sequence MR images in the prone and supine positions with red ovals designating the same tumor in the same axial slice. Changes in patient setup cause the tumor to move, yielding the diagnostic scan in (a) less valuable for locating the tumor in the surgical setup, shown in (b).

pendant breasts, while surgical presentation is in the supine position. An example of this challenge is displayed in Fig. IV.7, where the breast undergoes significant shape change between the prone and supine positions causing the tumor to deform and change location.

Current localization strategies used in the operating room (OR) include intraoperative ultrasound, wire guided approaches, and radio-guided occult lesion localization. Prospective studies report that wire guide localization results in positive margins in 38-43% of patients undergoing BCT [24, 102]. Intraoperative ultrasound (iUS) has been shown to improve BCT [25]. However, iUS is limited by the fact that only 50% of non-palpable tumors are visible by ultrasound in the breast [215]. The shortcomings of radio-guided occult lesion localization is that the radioisotope must be accurately placed into the tumor and diffusion of the radiotracer into surrounding tissue decreases accuracy of the tumor location [215].

Due to the current limitations of intraoperative tumor localization approaches, the efficacy of using MR data alignment strategies has been investigated but challenges in surgical presentation have been identified. There is little doubt that the use of MR data to influence surgical planning has important implications in the surgical management of patients [196, 221]. We believe that better image-to-physical data alignment strategies can be used more directly for better surgical management. To achieve this, methods using biomechanical models for prone-to-supine registration of MR images have been suggested [53, 222] . Recently, utilization of supine MR images for surgical guidance have been consid-

ered in frameworks for image guided breast surgery [54, 223, 224]. Alignment of pre-surgical supine MR images to surgically oriented MR images using surface markers has also been shown to be feasible [55]. Preoperative supine MR images registered using surface markers coupled with an intraoperative optical scan of the breast has also demonstrated qualitative alignment value [46]. While encouraging, the integration of supine MR images, optical tracking and digitization technology, patient specific biomechanical models for nonrigid registration, and tracked ultrasound for subsurface feature localization has yet to be realized as a surgical guidance platform for breast conserving surgery. This paper integrates these components and reports preliminary experiences with this surgical platform in two patient cases. In addition, subsurface target accuracy is assessed independently using tracked ultrasound imaging of echogenic tumors in both cases.

IV.3.2 Methods

Two breast cancer patients scheduled for surgery were selected in a Vanderbilt IRB approved bystander study to evaluate the feasibility and accuracy of our image guidance platform. In Fig.IV.8, a schematic overview demonstrates the structure of the proposed system with required data inputs and generalized outputs at each step. Both subjects had ultrasound visible tumors. While our guidance platform does not require ultrasound visible tumors, their echogenic visibility in this study was particularly useful for evaluating the subsurface alignment accuracy of our registration approach.

IV.3.2.1 Preoperative Data Collection

Supine MR Imaging

Preoperative supine MR images were acquired for each patient and were used to create patient specific biomechanical models of the breast tissue, chest wall, and tumor. MR visible adhesive skin fiducial markers (IZI Medical Products, Owing Mills, MD) were placed over ink markings distributed across the breast surface. The patient was carefully positioned in a closed bore 3T Achieva MR scanner (Philips Healthcare, Best, The Netherlands). A 16-channel sensitivity encoding (SENSE) torso coil was situated carefully as to not deform the breast, and the ipsilateral arm was placed above the patient's head to more closely replicate surgical presentation. High resolution anatomical images were acquired with a T_1-weighted, 3D turbo field echo sequence with fat suppression, a field of view of $200\times200\times160$ mm^3, and a reconstructed voxel size of $0.391\times0.391\times1$ mm^3. Recently, we have achieved successful

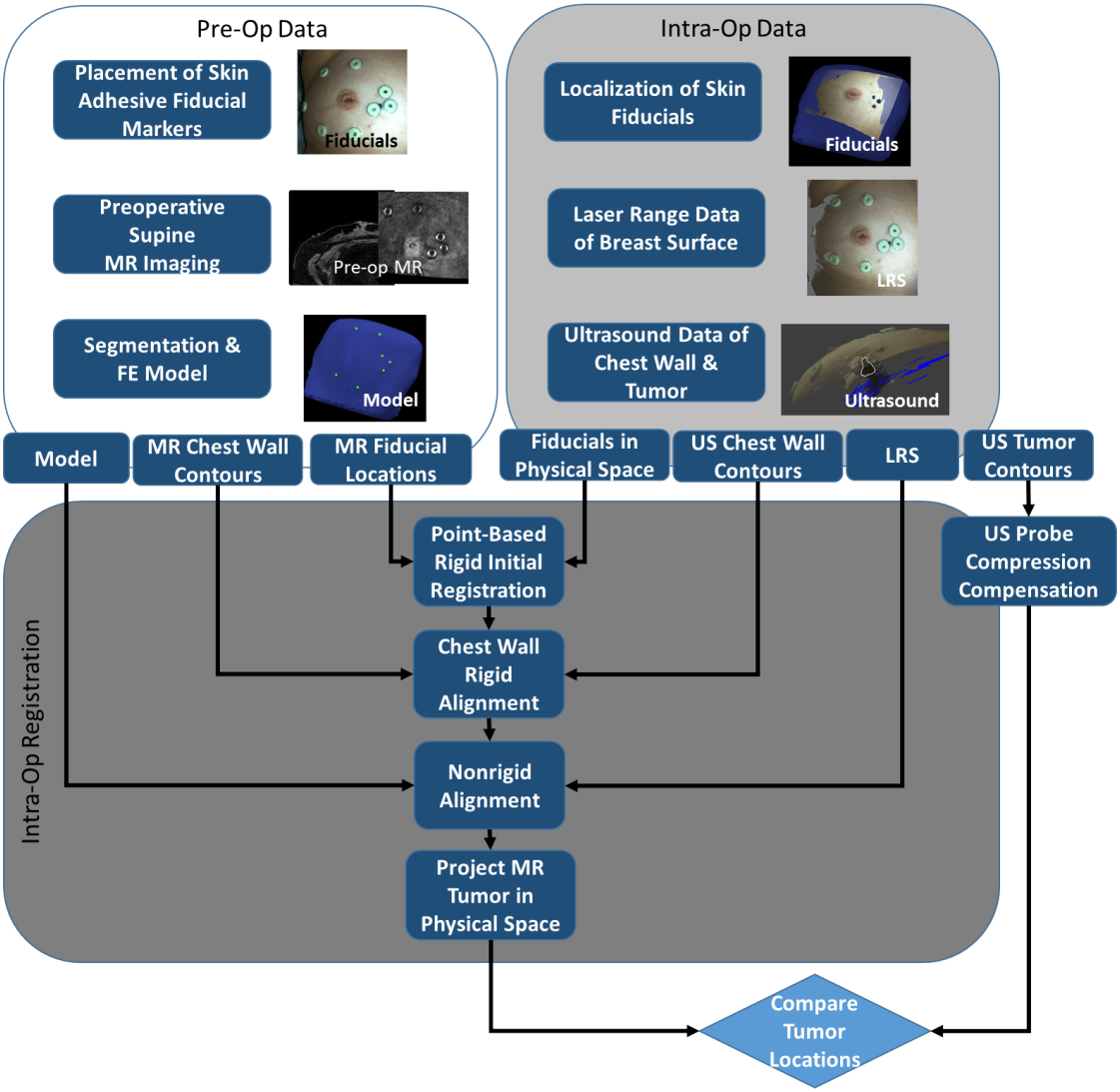

Figure IV.8: Overview of surgical guidance platform and validation framework. The preoperative (preOp) and intraoperative (intraOp) data panels summarize the important information gathered at each step. This information is then systematically incorporated into an intraOP registration framework. The final outcome is a preoperative tumor mapped to physical space which can then be quantitatively compared to the location of the tumor in the OR.

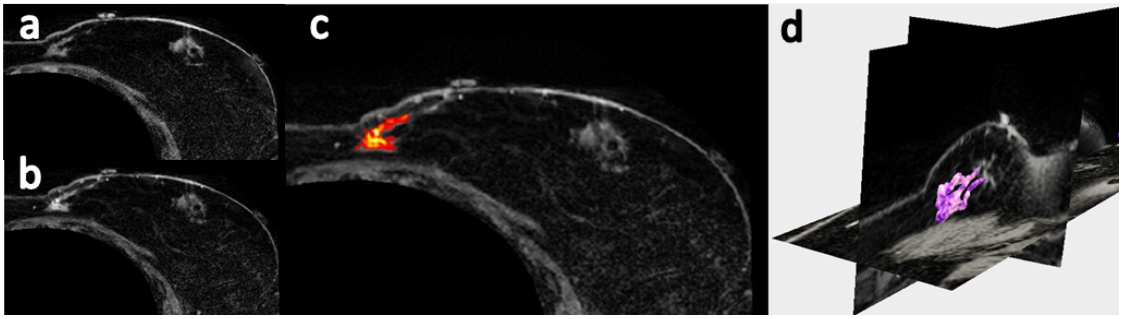

Figure IV.9: Axial slices of supine MRI of patient volunteer with (a) pre-contrast, (b) post-contrast injection,(c) contrast-enhanced image with colored overlay showing tumor, and (d) 3D segmentation of tumor (magenta).

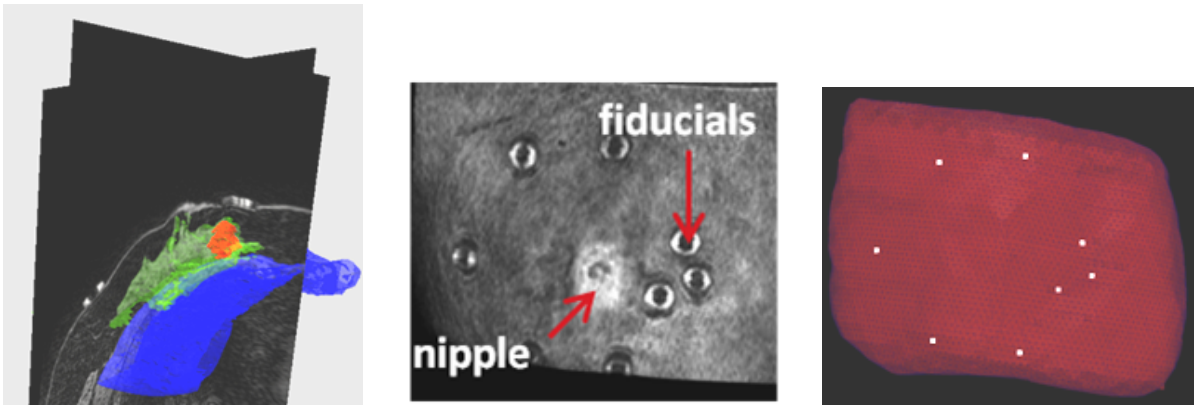

(a) (b) (c)

Figure IV.10: Segmentation of preoperative supine MR images: (a) segmentation of glandular tissue in green, chest wall in blue, and tumor in red. (b) is a volume render of the supine MR image, (c) preoperative mesh showing location of fiducial centers in white.

acquisitions of contrast enhanced supine images, an example of a contrast enhanced image volume of a patient volunteer is shown in Fig. IV.9. For the patient subjects studied herein, tumors were identified from the diagnostic MR supine images and were segmented semi-automatically.

Patient Specific Model

The supine image volume from each patient was segmented into breast tissue, tumor, and chest wall (pectoral muscle) using a semi-automatic segmentation technique by Insight Registration and Segmentation Toolkit (ITK)-SNAP [199]. Fig. IV.10a illustrates the segmentation step for patient 1. The locations of the synthetic fiducial center points were manually determined and recorded (Fig. IV.10b). Following segmentation, a binary mask of the whole breast was used to generate an isosurface using a

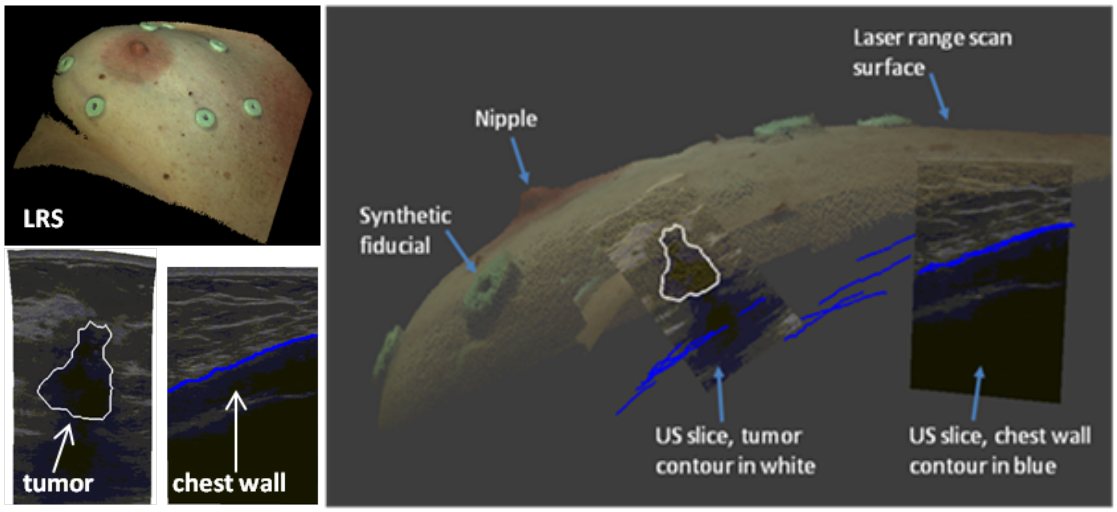

(a) (b)

Figure IV.11: (a) Top: LRS scan of patient 2 breast. Bottom left: compression corrected ultrasound image with tumor contour in white. Bottom right: ultrasound image with chest wall contour in blue. (b) Fusion display of tracked intraoperative data containing a textured point cloud, adhesive fiducial markers, tracked ultrasound images, tumor contour (white), and chest wall contours (blue).

standard marching cubes algorithm [200]. The isosurface was then smoothed with a radial basis function using FastRBF Toolbox (Farfield Technologies, Christchurch, New England). From this surface, a finite element tetrahedral mesh was generated using a custom mesh generator [202] with a mesh edge-length resolution of approximately 3 mm (Fig. IV.10c).

IV.3.2.2 Mock Intraoperative Data Collection

As an initial investigation, a mock intraoperative setup to collect simulated intraoperative data was performed for each patient. In this study, mock intraoperative data was collected to avoid workflow disruptions in the OR and was performed on the same day as preoperative imaging to minimize patient volunteer time. The true intraoperative scenario would involve intraoperative data, such as that shown in Fig. IV.11, to be collected during surgery. To address realistic patient conditions in the mock setup, positioning was performed by a surgical oncologist, to accurately depict OR positioning. Once complete, skin fiducials are digitized with an optical stylus, a laser range data is acquired, and an ultrasound examination is performed. In the following subsections, the extent of this data and its integration is explained.

Surface and Feature Digitization

A custom-built, optically tracked laser range scanner (Pathfinder Technologies, Inc, Nashville, TN, USA) was used to digitize the breast surface by sweeping a laser line over the breast surface and recording geometric points along with color information of the visible field (Fig. IV.11a top, Fig. IV.11b), yielding a textured point cloud with known 3D coordinates in physical space. The physical space points corresponding to the MR visible fiducial center points are determined by the black ink markings that were placed on the patient's skin prior to adhering the MR visible fiducials. An optically tracked stylus was used to collect the location of the ink markings. The textured point cloud was used to confirm the location of the fiducial points by comparing the coordinates collected by the tracked stylus with the field of view color texture information collected from the laser range scanner. All geometric measurements were made with a Polaris Spectra (Northern Digital, Waterloo, ON, Canada) optical tracking system.

Ultrasound Exam

The ultrasound portion of this study was performed in two parts: (1) target B-mode imaging of tumor and (2) chest wall swabbing. Fig. IV.11a bottom left and Fig. IV.11a bottom right show representative contours of each, respectively. Ultrasound images were acquired using an Acuson Antares ultrasound machine (Siemens, Munich, Germany) using a VFX13-5 linear array probe set at 10 MHz. The depth was set at 6 cm to maintain visibility of the chest wall throughout the exam. A passive optically tracked rigid body was attached to the ultrasound transducer. The tracked ultrasound was calibrated using the method developed by Muratore and Galloway Jr [204] that takes multiple b-mode ultrasound images of a tracked stylus tip in the imaging plane to develop a rigid transformation between the image plane and physical space. Once calibrated, all pixels in the ultrasound plane have a corresponding 3D coordinate in physical space.

In addition to optical tracking for determining the location of ultrasound visualized structures, it is also important to correct the localization data of structures that are affected by ultrasound probe compression, namely the tumor (chest wall was assumed rigid). More specifically, since preoperative supine MR images are acquired without this compression, a correction scheme to account for deformation induced by the probe itself is needed in all ultrasound images of the echogenic tumor. Reported in [206], the fidelity of the method we utilized demonstrated reduced subsurface localization errors due to

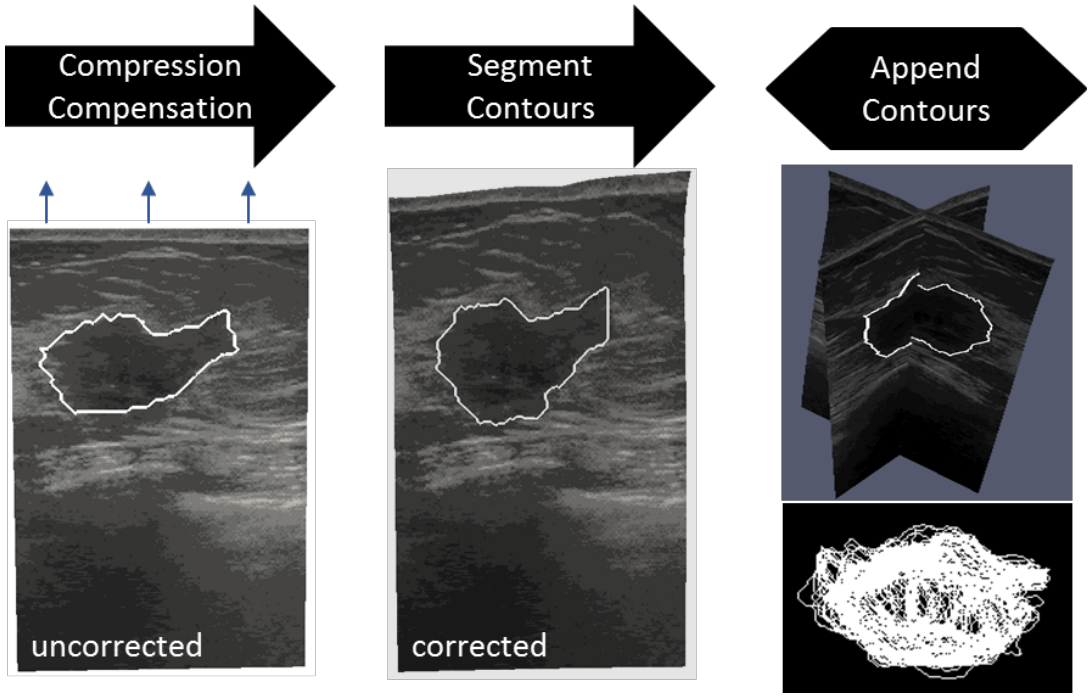

Figure IV.12: Steps involved in processing tracked intraoperative ultrasound data. The ultrasound images are first corrected for tissue compression exerted by the ultrasound transducer. The tumor contour is then segmented in each 2D slice. Lastly, all contours are appended to form a 3D representation of the intraoperative tumor.

ultrasound probe compression by 67.8% and 51.6% in phantom and clinical experiments respectively. For the work reported in this study, it was particularly important to utilize these methods as tumor localization was serving as the primary means for accuracy evaluation of our platform.

Fig. IV.12 provides a visual overview of the processing steps involved in acquiring tracked ultrasound data of the intraoperative tumor volume. Tumor borders are semi-automatically segmented using a custom implementation of the Livewire technique [205]. The acquired tumor ultrasound image/contour is then corrected for probe deformation and each is appended, yielding a 3D point cloud set. Similar steps are performed for the chest wall but probe deformation compensation is not necessary. Fig. IV.11b shows a comprehensive representation of all digitization data rendered consistently within physical space; textured point cloud, synthetic fiducial landmarks, and tracked ultrasound images of both probe-corrected tumor and chest wall ultrasound slices with segmented contours.

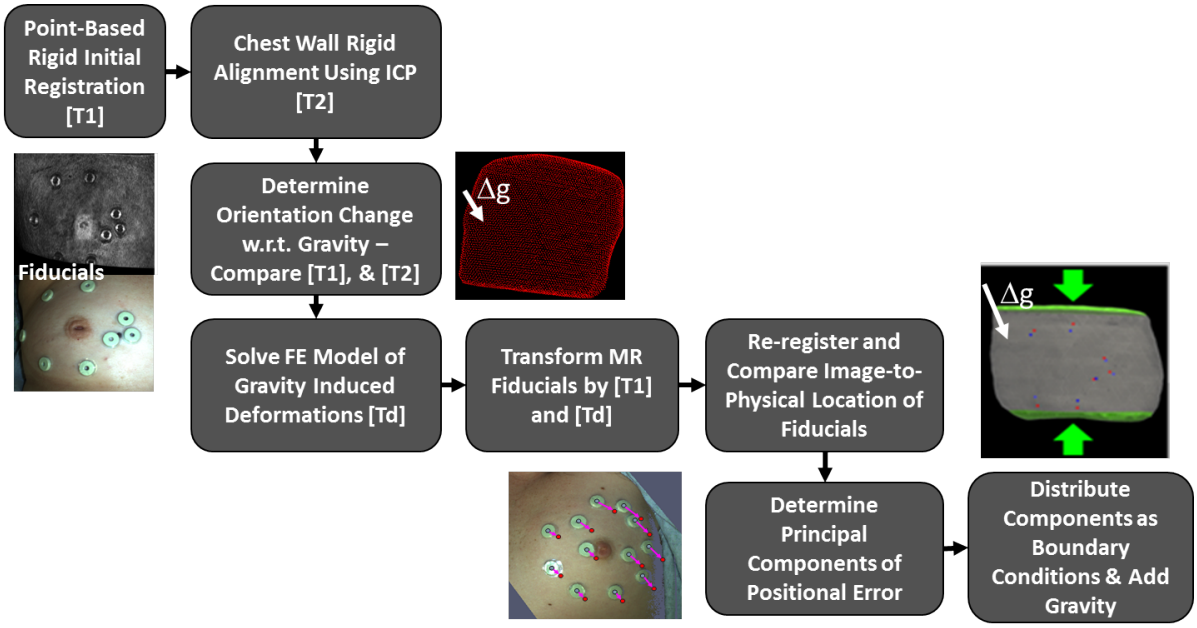

Figure IV.13: Overview of the registration process beginning with rigid initialization and concluding with full nonrigid model compensation.

IV.3.2.3 Registration Method

The entirety of our registration approach is captured in Fig. IV.13. Briefly described, an initial rigid alignment is performed using the synthetic fiducials adhered to the breast. Once complete, a series of steps is conducted to estimate the influence of gravity-induced and ipsilateral arm position changes between supine imaging and surgical configurations. The influence of these variables is realized as a gravitational inducing body force and boundary conditions which are applied to a biomechanical model of the breast. Once complete, the combined rigid and nonrigid transformation provides a means to map preoperative tumor locations into physical space which can then be subsequently compared with a separate independent ultrasound identified tumor localization.

Rigid Alignment

An initial rigid alignment was performed by registering the MR-digitized marker locations to their intraoperative counterparts using a traditional 3D point based singular value decomposition registration algorithm [217]. The point based registration algorithm finds the optimal translation and rotation to

minimize the fiducial registration error (FRE) as defined by:

$$FRE = \sqrt{\frac{1}{N}\sum_{i=1}^{N}(R(x_i+\Delta x_i))+t-(y_i+\Delta y_i)} \tag{IV.4}$$

where x_i and y_i are 3×1 vectors of corresponding points in two spaces, Δx_i and Δy_i are the fiducial localization errors for each point in the two spaces, N is the total number of fiducials, R is a 3×3 rotation matrix and t is a 3×1 vector containing displacements. The resulting translation vector and rotation matrix are applied to the preoperative data to provide an initial alignment with the intraoperative space.

Quantification of Gravity-induced Deformations

Based on initial studies investigating the use of point-based registration of skin fiducials, it was found that significant rotation of the breast occurs relative to the chest wall between supine imaging and intraoperative presentation in some cases. This results in a body force based deformation whereby the breast becomes free to move under the influence of gravity. To estimate this change, we have elected a novel strategy. The chest wall is designated from the preoperative supine images during our breast model building process (Section IV.3.2.1). In addition, chest wall contours are also identified and segmented from our tracked ultrasound examination (Section IV.3.2.2). Using the fiducial-based registration (Section IV.3.2.3) as an initial configuration, a traditional iterative closest point (ICP) registration [118] was employed between the transformed preoperative chest wall points and the intraoperative chest wall contours as digitized by tracked iUS. The rotation matrix resulting from the ICP registration is applied to the intraoperative gravity vector (assumed to be in the direction normal to the patient's bed). Details of this approach are outlined in Algorithm 1.

Algorithm 1 Algorithm for finding gravity-induced deformations using ICP registration

1. Initialize by transforming preoperative chest wall contours to intraoperative space using transformation from IV.3.2.3
2. Perform an ICP registration between MR chest-wall surface and iUS chest wall contours
3. Extract the rotation matrix from the final transformation and apply to the gravity vector in intraoperative space

$$\Delta g = R * g_{intraop} \tag{IV.5}$$

where $g_{intraop}$ is a 3×1 vector containing the unit direction normal to the patient bed in intraoperative space

Mechanics-based Nonrigid Correction

Deformations due to gravity-induced changes derived from Algorithm 1 and tissue migration of the breast due to ipsilateral arm movement are estimated using a 3D linear elastic model. The model employs the Navier-Cauchy equations and generates a displacement field for correction and is shown here:

$$\nabla \cdot (G\nabla u) + \nabla(\frac{G}{1-2\nu}(\nabla \cdot u)) + \rho(\Delta g) = 0 \tag{IV.6}$$

where υ is Poisson's ratio, G is the shear modulus of elasticity ($G = E\,/\,2(1+\nu)$), u is the 3D displacement vector, ρ is the tissue density, and Δg is the change in gravitational acceleration constant with respect to imaging and surgical presentations. Equation IV.6 was solved using the Galerkin Method of Weighted Residuals with linear Lagrange polynomials defined locally on the tetrahedral elements as the supporting basis and weighting functions. Solving this system results in displacement vectors defined at each node that satisfy static equilibrium conditions. The displacements are then applied to deform the preoperative mesh. In this work, an elastic modulus (E) of 1 kPa, tissue density of 1000 kg/m^3, and Poisson's ratio of 0.485 were applied for the whole breast volume.

1st Model Solve- Application of Gravity-induced Deformations

Gravity induced deformations were simulated by supplying the elastic model with a body force of tissue weight based on the change in acting gravity direction as determined in Section IV.3.2.3. We again assume that the chest wall is a rigid fixed structure. Therefore, the boundary conditions applied to this model solve imposed fixed chest wall nodes (zero displacement) with stress-free boundary conditions elsewhere. The displacements generated from this model solve were applied to the preoperative mesh and used to estimate the remaining positional error of fiducial targets.

Final Model Solve

Nonrigid deformations of the breast due to ipsilateral arm movement were accounted for by applying Dirichlet boundary conditions at control surfaces along the inferior-superior surfaces of the model mesh based on preoperative imaging data. The nodes corresponding to the interior chest wall and the medial breast surface were fixed. The medial breast face was fixed because negligible movement occurs in the vicinity of the patient's sternum. The remainder of the breast surface; i.e., the visible breast during presentation, was designated as stress free.

The locations, direction and magnitude of the applied Dirichlet boundary conditions for the inferior-superior surfaces were determined by analyzing the misalignment between the co-registered surface fiducials after gravity-induced changes were taken into account. In both patient cases, a reduced stretching of the breast between preoperative and intraoperative states was observed and used to determine model displacement boundary conditions at the inferior-superior surfaces. This reduced stretching phenomenon is shown in Fig. IV.14(a,c) where the preoperative intra-fiducial distances (red arrows) are larger than the intraoperative intra-fiducial distances (blue arrows). One relatively simple approach to correction is to perform a principal component analysis (PCA) on the difference vector between the co-registered fiducial points to determine the direction in which the largest deformation has occurred. PCA is performed after the displacement field from the first model solve (Section IV.3.2.3) has been applied to the preoperative FE mesh and re-registered using the new locations of the preoperative fiducials. The largest distance vector between the gravity transformed preoperative and intraoperative intra-fiducial locations was used to approximate the magnitude of stretching/compression. Being consistent with a simple deployment strategy, the approximated displacement application was then distributed evenly among two control surfaces, as can be seen in Fig. IV.14(b,d). The proposed registration method requires only two model solves, providing a fast correction strategy that can be readily adapted in the operating room. Given the nature of breast deformation and the reduced domain of the breast analyzed, this initial realization is purposefully designed to be work-flow friendly, operationally robust, and constrained to establish a baseline understanding of efficacy. In the discussion below, avenues for improvement are suggested.

IV.3.2.4 Registration Assessment

Surface markers were used to quantify registration accuracy by calculating the root mean square fiducial registration error (FRE). FRE is a measure of overall misalignment between fiducials and captures fiducial localization errors as well as nonrigid movements. It is important to note that fiducial location differences between image and physical space were not used as direct displacement boundary conditions in the model, but only as a measure of fit with respect to applied deformations from gravity-induced changes and inferior-superior control surfaces. With respect to subsurface targeting accuracy, tracked ultrasound image contours of the tumor were compared to their registered preoperative counterpart. More specifically, the centroid location of the preoperative segmented tumor is mapped by the

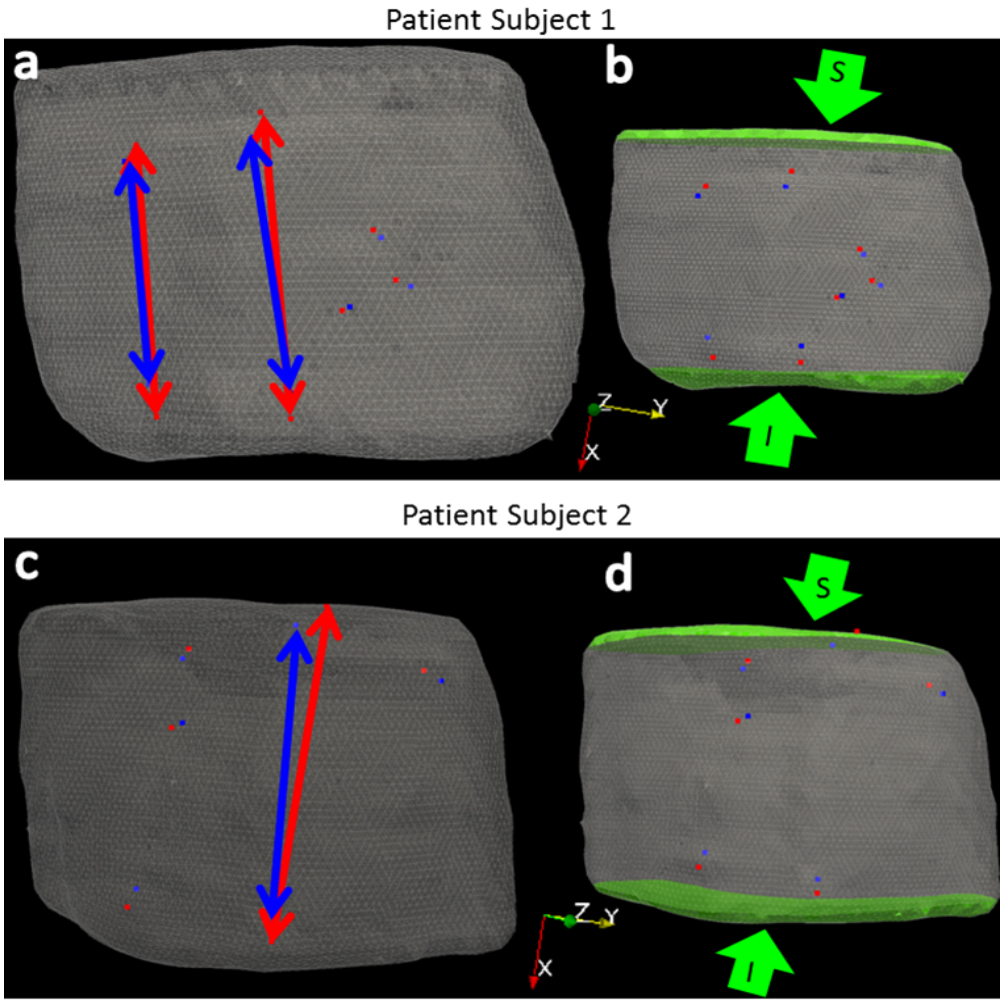

Figure IV.14: (a,c) preoperative mesh with arrows showing preoperative (red) and intraoperative (blue) intra-fiducial distances, (b,d) green arrows point to direction of applied boundary conditions to inferior (I) and superior(S) breast faces highlighted in green.

process shown in Fig. IV.13 and compared to the centroid location of the appended 3D tracked iUS tumor contours as shown in Fig. IV.12. The centroid of a finite number of points was computed as follows:

$$C = [C_x, C_y, C_z] = \frac{\sum_{i=1}^{k} [P_{ix}, P_{iy}, P_{iz}]}{k} \tag{IV.7}$$

where k is the number of points in the domain and P_i is a point in space. Using equation IV.7, The Euclidean distance ($l_2 - norm$) between the intraoperative tumor centroid ($C_{intraop}$) and preoperative tumor centroid (C_{preop}) was used to measure target registration error: Centroid Difference= $||C_{intraop} - C_{preop}||$.

IV.3.3 Results

Patient 1

The initial rigid alignment of the synthetic skin fiducials for patient 1 yielded an FRE 7.5 mm. Figure IV.15(a-c) show results from the rigid registration. The tumor centroid difference between the mapped preoperative and intraoperative states before ultrasound probe compression correction of the intraoperative tumor was 7.5 mm. After probe-to-tissue compression compensation, the tumor centroid difference was 6.5 mm. The iterative closest point registration of the intraoperative and preoperative chest-walls revealed that negligible rotation of the torso occurred for patient 1. Therefore, a gravitation body force was not applied. Principal component analysis of the difference in preoperative and intraoperative fiducial locations revealed a vector supporting approximately 20 mm maximum intra-fiducial distance which its largest component reflective of deformation was along the inferior-superior axis. The difference in intra-fiducial distances can be visualized in Fig. IV.14a where the red arrows point to preoperative fiducials and blue arrows point to intraoperative fiducials. This maximum intra-fiducial distance difference was distributed evenly among the two control surfaces. A 10 mm displacement vector was applied to each node on the inferior and superior breast surfaces (green surface shown in Fig. IV.14b). The green arrows in Fig. IV.14b show the direction of the applied displacements. Using these boundary conditions to drive the elastic model, the nonrigid corrected FRE was 2.9 mm and the deformation corrected tumor centroid difference was 5.5 mm. In Fig. IV.15d, we can observe the improved alignment between the MR-rendered tumor and an ultrasound-visible counterpart (white contour) for patient 1.

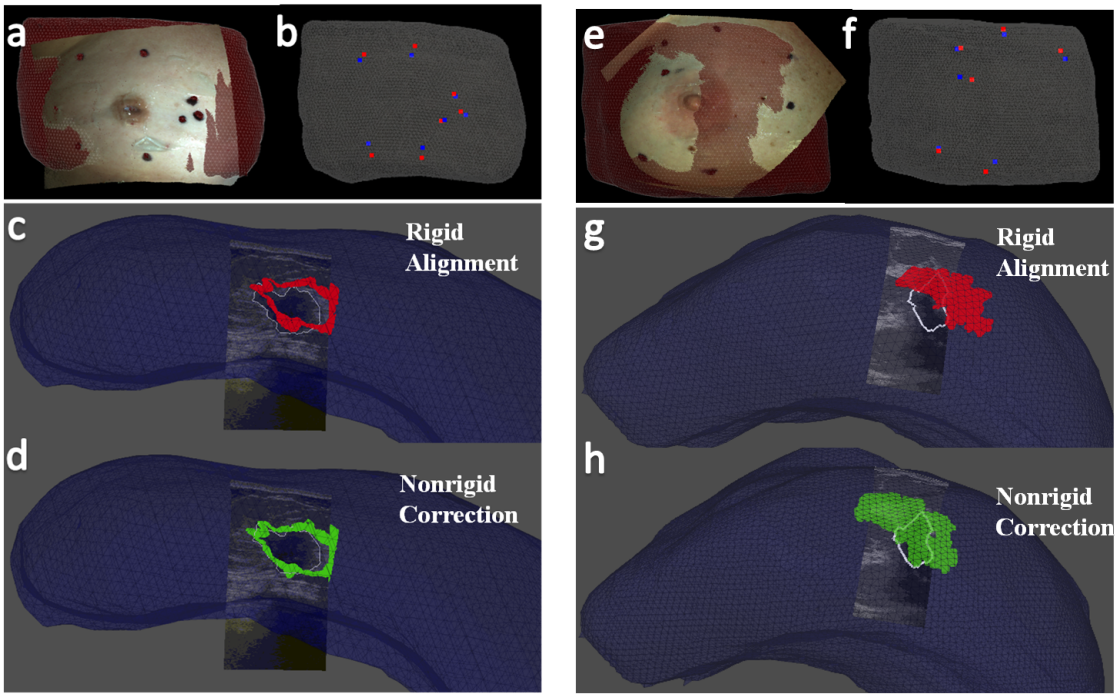

Patient 1 Patient 2

Figure IV.15: Patient 1(a-d) and Patient 2 (e-h). (a,e) co-registered textured point cloud and preoperative mesh. (b,f) co-registered preoperative fiducials (red) and intraoperative fiducials (blue). (c,g) intraoperative ultrasound image with white tumor contour overlaid on preoperative rigid aligned tumors in red. (d,h) intraoperative ultrasound image with white tumor contour overlaid on preoperative nonrigid corrected tumors in green.

Patient 2

Initial rigid alignment of the synthetic skin fiducials for patient subject 2 returned an FRE of 8.8 mm. Fig. IV.15(e-g) shows results from the rigid registration. The tumor centroid distance between mapped preoperative and intraoperative states before ultrasound compression compensation of the tumor contours was 14.7 mm. The tumor centroid distance after probe-to-tissue compensation was 12.5 mm. Following gravitational direction correction, the FRE improved negligibly to 8.5 mm and with a more considerable correction to the tumor centroid distance decreasing to 8.4 mm. As anticipated, principal component analysis following gravity-induced deformation compensation revealed that the largest deformations occurred along the patient's inferior-superior axis. The largest difference in the intra-fiducial distances was 50 mm. Red and blue arrows in Fig. IV.14c show the largest difference in preoperative and intraoperative intra-fiducial distances, respectively. The maximum intra-fiducial distance difference was distributed evenly among the two control surfaces. The green arrows in Fig. IV.14d point to the direction of applied displacement boundary conditions with a 25 mm displacement applied at each breast face (highlighted green surface in Fig. IV.14d). The nonrigid correction resulted in an FRE of 7.4 mm and tumor centroid distance of 5.4 mm. In Fig. IV.15h, we can observe the improved alignment between MR-rendered tumor and the ultrasound-visible counterpart (white contour) for patient 2.

IV.3.4 Discussion

We have presented two patient subjects as an initial investigation towards the realization of a supine image guided surgical platform. In general, the results show that initial rigid alignments are not sufficient and a nonrigid correction is necessary to obtain a clinically relevant image-to-physical alignment. In each case, arm movement between the preoperative and intraoperative patient setups caused a change in stretch to the breast tissue along the patient's inferior-superior axis. Tissue deformation exerted by the ultrasound probe required correction to improve the fidelity of using tracked ultrasound images of the tumor as a means to assess subsurface target registration error. In this study, a somewhat"open-loop", i.e. non-iterative, correction strategy was used in that an initial fiducial registration error was analyzed, body forces and boundary condition were derived, a model was executed, and finally a nonrigid correction was provided. While arguably a coarse nonrigid deformation correction approach, the results are encouraging and speak to the promise of supine image-guided breast surgery. In the future, an iterative optimization strategy will be developed to find the best correction possible driven by all of

the information available intraoperatively. Options for additional data already exist. The corrections shown in Fig. IV.15 are driven by synthetic fiducial error. This is an admittedly sparse source of data to drive the correction process and other possibilities exist in our approach. For example, while not used in this work, the laser range data shown in Fig. IV.11 could serve within a shape conformity metric and employed as a constraint to the nonrigid registration framework.

Several sources of error may contribute to the reported registration inaccuracy. The tracking error of our system has been reported as sub-millimetric for passively tracked rigid stylus bodies [225]. However, multiple reference targets were attached on range-based targeting devices (laser range scanner and ultrasound). Our tracked laser range scanner has been characterized previously at 2.2 +/- 1.0 mm [203] although its use in this particular work was minimal. With respect to the tracked ultrasound imaging, in studies not reported here we have found our average target registration error to be 1.5-2.5 mm in typical tracking experiments [206]. It is difficult to predict how these errors will combine due to the nature of the registration process. More specifically, our registration approach samples both far-field (chest wall) and near-field (synthetic fiducials) structures which likely constrains internal target error; more study is needed.

Other sources of error between MR-localized fiducial and co-localized ink markings in physical space could be present. While some compensation for iUS error was performed, the validation metrics themselves still have some error. The contour digitization of the tumor using tracked ultrasound may not represent a comprehensive digitization of tumor volume and as a result could produce discrepancies of the tumor volume centroid as compared to its preoperative counterpart. In this study, care was taken to acquire ultrasound images of the tumor in orthogonal planes and at multiple angles to best digitize the whole tumor volume. Despite this care, it is unlikely that the measurement is as rigorous as its tomographic counterpart in MR. Another source of error is our use of a linear elastic model for the nonrigid correction of breast tissue. While small-strain approximations are likely violated, we have found linear models to behave reasonably well in such gross nonrigid alignment procedures. In other work [226] , we have compared linear and nonlinear approaches (linear vs co-rotational finite element approaches) with similar registration problems. The observed differences between these models usually have been quite modest when compared to gross misalignments and instrument error. While all of these errors need further characterization, the results in Fig. IV.15 are difficult to discount. In each we see a marked improvement in alignment between ultrasound-visualized intraoperative tumor contour and the

preoperative tumor.

IV.3.5 Conclusion

The work reported herein establishes a preliminary realization of an image guided breast surgery approach using supine MR images. A workflow friendly alignment procedure using rigid and nonrigid registration methods is proposed and preliminary data in two patients is reported. The two cases represent a reasonable extent of the configurations possible during image-guided lumpectomy with the first patient (small breast volume) not experiencing gross volumetric misalignment after rigid registration, and the second (large breast volume) showing large shifts of the subsurface tumor target. In each, our investigational correction methodology showed considerable improvement in alignment both in quantitative metrics as well as visual overlays. To our knowledge, this work represents the first comprehensive image guided breast surgery platform using supine MR and nonrigid model-based registration methods that has been tested under appropriate *in vivo* clinical conditions with subsurface target registration errors being reported using echogenic tumors. The results are very encouraging at this early stage and many avenues for future work to improve guidance alignment are possible.

CHAPTER V

Quantification of Patient Specific Mechanical Properties

V.1 Summary and Contributions

In this chapter, a novel method to quantify patient specific breast tissue stiffness was developed. As noted in II.6, the literature reported biomechanical properties for breast tissue vary greatly. For example, *ex vivo* testing reports a range of 0.69 - 20 kPa for adipose tissue and 0.73-271 kPa for glandular tissue (see table II.1). For *in vivo*, elastography-based approaches, the range of reported values are also unacceptably large (0.41-25 kPa for adipose, 0.9-45 kPa for glandular [161]). Variations in reported stiffness properties are mainly due to differences in testing methodologies, continuum assumptions, measurement errors, and natural inter and intra patient differences in tissue elasticity. The use of literature values of breast tissue stiffness to populate patient-specific biomechanical models is inadequate due to these discrepancies in reported stiffness values. Furthermore, breast mechanical properties vary greatly between subjects so generalized applications of mechanical properties in biomechanical models used for clinical guidance is not ideal. The term *patient-specific* often implies that highly resolved geometric models are created from individual patient anatomy. In an extension to this broad definition, we have developed a method to further incorporate patient specific mechanical property parameters by estimating the stiffness of the underlying breast tissue to improve the accuracy of these models. Focus was placed on creating a framework to be implemented within an image guided breast surgery workflow.

In this stiffness estimation framework, only a single additional two minute MR scan is required beyond the current preoperative image guided breast surgery framework and is driven by two supine gravity loaded configurations of the breast. The method takes advantage of image registration principles to capture the driving deformation source (i.e. a change in the direction of gravitational loading). In this study, we demonstrate feasibility of this approach in humans using ten unique stiffness estimates of fibroglandular and adipose tissue in healthy volunteers and measure reproducibility in five test retest datasets. To our knowledge, we are the first to perform *in vivo* reproducibility studies of a gravity-based stiffness estimation method. From this work, we established a comprehensive stiffness estimation procedure using deformations representative of supine breast cancer interventions. Using our unique tissue

excitation technique and novel calculation of the driving gravity induced body forces, we produced absolute stiffness parameter estimates for ten unique image volumes which to our knowledge has never been studied as extensively. In addition, the methodology we have investigated is completely compatible with a supine breast image-guided surgery methodology. This study also reports important observations regarding the resolution of mechanical properties with respect to displacement extent and image intensity feature volumes. Overall, the results are very encouraging, demonstrating that absolute and reproducible measures are possible and an investigation towards optimization methods to adapt this method towards inverse heterogeneous mechanical property reconstruction remain as future work.

V.2 Breast tissue stiffness estimation for surgical guidance using gravity-induced excitation

The work in this chapter appears in:

Griesenauer, R. H., Weis, J. A., Arlinghaus, L. R., Meszoely, I. M., and Miga, M. I. "Breast tissue stiffness estimation for surgical guidance using gravity-induced excitation.", Physics in Medicine and Biology 62.12 (2017): 4756.

Abstract

Tissue stiffness interrogation is fundamental in breast cancer diagnosis and treatment. Furthermore, biomechanical models for predicting breast deformations have been created for several breast cancer applications. Within these applications, constitutive mechanical properties must be defined and the accuracy of this estimation directly impacts the overall performance of the model. In this study, we present an image-derived computational framework to obtain quantitative, patient specific stiffness properties for application in image-guided breast cancer surgery and interventions. The method uses two MR acquisitions of the breast in different supine gravity-loaded configurations to fit mechanical properties to a biomechanical breast model. A reproducibility assessment of the method was performed in a test-retest study using healthy volunteers and was further characterized in simulation. In five human data sets, the within subject coefficient of variation ranged from 10.7% to 27% and the intraclass correlation coefficient ranged from 0.91-0.944 for assessment of fibroglandular and adipose tissue stiffness. In simulation, fibroglandular content and deformation magnitude were shown to have significant effects on the shape and convexity of the objective function defined by image similarity. These observations provide an important step forward in characterizing the use of nonrigid image registration methodologies in conjunction with biomechanical models to estimate tissue stiffness. In addition, the results suggest that stiffness estimation methods using gravity-induced excitation can reliably and feasibly be implemented in breast cancer surgery/intervention workflows.

V.2.1 Introduction

Tissue stiffness interrogation plays a critical role in breast cancer from self-examinations and tumor staging to palpation guided biopsies and surgery. Unfortunately, not all clinically relevant breast lesions are palpable. For example, ductal carcinoma in situs are rarely palpable and are usually diagnosed by microcalcifications seen in x-ray mammography [227]. These early stage cancers and other clinically

occult breast lesions make tumor localization difficult for biopsies and surgical tumor removal [215]. These localization complications directly contribute to unacceptably high reoperation rates for breast conserving surgery (20-40% [21]). For this reason, enhanced tumor localization strategies have been suggested and include using image guidance systems that rely on patient specific biomechanical breast models to predict tumor locations for biopsies and surgical removal [104, 154]. Image guided breast surgery (IGBS) is performed by registering pre-surgical images to the same 3D coordinate space as the operating room. The fundamental concept of IGBS is to track the position of surgical instruments using optical or electromagnetic sensors and determine their location with respect to the physical position of the tumor as determined by registered preoperative imaging data, i.e. an image-to-physical registration. For procedures involving soft tissue, such as the breast, deformation between the preoperative image and the operating room position is inevitable; the preoperative images no longer match the surgical reality. For this reason, IGBS relies on a nonrigid alignment between image and patient. One such methodology relies on patient specific biomechanical models to deform the preoperative data to match the geometric configuration of the breast in the operating room. The term patient-specific often implies that highly resolved geometric models are created from individual patient anatomy. In an extension to this broad definition, we have developed a method to further incorporate patient specific mechanical property parameters by estimating the stiffness of the underlying breast tissue to improve the accuracy of these models.

Mechanical models for breast deformation have also been created for needle path and biopsy planning [148, 228] breast augmentation planning and simulation [150–152] and radiation therapy targeting [153]. Within these applications, various material constitutive models have been employed. For example, breast tissue has been modeled as nonlinear or linear elastic, isotropic or anisotropic, and homogeneous or heterogeneous depending on the application, deformation magnitude, and desired accuracy.

With respect to applications, many biomechanical models have been used for predicting breast deformation in biopsy and simulating mammographic compressions. These applications are usually driven by displacement boundary conditions that compress the breast into biopsy and/or mammogram geometries [229]. An estimate of relative stiffness for different breast tissue types is usually sufficient for these applications due to the indeterminate nature of displacement boundary conditions. However, when contact forces or gravitational loading conditions are applied, absolute material property values are required. There are several models that incorporate gravitational loading and/or contact forces for

applications in aligning prone and supine images [153], modeling mammographic compressions [146], and performing image-to-physical space registration of preoperative breast image volumes for use in guiding surgery [154]. In many of these studies, the material properties are estimated using literature values and are not patient specific. In addition, a recent review of the biomechanical properties of breast tissue [161] reported a large variation in stiffness properties for fibroglandular, adipose, ductal carcinoma in situ, and invasive ductal carcinomas. Variations in reported stiffness properties are mainly due to differences in testing methodologies, continuum assumptions, measurement errors, and natural inter and intra patient differences in tissue elasticity. Breast material properties vary greatly between subjects so generalized applications of mechanical properties in biomechanical models used for clinical guidance is not ideal. For example, variations in material properties among subjects have been attributed to age (more adipose, less fibroglandular tissue [162] and breakdown of connective tissue), genetic factors, and hormonal changes [163]. Therefore, for procedure planning and guidance purposes, patient specific in-vivo mechanical property estimation is likely to result in improved accuracy.

In most conventional techniques to estimate absolute stiffness properties, a known force or pressure must be applied followed by an observed measurement of tissue deformation. In the methodology described in this study, changes in the direction of gravitational loading are used as the known excitation force and magnetic resonance imaging (MRI) is used to quantify tissue deformation. One advantage to the methodology is that breast mechanical properties are being determined in a testing configuration that is extremely close to its surgical counterpart. Others have also made similar investigations. In Chung et al. [145], a method is reported that estimates material properties using gravity induced deformations within the context of modeling mammographic compression. With that work, a gel phantom with a simplistic breast shape was imaged in two gravity loaded configurations (0 and 10.5 inclines off the superior-inferior axis). A single optimal material parameter was found by minimizing the root mean square (RMS) distance error between model predicted and experientially acquired surface points. In similar work, the concept of using multiple gravity-loaded configurations to estimate mechanical properties was further reported in Gamage et al. [230] using a two-layered gel cantilever beam. *In vivo* realizations of generating stiffness estimates by fitting model parameters to observed deformations due to changes in gravitational loading have been performed [143, 151, 231] . In del Palomar et al. [151] , a single material constant was iteratively adjusted to minimize residual errors of 7 surface landmarks between supine and standing breast configurations. In Rajagopal et al. [143] , MR image volumes of

the prone breast submerged in water were used to represent a gravity-free mechanical reference state. In this configuration, buoyancy forces were estimated to counteract the effects of gravity. Neutral buoyancy images (gravity-free) and prone images (gravity-loaded) were used to estimate a single material property. A similar study using submerged and unsubmerged prone breast images reproduced this technique [231] , except individual stiffness properties for fibroglandular and adipose tissue were used as opposed to a single material definition for the whole breast. In Rajagopal et al. [143], the purpose was to validate a computational approach for estimating the gravity-free reference state of the breast for applications in prone to supine registration. In both studies, the authors concede that submerging the breast in water during the MRI exam is not clinically practical for routine study.

While mechanical property estimations using gravity induced deformations have been performed in gel phantoms, there is a lack of data showing feasibility of this concept in human subjects in terms of reliable tissue stiffness identification with techniques amenable to clinical settings. In [143, 231] , the gravity-induced excitation (submerged/unsubmerged prone breasts) is not clinically feasible. In [151] , errors induced by nonlinearity and gravitational pre-stress may have been compounded by very large deformations between supine and standing breast configurations. Overall, while estimates of mechanical properties *in vivo* have been produced using gravitational excitation, they represent only a feasibility sampling of one to two subjects with no sense of methodological repeatability and reproducibility [143, 151, 231] . We address these limitations and challenges in this paper by developing a stiffness estimation framework that is based on two supine gravity loaded configurations of the breast. Our method takes advantage of image registration principles to capture the driving deformation source (i.e. a change in the direction of gravitational loading). We use rich image similarity data rather than spare point displacement errors used in all previously reported gravity-based stiffness estimation methods. Validation work has been performed in phantoms using image similarity to drive mechanical property estimation [179, 182, 232] . In [232] , stiffness ratios as determined by mechanical testing of the phantom material were compared with stiffness ratios as determined by an *in vivo* stiffness estimation that relies on the same image similarity parameters used in this current study. The percent errors between the mechanical testing ratios and image-derived stiffness estimations were 8-12%. In this study, we demonstrate feasibility of this approach in humans using ten unique stiffness estimates of fibroglandular and adipose tissue in healthy volunteers and measure reproducibility in five test-retest datasets. To our knowledge, we are the first to perform *in vivo* reproducibility studies of a gravity-based

stiffness estimation method.

V.2.2 Methods

Theory

Before describing each component of our novel stiffness estimation algorithm, an overview is outlined in Fig. V.1, beginning with the acquisition of two supine volumetric images. The first image is acquired with the subject in the supine position. The subject is then slightly rotated along the longitudinal axis of the body by placing a support wedge posterior to the breast and imaged again. Gravity-induced deformations occur due to a change in tissue weight distribution. A biomechanical model is used to simulate breast deformations that occur between the two image acquisitions. The forward model is solved with a range of stiffness properties for each tissue type. An image similarity metric is used to calculate the residual error between the model deformed and experimentally acquired image. Patient specific stiffness property values are selected by optimizing the image similarity metric.

Image Acquisition and Preprocessing

Magnetic resonance (MR) images of the breast are typically acquired using a dedicated breast coil with the patient lying in the prone position with freely hanging breasts. However, supine MR images are desirable within the context of surgical navigation because they more closely represent the surgical position. This position also readily allows for gravity induced deformations amenable to the proposed stiffness estimation method. After informed written consent in an IRB approved study, the study volunteer was positioned in a 3T Achieva MR scanner (Philips Healthcare, Best, The Netherlands). A 16-channel sensitivity encoding torso coil (SENSE XL Torso Coil, Philips Healthcare) was situated carefully as to not induce unnatural deformations to the breast. The ipsilateral arm was placed above the volunteers head as to not deform or provide external support to the breast (somewhat similar to the lateral arm extension that occurs during lumpectomy procedures). The healthy subject image data was acquired with: TR=7.422 ms, TE=3.91 ms, and flip angle= 10 degrees using SENSE parallel imaging (acceleration factor = 2). High resolution anatomical images were acquired with a T_1-weighted, 3D turbo field echo sequence with fat suppression, a field of view of 200 mm $\times$ 200 mm $\times$ 160 mm, and a reconstructed voxel size of 0.391 mm $\times$ 0.391 mm $\times$ 1 mm. The duration of each image volume acquisition was 120.6 seconds.

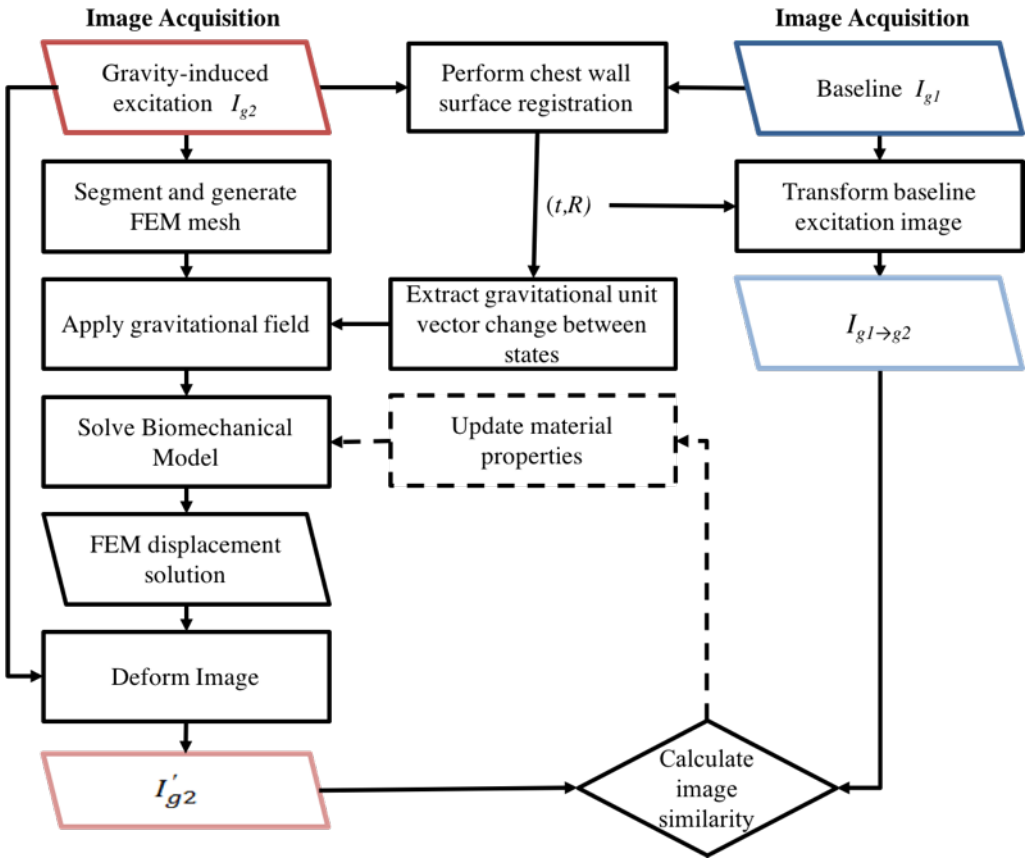

Figure V.1: The stiffness estimation framework begins with the acquisition of two gravity loaded image volumes (see Fig. V.2). A rigid alignment between the two configurations is performed using only chest wall intensity information. The rigid registration procedure results in a translation, t, and rotation, R, that is used to transform I_{g1} to be rigidly aligned with the chest wall in I_{g2} (see Fig. V.4). Also from R, a change in gravitational loading is quantified. A FEM mesh and biomechanical model is built from I_{g2} . A displacement field is generated from solving the biomechanical model and is used to deform I_{g2} . An image similarity metric is calculated between the model deformed image (I'_{g2}) and the rigidly aligned baseline image ($I_{g1\rightarrow g2}$). Stiffness properties are extracted when the calculated image similarity is optimized. An optimization procedure can be employed to iteratively update the material properties until the image similarity metric is minimized.

Image volumes were acquired before and after a gravity-induced excitation for each volunteer. The mechanical excitation for this method involves slightly rotating the subject along the longitudinal axis of the body by placing a 15° foam support wedge posterior to the torso side with the breast being imaged. The torso rotation causes a change in the baseline patient configuration with respect to the acting direction of gravity. Gravity induced deformations occur as a result of changes in tissue weight distributions with the rotating torso. Central axial image slices of the baseline and gravity-induced excitation configurations are shown for a representative subject in Fig. V.2.

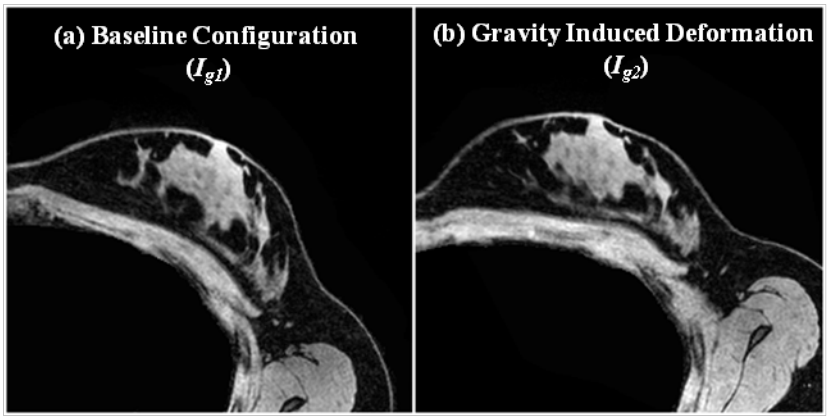

Figure V.2: Two representative gravity loaded configurations used as input images in the stiffness estimation method. (a) represents the baseline configuration (I_{g1}) while (b) represents the breast after a gravity induced excitation ($Ig2$).

For computational efficiency, image volumes were downsampled to 256 × 256 × 160 with voxel sizes of 0.78 mm × 0.78 mm × 1 mm. The breast (excluding chest wall muscles) was segmented from the gravity-induced configuration (I_{g2}) using ITK-SNAP [199]. A region based segmentation method was used to automatically classify breast tissue into two types: adipose and fibroglandular. The Markov Random Field (MRF)-based algorithm, implemented using The Insight Toolkit (ITK) [233], assumes that adjacent pixels likely belong to the same tissue type or class and performs segmentation using intensity similarity between adjacent pixels. Following segmentation, a binary mask of the whole breast was used to generate a boundary surface using a marching cubes algorithm [200], implemented with the Visualization Toolkit (VTK) [201]. Following surface generation, radial basis function smoothing was applied using the FastRBFToolbox (Farfield Technologies, Christchurch, New Zealand). A volumetric tetrahedral finite element mesh with a nominal edge length of 3 mm was created from this surface using a custom mesh generator [202]. Fig. V.3a shows two orthogonal slices of a segmented supine breast

classified into adipose (white) and fibroglandular tissue (red) with the FE mesh overlaid in black.

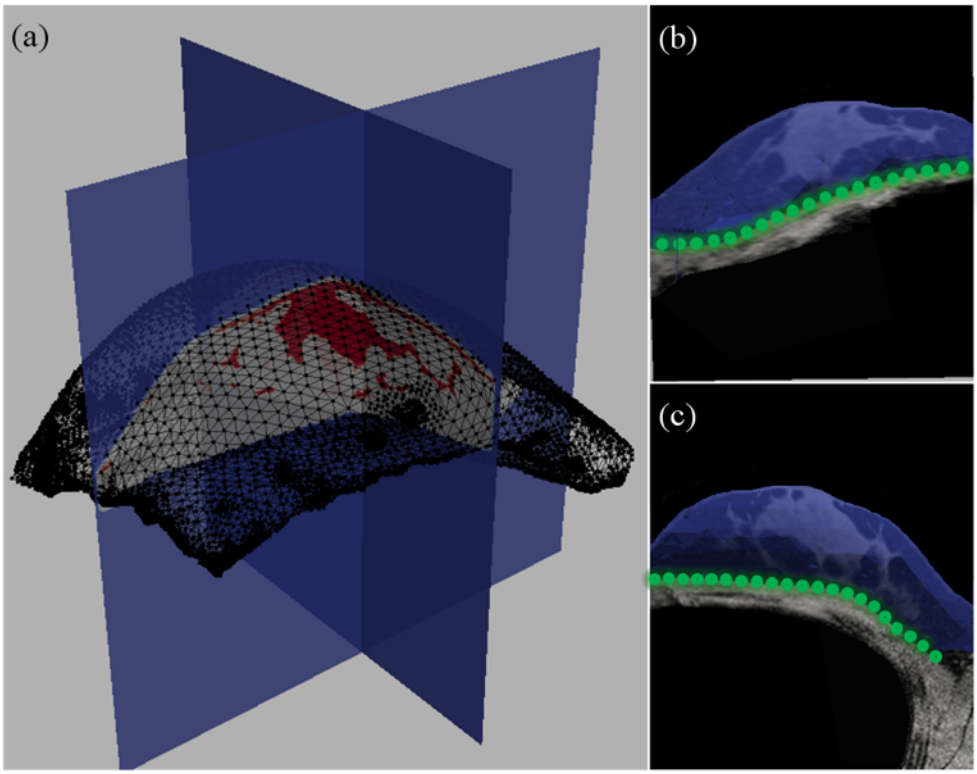

Figure V.3: (a) Tetrahedral mesh built from a representative gravity-induced configuration image (I_{g2}). The black wire outline shows surface elements of the mesh. Two orthogonal cuts of the segmented image volume along the axial and sagittal planes are shown with adipose represented in white and fibroglandular in red. Sagittal (b) and axial (c) slices of the I_{g2} image volume are shown with the mesh overlaid in blue. The green nodal spheres in (b, c) correspond to fixed boundary conditions along the chest wall. The rest of the mesh moves freely according to the applied body forces.

Biomechanical Model

In this study, we use a mechanics based computational model to simulate breast deformation. The partial differential equation that expresses a static stress distribution in a material in response to a known body force is shown in V.1.

$$\nabla \cdot \sigma = \beta \tag{V.1}$$

where σ is the stress tensor and β represents a body force. The stress-strain relationship according to Hooke's law is

$$\sigma = C\varepsilon \tag{V.2}$$

where C represents the stiffness tensor of a material and ε is a strain tensor. Biological tissue is often represented using linear strain elements depending upon the application, desired accuracy, and computational requirements. The full nonlinear formulation, known as Greens strain tensor, results in a nonlinear algebraic system that is computationally expensive while the linear approximation to Greens tensor (Cauchy tensor) often mishandles larger deformations. In this study, we employ a nonlinear corotational FEM formulation [126], which represents a compromise in terms of computational burden and accuracy between the full nonlinear strain tensor and the linear approximation. In the corotational model, large local rigid body movements are accounted for and the remaining shape change is handled by linear elastic mechanics (i.e. neglecting quadratic terms in Greens tensor). While not a nonlinear constitutive relationship per se, accounting for large local tissue rigid motion does not require an iterative nonlinear approach. Corotational FEM models have been widely used within the soft-tissue large deformation mechanics literature [126–128].With respect to constitutive behavior, the conventional stress-strain relationship, Hookes Law, requires two material property constants to describe any given tissue, namely, ν (Poissons ratio) and E (Youngs modulus). Youngs modulus represents the stiffness of a material and is optimized during the stiffness estimation process. Poissons ratio is the negative ratio of lateral to longitudinal strain in an axially loaded material and represents a characterization of compressibility. Since biological soft tissue is generally quite hydrated, we assume breast tissue to be slightly to nearly incompressible. Largely due to the challenge in soft-tissue material testing, there is sparse data on ν for breast tissue. As a result, ν was added as another degree of freedom in the model varying over the range of = 0.40 0.47. Equation V.3 shows the stress-strain relationship for a linear elastic, isotropic material.

$$\begin{bmatrix} \sigma_1 \\ \sigma_2 \\ \sigma_3 \\ \sigma_{23} \\ \sigma_{13} \\ \sigma_{12} \end{bmatrix} = \frac{E}{(1+\nu)(1-2\nu)} \begin{bmatrix} 1-\nu & \nu & \nu & 0 & 0 & 0 \\ \nu & 1-\nu & \nu & 0 & 0 & 0 \\ \nu & \nu & 1-\nu & 0 & 0 & 0 \\ 0 & 0 & 0 & \frac{1-2\nu}{2} & 0 & 0 \\ 0 & 0 & 0 & 0 & \frac{1-2\nu}{2} & 0 \\ 0 & 0 & 0 & 0 & 0 & \frac{1-2\nu}{2} \end{bmatrix} \tag{V.3}$$

Furthermore, the relationship between strain and displacement is $\varepsilon_{i,j} = 1/2(u_{i,j} + u_{j,i})$ where u defines a three-dimensional displacement field. Using linear basis functions defined on tetrahedral finite elements, we performed the Galerkin Method of Weighted Residuals to obtain a system of equations to

resolve the unknown displacement coefficients. Ultimately, we are interested in finding the mechanical properties of breast tissue that produce a displacement field that when used to deform the gravity excited image (I_{g2}) matches the baseline configuration image ($I_{g1\rightarrow g2}$).

Boundary Conditions

In our model, the chest wall is assumed to be a reliably rigid structure in relation to breast tissue. Therefore, rigid alignment using chest wall intensity information was performed to extract the relative rotation that occurred between the baseline configuration and the torso rotated image configuration. The following image processing steps were performed to extract the geometric change of the breast relative to the direction of gravity:

1. **Segment the chest wall muscles in each image**:

   The chest wall was semi-automatically segmented in each image using ITK-SNAP's implementation of the Snake's algorithm [207].

2. **Rigidly register the baseline and gravity-induced images**:

   A standard rigid registration [208] was performed using image contrast patterns of the *chest walls* in the two image volumes to transform the baseline image (I_{g1}) into the gravity-induced configuration space (I_{g2}). Fig. V.4 displays a representative result of such a registration. I_{g1} and I_{g2} chest wall image masks are highlighted to show the driving components of the registration (Fig. V.4a,V.4b). The transformation matrix (containing translation, t and rotation, R) is used to rigidly align the baseline image to the gravity-induced configuration image (Fig. V.4c). An overlay of the gravity-induced (I_{g2}) and registered baseline images ($I_{g1\rightarrow g2}$) are shown in Fig. V.4d and visually confirms that the chest wall muscle beneath the breast rigidly aligns compared to the breast tissue above that has deformed due to the difference in gravitational loading. Once aligned, rigid translational components are accounted for and the remaining tissue dissimilarity is due to rotational components that arise from gravity-induced deformations.

3. **Extract gravity differential vector:**

   The gravity differential vector can be extracted from the rotation matrix using (V.4):

$$\Delta\hat{g} = \hat{g}_1 - R * \hat{g}_1 \tag{V.4}$$

$$\beta = 9.8\frac{m}{s^2}\,\rho\,\Delta\hat{g} \tag{V.5}$$

where $\hat{g}_1$ is assumed to be unit vector normal to the MR table. In (V.5) , β is subsequently applied as a body force of tissue weight in the biomechanical model (V.1). The tissue density, ρ is assumed to be uniform and approximately equal to water,1000 kg/m^3. The model nodes associated with the chest wall are fixed in the x, y, and z directions, i.e. applied Dirichlet boundary conditions set to zero. Fig. V.3b and V.3c show central sagittal and axial image slices with the volumetric mesh overlaid in blue. The green spherical nodes represent the fixed posterior surface along the chest wall.

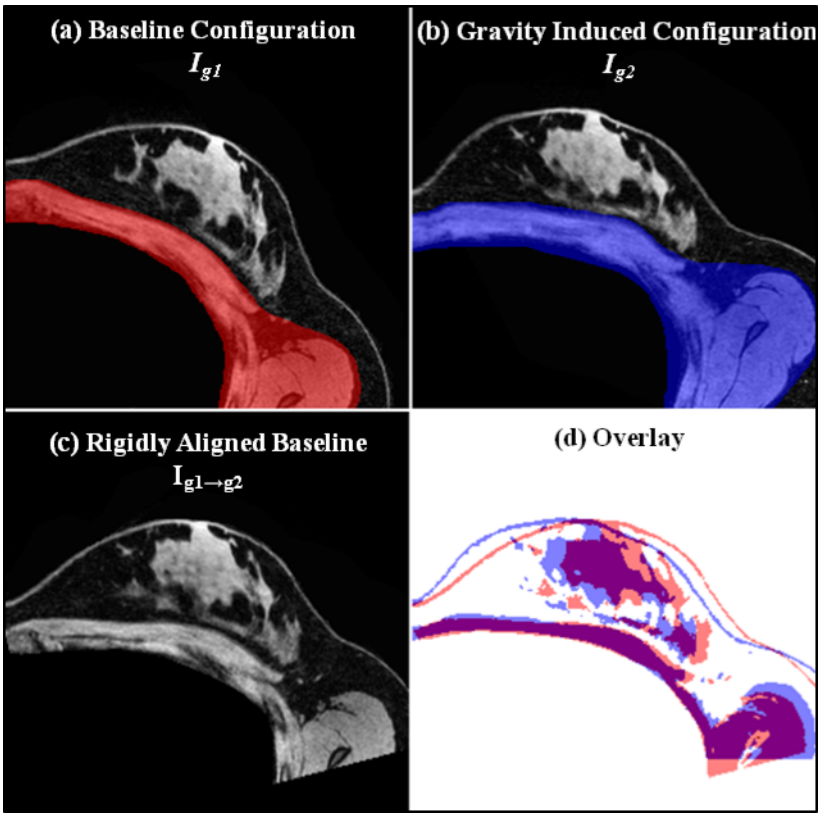

Figure V.4: Representation of the rigid alignment procedure described in Section V.2.2. Central axial slices are shown of the (a) baseline configuration image, and (b) gravity-deformed configuration with overlays of chest wall regions used in initial alignment. The transformation matrix extracted from the rigid registration is used to align the chest walls in the baseline configuration and the gravity-deformed configuration so that the resulting misalignment of breast tissue is due to deformations caused by the change in gravitational loading. In (c), we see the aligned baseline to the gravity-induced reference frame, and (d) contains image masks of the rigidly aligned baseline image ($I_{g1\rightarrow g2}$) (red) and gravity deformed image (I_{g2}) (blue). It is clear that the chest wall is relatively rigid compared to the mismatch in breast tissue structures due to gravity induced nonrigid deformation.

Stiffness Estimation

The stiffness estimation process first begins with generating an eroded binary mask of the torso-rotated image volume for the purpose of designating a zone in which to compute an image similarity metric between the model deformed image and the chest wall aligned baseline image. The Youngs modulus values for adipose and fibroglandular tissue were then estimated by performing an exhaustive search of the parameter space and selecting the set of properties that optimized the image similarity metric defined by eq. (V.6)

$$S = (1 - CC) \tag{V.6}$$

where S is the similarity metric to be minimized and CC is the image correlation coefficient defined by eq. (V.7).

$$CC = \frac{\sum_i (I'_{|g2|i} - \bar{I}'_{|g2|})(I_{|g1\to g2|i} - \bar{I}_{|g1\to g2|})}{\sqrt{\sum_i (I'_{|g2|i} - \bar{I}'_{|g2|})}\sqrt{\sum_i (I_{|g1\to g2|i} - \bar{I}_{|g1\to g2|})}} \tag{V.7}$$

where $I'_{|g2|i}$ and $I_{|g1\to g2|i}$ are the intensity values at pixel i for the model deformed and chest wall aligned baseline images, respectively. $\bar{I}'_{|g2|}$ and $\bar{I}_{|g1\to g2|}$ are the mean intensity values of the model deformed and chest wall aligned baseline images. CC has a value of 1 if two images are absolutely identical and a value of zero if completely uncorrelated.

Experiments

Test-retest reproducibility in human subjects

In an IRB approved study with informed written consent, healthy female volunteers over the age of 18 without evidence of pregnancy were recruited for a test-retest study to measure the reproducibility of this stiffness estimation technique. The five test-retest datasets are comprised of three healthy volunteers ages 21-36, with the left and right breasts of two volunteers and the left breast of a third volunteer. Due to differences in right/left breast volumes, fibroglandular content [234], tissue hydration levels [235], and a lack of data to suggest symmetry in material properties [236] we consider each breast to be an individual dataset. Therefore, this work presents a total of ten stiffness estimates and five test-retest datasets to determine method reproducibility. A reproducibility assessment was performed using a test-retest approach in which volunteers were scanned in a baseline position and re-set between the two-consecutive gravity-loaded configuration scans. Independent stiffness estimations were then performed for each baseline-gravity-deformed dataset using the methodology described above. The

parameter search space used in human subjects is summarized in Table V.1. The lower and upper bounds of the parameter search space for each tissue type was determined by encompassing the range of previously reported tissue stiffness values in quasi-static/low frequency shear wave MRE studies [161, 237–239].

Table V.1: Parameter space used in human subjects study:

Tissue Type	Lower Bound	Upper Bound	Step Size
Adipose	0.05 kPa	2.5 kPa	0.05 kPa
Fibroglandular	0.05 kPa	12 kPa	0.05 kPa
Poisson's Ratio	0.40	0.47	0.01

The test-retest variability was calculated as the absolute value of the difference between test-retest stiffness values expressed as a percentage of the mean of both stiffness values:

$$\Delta E(\%) = \frac{|E_1 - E_2|}{(E_1 + E_2)/2} \times 100 \tag{V.8}$$

where E_1 and E_2 are the test and retest stiffness estimations, respectively. Test-retest variability was calculated for each tissue type and is commonly reported in quantitative imaging studies [240, 241] as a measure of standardized variability in measurement errors across subjects. The mean test-retest variability across all datasets is reported as $m\Delta E$. The between subject standard deviation (SD) and within subject standard deviation (wSD) was reported to further assess variability and reproducibility. The wSD was calculated according to [242] as follows:

$$wSD = \frac{\sqrt{\frac{\sum_{i=1}^{n}(E_{1i} - E_{2i})^2}{n}}}{\sqrt{2}} \tag{V.9}$$

where n represents the number of test-retest datasets. The coefficient of variation (CV) and within subject coefficient of variation (wCV) was calculated by dividing SD and wSD by the overall parameter mean for each tissue type. We calculated the intraclass correlation coefficient (ICC) [243], which relates the magnitude of measurement error to the inherent variability between subjects using equation V.10. High ICC values indicate that the measurement errors are low in comparison to the true difference between subjects and takes a value between 0 and 1.

$$ICC = \frac{(SD)^2}{(SD)^2 + (wSD)^2} \tag{V.10}$$

Simulation

Simulations were performed to investigate the sensitivity of the objective function to two aspects of the testing framework, (1) adipose-to-fibroglandular tissue volume content, and (2) torso rotation extent. In the simulation framework, a model with known material properties, boundary conditions, and gravity-induced excitation was used to create model-deformed images from baseline image volumes. Material properties for adipose and fibroglandular tissue were selected using the approximate average stiffness values from the human subjects study (adipose and fibroglandular stiffness of 0.25 kPa and 2 kPa, respectively were used as ground truth). For each subsequent simulation set, stiffness property values were incrementally assigned based on the parameter search space with bounds described in Table V.2, a forward corotational linear elastic model was solved to obtain the displacement field, and the field was interpolated onto the baseline image to create a simulated gravity-deformed image. The image-intensity similarity metric described by Eq. V.7 was then calculated between the baseline and model-deformed image volumes. In addition to similarity, a displacement error metric (Eq. V.11), was also calculated as a measure of difference.

$$\text{RMS Displacement Error} = \frac{1}{N}\sum_{i=1}^{N} |d_{true,i} - d_{model,i}|^2 \tag{V.11}$$

where N is the number of nodes in the FEM mesh, $d_{true,i}$ are the true nodal displacements provided by the FEM simulation in this case, and $d_{model,i}$ are the FEM nodal displacements generated by the current mechanical property model parameters.

Table V.2: Parameter space used in simulation study:

Ground truth is 0.25 kPa and 2 kPa for adipose and fibroglandular, respectively

Tissue Type	Lower Bound	Upper Bound	Step Size
Adipose	0.1 kPa	0.5 kPa	0.05 kPa
Fibroglandular	1 kPa	4 kPa	0.05 kPa

To study the effect of adipose-to-fibroglandular tissue volume, baseline image volumes from four healthy volunteers were chosen to represent breasts with low (12%), moderate (24%), and high (33

& 39%) fibroglandular contents. A parameter sweep was performed for each simulation set with an applied body force generated from an approximate 30° rotation about the longitudinal axis of the body. Investigations on the extent of torso-rotation were performed using the moderate level fibroglandular content image volume. The effect of gravity induced deformation magnitude was explored by performing simulation parameter estimations using three angles of rotation corresponding to approximately 15°, 30°, and 45° rotations along the longitudinal axis.

V.2.3 Results

Healthy Volunteers

A representative summary of the parameter sweep search results are shown in Fig. V.5 for two test-retest datasets. A central axial slice of the baseline image is shown in Fig. V.5 (a) for each stiffness estimation procedure. Masked overlays of the baseline image (gray), gravity-induced configuration image (blue), and model-optimized image (red) are shown to the right of the anatomical baseline image. While single axial image slices are shown for display purposes, property estimations and error calculations were volumetric. Qualitative assessment of these images show a significant improvement in image alignment when stiffness properties are optimized. Below each image set are the image similarity error maps (d). The contour plots show the value of the image similarity metric for each adipose (x-axis) fibroglandular (y-axis) combination sampled. Each has an elongated minimum region suggesting greater sensitivity to adipose value contrast.

Quantitatively, the method provides reliable stiffness values for both adipose and fibroglandular tissue. The demographic information and test-retest stiffness estimations are summarized in Table V.3. The optimal Youngs modulus values for adipose and fibroglandular tissue were determined by selecting the parameters responsible for producing the best image similarity metric. Among the five test-retest datasets, the highest stiffness properties came from the youngest volunteer (Sets 1 and 2). The ratio of adipose tissue between the left (Set 1) and right (Set 2) breasts ranged from 1.16 to 1.8. The ratio of fibroglandular tissue between the left (Set 1) and right (Set 2) breasts ranged from 4.5-6.2. Set 3 and Set 4 also represent the left and right breasts from the same subject with adipose ratios ranging from 2 to 2.5 and fibroglandular ratios ranging from 1.4-4.2.

Reproducibility and variability statistics for the five test-retest datasets are summarized in Table V.4. Test-retest statistics were calculated for the optimal stiffness parameters. The wCV for fibrog-

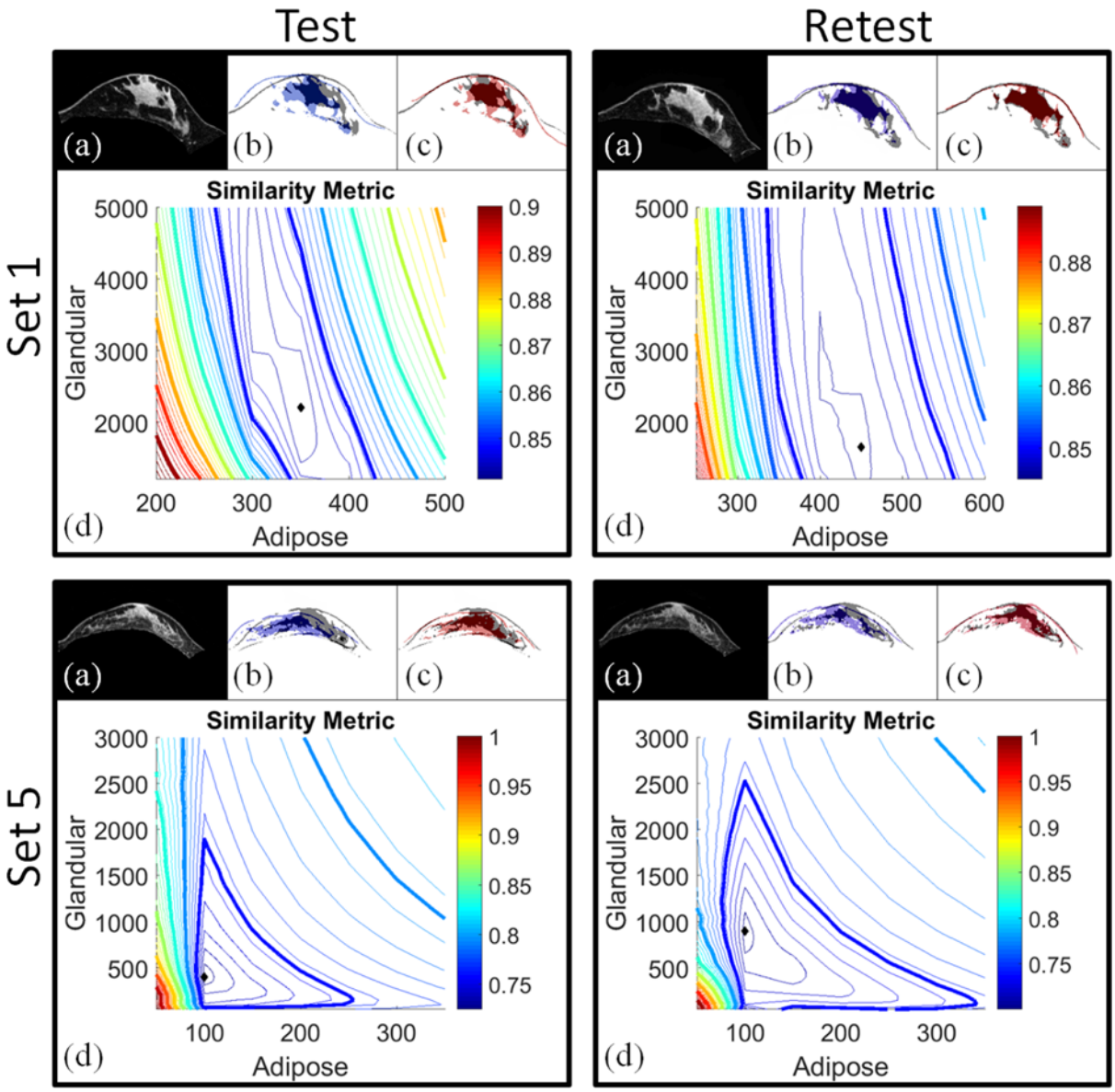

Figure V.5: Summary of the stiffness estimation results for Set 1 and Set 5. Image alignment comparisons are displayed in panels (a-c) for each test-retest set. In (a), axial anatomical image slices are shown for the baseline configurations. (b) contains masked versions of the baseline configuration image (gray) and gravity-induced configuration image (blue). In (c), masked image slices of the model-deformed configuration with optimized stiffness values are shown in red overlaid with the baseline configuration (gray). Qualitatively, there is significant improvement in the baseline image alignment when model-optimized stiffness parameters are used. Similarity metric maps are shown in (d) where the diamond in each map represents the minimum value of the contour plot (i.e. the optimal stiffness parameters). Contours represent the error in image similarity for each adipose-glandular value sampled.

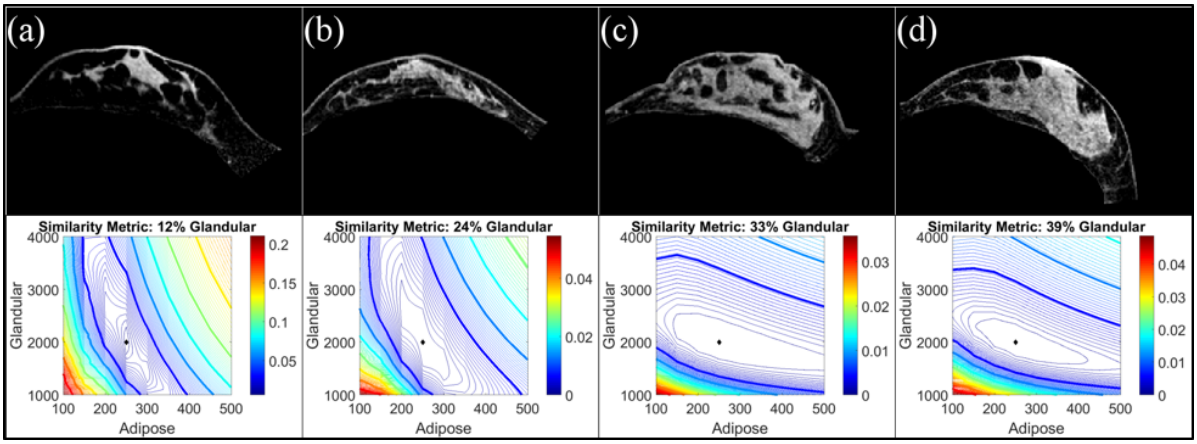

Figure V.6: Simulation results investigating the effect of fibroglandular content on the form of the similarity metric. Baseline images are shown from subjects with fibroglandular tissue volume contents of (a) 12%, (b) 24%, (c) 33%, (d) 39%. Using a 30° change in the gravitational unit vector and Youngs modulus values of 0.25 kPa (adipose) and 2 kPa (fibroglandular), simulated gravity-deformed images were created for each baseline image shown in the top panel. The bottom panel shows the resulting similarity error contour maps. The diamond represents the error map minimum.

landular tissue was 10.7% with respect to optimal parameter selection. The wCV for adipose tissue was 17.6%. A high reliability parameter (ICC) was observed for fibroglandular tissue at 0.994 and adipose at 0.91 using optimal properties. Overall, the wCV and ICC values combine to show reliable parameter estimates and indicate that the measurement error was substantially low compared to the true difference between subject breast tissue stiffness properties. We note that the Poissons ratio selected for optimal stiffness property determination used the full range (shown in Table V.1) in the best fit process. Given that we did not explicitly fit ν within each tissue type, allowing to float among a limited range of possible values tended to regularize the inverse problem.

Simulations

Effect of fibroglandular tissue

Fibroglandular content affects the shape of the similarity metric map. As shown in Fig. V.6, low fibroglandular content results in poor contrast in resolving fibroglandular tissue as evidenced by a lack of objective function gradient across varying values of fibroglandular stiffness. In contrast, the dramatic objective function gradients across varying adipose tissue values speak to considerable contrast. To some degree expected, we see a shift in convexity of the objective function with better contrast in the fibroglandular tissue with increased fibroglandular content along with a more dramatic gradient.

Table V.3: Stiffness estimation results for each test/retest dataset.

Demographics for each set:

	Age	Breast Volume (cm^3)	Fibroglandular Content(%)
Set 1	21	85	12
Set 2	21	84	16
Set 3	35	69	27
Set 4	35	61	22
Set 5	36	42	21

Test/Retest Results: Optimal Young's Modulus values (kPa) for adipose and fibroglandular tissue are reported for all 5 test/retest datasets. θ is the angle of rotational about the longitudinal axis of the body calculated from $\Delta\hat{g}$)

	$\Delta\hat{g}$	Optimal Adipose (kPa)	Optimal Fibroglandular (kPa)
Set 1			
Test	15.5	0.35	2.25
Retest	6.9	0.45	1.65
Set 2			
Test	9.2	0.30	10.30
Retest	8.6	0.25	10.15
Set 3			
Test	14.3	0.20	0.55
Retest	8.0	0.25	1.05
Set 4			
Test	18.9	0.10	0.25
Retest	13.2	0.10	0.35
Set 5			
Test	18.3	0.10	0.40
Retest	17.2	0.10	0.90

Table V.4: Reliability and variability statistics for adipose and fibroglandular tissue:The mean stiffness values are reported in kPa, SD and CV are the between subject standard deviation and coefficient of variation, wSD and wCV are the within subject standard deviation and coefficient of variation. $m\Delta E$ is reported as the percent mean $m\Delta E$ across all test/retest datasets and ICC is the intraclass correlation coefficient. n= 5 test/retest datasets.

Tissue Type	Mean	SD(CV)	wSD(wCV)	$m\Delta E$	ICC
Adipose	0.22	0.123(0.559)	0.0387 (0.176)	13.08	0.91
Fibroglandular	2.785	3.97(1.426)	0.2987(0.107)	41	0.994

Effect of gravity-induced deformation magnitude

Amplification of the gravity induced deformation via increased torso rotation directly impacts the convexity of the similarity metric as well as the shape of the RMS displacement error. In Fig. V.7, the three panels show an increase in deformation magnitude from left to right. Gray masks of a central axial slice of the baseline image are overlaid with magenta masks of the (a) 15°, (b) 30°, and (c) 45° rotated simulation images. Below each masked overlay are the image similarity metric and displacement error maps for each rotation. The displacement error maps are marked to indicate the contour levels that approximate the full (0.8 mm) and half (0.4 mm) in-plane voxel sizes.

As the deformation magnitude increases, the convexity of the error metrics increases. The average and maximum deformation magnitude caused by the simulated excitation was 2.8 (max = 6.3) mm, 5.7 (max = 12.9) mm, and 8.1 (max=18.6) mm for the 15°, 30°, and 45° rotation levels, respectively. Contour levels far below the voxel size indicate a limit in stiffness property resolution as changes in the image similarity cannot be detected below these levels. Elongation of the image similarity objective function maps is observed when compared to the RMS displacement error maps (which is a representation of true error). This observation may be attributed to the non-exact nature of feature comparison when using image similarity, image downsampling, partial volume effects, smoothing, and edge effects.

V.2.4 Discussion

In this study, we established a comprehensive stiffness estimation procedure using deformations representative of supine breast cancer interventions. Using our unique tissue excitation technique and novel calculation of the driving gravity induced body forces, we produced absolute stiffness parameter esti-

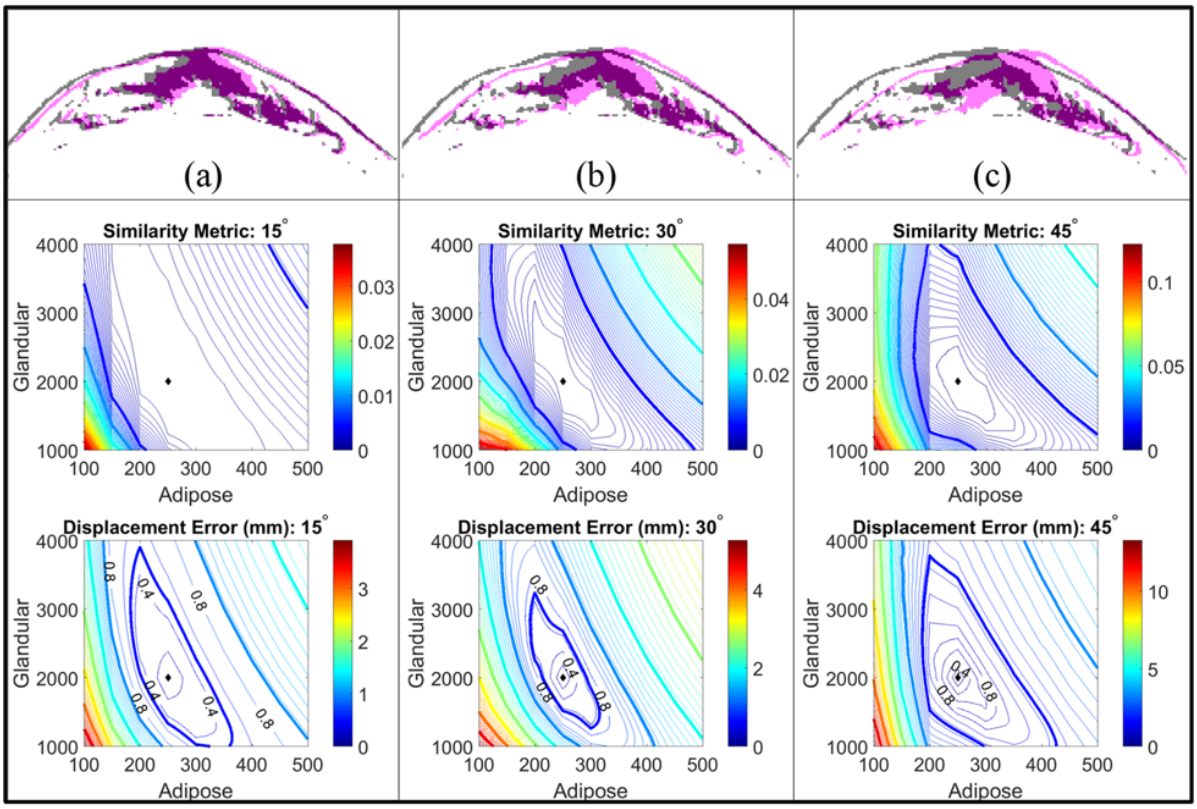

Figure V.7: Simulation results investigating the effect of deformation magnitude on the form of the error metrics. 15 (a), 30 (b), and 45 (c) degree changes in gravitational loading conditions with Youngs modulus values of 0.25 kPa (adipose) and 2 kPa (fibroglandular) were used to simulate gravity-deformed images with increasing (from left to right) deformation magnitudes. Contour plots of the image-based similarity metric are shown above the nodal displacement error contour maps for each rotation level. The displacement error maps are marked to indicate the contour levels that approximate the full (0.8 mm) and half (0.4) in-plane voxel sizes. The diamonds indicate the minimum value in each contour plot.

mates for 10 unique image volumes which to our knowledge has never been studied as extensively. In addition, the methodology we have investigated is completely compatible with a supine breast image-guided surgery methodology previously reported [154]. This clinically amenable workflow requires no complicated motion-sensitive imaging sequences or highly specialized equipment to induce and measure tissue deformations. This study reports important observations regarding the resolution of mechanical properties with respect to displacement extent and image intensity feature volumes. Overall, the results are very encouraging, demonstrating that absolute and reproducible measures are possible and an investigation towards optimal imaging sequences to ensure satisfactory resolution of the objective function are suggested for future work.

While MR images were used in this work, the method has been shown to be somewhat modality independent [167], as its estimates mechanical properties using image similarity metrics rather than relying on displacement measurement techniques inherent to a specific imaging modality (the method has been used previously with CT images and optical images [166, 184]). However, this work goes further than the closely-related investigations of the elastography method called Modality Independent Elastography (MIE) [166, 167, 176, 182, 184, 232]. More specifically, previous MIE investigations were only successful in predicting soft-tissue stiffness ratios between adipose, fibroglandular, and tumor due to the use of indeterminate displacement boundary conditions. In this study, we deploy an adaptation that uses gravitational body forces for excitation, which as equation III.8 shows, transforms the approach to generating absolute quantitative stiffness tissue values.

To our knowledge, this study reports the first test-retest reproducibility assessment of an MRI- derived, absolute quantitative breast tissue stiffness estimation method using gravity-induced excitations. Our test-retest wCV (wCV-10.7% and 17.6% for fibroglandular and adipose, respectively) and ICC (ICC- 0.994 and 0.91 fibroglandular and adipose, respectively) values are comparable to other quantitative imaging reproducibility studies. In Weis et al. [232], the reproducibility of the MIE method in murine breast cancer models was studied. The wCV ranged from 13% at the bulk level to 32% at the voxel level. The ICC values reported in [232] ranged from 0.70-0.99. Due to our modest sample size, robust statistical analysis for true significance is limited; however, this work is suggestive and quite encouraging.

From the perspective of clinical workflow, this work suggests various improvements to the image acquisition and mechanical excitation procedure that can be adapted to improve the performance of

the method. The shifts in convexity of the similarity objective function maps shown in Fig. V.6 and Fig. V.7 was a significant finding in the simulation studies. These results indicate that a lack of signal (or decreased image volume texture) in either tissue type will cause the objective function to provide less contrasting gradients with respect to the tissue-type of decreasing signal content. In future studies, weighting schemes and adjustment of image acquisition sequences will need to be studied to further investigate this observation and perhaps develop novel image acquisition frameworks to maximize contrast performance. For example, in previous MIE studies, simultaneous MRI acquisitions of fat-only and water-only images were performed using a commercially available Dixon sequence [183]. We can utilize these image sequences to improve objective function sensitivity depending on tissue-type content. Similarly, we also observed in this study that amplifying the deformation magnitude by increased torso rotation will better condition the objective function for future inverse property reconstruction methods. The degree of rotation in the volunteer study overall best corresponds to the 15° rotation in the simulation study. We experimentally observed that increased torso rotations are particularly important for small and/or stiff breast volumes. Therefore, we can customize our image acquisition protocol to accommodate breast density. Lastly, all of these observations will be particularly important as we use this information to advance the performance of inverse reconstruction procedures based on similarity (e.g. MIE).

With respect to limitations of this work, in addition to our modest sample sizes, the average volunteer age was 30, which is relatively young compared to the average breast cancer patient. It is likely that additional work would be needed to resolve aspects that vary with age. Across all subject types, it is likely that more advanced nonlinear constitutive relationships will be needed in the future to further improve accuracy of such methods. Similarly, quasi-static excitation neglects a potentially rich source of time-varying viscoelastic effects that may be important for interactive IGBS systems. Additionally, we also need to consider the accuracy of boundary conditions. While the model accounts for gravity induced deformations, it ignores contributions from Coopers ligaments, pectoral muscle forces, and rigid registration errors during the initial alignment procedure. Understanding the impact of these missing factors and sources of error is an important direction for improving performance. Clearly, another limitation is that we prescribe the tissue types as isotropic and homogeneous. In future work, spatially discretized region-based mechanical property reconstructions, similar to that of the MIE methodology, may be needed to create better geometric maps of tissue stiffness. With this last item, these capabilities

tend to be goals within diagnostic elastography applications. In terms of image acquisition protocols, there are areas to be improved. The image acquisition methods performed in this study were adapted from an existing prone imaging protocol [244]. For a healthy volunteer, the signal to noise ratio (SNR) calculated according to [245] was measured in a prone and supine setup using the image parameters defined in Section 2.2. In the prone acquisition, a dedicated breast coil (16-channel receive double-breast coil, Philips Healthcare, Best, The Netherlands) was used. The SNR in the prone images was 55.8 while the supine image SNR was 27.2. The reduced SNR in the supine images is due to respiratory and motion artifacts while also compounded by the fact that the torso coil used in the study is not optimized for breast imaging. An avenue worth pursuing in the future is to use respiratory-triggered MR acquisitions, which have been shown to improve the SNR of supine breast images [245].

As the work moves forward, we must establish which features are most important for the accurate execution of IGBS. Nevertheless, it is encouraging that our preliminary stiffness values are within range of low frequency, minimal pre-compression elastography methods. For example, in Chen et al. [237], a non-compressive elastography system with relatively low frequency shear waves (40 Hz) was tested in 7 healthy subjects. The stiffness range for adipose tissue was 0.25 0.41 kPa and 0.46 0.9 kPa for fibroglandular tissue. In Lorenzen et al. [239], MR elastography values for 20 patients and 15 healthy volunteers were reported with 0.5 - 4 kPa (median = 1.7 kPa) for adipose tissue and 1-15 kPa (median = 2.5 kPa) for fibroglandular tissue. Traditionally, magnetic resonance elastography studies report stiffness values in terms of shear modulus (G), which can be approximated to Youngs modulus by $E = 3G$. With our quasi-static study herein, we report mean stiffness values of adipose tissue to be 0.2 +/- 0.1 kPa and 2.8 +/- 4.0 for fibroglandular tissue. As breast tissue properties have shown to be frequency dependent (increased reported stiffness values with increased frequency and precompression [161], [174], [164]), we obtained lower stiffness values in this study than measured by dynamic based excitation methods.

V.2.5 Conclusion

In summary, we have established a novel quantitative breast tissue stiffness estimation framework amenable to clinical workflows associated with interventional/surgical image-guided environments. We characterized the performance of the method in simulation and established the test-retest reproducibility of the resulting stiffness values *in vivo* in healthy volunteers. The feasibility and reproducibility

of the stiffness estimation method presented here is encouraging and several future opportunities for improvement and implementation into other applications exist. The framework suggested in this work can be seamlessly integrated and adds only a single additional two minute scan to a supine imaging procedure. With this single additional scan, we realize an ability to develop patient-specific breast geometric models with appropriate quantitative stiffness estimates for use within novel image guided-breast surgery systems with no specialized equipment and using standard imaging sequences available on traditional clinical MR scanners.

CHAPTER VI

Incorporation of Patient Specific Parameters for Image Guided Breast Surgery

VI.1 Summary and Contributions

In Chapter V, a gravity-based stiffness estimation method was introduced. Here, parameter sweeps were performed, sampling stiffness values for adipose and fibroglandular tissue. A biomechanical model was solved for each adipose-fibroglandular stiffness value. The displacement field generated by the model was then used to deform the gravity-induced excitation image. A measure of image similarity was then calculated between the model-deformed image and baseline image for each adipose-fibroglandular stiffness value set. The minimal value of this similarity map was chosen to obtain the optimal stiffness values. While the framework for the stiffness estimation method was tested, and shown to be promising for work in image-guided breast surgery, performing a parameter sweep on a sufficient search space with acceptable discretization of said search space is extremely time consuming. Therefore, in this study, we perform an investigation into the use of optimization routines to reconstruct the values of patient specific breast tissue stiffness. An interesting set of observations were reported in [246] that prompted this investigation. For example, the shape of the objective function changes according to the fibroglandular content of the breast and the magnitude of deformation induced during gravity-excitation. Due to inevitable differences in patient breast size, fibroglandular content, deformation levels, and stiffness values, we opted to test a variety of optimization methods to determine the most appropriate method to use going forward in the context of image-guided breast surgery.

In this study, we reduced the computation time to obtain the optimal stiffness values (i.e. find the similarity error minimum) by two to three orders of magnitude when compared with the parameter sweep method used in Ch. V. All eight unique breast stiffness calculations converged to the minimum with less than 20% errors (when compared to the parameter sweep minimum). Furthermore, the optimization routine employed found a lower minimum than the parameter sweep method approximately two-thirds of the time. Finally, an investigation towards heterogeneous elastic property reconstruction was performed. Heterogeneous property reconstruction is not feasible using parameter sweep methods as the number of model solves required would be too burdensome. However, with the optimization routine developed in this study, heterogeneous property reconstruction becomes feasible. This feasi-

bility study moves our novel stiffness method towards becoming an elastography technique. While the need to obtain homogeneous properties for applications in image guided breast surgery was addressed in this study, the step towards an elastographic approach has several avenues for future exploration.

VI.2 Towards quantitative quasi-static elastography with a gravity-induced deformation source

The work in this chapter appears in:

- R. H. Griesenauer, J. A. Weis, L. R. Arlinghaus, I. M. Meszoely, and M. I. Miga, "Towards quantitative quasi-static elastography with a gravity-induced deformation source", SPIE Medical Imaging: Image-guided Procedures, Robotic Interventions, and Modeling Conference, Vol. 10135, 2017

- Griesenauer, R. H., Weis, J. A., Arlinghaus, L. R., Meszoely, I. M., and Miga, M. I. "Towards quantitative quasi-static elastography with a gravity-induced deformation source for Image Guided Breast Surgery." Journal of Medical Imaging. In preparation.

Abstract

Biomechanical breast models have been employed for applications in image registration and analysis, breast augmentation simulation, and for surgical and biopsy guidance. Accurate applications of stress-strain relationships of tissue within the breast can improve the accuracy of biomechanical models that attempt to simulate breast movements. Reported stiffness values for adipose, glandular, and cancerous tissue types vary greatly. Variations in reported stiffness properties are mainly due to differences in testing methodologies and assumptions, measurement errors, and natural inter patient differences in tissue elasticity. Therefore, patient specific, *in vivo* determination of breast tissue properties is ideal for these procedural applications. Many *in vivo* elastography methods are not quantitative and/or do not measure material properties under deformation conditions that are representative of the procedure being simulated in the model. In this study, we developed an elasticity estimation method that is performed using deformations representative of supine therapeutic procedures. Reconstruction of material properties was performed by iteratively fitting two anatomical images before and after tissue stimulation. The method proposed is work flow friendly, quantitative, and uses a non-contact, gravity-induced deformation source.

VI.2.1 Introduction

Breast cancer imaging modalities include x-ray mammography, ultrasound, and magnetic resonance imaging (MRI). In each modality, unique patient positioning confounds the use of diagnostic images

for surgical guidance. In x-ray mammography, the patient stands erect with the breasts compressed between two plates. During ultrasound exams, the patient is positioned supine with the ipsilateral arm placed above the patients head. MRI exams of the breast are typically performed with the patient lying prone with breasts pendant in the MRI coil chambers. During surgery, the patient is positioned supine with the ipsilateral arm placed perpendicular to the body. Each modality has unique benefits for the screening, diagnosis, and staging of breast cancer. However, there is limited utility in the use of diagnostic images for localizing tumors during surgery. For breast conserving therapy (BCT), which consists of a lumpectomy (removal of tumor and small amount of surrounding healthy tissue) followed by radiation therapy, localization of the tumor during surgery can be difficult. Reoperations due to the presence of residual tumor after an initial resection average 20-40% [21]. Furthermore, ductal carcinoma in situ (DCIS) is associated with a 3-fold increase in reoperation rates when compared to invasive carcinomas [15]. DCIS lesions have diffuse growth patterns and ill-defined margins when compared to invasive breast cancers [247]. Furthermore, DCIS extensions into intraductal tissue can be difficult to determine. Due to the mainstream usage of screening mammography, an increasing number of patients are being diagnosed with DCIS and early stage cancers. Therefore, precise strategies to localize the non-palpable DCIS lesions are needed. While intraoperative ultrasound has been shown to reduce the need for re-excisions [248], ultrasound cannot image most cases of ductal carcinoma in situ (DCIS) and is limited in detecting multifocal disease, bilateral breast cancers, and intraductal spread characteristics [59].

While MRI is considered the most sensitive and accurate imaging modality in the context of breast cancer [61, 62], the limited specificity of MRI provides some areas of improvement. There is some evidence that preoperative MRI causes overtreatment and is associated with an increase in the use of mastectomy, delay in treatment, and an increase in the number of additional biopsies [63, 64, 188]. Alternatively, several studies have disputed these claims arguing that MRI provides invaluable information regarding the extent of disease. In a prospective, randomized, multicenter study, a significant decrease in reoperation rates was reported between women who received a preoperative staging MRI vs. women who did not receive an MRI prior to lumpectomy [192]. Sung et al. published a retrospective analysis that concluded that reoperation rates among BCT patients were lower for women who received a preoperative MRI [193]. Several other studies report positive findings for improved preoperative staging using MRI [192–195, 249] . Overall, the argument surrounding the value of preoperative

MRI remains somewhat unclear. However, it is generally agreed upon that MRI provides the most accurate delineation of the size and extent of cancer and offers the highest sensitivity for intraductal extension involved in breast cancers [60, 250, 251].

Regardless, these diagnostic MR images are not particularly useful in the context of surgical planning and guidance. As previously discussed, preoperative MR images are acquired in the prone position with pendant breasts while surgery is performed with the patient lying supine. Several studies have reported significant displacements in breast tumors between the prone and supine positions on the order 18-60 mm [46–48]. These relatively large displacements render diagnostic images sub-optimal for use in surgical planning and navigation, which may contribute to studies finding little to no benefit of preoperative MRI for surgical use. Due to these realizations, several groups have investigated the use of preoperative MR images rendered in positions that more closely represent the surgical orientation. Prone-to-supine registration methods of MR images for use in guiding breast surgery have been developed [135, 136]. A more direct approach is to use MR images taken in the supine position to guide surgery. Supine breast imaging has been a topic of interest in several studies [223, 252, 253]. Furthermore, the use of supine breast MRI in the context of image guided breast surgery (IGBS) has been suggested in several frameworks [46, 54, 154, 224]. In the context of IGBS, preoperative supine breast images are registered to the physical space of the operating room to act as patient specific maps to assist surgeons in localizing discrete breast lesions. The patient specific aspect of these systems involves the creation of biomechanical computational models to correct for deformation that naturally occurs between the preoperative image and surgical space breast geometries.

In this study, we developed a method to further optimize the patient specific parameters of IGBS systems. In Fig. VI.1 the basic steps for IGBS is shown. The process begins with preoperative imaging of the breast in the supine position. Anatomical and morphological images are obtained at this step. Pre-processing of these images include segmentation of the breast tissue into adipose, fibroglandular, chest wall muscle, and tumor. From here, a FEM model is created to simulate breast tissue deformation during the intraoperative registration step. In the Intraoperative Registration step, the surface of the breast is digitized by an optical tracking system and a biomechanically assisted nonrigid registration is performed to render the preoperative data into the physical space of the operating room. Once this registration is complete, a guidance display of the co-registered preoperative image data is used to localize tumors and map out surgical plans. The extra step we are proposing to add and that will

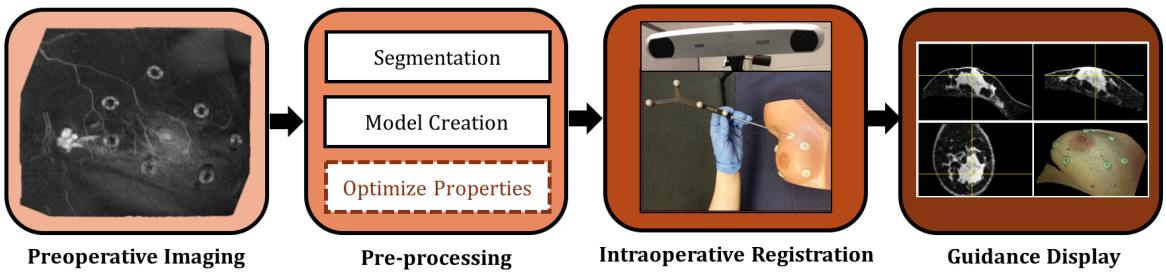

Figure VI.1: General framework for image-guided breast surgery. The process begins with preoperative imaging of the patient breast in the supine position. The Preoperative Imaging panel shows a representative MR volume rendering of a contrast-enhanced supine breast of a patient with breast cancer. The rendering shows a tumor with elevated image intensity and ring-shaped adhesive surface fiducials used during the Intraoperative Registration step. Pre-processing is performed after imaging, prior to surgery. At this step, patient specific stiffness properties are extracted to optimize the patient specific model. Intraoperative Registration is performed to transform the preoperative image and patient specific model into surgical space. Finally, the Guidance Display is used by the surgical team to localize tumors.

be elaborated upon in this study is during the pre-processing step. Here, we estimate the material properties of the patients breast tissue to be incorporated into the biomechanical model for improved accuracy.

An IGBS compatible stiffness estimation method was recently introduced [246] that relies on gravity induced deformations of the breast captured in an additional two-minute MRI scan. Here, parameter sweeps were performed, sampling stiffness values for adipose and fibroglandular tissue. A biomechanical model was solved for each adipose-fibroglandular stiffness value. The displacement field generated by the model was then used to deform the gravity-induced excitation image. A measure of image similarity was then calculated between the model-deformed image and baseline image for each adipose-fibroglandular stiffness value set. While the framework for the stiffness estimation method was tested, and shown to be promising for work in image-guided breast surgery, performing a parameter sweep on a sufficient search space with acceptable discretization of said search space is extremely time consuming. Therefore, in this study, we perform an investigation into the use of optimization routines to reconstruct the values of patient specific breast tissue stiffness. An interesting set of observations were reported in [246] that prompted this investigation. For example, the shape of the objective function changes according to the fibroglandular content of the breast and the magnitude of deformation induced during gravity-excitation. Due to inevitable differences in patient breast size, fibroglandular

content, deformation levels, and stiffness values, we opted to test optimization methods to determine the most appropriate method to use going forward in the context of image-guided breast surgery. In this study, simulation data was generated and human data was collected to test optimization performance. Furthermore, an exploration of the stiffness method for reconstructing a heterogeneous distribution of properties within the breast was performed.

VI.2.2 Methods

Overview of Stiffness Estimation Method

Optimization of patient specific breast tissue stiffness begins with acquisition of two gravity-loaded supine breast MR images. The baseline image is acquired with the patient lying supine with the ipsilateral arm placed above her head. Gravity excitation is administered by placing a foam wedge posterior to the breast being imaged. This causes a rotation about the longitudinal axis of the body which results in tissue deformation due to a change in tissue weight distributions with respect to gravity. From the gravity-excited image, an FEM model is created. In this framework, the chest wall is assumed to be a reliably rigid structure and is used to align the baseline and gravity-excited images. The chest wall in each image is segmented and a rigid registration is performed by maximizing the image similarity between the chest walls in each space. The transformation matrix yielded by this chest wall registration is used to transform the baseline image into the gravity-excited space. Now, the chest walls in each space are aligned and the resulting misalignment of the breast tissue is due to the nonrigid deformation caused by differences in gravitational loading. Also from the chest wall alignment, the differences in gravitational loading are quantified by using the rotational component of the transformation matrix to calculate the relative change in the acting gravity direction. The rotated gravity vector is applied as a body force of tissue weight in the biomechanical model. A biomechanical model is then solved to obtain a displacement field. The displacement field is interpolated onto the gravity-excited image to create a model-deformed image. Material properties are iteratively updated until the model-deformed image matches the chest wall-aligned baseline image. A visual representation of this process is shown in Fig. VI.2. and more descriptive detail of the framework can be found in [246].

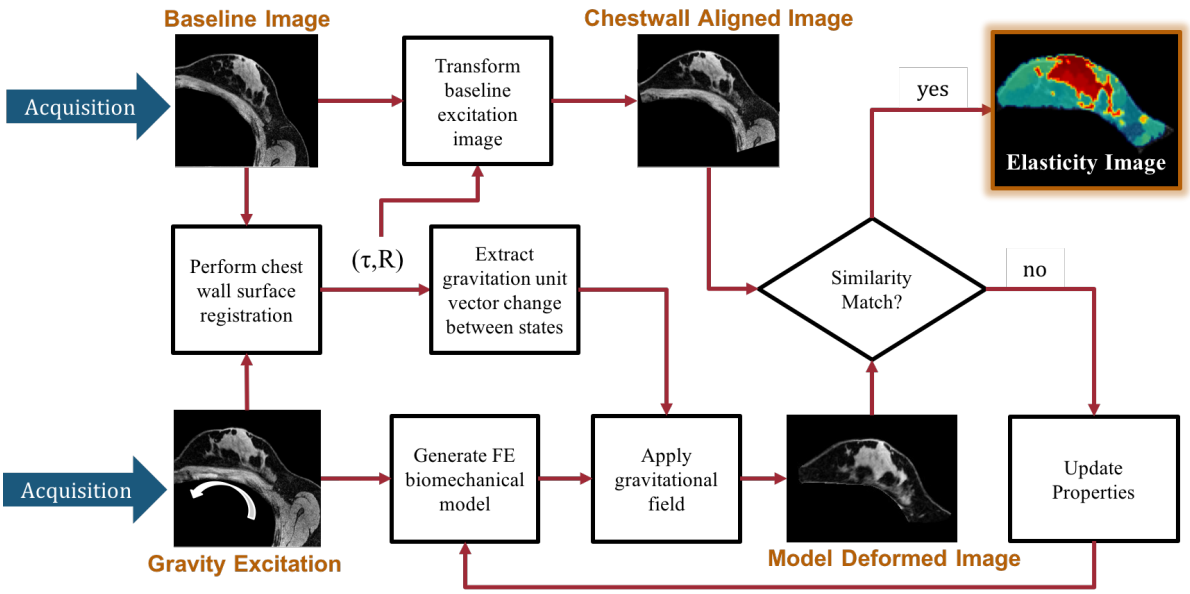

Figure VI.2: Overview of the process to optimize patient specific material properties. The algorithm estimates tissue elasticity by fitting two acquired anatomical images by minimizing a similarity metric between an experimentally acquired image and a model deformed image.

Human Volunteer Data

With IRB approval and informed consent, five healthy volunteers were enrolled to participate in this imaging study. The left and right breasts of three volunteers were scanned in a separate imaging setup to comprise a total of eight datasets. Furthermore, the left breast of the first volunteer was scanned twice in a test-retest setup to evaluate the reproducibility of a heterogeneous property reconstruction. With a lack of evidence to suggest otherwise, the quantitative stiffness of each breast was assumed to be unique. A baseline and gravity excited image was acquired in a Philips 3T Achieva MR scanner using a SENSE XL Torso Coil (Philips Healthcare, Best, Netherlands) with the following parameters: T_1-weighted, 3D turbo field echo sequence with fat suppression, a field of view of 200 mm $\times$ 200 mm $\times$ 160 mm, reconstructed voxel size of 0.391 mm $\times$ 0.391 mm $\times$ 1 mm, TR/TE = 7.422 ms / 3.91 ms, and flip angle = 20 degrees using SENSE parallel imaging (acceleration factor=2).

A FEM tetrahedral mesh was created from the gravity excited image (edge length = 3 mm). The difference in gravitational loading was approximated by calculating a gravity vector: $g_{rotated} = g_{baseline} - R \times g_{baseline}$, where $g_{baseline}$ was assumed to be unit vector normal to the MR table and R is the rotation matrix generated from the rigid chest wall alignment registration. A body force of tissue weight, $[9.8m/s^2 \times g_{rotated} \times \rho]$, was applied in a biomechanical model that assumes isotropic and

Hookean linear elastic behavior. Tissue density, ρ, was estimated as 1000 kg/m^3. Nodal positions corresponding to the chest wall were prescribed a fixed Dirichlet boundary condition with the assumption that the chest wall remains relatively static between the two configurations. Using these parameters, a forward biomechanical model with an FEM corotational formulation [126] was solved to obtain a displacement field. The displacement field was used to deform the gravity-excited image. An optimization procedure iteratively updates the stiffness properties of the breast tissue until the model-deformed image matches the baseline image. An expanded description of the methods involved in this approach can be found in [246].

Simulation Data

A simulation study was performed to assess the performance of the optimization methods with minimal noise contributions and to determine a representative true form of the objective function using similar clinical parameters. Model parameters were selected to form a representative simulated clinical dataset. These parameters include: 500 and 2000 Pa for the stiffness of adipose and glandular tissue, respectively, a Poissons ratio of 0.45, tissue density of 1000 kg/m^3, and a rotation relative to the initial direction of gravity ($g_{rotated}$) of 15 degrees. Using baseline images from five healthy volunteers with a range of fibroglandular content (8%,12%, 20%, 30%, and 40%), a forward model was solved with these simulation parameters and the resulting displacement field was interpolated onto the baseline image to create a simulated gravity-excited image. Fig. VI.3 shows representative baseline and simulation images and the corresponding deformation that drives the stiffness estimation procedure.

Optimization Procedures

Two optimization methods were studied along with a fine parameter sweep to identify the best methods to obtain patient-specific stiffness properties of breast tissue. Here, a conjugate gradient (CG) and a Levenberg-Marquardt (LM) algorithm were tested. A very brief overview of each method is given.

The steepest descent method reduces the sum of the squared errors by updating the optimization parameters in the direction of the greatest reduction of the least squares objective. The steepest descent method is a line search method that takes an initial guess, calculates the function gradient at this point, which finds the vector pointing in the direction of the steepest descent. Gradient descent methods are slow to converge especially when close to the minimum. The conjugate gradient method [254, 255]

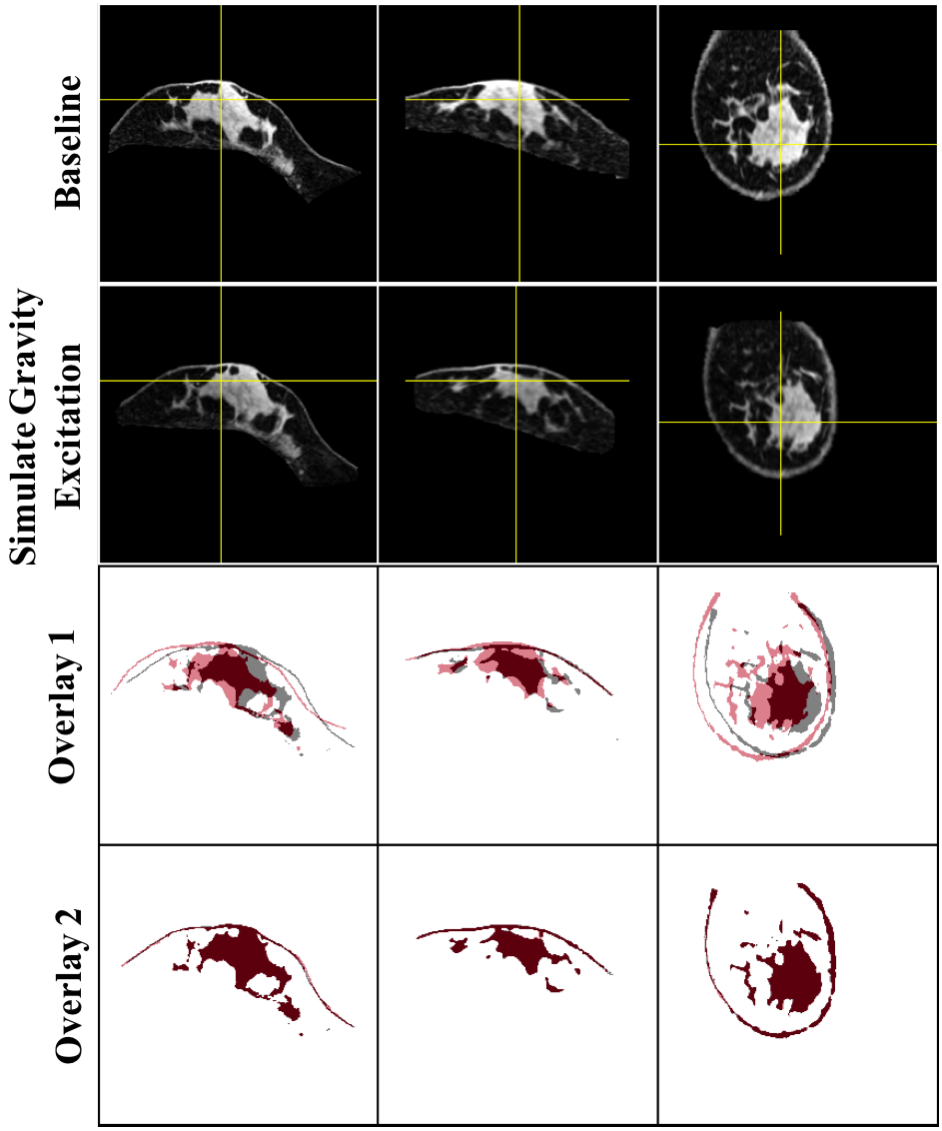

Figure VI.3: Representative images used in simulation study. The top row contains axial, sagittal, and coronal views of a baseline image. The middle row shows the same three orthogonal slices of the simulated gravity-induced configuration image. The third row (overlay 1) displays the simulated gravity-induced image as a red mask and baseline image as a gray mask. The fourth row (overlay 2) displays the simulated gravity-induced configuration and model deformed image using optimized reconstructed properties. Overlay 1 demonstrates the type of deformation yielded from the gravity induced excitation used in this method.

improves the method of steepest descent by reducing repetitious iteration steps. The CG method takes orthogonal steps to the function minimum which reduces step redundancies. Due to the reduction in iterations needed, CG methods are valuable for large dimension optimization problems. In this study, the gradient was calculated using a central-difference approximation and was performed using a custom implementation of the algorithm.

In the Levenberg-Marquardt [256, 257] method, a sum of squares is minimized from the zone-based image correlation coefficients. The LM method takes advantage of the gradient descent and the Gauss-Newton optimization methods. When close to the optimal, Gauss-Newton, a quadratically convergent fixed point method is the basis for the optimization procedure. The Gauss-Newton algorithm may not converge if the initial guess is far from the optimal. Therefore, if the procedure is far from the optimal, the optimization method follows a steepest descent basis. In this study, the Jacobian was calculated using a forward-difference gradient calculation (requiring one model solve per optimization variable). The LM method was implemented using the MATLAB R2015 (The Mathworks Inc., Natick, MA) lsqnonlin function.

To observe material property optimization performance, a parameter sweep was first performed on a moderate search space to obtain an objective function map. The objective function was determined using an image similarity metric calculated in five discrete zones within the image volume. The similarity metric is calculated from $S = |1 - CC|^2$, where CC is the image correlation coefficient. The correlation coefficient takes a value of 1 if the two images are the same and a value of zero if the two images are completely uncorrelated. The root mean squared (RMS) nodal displacement error was also calculated during the simulation parameter sweep. The RMS nodal displacement errors were not available during the *in vivo* human subject parameter sweep because the known correspondence of tissue features is ambiguous. In the simulation study, the search space for the parameter sweeps was 100-1000 Pa for adipose tissue and 100-4000 Pa for glandular tissue. The step size for each tissue type was 50 Pa for adipose tissue and 50 Pa for glandular tissue. In the human volunteer study, the parameter search space was 100-1000 Pa for adipose tissue and 100-10000 Pa for glandular tissue with step sizes of 25 Pa for adipose and 50 Pa for glandular.

After the parameter sweep was performed, an estimation of the true minimum was obtained by taking the minimum value of the objective function map. Due to large variations in breast stiffness, volume, and fibroglandular content, a range of initial guesses were used for the optimization procedures

to maximize successful convergence despite differences in the shape of objective function maps. The initial guesses were distributed around the ground truth values for the simulation data. For the human datasets, the following starting points were used as initial guesses: (1) 2000 Pa for adipose, 2000 Pa for glandular, (2) 500 Pa for adipose, 500 Pa for glandular, (3) 500 Pa for adipose, 2000 Pa for glandular, and (4) 100 Pa for adipose and 4000 Pa for glandular.

VI.2.3 Results

Simulation Data

The average solve time for the simulation data was 112.6 +/- 63.8 seconds. The solve time was defined as the total time it takes to perform one forward model solve (with three corotational iterations), deform the image, and calculate the objective function. From this, the average time to perform a parameter sweep was estimated. For the simulation parameter sweep performed in this study, a total of 1482 solves were executed. This translates to 46.3 hours if solved in series. If the search space were to be expanded (such as in the human case) or if the step size were to be decreased for a more resolved error map, the number of model solves required to create the map would increase. This fact illustrates the importance of performing an optimization procedure to obtain the objective function minimum. All but one of the initial guess values converged to the minimum for the simulation data for both the LM and CG methods. Table VI.1 shows the average and standard deviation of the converged reconstructed values in simulation for each case. Fig. VI.4 shows visually the tissue stiffness reconstruction results for the simulation data using the LM method. In Fig. VI.4(e), the initial guess starting at 500 for glandular and 500 for adipose did not converge to the minimum using the LM method, but did converge using the CG method. Fig. VI.5 shows the RMS nodal displacement error maps for the 12% and 20% fibroglandular simulation datasets. These error maps represent a true form of the objective function as they were calculated with absolute knowledge of point correspondences.

Human Data

The average solve time for the human data sets was 107.8 +/- 26 seconds. From this, the average time to perform a parameter sweep was estimated. The total number of solves for the human data set parameter sweep was 7722. Therefore, if the objective function error map were to be created in series, the total solve time for the parameter sweep would be 231.2 hours. This again illustrates the importance of an

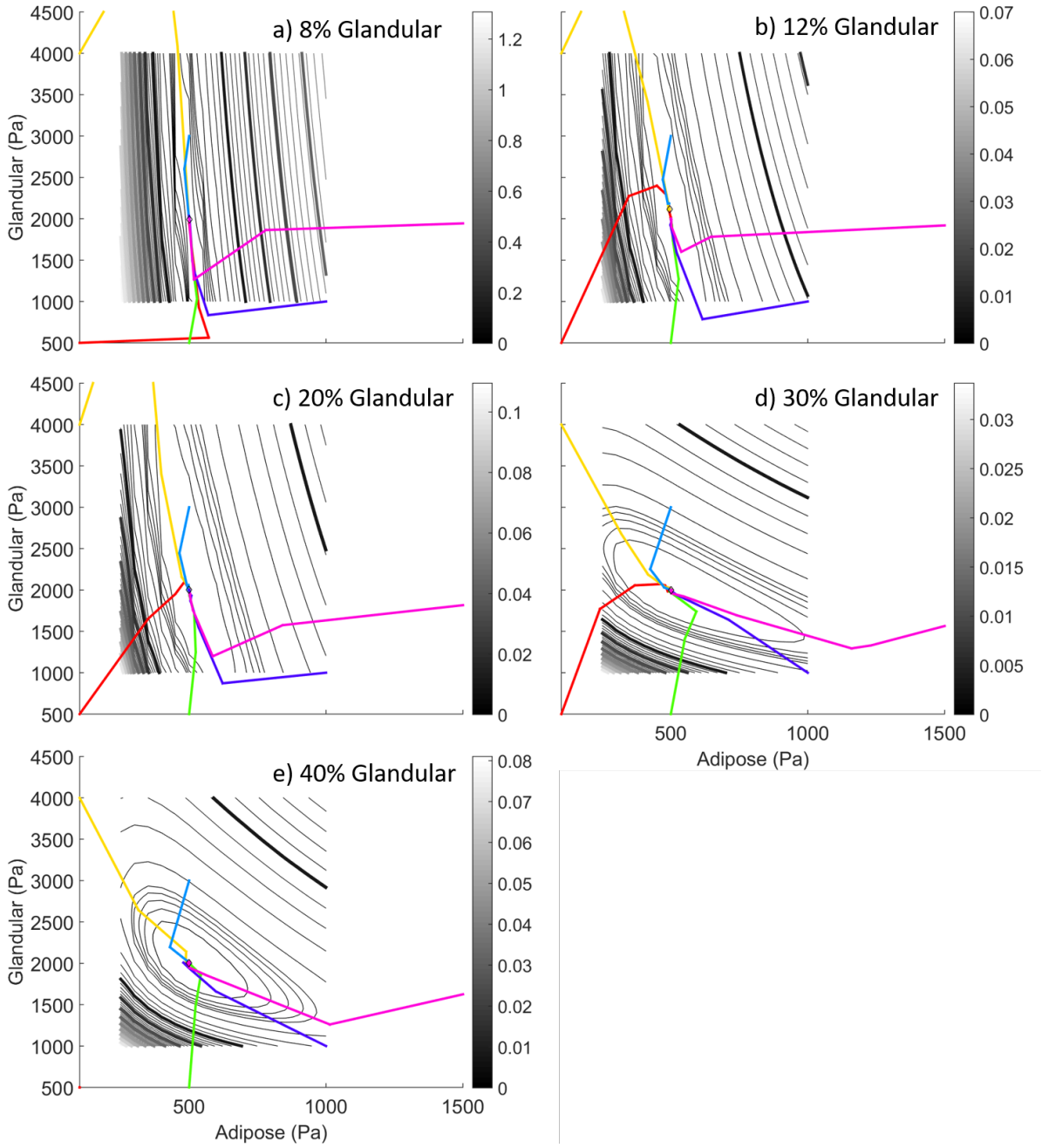

Figure VI.4: Tissue stiffness reconstruction results for simulation data. Each plot represents a simulation data set with a range of fibroglandular content (a) 8%, (b) 12%, (c) 20%, (d) 30%, and (e) 40 %. The black contour map is the objective function error map created from the parameter sweep. The contour values represent the objective function value at each adipose-glandular combination solved. The colored lines show the optimization iterations and results for the Levenberg-Marquardt (LM) method. Convergence sensitivity of the optimization was tested using a range of initial guesses (depicted as different colored lines overlaid on the error maps.)

Table VI.1: Reconstruction results for simulation data. Mean (standard deviation) values are reported in Pa for each simulation case.

	LM		CG	
	Adipose	Glandular	Adipose	Glandular
8% Glandular Tissue	500.2 (0.81)	1992.0 (35.5)	501.2 (5.5)	1998.2 (127.8)
12% Glandular Tissue	499.9 (0.53)	2002.7 (11.1)	499.2 (1.7)	2006.0 (27.7)
20% Glandular Tissue	500.6 (1.48)	1989.3 (24.4)	501.25 (1.5)	1976 (29.1)
30% Glandular Tissue	500.1 (0.33)	1999.9 (0.81)	500 (0)	1999.3 (0.26)
40% Glandular Tissue	499.5 (0.58)	2000.8 (2.17)	499.5 (0.99)	1999.35 (3.42)

optimization procedure to find the optimal set of stiffness values.

Fig. VI.6 shows three representative results for the human data reconstruction. Fig. VI.6(a,d) corresponds to case 1, VI.6 (b,e) represents case 4, and VI.6 (c,f) corresponds to case 5. Here, two representative optimization initial guesses are shown for each case (initial guesses at (500,500) and (2000,2000)). The objective function value per iteration is shown in Fig. VI.6 (d,e,f), while the downward path taken by the optimization procedure is shown overlaid on the parameter sweep error maps in Fig. VI.6 (a,b,c). For the human datasets, the minimum objective function value was selected out of all initial guess optimization runs. This minimum objective function and corresponding stiffness values were used to populate Table VI.2. The parameter sweep and optimization results for the 8 unique breast datasets are shown in Table VI.2. For each case, the global optimal properties were selected based on the overall minimum objective function value. These optimal properties are highlighted in green in Table VI.2. The CG method outperformed the LM method in most cases, with the parameter sweep maintaining the minimum for three cases. For all cases, the CG optimization achieved less than a 20% error when compared to the parameter sweep minimums. In six cases, the CG optimization found a lower minimum than the parameter sweep. In the three cases in which the CG method did not find a lower minimum, the percent errors from the true value ranged from 0.8% to 11.5% for adipose tissue and 13% to 18.3% for fibroglandular tissue.

An elastographic approach to stiffness estimation

A step towards heterogeneous determination of breast tissue mechanical properties was performed. Here, the breast was discretized into 20 unique regions. Each region was introduced as a degree of

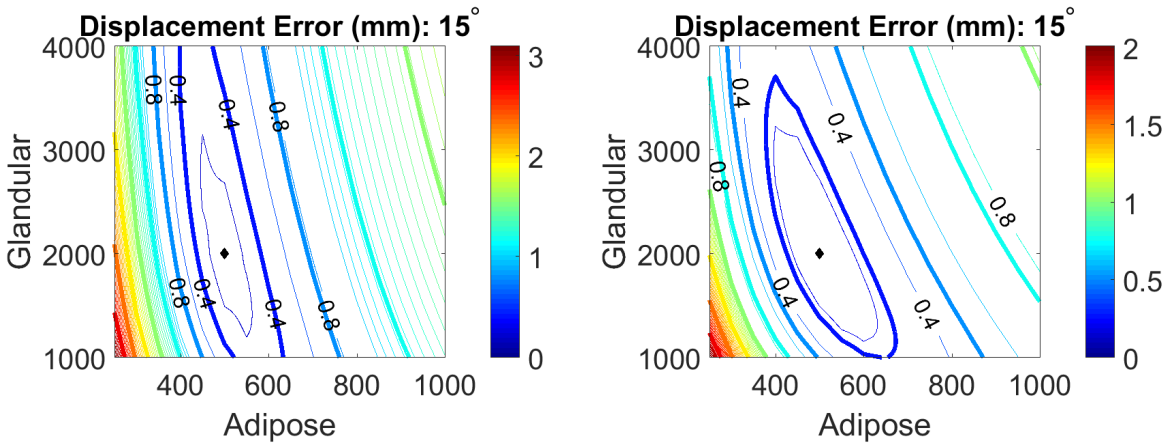

(a) 12% fibroglandular tissue content

(b) 20% fibroglandular tissue content

Figure VI.5: RMS nodal displacement errors for simulation parameter sweep for (a) 12% fibroglandular tissue and (b) 20% fibroglandular tissue. The x-axis contains the range of stiffness values sampled for adipose tissue. The y-axis is the range of stiffness values sampled for glandular tissue. The contour levels represent the nodal displacement error at that adipose-glandular combination. The contour map also shows the 0.4 mm and 0.8 mm contour levels which roughly corresponds to the half and full voxel sizes of the image volumes used in this study. The diamond shows the location of the minimum displacement error (i.e. the true properties))

freedom in the optimization routine. The optimization minimizes an objective function consisting of 10 zone-based correlation coefficients within the image volume that represents residual error between the model deformed image and the acquired baseline image. A conjugate gradient algorithm was used here due to the superior performance of the method in the human datasets. Similar to [232], spatial prior constraints were utilized that rely on image intensity knowledge to designate similar tissue types. This anatomical knowledge is used as a soft constraint in the optimization routine, which penalizes large variations among tissue types and acts to constrain stiffness values designated as the same tissue type to remain somewhat similar. Following reconstruction, the output is a volumetric distribution of absolute stiffness in each of the 20 regions. Cases 1 and 2 were used as a test-retest dataset, as they are both the left breast of the same subject. The test-retest dataset was acquired by reproducing the baseline and gravity-excited image in two imaging exams. Therefore, this data is totally unique to one another, but is of the same breast.

Fig. VI.7 shows the test-retest elastography results. The top panel contains central axial MR slices of the gravity-excited image for the test (left) and retest (right) cases. The middle panel shows the discretization of the breast as 20 regions (10 regions for each tissue type). The bottom panel in Fig.

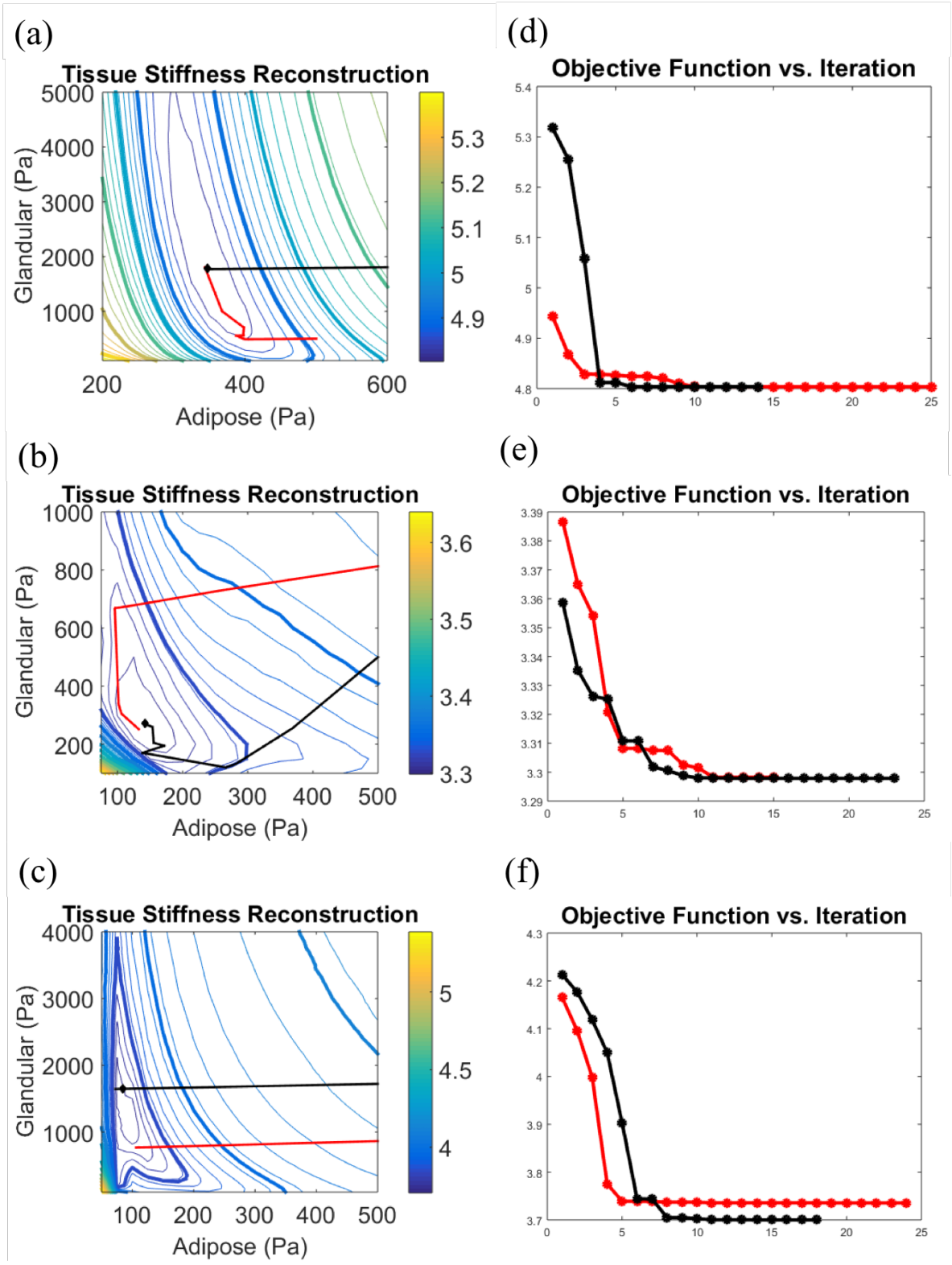

Figure VI.6: Summary of human data stiffness property reconstruction results for three datasets. (a,b,c) contain objective function contour plots demonstrating the shape of the objective function for three datasets. Overlaid onto these contour plots are optimization results for two starting points using the CG algorithm. The starting points shown here are (2000,2000) and (500,500). In (d,e,f), the value of the objective function at each iteration is shown for each starting initial guess.

Table VI.2: Reconstruction results for human data. Table containing parameter sweep and optimization results for the human datasets. All adipose and glandular values are reported in Pa. Note that cases 1 and 2 are of the same breast, acquired in a test-retest setup. The highlighted green cells represent the set of fibroglandular-adipose values that resulted in the overall minimal objective function.The solve time was defined as the total time it takes to perform one forward model solve (with three corotational iterations), deform the image, and calculate the objective function.

		Parameter Sweep		LM		CG	
	Solve Time (s)	Adipose	Glandular	Adipose	Glandular	Adipose	Glandular
1*	127.9	350	1650	356.5	1477.5	347.1	1780
2*	104.4	475	1600	448.3	1971.7	465	1824.9
3	94.2	650	6800	705.1	4165.2	687	5885
4	105.9	125	250	116.4	285.9	143.2	266.5
5	120.3	75	1300	73.1	1451.8	74.2	1576.8
6	155.1	200	2350	198.7	2016.4	201.7	1983.1
7	167.2	275	4950	274.9	6581.8	273.9	4000.2
8	101.7	675	5550	1248	6293	753.7	6533.6
9	59.9	100	450	108.2	372.8	96.2	412.7

VI.7 shows the reconstructed elastic property values for each region overlaid on a mask of the gravity-excited images. The average reconstructed values for fibroglandular tissue was 1783 Pa for the first test (case 1) and 2196 Pa for the retest set (case 2). The average test/retest values for adipose tissue were 336 Pa/450 Pa. The ratio of average fibroglandular tissue to average adipose tissue for the test/retest sets were 5.2/4.9. The retest case showed a larger variation in stiffness values within tissue types than the first test case.

VI.2.4 Discussion

In simulation, reconstructed stiffness properties converged at the global minimum despite initial guess. In clinical data, noise is introduced into the system, resulting in convergence of material properties into local minimums. However, with the introduction of four different starting points (initial guesses), an acceptable optimization (less than 20% error) was obtained in all cases. Fig. VI.6 (c,f) shows how one initial guess might find a global minimum while another gets caught in a local minimum.

We believe an error of less than 20% is acceptable for use with image guided surgery. As shown in Fig. VI.5, these errors are within an acceptable range as they introduce less than a 1 mm error into

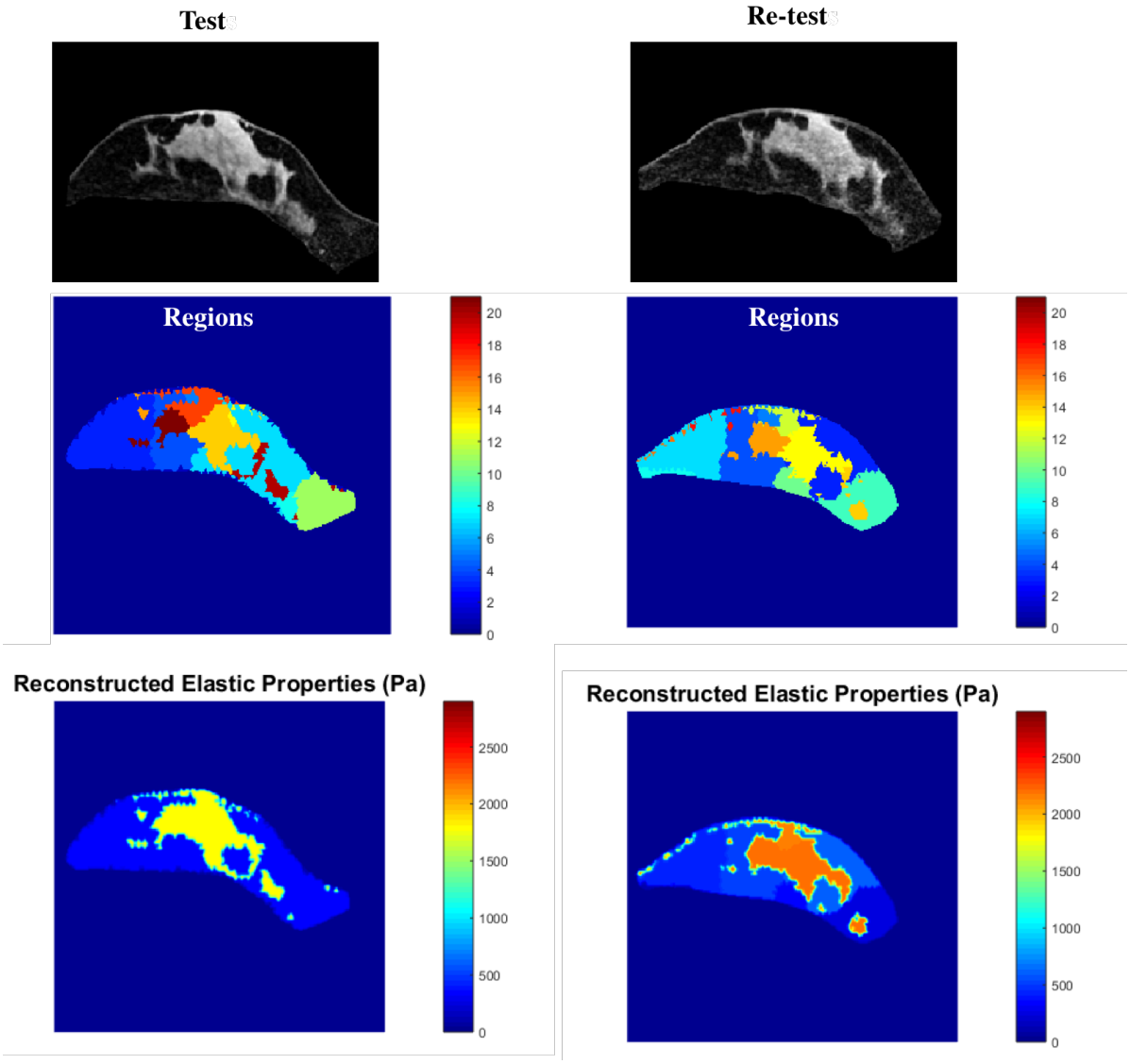

Figure VI.7: Test-retest elastography results of case 1 (left) and case 2 (right). The top figures show central axial slices of the gravity-excited anatomical MR image. The middle panels show the breast discretized into 20 unique regions. The bottom row shows the reconstructed property results for each set. The ratio of fibroglandular tissue to adipose tissue was 5.2 for the test set and 4.9 for the retest set.

the system. This can be seen from Fig. VI.5 where displacement errors between 1600 to 2400 Pa for glandular (+/- 20% of true glandular value) and 400 and 600 Pa for adipose (+/- 20% of true adipose value) lie approximately within the 0.8 mm contour level. The percent fibroglandular content of our clinical datasets was 18.3 +/- 8.7 (min = 7.7%, max = 32%). Furthermore, a study looking at the breast density of 230 women ages 32-77 reported a range of 7% to 28% for fibroglandular tissue content [258]. Therefore, the 12% and 20% glandular simulation datasets were the most representative of the human data.

Overall, reconstructing patient-specific stiffness parameters was successful using the conjugate-gradient algorithm. The number of iterations required to obtain a minimum in the human datasets using the CG method was 14.7 +/- 5.6 (min = 8, max =23). Therefore, the CG method can be used to obtain patient specific breast tissue properties with drastically less model solves than in a parameter sweep (recall the number of model solves in the parameter sweep was 7722). Despite the fact that each iteration in the CG method requires two model solves per optimization variable to evaluate the gradient, the total number of model solves needed to obtain an optimum is two to three orders of magnitude less than what is required during the parameter sweep.

The error maps associated with human subject data are more noisy than their simulation data counterparts. Furthermore, human data is subject to errors associated with arm-placement induced breast deformations that are not captured by the gravity-based reconstruction model. While care was taken to reproduce the same arm positioning in the baseline and gravity-induced images, further analysis will be performed to investigate the influences of arm position differences. In addition, noise and artifact reduction techniques during the MR image-acquisition phase will be explored.

A step towards heterogeneous property reconstruction was performed using a test-retest dataset. The ratio of fibroglandular tissue to adipose tissue was 5.2 for the test set and 4.9 for the retest set. As shown in Fig. VI.7, in reconstructing 10 regions for adipose tissue and 10 regions for glandular tissue, little heterogeneity within tissue types was found. While moving to this elastography approach was shown to be feasible, a finer amount of discretization (i.e. more regions) is currently under investigation to resolve stiffness differences within tissue types. Beyond the levels of discretization, the number of zones used during the image similarity calculation and level of spatial prior weighting should be studied to obtain optimal reconstruction behavior.

VI.2.5 Conclusion

In this study, a method to obtain patient specific homogeneous and heterogeneous breast tissue mechanical properties was tested. In the homogeneous tissue reconstruction setting, which was developed for use in image guided breast surgery applications, optimization convergence errors were found to introduce less than a 1 mm error into the guidance system. We demonstrated that the novel gravity-based stiffness estimation method is also capable of reconstructing heterogeneous stiffness properties with several avenues existing for future applications.

Acknowledgments

The authors would like to acknowledge the support of the National Institutes of Health through K25CA204599, R21EB022380 and the National Science Foundation for a Graduate Research Fellowship awarded to R.H.G.

CHAPTER VII

Future Directions and Conclusions

VII.1 Establishing a validation framework for image guided breast surgery

In this section, work regarding the establishment of mock surgical setups and validation frameworks for IGBS is discussed. Two validation approaches were developed, a breast phantom surgical setup and the collection of mock intraoperative-preoperative datasets via MR imaging. Each of the approaches have unique benefits that will be outlined in their respective sections. In each section, quantitative analysis of the nature and extent of breast deformation between preoperative and intraoperative settings was performed to ensure that the mock-testing and validation frameworks were representative of the surgical problem domain. Assumptions were made that rely on estimating the main sources of deformation between the preoperative and intraoperative breast geometries. For example, the preoperative state is associated with the patient in the supine position with the ipsilateral arm placed above her head. The intraoperative state is the result of the patient lying in the supine position with the ipsilateral arm placed out perpendicular from the body. The arm placement in each space is estimated to be a main cause of breast deformation. Another estimated source of deformation is variances in the angle between the patient's coronal plane and the surgical or MR table. As seen in Chapters V and VI, even small rotations of the patient along the longitudinal axis of the body can have gravity-induced deformation effects.

Phantom Setup for IGBS

The motivation for this work was that in order to properly validate non-rigid correction algorithms and image guidance techniques, there is a need to take quantitative measurements in a controlled manner. Furthermore, individual differences in the clinical setting limit reproducibility, which is an issue that can be remedied by the use of a phantom. A phantom setup was developed for validating image-guided breast surgery registration algorithms. Initial work to develop this phantom setup was performed by purchasing a commercially available breast phantom (Breast Probe, SIMULAB Corporation, Seattle, WA). While the shape of this phantom was anatomically representative of the breast geometry, the phantom material was uncharacteristically stiff. Therefore, alternative materials were experimented

with, including silicone gel (Ecoflex, Smooth-On, PA) and Poly(vinyl)alcohol (PVA). While both materials were less stiff than the commercial breast phantom, PVA was selected for further study due to its ultrasound-compatible properties. This phantom set-up is capable of representing breast adipose tissue, parenchyma, and breast tumors. A study was then designed to assess the breast phantom setup's ability to reproduce similar breast deformations as seen in clinical pre/post operative breast measurements.

In a preliminary study, adhesive fiducial markers were distributed across the breast surface of a healthy volunteer. Fiducial marker locations were recorded and a laser range scan was acquired for two arm positions, i.e. preoperative and intraoperative setups. Figure VII.1 shows the resulting displacements in the x,y, and z directions along with the overall magnitude of displacement overlaid on a textured 3D pointcloud of the breast in the arm-above-head position. From this preliminary exploration, it is evident that deformations of the breast occur on the orders of 18-28 mm over the whole breast surface in a nonrigid manor. The magnitude of displacement was shown to be larger on the lateral side of the breast, which is expected as it is closer to the source of deformation.

A follow-on study, found in Appendix C, was prompted from this preliminary dataset. Breast deformations that occur clinically from the preoperative state to the intraoperative state were characterized by analyzing deformations seen in three patients scheduled for a lumpectomy and in four healthy volunteers in mock surgical setups. The data from patients and healthy subjects were acquired under an Institutional Review Board (IRB) approved study. Fiducial markers were used to calculate fiducial registration error (FRE), a measure of overall landmark misalignment, and an intrafiducial (IF) distance distribution, used to determine both magnitude and direction of clinical deformation. The differences in FRE and IF distance distribution between the two positions were reported to establish a non-rigid surface deformation characterization. Analysis of non-rigid deformation between the supine MR images and mock intraoperative breast configuration yielded a positive correlation between breast volume and the amount of deformation. The fiducial registration error (FRE), was calculated for all cases. FRE indirectly captures an estimate of non-rigid changes by looking at changes with respect to breast volume. The assumption is that fiducial localization error (FLE) is similar among women with different breast volumes but that soft tissue changes due to arm motion would be exacerbated with larger breast women. More specifically, the effects of chest wall attachments would inhibit deformation in smaller breast women.

Also of note, in a qualitative comparison of the maximum IF distance distribution differences,

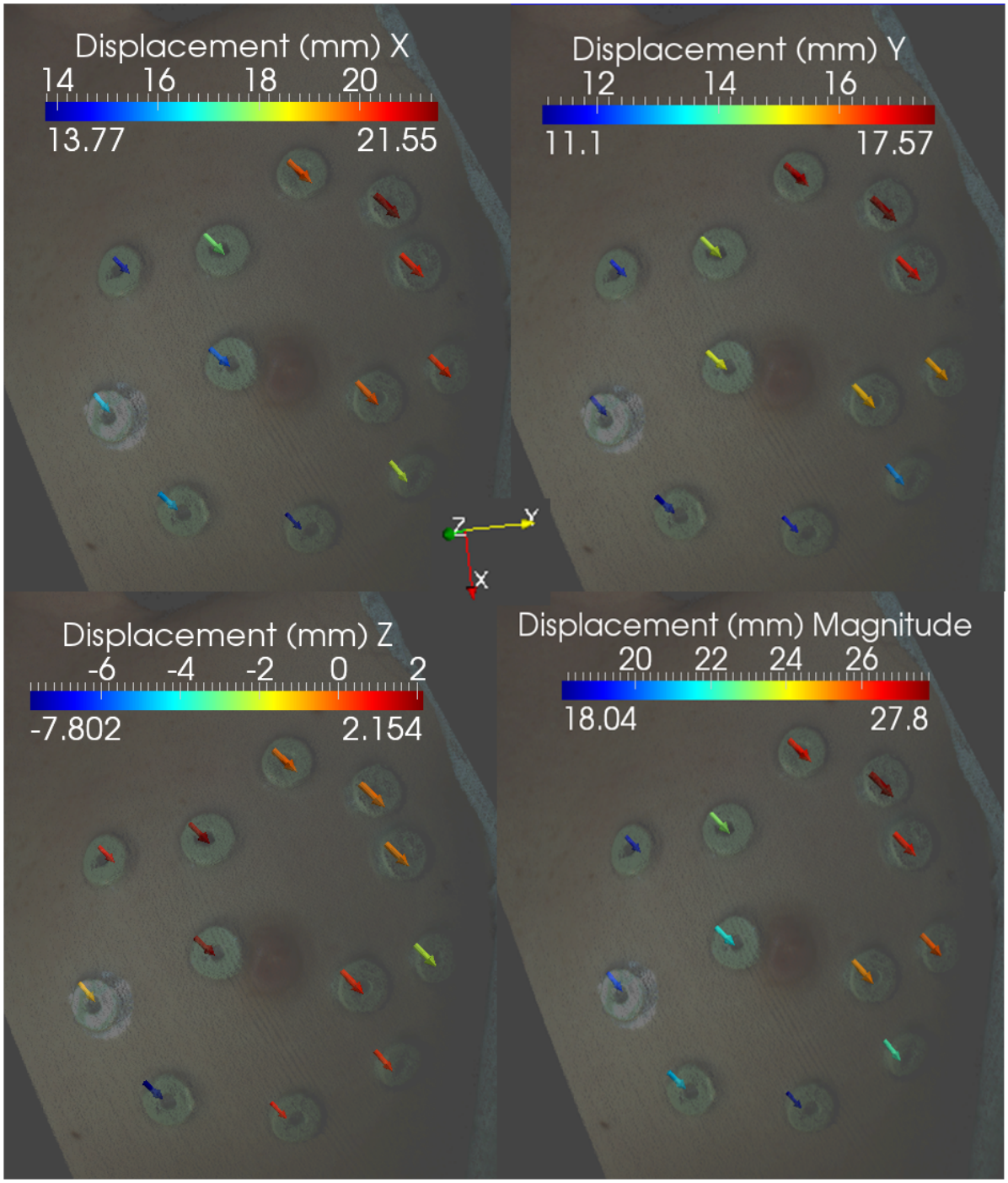

Figure VII.1: In a volunteer study, fiducials were distributed across the breast. Fiducial points were digitized and a laser range scan was obtained with the ipsilateral arm placed above the subjects head. The subjects arm was then placed perpendicular to the body and the fiducial centers were re-digitized. The images in this figure show the x,y,z and total magnitude of the displacement of the fiducial points between the two arm setups overlaid on the textured point cloud produced from the laser range scan of the arm-above-head position. It can be seen that most movement occurred along the X and Y axis. The magnitude of displacement is also shown with movements on the orders of 1.8-2.7 cm

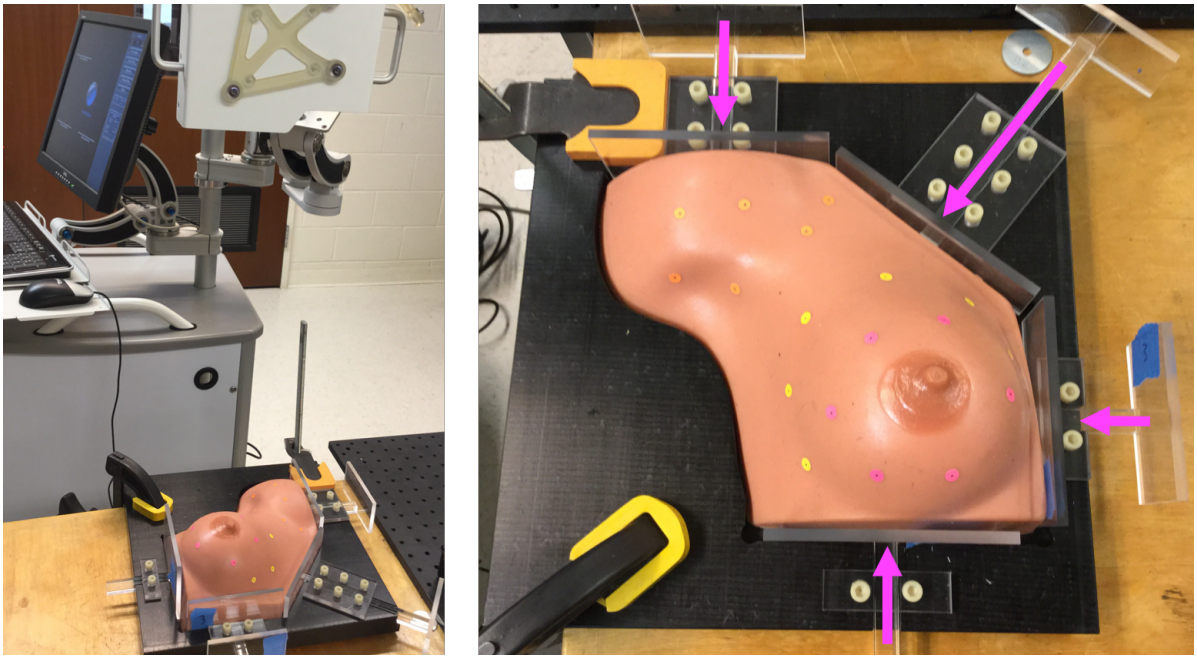

Figure VII.2: The phantoms presented here closely resemble surface anatomy, mimicking not only the shape of the breast itself, but the surrounding tissue ipsilateral arm region as well. A deformation apparatus was created with four manipulators able to induce and hold compressive forces on the breast. All four manipulators can be deployed at once, individually, or in some unique configuration. The base of the deformation frame contains a 1 cm depression machined to have the same contour as the breast phantom mold. This allows the breast phantom to sit flush in the base and hold applied deformations while minimizing slip. It should be noted that the deformation apparatus only provides compressional forces on the phantom; however, the clinical deformation can still be reproduced, based on the results from the principle component analysis which showed that primary deformation occurs along the patients superior-inferior axis, and secondary deformation occurring along the medial-lateral axis.

most deformation occurred along the subjects inferior-superior axis, with minor deformations occurring along the subjects medial-lateral axis. The clinical deformation analysis was used to characterize the directions and magnitude of deformation between the supine MR imaging environment and the supine intraoperative state. This analysis was then used as a guideline to develop the phantom and fine tune its material properties. The study found that the phantom setup quantitatively mimicked clinical deformation in terms of magnitude, direction, and location of movement between the two states. Figure VII.2 shows the commercial breast phantom and device used to induce phantom deformations.

A limit in terms of experimental procedure is the poor stability of the PVA gel once removed from the low storing temperature and exposed to room temperatures for an extended period of time. The phantom starts to essentially disintegrate. Investigating the phantom created in [259] is recommended.

Here, the PVA *"slime"* is enclosed within a soft latex shell. This latex shell could mimic the support and elasticity of skin over the much softer and more fluid breast tissue.

Image volume datasets in preoperative and pseudo-intraoperative patient setups

True breast deformation is difficult to reproduce in a laboratory setting due to the influences of pectoral muscles and cooper's ligaments as well as breast stiffness and fibroglandular content variations among women. To obtain a more realistic set of data that represents the preoperative and intraoperative breast geometries, an IRB approved study was performed to acquire two MR image volumes of six healthy volunteers and one patient volunteer. Analysis of breast deformation between preoperative and intraoperative breast geometries was performed to quantify the magnitude and directional patterns of breast deformation to inform the development of biomechanical model assisted nonrigid image-to-physical space registration algorithms. While traditional magnetic resonance imaging (MRI) of the breast involves a dedicated breast coil with the patient lying in the supine position, our proposed image guidance system adapts MR breast imaging protocols to be performed in the supine position. While supine MR images of the breast are more representative of the surgical state, significant deformation occurs due to changes in patient positioning and ipsilateral arm placement. During breast conserving surgery, the ipsilateral arm is placed perpendicular to the body. Due to the geometric constraints within a close-bore MR scanner, the ipsi-

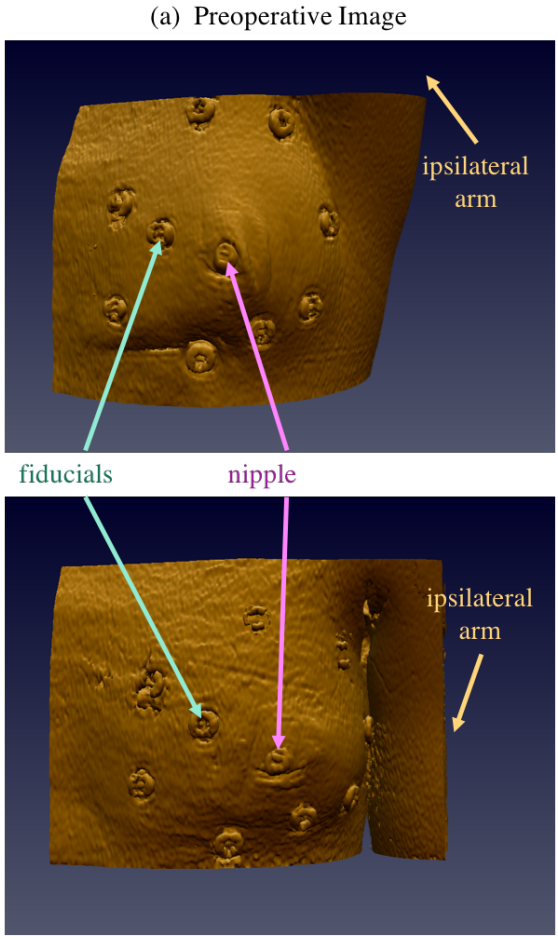

Figure VII.3: Representative MR volume renders used to quantify breast deformation. (a) Shows the preoperative position in which the patient is positioned supine with the ipsilateral arm placed above her head. (b) Shows the pseudo-intraoperative breast geometry with the arm placed parallel to the body.

lateral arm is placed above the patients head. Therefore, the motivation of this work was to quantify breast tissue movement between preoperative and intraoperative positioning and to identify whether or not the deformation on the surface of the breast is coupled with deformations within the subsurface breast structures. Determination of this coupling is important as nonrigid registration algorithms have historically relied on surface measurements to drive registration.

Due to our interest in subsurface feature deformation, volumetric images of the breast were taken in the preoperative (Fig. VII.3(a)) position and a pseudo-intraoperative position (Fig. VII.3(b)). The pseudo-intraoperative position was represented by placing the ipsilateral arm parallel to the body. This position was estimated to induce slightly larger deformations than the surgical position (i.e. arm out perpendicular from the body), but allowed for the calculation of upper limits on how much deformation can be expected to occur between preoperative imaging and surgery. Twelve individual breast image datasets (preoperative-pseudo-intraoperative sets) were acquired. The dataset encompasses the left and right breasts from five healthy volunteers, the left breast of a sixth volunteer, and the right breast of a breast cancer patient. Corresponding surface and subsurface breast features were selected for each dataset. Analysis of these features were performed to measure deformation magnitude, locate common areas of large deformation, and quantify deformation patterns. Fig. VII.4 shows the average magnitude of deformation between the preoperative and pseudo-intraoperative breast geometries as measured by differences in intra-feature differences.The surface and subsurface deformation magnitudes are shown for each case and indicate that surface and subsurface breast tissue deform at similar magnitudes. Over all 12 datasets, the average surface feature deformation was 7.5 +/- 2.8 mm while the average subsurface feature deformation was 7.13+/- 3.1 mm. In a paired t-test, no difference was found between the surface and subsurface feature deformation. The Pearson Correlation coefficient between the surface and subsurface features was 0.934. From this analysis, we can conclude that the level of deformation on the surface of the breast is coupled with the magnitude of deformation in the subsurface breast tissue.

Fig. VII.5 shows the results of the deformation pattern analysis. Principle component analysis (PCA) of the intra-feature distance differences revealed that most deformation occurs along the patients superior-inferior axis for both surface and subsurface features. Fig. VII.5 shows the direction of feature movement and is visualized along the subjects superior-inferior, medial-lateral, and anterior-posterior axis, respectively. The principal components as shown (blue-primary, green-secondary, and red-tertiary) express the average amount of variance within preoperative and pseudo-intraoperative

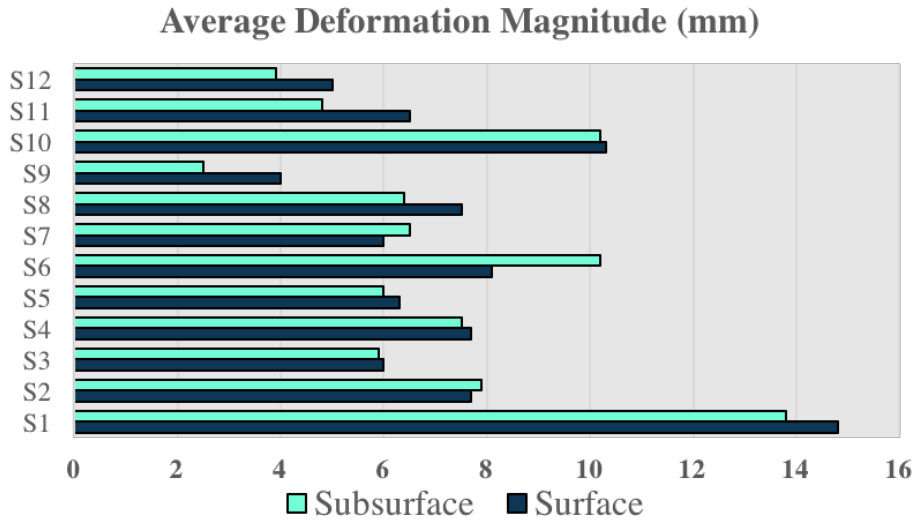

Figure VII.4: Average surface and subsurface magnitudes as defined by intra-feature distance differences for each dataset.

breast tissue deformation. The blue primary vectors point roughly in the same direction for each corresponding view point showing similar movements between surface and subsurface features. Overall, the analysis shows that the magnitude and pattern of deformation measured on the surface is predictive of subsurface deformation characteristics. Therefore, the analysis supports the assumption to use surface data to drive nonrigid registration procedures. In future work, biomechanical model-assisted image-to-physical space registration algorithms will be tested using the same 12-case dataset. The benefit of using this dataset for algorithmic testing (rather than preoperative image volumes and intraoperative surface data alone) is that subsurface targets are available in each space that provide the critical ability to quantify subsurface target registration errors.

VII.2 Future Study Recommendations

Image Guided Breast Surgery

To generalize the nonrigid correction strategy, an iterative optimization driven by the available intraoperative data (such as that available in Figure VII.6) should be employed. The preliminary results from Chapter IV show that initial rigid alignments are not sufficient, especially for larger breast volumes. Chapter IV presents an arguably coarse nonrigid deformation correction approach that has been applied to two patient subjects. The model was driven by synthetic fiducial error, which is an admittedly

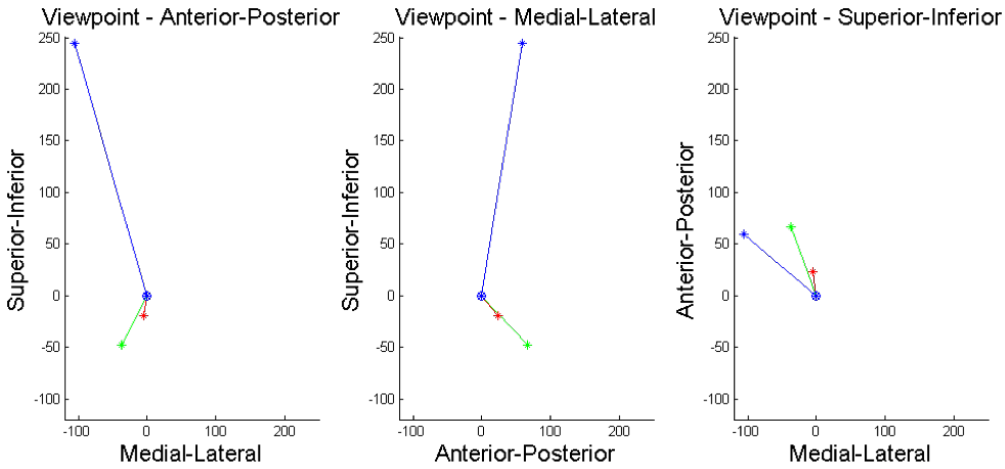

(a) Breast Surface Fiducials

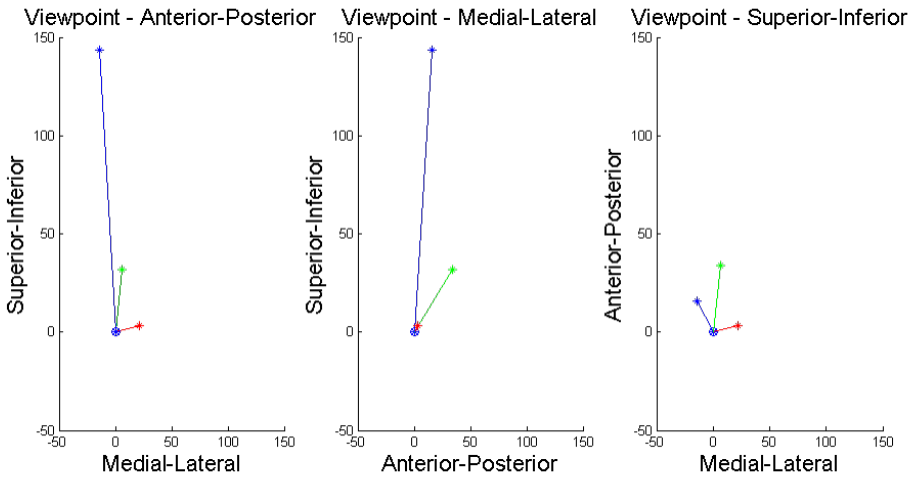

(b) Breast Subsurface Features

Figure VII.5: Results of a principal component analysis on the intra-feature distance differences for (a) surface features and (b) subsurface features. The blue, red, and green vectors represent the primary, secondary, and tertiary principal components respectively. Vector magnitudes are expressed as voxels.

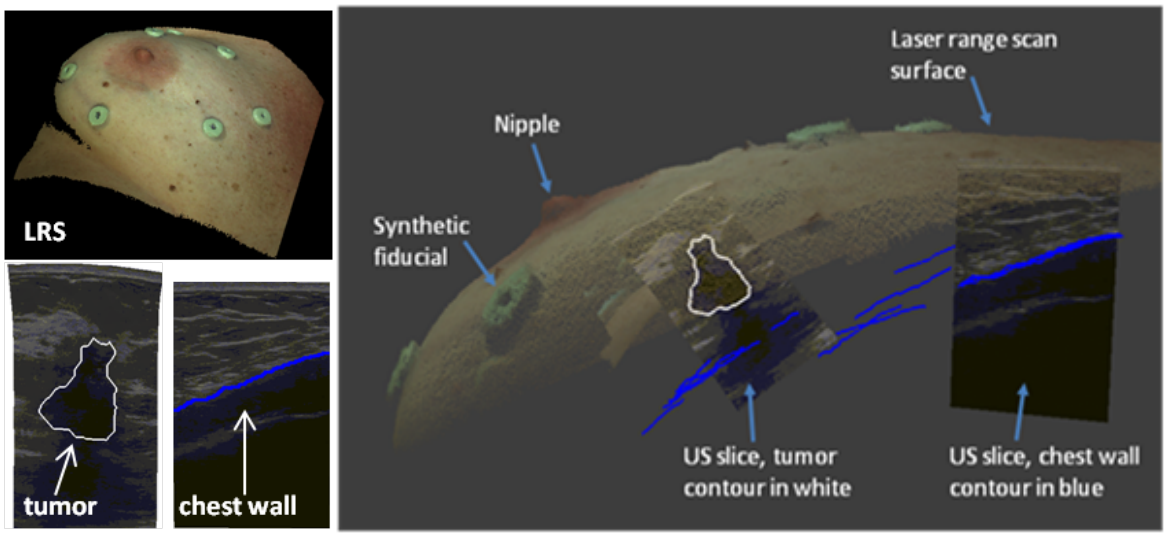

(a) (b)

Figure VII.6: (a) Top: LRS scan of patient 2 breast. Bottom left: compression corrected ultrasound image with tumor contour in white. Bottom right: ultrasound image with chest wall contour in blue. (b) Fusion display of tracked intraoperative data containing a textured point cloud, adhesive fiducial markers, tracked ultrasound images, tumor contour (white), and chest wall contours (blue).

sparse source to drive the correction process. One recommendation would be to develop a closed loop optimization strategy driven by data available intraoperatively to provide a more robust and work flow friendly approach for nonrigid correction. Another suggestion would be to perform an investigation into the use of various objective functions and model approaches to create a fast and accurate non rigid correction strategy for image guided breast surgery. To test this model correction approach, data should be collected from phantoms and validating the algorithm with the preoperative-pseudo-intraoperative patient setups. An optimal nonrigid correction strategy for intraoperative registration would include the following characteristics: generalizable to patients of different breast sizes and age, provide fast corrections for intraoperative registration, and consistently obtains clinically relevant accuracy. In our studies, we estimate that clinically relevant accuracy include 5 mm or less because margins of healthy tissue beyond this value could result in unfavorable cosmetic outcomes. A workflow friendly nonrigid correction technique will include as much pre-calculation and intraoperative automation as possible. Therefore, building models, designating boundary conditions, and performing as many pre-calculations (such as patient-specific breast tissue stiffness) as possible before entering the operating room should be the goal as the non rigid method is developed. However, compromises on speed may be made to

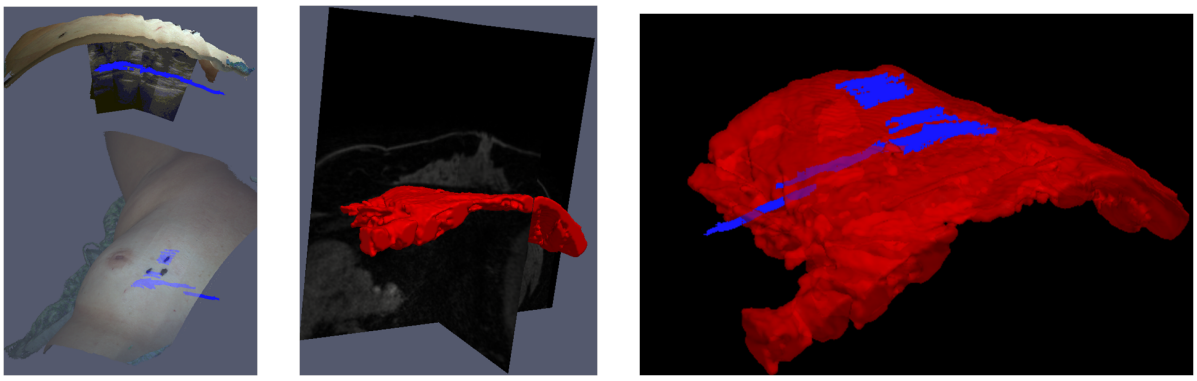

(a) (b) (c)

Figure VII.7: (a) Top: Ultrasound images of the chest wall with chest wall contours shown in blue rendered below the LRS in physical space. Bottom: transparent overlay of the LRS showing ultrasound contours of the chest wall in blue. (b) Segmentation of the preoperative chestwall from the MR image volume. (c) Rigid registration of the preoperative chestwall (red) to the intraoperative tracked ultrasound digitized chest wall contours (blue)

assure that the nonrigid corrections are accurate.

Another recommendation would be to investigate a variety of objective function configurations. There is a high value for known correspondence of points on the breast to drive registration. Also, initializing the registration with a chest wall alignment may prove beneficial (see Fig. VII.7 for chest wall data examples). Intraoperative data such as the 3D point cloud from the tracked LRS, digitized fiducial points, and digitized chest wall contours should be evaluated as ways to measure the intraoperative data to preoperative model fit. Overall, the objective function could have this basic form:

$$\psi^2 = \alpha_1 (Y - [S]\hat{Y})^2_{LRS} + \alpha_2 (Y - [S]\hat{Y})^2_{fiducial} + \alpha_3 (Y - [S]\hat{Y})^2_{chest} \tag{VII.1}$$

where Y contains a vector of points in the intraoperative space, $\hat{Y}$ is a vector of points extracted from the preoperative model after being updated by $\{u\}$, [S] is a sampling matrix that acts upon $\hat{Y}$ to obtain points that correspond to the measurements in Y, the α values represent weighting parameters.

As far as the treatment of boundary conditions, preliminary investigations indicate that arm movements and gravity induced changes are the main physical causes for breast deformations between the preoperative and intraoperative states. Boundary conditions and body forces that model these deformations should then be applied to simulate this behavior. Overall, the groundwork has been performed and there are tools and preliminary data available to begin testing of an improved nonrigid registration

algorithm.

Breast Tissue Stiffness Reconstruction

There are several avenues worth exploration for the supine breast tissue stiffness method developed in this thesis. Performing a larger study encompassing breast cancer patients to further validate this approach is recommended Specific investigations for future consideration include:

1. Investigation into more advanced nonlinear constitutive relationships to improve the accuracy of the stiffness estimation method. This may be especially important with the addition of breast cancer patients.

2. Investigation into time-vary viscoelastic effects of breast tissue that may be important for tool-tissue interaction models for image guided breast surgery.

3. Exploration of the force contributions from Coopers ligaments, pectoral muscle forces, and differences in arm-placement between the baseline and gravity-excited images.

4. Methods for reducing noise and image artifacts during the MRI acquisition of the supine images. For example, respiratory gating has been shown to improve the signal-to-noise ratio of supine breast images.

5. An investigation into the effects of image resolution should be performed. Currently, the images are acquired with voxel sizes of 0.391 mm $\times$ 0.391 mm $\times$ 1 mm and are downsampled to 0.78 mm $\times$ 0.78 mm $\times$ 1 mm for computational efficiency. It would be interesting to investigate whether or not accuracy could be improved if the images were not downsampled. Since optimization of patient properties is meant to be performed in the preoperative setting, increased computation times could be permissible.

6. Further analysis on an elastography extension of this approach. There are several factors that can be explored here including: discretization levels (number of regions to designate a unique property), number of zones for image similarity computation, level of spatial prior weighting, weighting of glandular tissue during reconstruction, and starting values for optimization.

A prone elastography method was also studied (see Appendix B) that provides alternative methods for obtaining patient specific mechanical properties. Overall, the immediate need for stiffness properties

for IGBS has been addressed in this thesis. However, several opportunities exist to expand and better understand this stiffness estimation process.

VII.3 Thesis Conclusion

The groundwork for an image guidance system for breast cancer surgery has been laid. This is the first surgical guidance system to incorporate not only patient specific anatomy via high resolution contrast enhanced image volumes, but also patient specific physical parameters through a novel stiffness estimation framework. Building upon this framework will ultimately lead to a superior tumor localization tool for breast cancer surgery and a reduction in the amount of reoperations caused by incomplete tumor removal.

Appendices

Appendix A

Lumpectomy Re-excision Cost Analysis

A.1 Introduction

To estimate the financial burden of lumpectomy re-excisions in the United States, a decision model tree was modified from [13]. A decision tree is a graphical representation of decisions and their possible consequences. In this analysis, the probability of re-excision was altered to calculate the costs associated with surgical re-excisions for breast conserving therapy. In Fig. A.1, the decision tree determined in Abe et al. [13] was reproduced. Here, the model assumed a population of 140,000 patients undergoing breast conserving surgery in a year. This estimate assumes that of 230,000 new breast cancer cases each year, approximately 60% of these patients will undergo breast conserving therapy. Another assumption is that only one additional surgery was required to achieve a negative margin. Finally, the cost model assumes that for local recurrence cases, a mastectomy is performed and that all BCT patients undergo a sentinel lymph node biopsy.

Patients receiving an initial lumpectomy were classified into three groups: negative margin, close margin, and positive margin. From here, the decision tree branched these groups into candidates receiving a second surgery for margin re-excision and patients who did not undergo margin re-excision. For accurate cost analysis, the re-excision vs. no re-excision groups were then stratified by whether or not local recurrence occurs (causing an increase in treatment cost). Reimbursement rates from the 2013 Center for Medicare and Medicaid Services (CMS) were used to estimate surgical costs. Probabilities of margin status and local recurrence rates come from the weighted average of 10 published studies (n=5639 patients) between 1990 and 2015. Data from two studies (n=697 patients) were used to estimate the probability of re-excision. These studies can be found in [13].

To estimate the differences between treatment costs for negative and positive (or close) margins, the probabilities from Fig. A.1 were altered to reflect a re-excision rate of 100% for close or positive margins. Fig. A.2 shows the new adjusted probabilities and the new treatment cost. Fig. A.3 shows the decision tree that estimates treatment costs when no re-excisions are performed. Taking the difference between the treatment costs in Fig. A.2 and A.3, we can estimate the cost associated with margin re-excision.

A.2 Summary Statement

The addition surgical cost of re-excisions in the close and positive margin groups is $53 million. The analysis underestimates the total cost associated with lumpectomy re-excision rates as it does not include facility-based costs, outpatient costs, or adjuvant therapies. It also assumes that only one additional surgery will be required to obtain a negative margin. Furthermore, the use of CMS reimbursement rates underestimates true costs as private payers typically reimburse up to 20-30% higher than CMS.

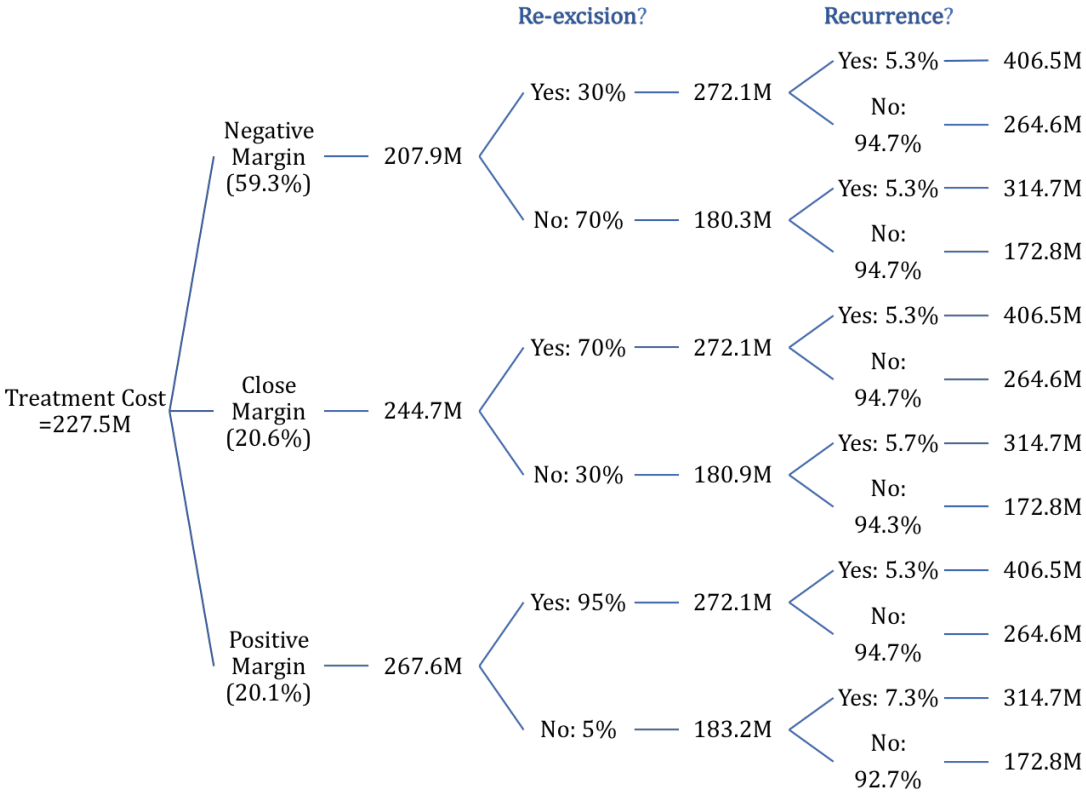

Figure A.1: Decision Tree with Probabilities Estimated From Abe et al. [13]

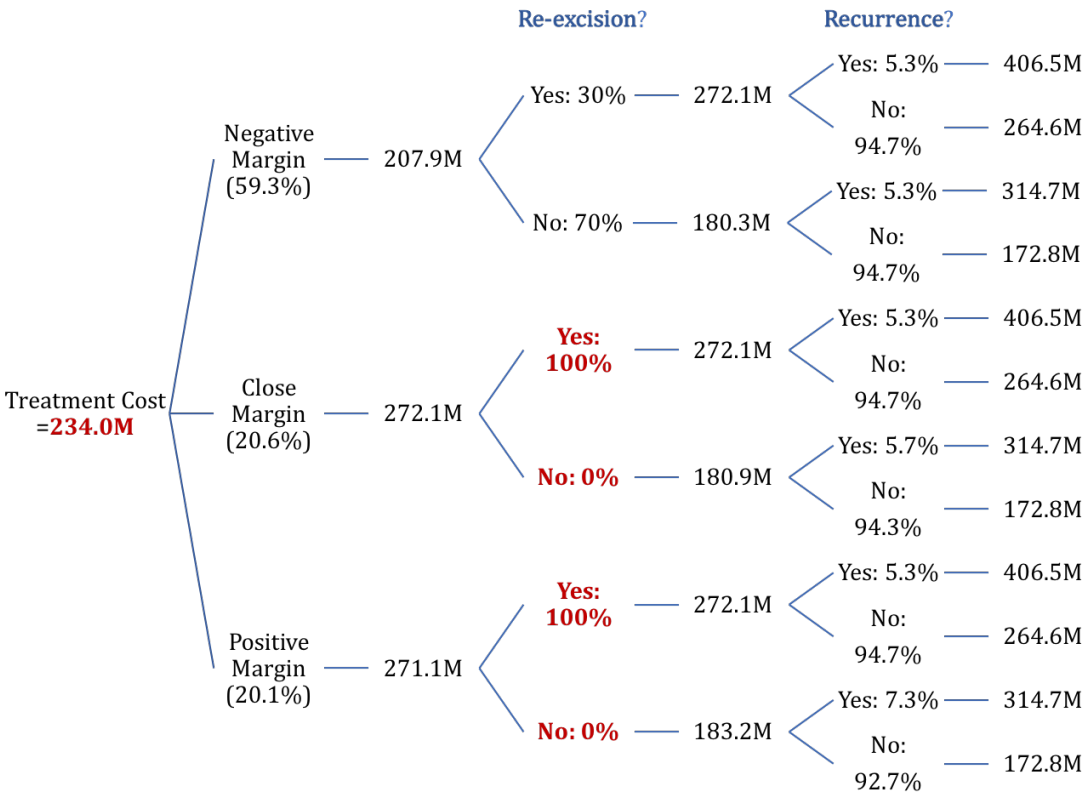

Figure A.2: Decision Tree for Re-excisions for Positive and Close Margins

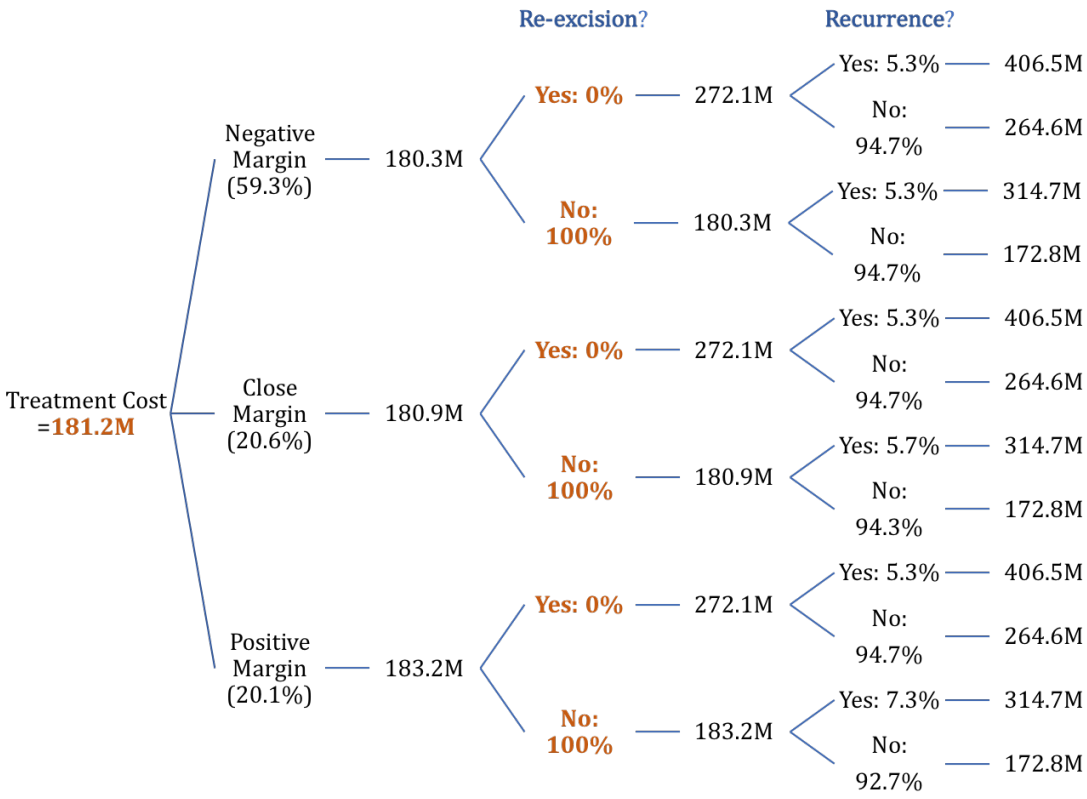

Figure A.3: Decision Tree for No Re-excisions for Positive and Close Margins

Appendix B

Alternative and expanded methods for patient specific mechanical properties

B.1 The Modality Independent Elastography Method

Modality Independent Elastography (MIE) [167], patented in 2007 (US7257244B2), is a method that is capable of measuring patient specific, *in vivo*, mechanical properties of underlying breast structures. Although this method does not rely on a specific imaging modality, magnetic resonance images (MRI) were used in preliminary studies due to their high resolution and clinical adaptability into breast cancer workflows. In general, MIE works by imaging an organ or tissue of interest in an undeformed and deformed state. Next, reconstruction of mechanical properties is performed by iteratively deforming the undeformed image using a biomechanical model until an image similarity metric is met. The output of the MIE algorithm is a relative elasticity map.

Magnetic resonance image volumes are pre-processed by removing background structures and designating tissue types as glandular, tumor, or adipose. Next, a finite element mesh is generated. A demons non-rigid registration is performed between the deformed and undeformed images to obtain a displacement field that maps the undeformed image to the deformed state. A more in depth description of this process is described in [176]. This displacement field is extracted and automatically applied as displacement boundary conditions on the surface of the finite element mesh. Deformation between the undeformed and deformed states are then simulated using a computational mechanical model. Distributions of mechanical elasticity are iteratively reconstructed using a conjugate gradient algorithm with an adjoint method evaluation of the gradient. This optimization minimizes an objective function consisting of image volume zone-based correlation coefficients that represent the residual error between the model simulated deformed image and the acquired deformed image. Following reconstruction, the output of the algorithm is a volumetric distribution of relative elasticity. Figures B.1 and B.2 contain the input images and relative elasticity map that resulted from a healthy volunteer and breast cancer patient, respectively.

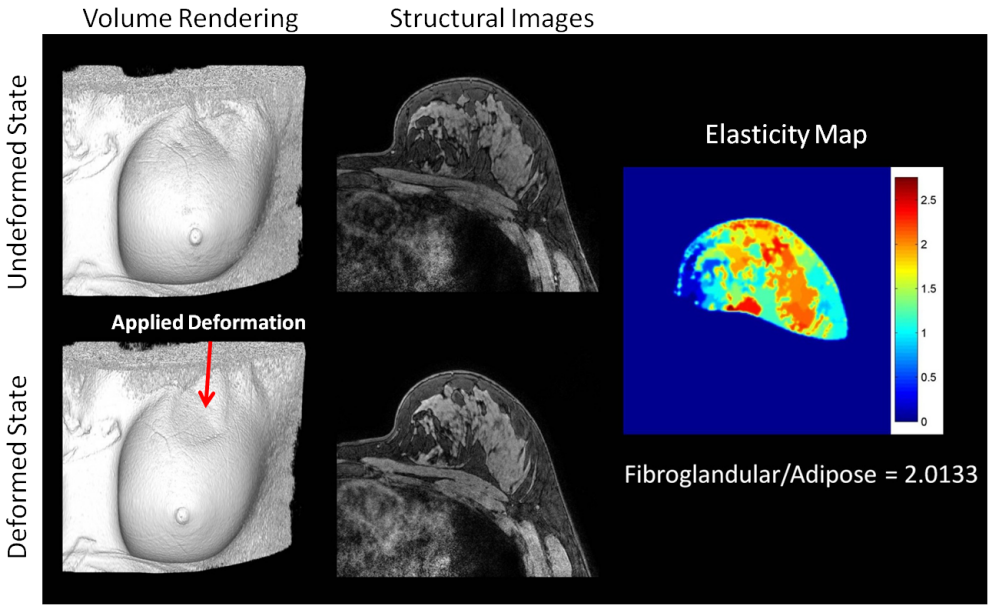

Figure B.1: MIE result for a healthy volunteer. The far left panel contains volume renderings of the volunteer breast, the middle panel displays T_1-weighted structural images of the breast. The top two images represent the undeformed (or fixed) state while the bottom two images represent the deformed (or moving) state. The far right image shows an elasticity map containing the resulting elasticity ratios. The average fibroglandular-to-adipose ratio was 2.

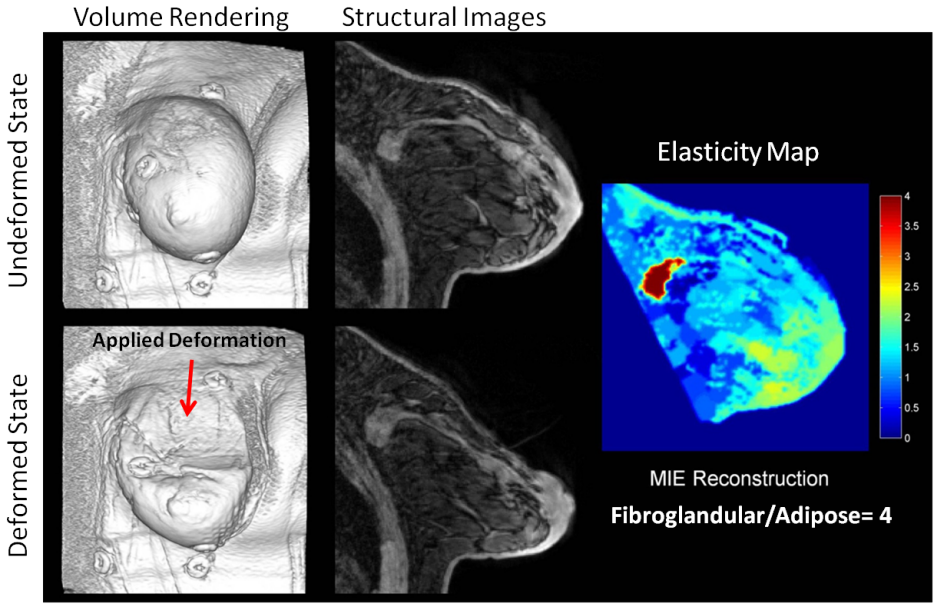

Figure B.2: MIE result for a patient volunteer. The far left panel contains volume renderings of the volunteer breast, the middle panel displays T_1-weighted structural images of the breast. The top two images represent the undeformed (or fixed) state while the bottom two images represent the deformed (or moving) state. The far right image shows an elasticity map containing the resulting elasticity ratios. The average tumor-to-adipose ratio was 4.

B.2 Device Design

Design Criteria

Design criteria for the inflation device for human subjects include: compatibility with MR and CT scanners, reliable for repeat setups, stable in the magnet, generalized for patients of all breast size, and able to control inflation outside of the imaging scan room. Generalization of the device for all patients requires a low profile design and capable of applying similar deformations to all breast shapes and sizes. Furthermore, the device must accommodate existing breast imaging setups. For example, MR images of the breast are typically acquired with a dedicated breast coil with the patient lying in the prone position with freely hanging breasts. Breast coils used in MR imaging have either an open or closed coil design. Figure B.3 shows an example of an open B.3a and closed B.3b coil design. When a closed coil is used, the breast cannot be accessed from the side, which was a major consideration in the device design.

(a) (b)

Figure B.3: MR coil design examples: (a) open coil setup where the breast is accessible from the side. (b) closed coil set up.

Breast Deformation Device

The device primarily consists of two plates, a base plate and an upper plate, which are connected by three or four upright guide-rods which are located symmetrically about the periphery of plates in a circular fashion. The upper plate can glide in a vertical fashion along the guide-rods above the base plate.

The base plate Fig. B.4a) is beveled on the bottom to better conform to the curved bottom of the coil. The upper plate (Fig. B.4b) is shelled out in order to allow for the guide-rod motion when the device is in compression. The guide-rods (Fig. B.5) have a small head at the upper end, which acts as a backstop for the upper plate when it is in extension, preventing the device from overextending/overcompressing. The guide-rods have threads on the lower end that secure it to the base plate. Finally, a top plate (Fig. B.4b) covers the upper plate to prevent contact of the patient with the guide-rods and provide a surface off which to compress. The guide-rods are placed through the upper plate and screwed into the base plate to its corresponding hole. The remaining screws are installed in a similar fashion. The top plate is then secured to the upper plate with four very small screws. These screws are recessed as to prevent contact with the patient. An actuation device, such as an air bladder, can be placed centrally between the plates. The air bladder is attached to a 30 ft air hose that is fed through a small slot in the scanning room to make it available for outside control. The hose is then attached to a pump with a valve to hold or release air. The deformation device compresses the breast from the bottom of the breast coil towards the patient's chest wall, allowing for reproducible compression of the breast and subsurface tissue targets.

B.3 *In Vivo* Results

The subject was placed on a MammoTrack table with a 16-channel receive double-breast coil (Philips Healthcare, Best, The Netherlands). A THRIVE (T_1-weighted, **h**igh **r**esolution **i**sotropic **v**olume **e**xcitation) sequence with fat suppression is used to acquire high resolution anatomical scans of the breast. The MR parameters typically used in these scans are included in table B.1

Table B.1: MRI Parameters for Prone Breast Imaging

Repetition Time (TR)	Echo Time (TE)	Field of View (FOV)	Matrix Size	Scan Time (mm:ss)	Number of Signal Averages (NSA)
6.4 ms	3.4 ms	$192 \times 192 \times 160\ mm^3$	384 x 383	02:48	1

In a test-retest setup, the right breast of a volunteer was scanned four times. The first scan produced an "undeformed" image (Fig. B.7a) where the device was in contact with the breast but remained uncompressed. The second scan produced a "deformed" image (Fig. B.7b) by fully inflating the air

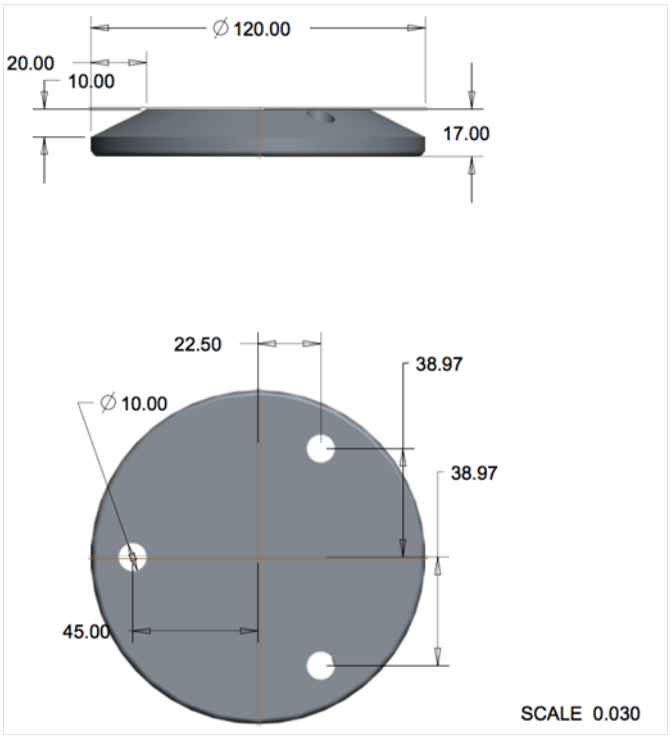

(a)

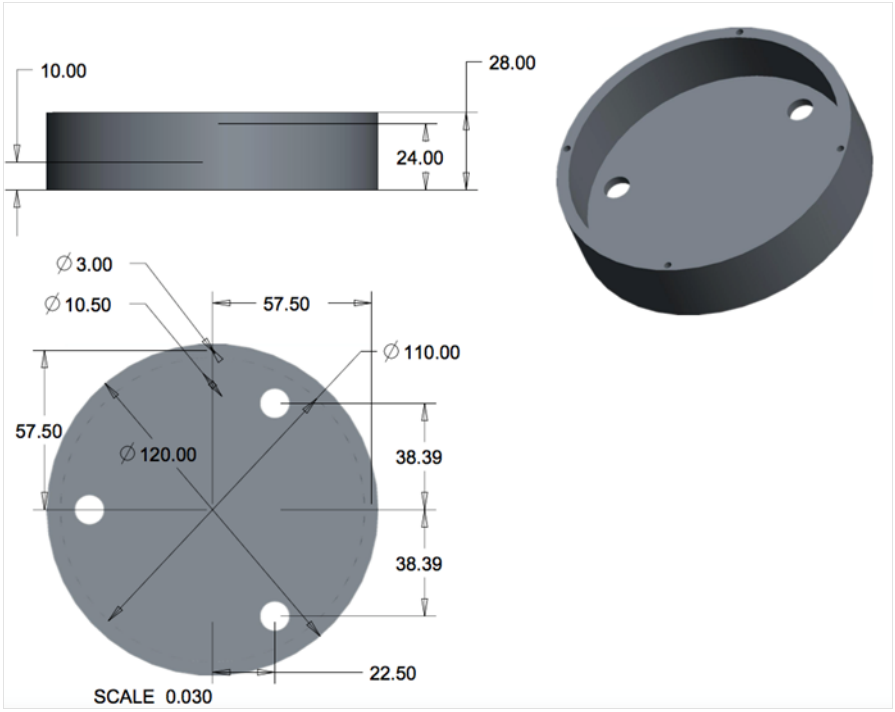

(b)

Figure B.4: Design measurements for the base plate (a) and the upper plate (b). The upper plate glides in a vertical fashion along guide-rods attached to the base plate. All measurements are in mm.

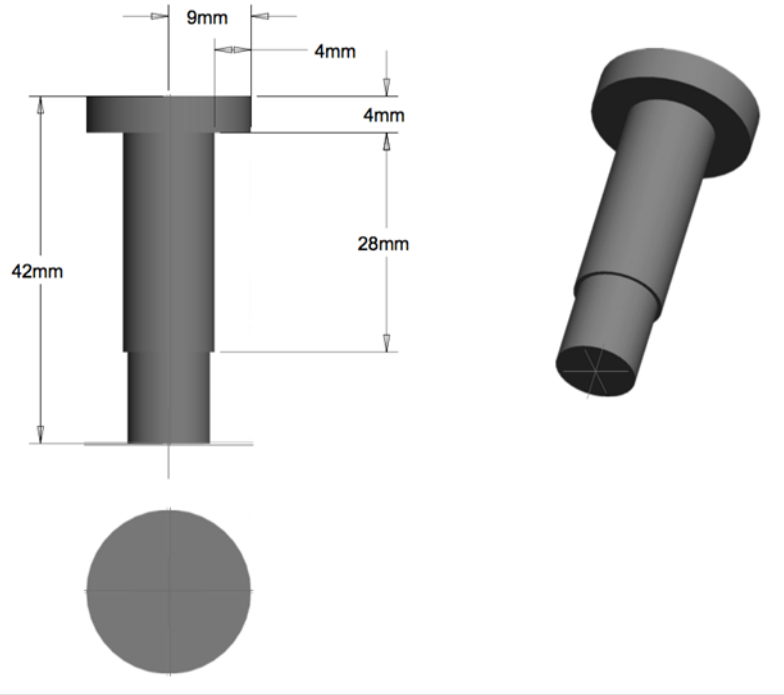

Figure B.5: Design and measurements for the guide-rods. The guide-rods shown allow the upper plate to move vertically towards or away from the base plate. The guide-rods have a small head at the upper end, which acts as a backstop for the upper plate when in extension. This prevents the device from over-extending. All measurements are in mm.

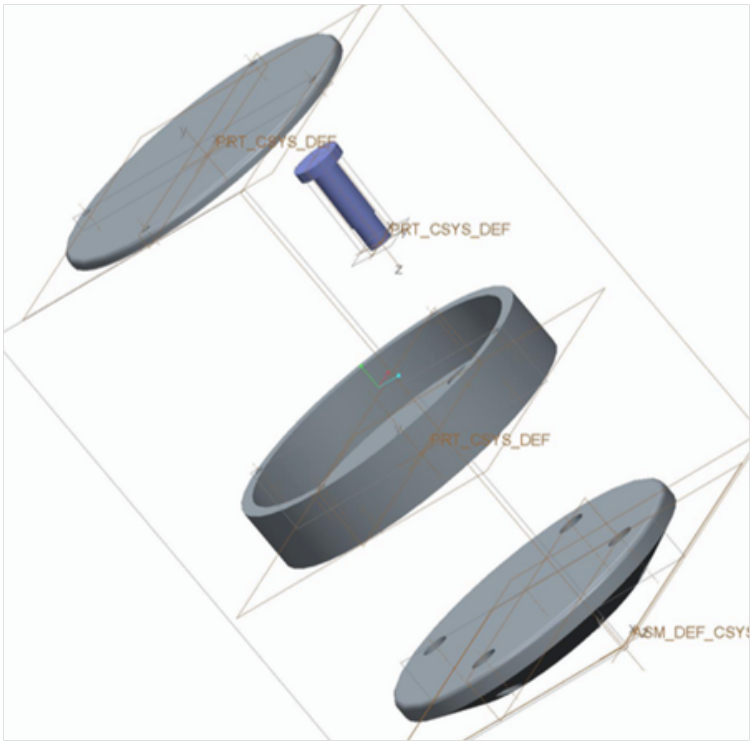

(a)

(b)

Figure B.6: (a) Shows how the upper plate, base plate, and guided rods are assembled. (b) is the final machined device with a rectangular air bladder between the base plate and upper plate. When inflated, the upper plate extends away from the base plate.

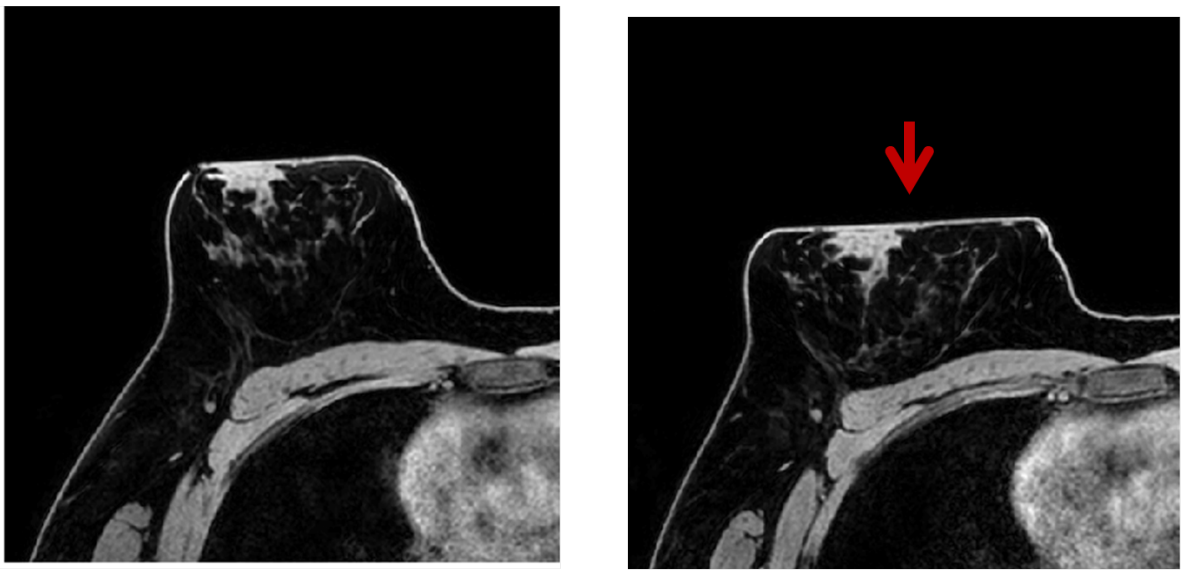

(a) Undeformed (b) Deformed

Figure B.7: Undeformed and deformed images produced using deformation device described in Chapter B.2. The red arrow in (b) shows the location and direction of deformation.

bladder from outside the imaging suite. The full inflation guarantees that the device will raise approximately 2 cm. The volunteer was then removed from the scanner and the device was re-set. The third and fourth scans were obtained to measure how well the device can reproduce similar deformations in the breast in repeat setups. The third scan was a retest of the "undeformed" image and the fourth scan was a retest of the "deformed" image. Figure B.8 show the test-retest results of our compression device induced deformation. The maximum difference in induced deformations was 1.25 mm, which can be seen in the coronal views. Overall, the setup was extremely repeatable, with average deformation differences being 0.42 mm. A resulting elastogram is shown in Fig. B.9.

B.4 Conclusion

The MIE method has been refined in several publications with applications in breast elastography [134, 167, 177, 260]. Opportunities to include MIE in assessing and predicting response to neoadjuvant chemotherapy have been discussed [181]. Recently, the reliability and reproducibility of MIE in a murine model of breast cancer has been reported [232]. However, the reliability of MIE in a clinical setting has not been robustly tested. A device to create reproducible breast deformations is crucial to the testing and development of MIE in clinical settings. It will also make possible the first study to

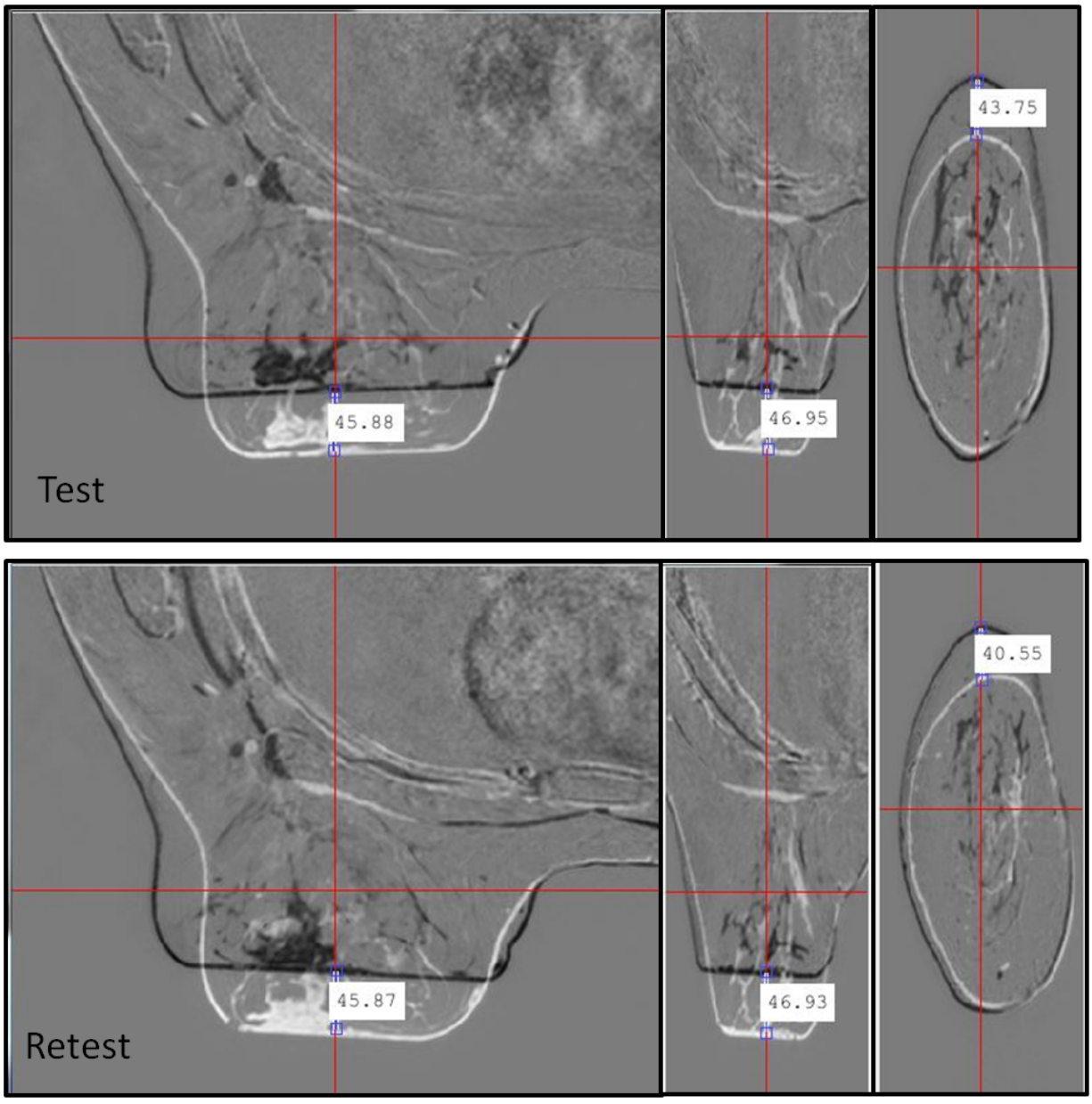

Figure B.8: Test-retest deformation results. Top panel contains the deformed image (black) and undeformed image (white) overlaid for the first test. The bottom panel contain the images produced in the second test (Retest). The top and bottom panels show (from left to right) axial, sagittal, and coronal views of the breast. The measurements (in pixels) shown on each image comparison are the differences between the deformed and undeformed breast surface. Reconstructed voxel sizes are $[0.391mm^3 \times 0.391mm^3 \times 1mm^3]$ for all images.

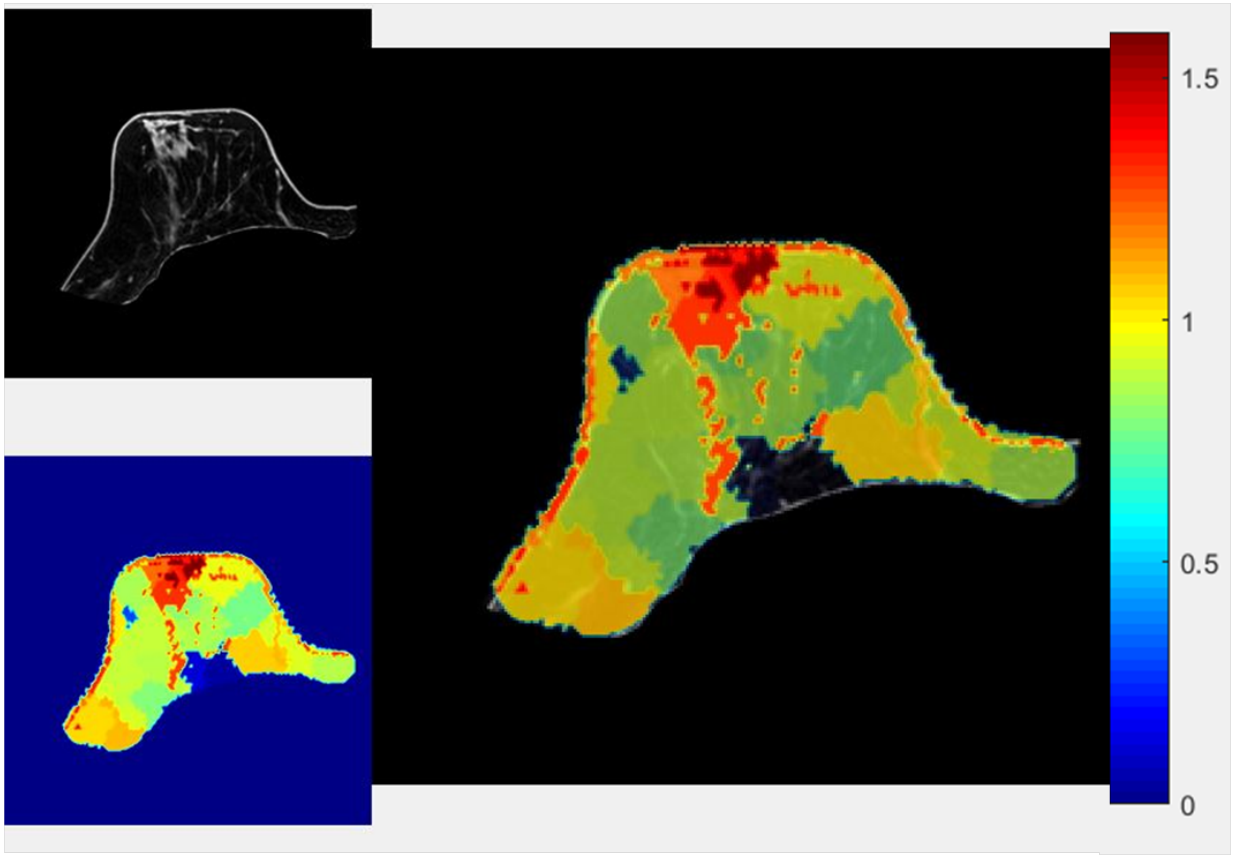

Figure B.9: Resulting elastogram using the MIE method and deformation device. Areas associated with glandular tissue are on average 30% stiffer than adipose areas.

perform a robust analysis on repeatability and reproducibility of elasticity values produced by MIE in human subjects.

Appendix C

Characterization of a Phantom Setup for Breast Conserving Cancer Surgery

C.1 Summary and Contributions

This study introduces a phantom setup for breast conserving surgery. We quantitatively analyzed breast surface deformation between preoperative and intraoperative breast states using breast cancer patients and healthy volunteers in the supine imaging-to-intraoperative positioning. Using this analysis, we designed a breast-mimicking phantom capable of realistic breast deformation as a way to test and validate platforms for image guided breast surgery. This manuscript was constructed by Jacob Chadwell, an undergraduate researcher under my direction in the lab. My specific contributions to this manuscript are as follows: I designed the study and acquired all human data for this manuscript, created the design goals for the phantom manipulation device, researched and selected the commercial breast phantom, developed the PVA breast phantom protocol, directed the acquisition of phantom data, outlined the data analysis methods, and wrote significant portions of this manuscript. While I am not the primary author of this manuscript, I have included it as an appendix due to my significant contributions along with the relevance of the phantom setup to this thesis. This manuscript appears in:

- J. T. Chadwell, R. H. Conley, J. A. Collins, I. M. Meszoely, and M. I. Miga, 'Characterization of a phantom setup for breast conserving cancer surgery', SPIE 2016 Medical Imaging: Image-Guided Procedures, Robotic Interventions, Vol. 9786, 2016

Abstract

The purpose of this work is to develop an anatomically and mechanically representative breast phantom for the validation of breast conserving surgical therapies, specifically, in this case, image guided surgeries. Using three patients scheduled for lumpectomy and four healthy volunteers in mock surgical presentations, the magnitude, direction, and location of breast deformations was analyzed. A phantom setup was then designed to approximate such deformations in a mock surgical environment. Specifically, commercially available and custom-built polyvinyl alcohol (PVA) phantoms were used to mimic breast tissue during surgery. A custom designed deformation apparatus was then created to reproduce deformations seen in typical clinical setups of the pre- and intra-operative breast geometry. Quantita-

tive analysis of the human subjects yielded a positive correlation between breast volume and amount of breast deformation. Phantom results reflected similar behavior with the custom-built PVA phantom outperforming the commercial phantom.

C.2 Introduction

Treatment for early stage breast cancer usually involves a lumpectomy and radiation treatment, together known as breast conservation therapy (BCT). BCT has the risk of reoperation due to difficulty in determining tumor borders intraoperatively. A comprehensive framework for image- guided breast surgery using supine magnetic resonance (MR) images, patient specific biomechanical models, and intraoperative ultrasound has been proposed [154, 224] as a superior intraoperative tumor localization strategy. A mock surgical setup that could be used to evaluate data acquisition and registration methods for such surgical systems would be of great value. Therefore, in this study, a phantom setup with realistic breast geometry and elasticity is described along with a custom deformation apparatus designed to reproduce breast tissue deformation seen between preoperative images of the breast and the intraoperative configuration of the breast.

The preoperative state within the imaging unit is associated with the subject in the supine position with the ipsilateral arm placed above her head. The intraoperative state involves the subject in the supine position with the ipsilateral arm placed out approximately perpendicular from the body. The breast deforms considerably between the two states. Ebrahimi et al. report the tumor center of mass difference between two supine setups in [55]; one with the arm parallel to the body, and one with the arm above the patients head. The center of mass difference of the tumor between these two arm positions averaged 2.78 cm and ranged between 1 and 4.6 cm. This study indicates that significant deformation occurs due to differences in ipsilateral arm placement. The motivation for the work presented here is that in order to properly validate non-rigid correction algorithms and image guidance techniques, there is a need to take quantitative measurements in a controlled manner. Furthermore, individual differences in the clinical setting limit reproducibility, which is an issue that can be remedied by the use of a phantom. Commercial breast phantoms are available, such as the Breast Probe (SIMULAB Corporation, Seattle, WA) and the Complex Breast Phantom (SynDaver Labs, Tampa, FL), and while they do represent surface anatomy, they do not represent physiologic elasticities and deformation characteristics.

C.3 Methods

Analysis of Clinical Breast Deformation

Breast deformations that occur clinically from the preoperative state to the intraoperative state were characterized by analyzing deformations seen in three patients scheduled for a lumpectomy and in four healthy volunteers in mock surgical setups. The data from patients and healthy subjects were acquired under an Institutional Review Board (IRB) approved study. In the fourth volunteer, MR images and mock intraoperative data was acquired for both breasts, yielding seven total data sets. The magnitude and direction of breast surface deformation was measured using MR-visible fiducial markers, as seen in Fig. C.1 (IZI Medical Products, Owing Mills, MD). MR images of the breast in the supine configuration were acquired using a 16- channel sensitivity encoding (SENSE) torso coil. The coil was situated as to not apply any unnatural deformations to the breast. High resolution anatomical images were acquired using a T_1-weighted sequence with fat suppression. Fiducial center points in the MR images were manually determined. In the mock surgical setup, the geometric coordinates of the synthetic surface fiducials were acquired using an optically tracked stylus and NDI Polaris Spectra (Northern Digital, Waterloo, ON, Canada). The fiducial markers were used to calculate fiducial registration error (FRE), a measure of overall landmark misalignment, and an intrafiducial (IF) distance distribution, used to determine both magnitude and direction of clinical deformation. The differences in FRE and IF distance distribution between the two positions were reported to establish a non-rigid surface deformation characterization. Breast volume for each subject was also determined by semi-automatic segmentation of the breast tissue.

The differences in intrafiducial distances between the preoperative imaging environment and intraoperative configuration represent the magnitude of non-rigid deformation occurring between the two states. A covariance matrix of these values was computed, and used to find the principle axes of deformation by solving for the eigenvalues and eigenvectors. These eigenvectors provide a quantitative representation of the anatomically-relevant directions of principle deformation associated between the two presentation states. By registering all physical space fiducials in the surgical presentation to the MR counterparts, trends among the principal directions can be compared and correlated to standard anatomical directions due to the uniformity of MR patient imaging.

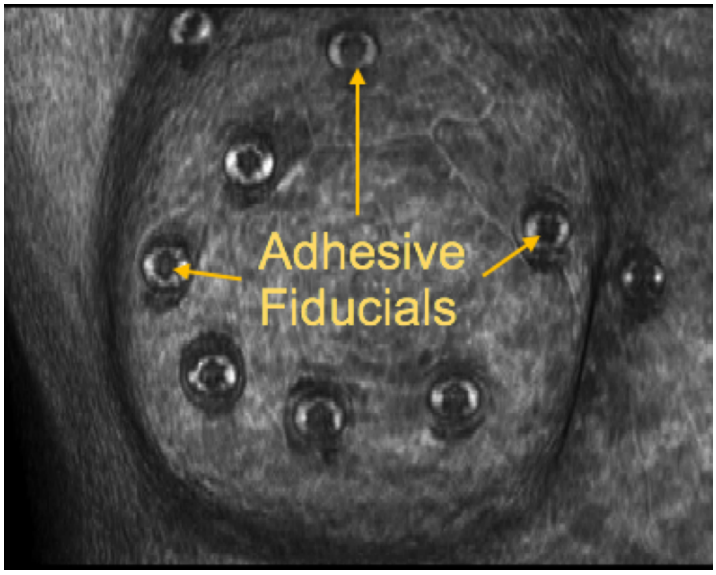

Figure C.1: Volume render of breast in supine position with synthetic, MR-visible fiducial markers

Phantom Design

Poly(vinyl) alcohol (PVA), a synthetic polymer commonly used for approximating soft tissue [261], was used to simulate breast tissue. The phantoms were developed with the ability to include features such as elastically-representative fibroglandular tissue and tumors. This setup has been used previously in breast phantoms used for sonographic validation within microwave imaging systems [262]. However, the phantoms presented here are able to be used without a shell encasement, a limitation commonly associated with many existing phantoms for sonographic use [263–265]. This makes the setup well-suited for validation of intraoperative surgical guidance methods and tomographic imaging, regardless of whether the phantoms are used in the supine or pendant position. We should also note that the phantoms presented here closely resemble surface anatomy, mimicking not only the shape of the breast itself, but the surrounding tissue ipsilateral arm region as well.

Phantom Preparation

The mold for the breast phantom was similar to the one shown in Fig. C.2a which is the Breast Probe phantom from SIMULAB Corporation (Seattle, WA). The phantom mold was coated with small beads for tracking. These beads became embedded in the surface of the phantom upon freezing. Beads were used because adhesive fiducial markers do not adhere well to the phantom surface. Each phantom was prepared by combining water and 7% by mass of (poly)vinyl-alcohol (Sigma Aldrich 341584), which

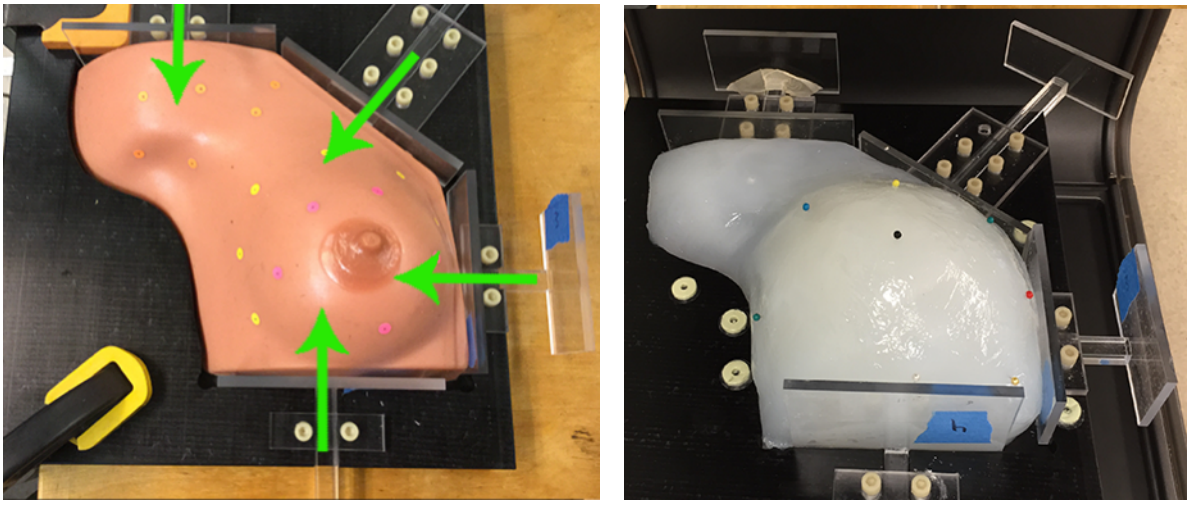

(a) a (b) b

Figure C.2: (a) SimuLab Breast Probe, and (b) PVA phantom in deformation apparatus. Green lines illustrate directions compression can be applied to phantom

was then heated to 80 degrees C. 10% by volume of glycerin was added (Sigma Aldrich G7893), then placed on a stirring stand until significantly cooled (this cooling is not explicitly necessary, but assisted in keeping beads in place while pouring). The solution was carefully poured into the molds and left uncovered in the freezer for at least 14 hours, then thawed for another 14 hours. It was discovered that leaving the phantoms uncovered in the mold is crucial to achieving the proper stiffness, due to the rate the phantoms dry while freezing/thawing.

Deformation Apparatus

A deformation apparatus was created with four manipulators able to induce and hold compressive forces on the breast (Fig. C.2a, C.2b). All four manipulators can be deployed at once, individually, or in some unique configuration. The base of the deformation frame contains a 1 cm depression machined to have the same contour as the breast phantom mold. This allows the breast phantom to sit flush in the base and hold applied deformations while minimizing slip. It should be noted that the deformation apparatus only provides compressional forces on the phantom; however, the clinical deformation can still be reproduced, based on the results from the principle component analysis which showed that primary deformation occurs along the patients superior-inferior axis, and secondary deformation occurring along the medial-lateral axis.

Measuring Phantom Deformation

Two phantom materials were compared in this phantom setup. The first material was a commercially available breast phantom with realistic synthetic tissue (SIMULAB Corporation, Seattle, WA Fig. C.2a). The second analysis was done using the PVA gel described above. Each phantom was placed in the deformation base and markers were dispersed on each surface. Surface markers were digitized for the baseline (undeformed) and deformed state using an optically tracked stylus. FRE and IF distance distribution differences were calculated for each phantom and compared to the clinical data sets.

C.4 Results

Clinical Breast Deformation

Analysis of non-rigid deformation between the supine MR images and mock intraoperative breast configuration yielded a positive correlation between breast volume and the amount of deformation. The fiducial registration error (FRE), was calculated for all cases. FRE indirectly captures an estimate of non-rigid changes by looking at changes with respect to breast volume. The assumption is that fiducial localization error (FLE) is similar among women with different breast volumes but that soft tissue changes due to arm motion would be exacerbated with larger breast women. More specifically, the effects of chest wall attachments would inhibit deformation effects in smaller breast women. Fig C.3a is a graph showing the correlation between breast volume and FRE for the 7 human subjects. The correlation coefficient between volume and FRE is 0.93. Fig. C.3b shows the maximum IF distance distribution difference between preoperative and intraoperative states also as a function of subject breast volume.

While not as strong a correlation as FRE, the maximum IF distance distribution difference correlated with volume with a 0.74 correlation coefficient. Across the subject population the FRE average, and maximum IF average was 6.0 +/- 2.1 mm, and 13.8 +/- 6.5 mm, respectively. Also of note, in a qualitative comparison of the maximum IF distance distribution differences, most deformation occurred along the subjects inferior-superior axis, with minor deformations occurring along the subjects medial-lateral axis.

The principle component analysis performed on the seven human cases confirmed this quantitatively. Fig. C.4 shows the three principle components of deformation for each case with the average also shown. Analyzing the breast fiducials from the supine MR preoperative state to the supine intra-

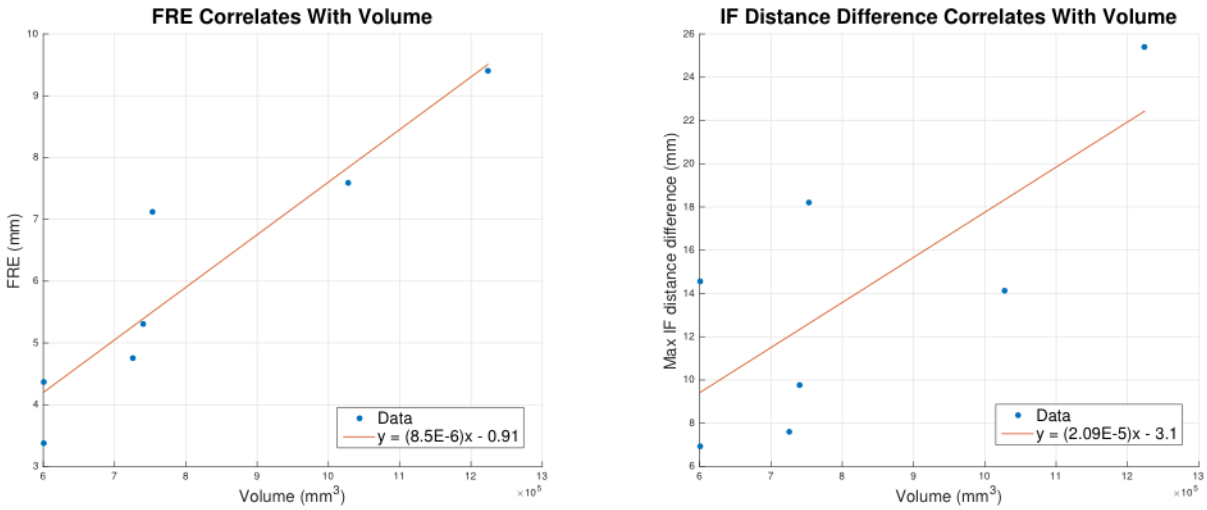

Figure C.3: The relationship between breast volume and (a) fiducial registration error, and (b) and maximum intrafiducial distance differences associated with the tracked adhesive fiducial markers distributed on the breast surface.

operative state, the largest motion is approximately in the superior-inferior direction, and the second largest is approximately in the medial-lateral direction. Based on the PCA analysis, the motion in the superior-inferior direction is approximately 2.3 times greater than medial-lateral motion, and 6.2 times greater than anterior-posterior motion on average.

Phantom Deformation

Each phantom (Breast Probe, and our molded PVA-gel) had a volume of 7.2 105 mm^3. The FRE between mock preoperative and intraoperative states for the commercial phantom and PVA gel phantom was 3.8 mm, and 5.05 mm, respectively. When comparing that to the clinical results of Fig. C.3a, the FRE value for the PVA phantom more closely matched the expected value for this breast volume (5.2 mm in Fig. C.3a) than the commercial phantom. The maximum IF distance distribution difference between mock preoperative and intraoperative states for the commercial and PVA gel phantom was 8.31 mm, and 13.28 mm, respectively. When comparing to Fig C.3b, the PVA gel phantom provided deformations closer to those seen clinically (11.95 mm in Fig C.3b).

The clinical deformation analysis was used to characterize the directions and magnitude of deformation between the supine MR imaging environment and the supine intraoperative state. This analysis was then used as a guideline to develop the phantom and fine tune its material properties. It should be noted that supine MR imaging was used for its more accurate representation of the breast during

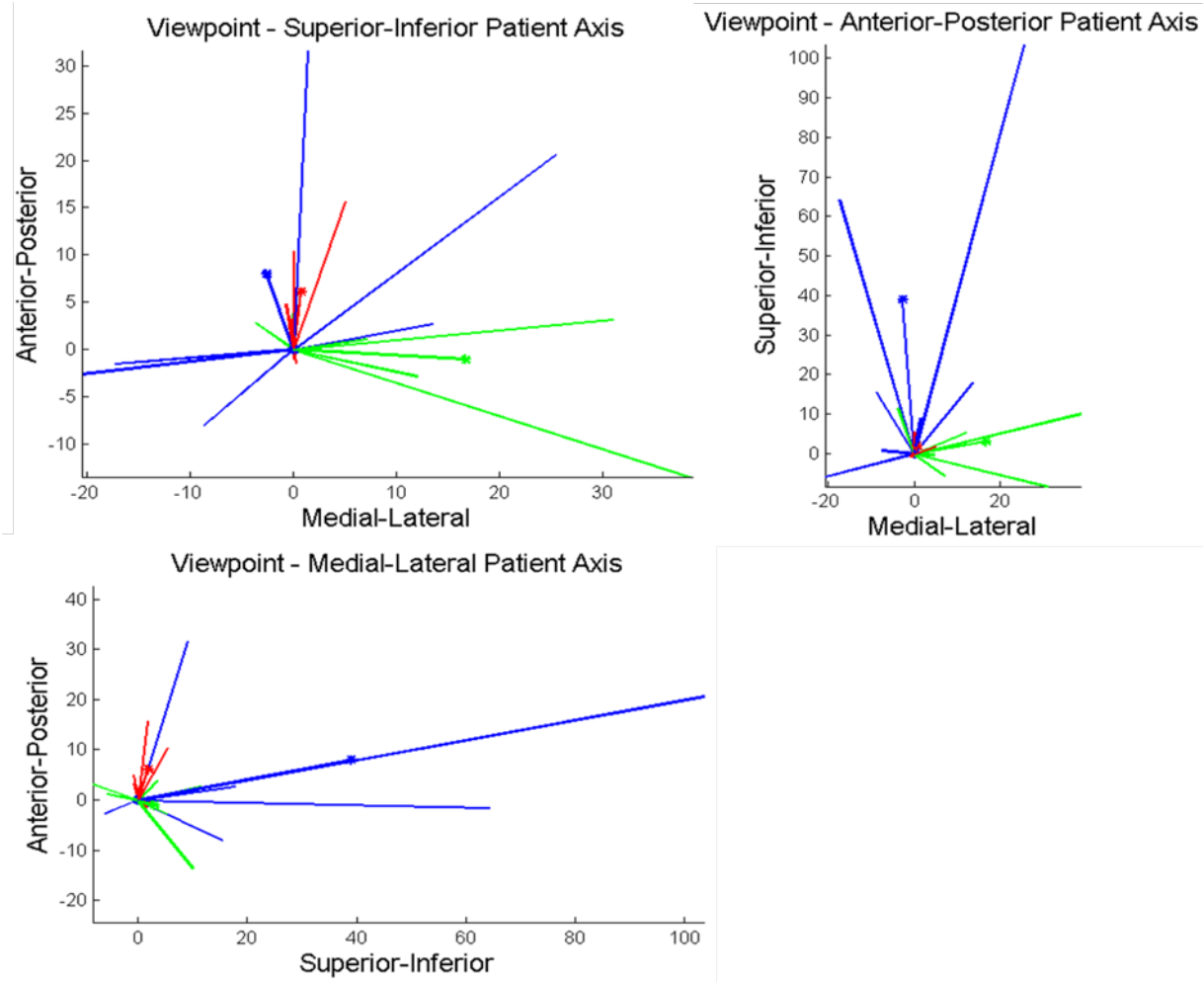

Figure C.4: Results from principle component analysis of breast deformations reveal primary (blue lines), secondary (green lines), and tertiary (red lines) principle components for each of 7 cases. The asterisk designated lines represent the average principal component directions over all 7 cases. Note, vector magnitudes are expressed in voxels.

the lumpectomy procedure [224]. As noted earlier, the deformation apparatus applies compressional forces on the phantom. While this force does not mimic the physiological counterpart with respect to the deformation, it does embody the effects of those sources of deformation in terms of magnitude, direction, and location of movement between the two states.

C.5 Conclusion

In this study, we quantitatively analyzed breast surface deformation between preoperative and intraoperative breast states using breast cancer patients and healthy volunteers in the supine imaging-to-intraoperative positioning. Using this analysis, we designed a breast-mimicking phantom capable of realistic breast deformation as a way to test and validate platforms for image guided breast surgery. The representative PVA breast phantom was shown to be a viable option for the use in evaluating image guidance systems for breast surgery.

C.6 Acknowledgments

This work was supported in part by the Vanderbilt University School of Engineering Summer Research Program, the Vanderbilt Institute in Surgery and Engineering (VISE) Center Summer Fellows Program, the VISE Pilot Grant Award Program, and the National Science Foundation Graduate Research Fellowship Grant awarded to RHC.

BIBLIOGRAPHY

[1] Abbas Samani, Judit Zubovits, and Donald Plewes. Elastic moduli of normal and pathological human breast tissues: an inversion-technique-based investigation of 169 samples. *Physics in medicine and biology*, 52(6):1565, 2007.

[2] Thomas A Krouskop, Thomas M Wheeler, Faouzi Kallel, Brian S Garra, and Timothy Hall. Elastic moduli of breast and prostate tissues under compression. *Ultrasonic imaging*, 20(4): 260–274, 1998.

[3] Parris Wellman, Robert D Howe, Edward Dalton, and Kenneth A Kern. Breast tissue stiffness in compression is correlated to histological diagnosis. *Harvard BioRobotics Laboratory Technical Report*, pages 1–15, 1999.

[4] Takeshi Umemoto, Ei Ueno, Takeshi Matsumura, Makoto Yamakawa, Hiroko Bando, Tsuyoshi Mitake, and Tsuyoshi Shiina. Ex vivo and in vivo assessment of the non-linearity of elasticity properties of breast tissues for quantitative strain elastography. *Ultrasound in medicine & biology*, 40(8):1755–1768, 2014.

[5] Terese Winslow LLC. Anatomy of female breast, 2011. URL https://peoniesandpancakes.files.wordpress.com/2013/10/cdr0000415520.jpg. Online; accessed April 14, 2015.

[6] Quadrants of the breast, 2011. URL https://o.quizlet.com/pgUrLPf5g6WnK6w6It0H3g_m.png. Online; accessed April 14, 2015.

[7] Keith Bridwell. Anatomical planes of the body, 2010. URL http://www.spineuniverse.com/sites/default/files/legacy-images/dp_planes-BB.gif. Online; accessed April 14, 2015.

[8] via National Cancer Institute Alan Hoofring Public domain. Mammogram, 2003. URL https://visualsonline.cancer.gov/details.cfm?imageid=4361. Online; accessed April 25, 2017.

[9] Dr. Dwight Kaufman. National Cancer Institute. Mammogram with obvious cancer, 1994. URL https://upload.wikimedia.org/wikipedia/commons/3/35/Mammogram_with_obvious_cancer.jpg. [Online; accessed April 25, 2017].

[10] LLC. Millennium Medical Group. Ultrasound, 2015. URL http://mmg-clinics.com/wp-content/uploads/2013/01/sono.png. Online; accessed April 14, 2015.

[11] Mayo Foundation for Medical Education and Research. Breast mri, 2015. URL http://www.mayoclinic.org/tests-procedures/breast-mri/details/what-you-can-expect/rec-20239454. Online; accessed April 14, 2015.

[12] Germany Brainlab. Neuronavigation vectorvision, 2014. URL http://www.rumex.ru/imagecache/800x800/1152_3097_t1385120060_800x800.jpg. Online; accessed April 14, 2015.

[13] Shoko E Abe, Joshua S Hill, Yimei Han, Kendall Walsh, James T Symanowski, Lejla Hadzikadic-Gusic, Teresa Flippo-Morton, Terry Sarantou, Meghan Forster, and Richard L White. Margin re-excision and local recurrence in invasive breast cancer: A cost analysis using a decision tree model. *Journal of surgical oncology*, 112(4):443–448, 2015.

[14] Rebecca L Siegel, Kimberly D Miller, and Ahmedin Jemal. Cancer statistics, 2016. *CA: a cancer journal for clinicians*, 66(1):7–30, 2016.

[15] Linnea Langhans, Maj-Britt Jensen, Maj-Lis M Talman, Ilse Vejborg, Niels Kroman, and Tove F Tvedskov. Reoperation rates in ductal carcinoma in situ vs invasive breast cancer after wire-guided breast-conserving surgery. *JAMA surgery*, 2016.

[16] Amanda M Schulman, Jennifer A Mirrielees, Glen Leverson, Jeffrey Landercasper, Caprice Greenberg, and Lee G Wilke. Reexcision surgery for breast cancer: an analysis of the american society of breast surgeons (asbrs) masterysm database following the sso-astro no ink on tumor guidelines. *Annals of surgical oncology*, 24(1):52–58, 2017.

[17] Hiram S Cody III and Kimberly J Van Zee. Reexcisionthe other breast cancer epidemic, 2015.

[18] Lindsey A. Torre, Freddie Bray, Rebecca L. Siegel, Jacques Ferlay, Joannie Lortet-Tieulent, and Ahmedin Jemal. Global cancer statistics, 2012. *CA: A Cancer Journal for Clinicians*, 2015.

[19] Bernard Fisher, Madeline Bauer, Richard Margolese, Roger Poisson, Yosef Pilch, Carol Redmond, Edwin Fisher, Norman Wolmark, Melvin Deutsch, Eleanor Montague, et al. Five-year results of a randomized clinical trial comparing total mastectomy and segmental mastectomy with or without radiation in the treatment of breast cancer. *New England Journal of Medicine*, 312(11):665–673, 1985.

[20] Benjamin D Smith, Jing Jiang, Ya-ChenTina Shih, Sharon H Giordano, Jinhai Huo, Reshma Jagsi, Adeyiza O Momoh, Abigail S Caudle, Kelly K Hunt, Simona F Shaitelman, et al. Cost and complications of local therapies for early-stage breast cancer. *Journal of the National Cancer Institute*, 109(1):djw178, 2017.

[21] Jeffrey Landercasper, Eric Whitacre, Amy C Degnim, and Mohammed Al-Hamadani. Reasons for re-excision after lumpectomy for breast cancer: Insight from the american society of breast surgeons masterysm database. *Annals of surgical oncology*, 21(10):3185–3191, 2014.

[22] M Rosselli Del Turco, A Ponti, U Bick, L Biganzoli, G Cserni, B Cutuli, T Decker, M Dietel, O Gentilini, T Kuehn, et al. Quality indicators in breast cancer care. *European journal of cancer*, 46(13):2344–2356, 2010.

[23] Dustin L Eck, Stephanie L Koonce, Ross F Goldberg, Sanjay Bagaria, Tammeza Gibson, Steven P Bowers, and Sarah A McLaughlin. Breast surgery outcomes as quality measures according to the nsqip database. *Annals of surgical oncology*, 19(10):3212–3217, 2012.

[24] Tanir M Allweis, Zvi Kaufman, Shlomo Lelcuk, Itzhak Pappo, Tami Karni, Shlomo Schneebaum, Rona Spector, Asher Schindel, Dan Hershko, Moshe Zilberman, et al. A prospective, randomized, controlled, multicenter study of a real-time, intraoperative probe for positive margin detection in breast-conserving surgery. *The American Journal of Surgery*, 196(4):483–489, 2008.

[25] Karole M Davis, Chiu-Hsieh Hsu, Marcia E Bouton, Krista L Wilhelmson, and Ian K Komenaka. Intraoperative ultrasound can decrease the re-excision lumpectomy rate in patients with palpable breast cancers. *The American surgeon*, 77(6):720–725, 2011.

[26] Stijn van Esser, Monique GG Hobbelink, Petra HM Peeters, Erik Buskens, Iris M Van der Ploeg, Willem PTHM Mali, Inne HMB Rinkes, and Richard van Hillegersberg. The efficacy of'radio guided occult lesion localization'(roll) versus' wire-guided localization'(wgl) in breast conserving surgery for non-palpable breast cancer: A randomized clinical trial–roll study. *BMC surgery*, 8(1):9, 2008.

[27] Rebecca L Klein, Julie A Mook, David M Euhus, Roshni Rao, Ralph T Wynn, Amy B Eastman, and A Marilyn Leitch. Evaluation of a hydrogel based breast biopsy marker (hydromark®) as an alternative to wire and radioactive seed localization for non-palpable breast lesions. *Journal of surgical oncology*, 105(6):591–594, 2012.

[28] Charles E Cox, Norbert Garcia-Henriquez, M Jordan Glancy, Pat Whitworth, John M Cox, Melissa Themar-Geck, Ronald Prati, Michelle Jung, Scott Russell, Kristie Appleton, et al. Pilot study of a new nonradioactive surgical guidance technology for locating nonpalpable breast lesions. *Annals of surgical oncology*, 23(6):1824–1830, 2016.

[29] Mark J Dryden, Basak E Dogan, Patricia Fox, Cuiyan Wang, Dalliah M Black, Kelly Hunt, and Wei Tse Yang. Imaging factors that influence surgical margins after preoperative 125i radioactive seed localization of breast lesions: Comparison with wire localization. *American Journal of Roentgenology*, 206(5):1112–1118, 2016.

[30] Neslihan Cabioglu, Kelly K Hunt, Aysegul A Sahin, Henry M Kuerer, Gildy V Babiera, S Eva Singletary, Gary J Whitman, Merrick I Ross, Frederick C Ames, Barry W Feig, et al. Role for intraoperative margin assessment in patients undergoing breast-conserving surgery. *Annals of Surgical Oncology*, 14(4):1458–1471, 2007.

[31] Roger A Graham, Marc J Homer, Cynthia J Sigler, Homa Safaii, Christopher H Schmid, DJ Marchant, and TJ Smith. The efficacy of specimen radiography in evaluating the surgical margins of impalpable breast carcinoma. *AJR. American journal of roentgenology*, 162(1):33–36, 1994.

[32] Anees Chagpar, Tina Yen, Aysegul Sahin, Kelly K Hunt, Gary J Whitman, Frederick C Ames, Merrick I Ross, Funda Meric-Bernstam, Gildy V Babiera, S Eva Singletary, et al. Intraoperative margin assessment reduces reexcision rates in patients with ductal carcinoma in situ treated with breast-conserving surgery. *The American journal of surgery*, 186(4):371–377, 2003.

[33] Roberto Gennari, Viviana Galimberti, Concetta De Cicco, Stefano Zurrida, Felipe Zerwes, Francesca Pigatto, Alberto Luini, Giovanni Paganelli, and Umberto Veronesi. Use of technetium-99m–labeled colloid albumin for preoperative and intraoperative localization of nonpalpable breast lesions. *Journal of the American College of Surgeons*, 190(6):692–698, 2000.

[34] Freddy T Nguyen, Adam M Zysk, Eric J Chaney, Jan G Kotynek, Uretz J Oliphant, Frank J Bellafiore, Kendrith M Rowland, Patricia A Johnson, and Stephen A Boppart. Intraoperative evaluation of breast tumor margins with optical coherence tomography. *Cancer research*, 69 (22):8790–8796, 2009.

[35] Karla Esbona, Zhanhai Li, and Lee G Wilke. Intraoperative imprint cytology and frozen section pathology for margin assessment in breast conservation surgery: a systematic review. *Annals of surgical oncology*, 19(10):3236–3245, 2012.

[36] Matthew D Keller, Elizabeth Vargis, Nara de Matos Granja, Robert H Wilson, Mary-Ann Mycek, Mark C Kelley, and Anita Mahadevan-Jansen. Development of a spatially offset raman spectroscopy probe for breast tumor surgical margin evaluation. *Journal of biomedical optics*, 16(7): 077006–077006, 2011.

[37] Timothy E Doyle, Rachel E Factor, Christina L Ellefson, Kristina M Sorensen, Brady J Ambrose, Jeffrey B Goodrich, Vern P Hart, Scott C Jensen, Hemang Patel, and Leigh A Neumayer. High-

frequency ultrasound for intraoperative margin assessments in breast conservation surgery: a feasibility study. *BMC cancer*, 11(1):444, 2011.

[38] Abigail S Haka, Zoya Volynskaya, Joseph A Gardecki, Jon Nazemi, Joanne Lyons, David Hicks, Maryann Fitzmaurice, Ramachandra R Dasari, Joseph P Crowe, and Michael S Feld. In vivo margin assessment during partial mastectomy breast surgery using raman spectroscopy [? q1: Running head: Raman margin assessment at partial mastectomy. short title ok? q1]. *Cancer Research*, 66(6):3317–3322, 2006.

[39] RG Pleijhuis, GC Langhout, Wijnand Helfrich, George Themelis, A Sarantopoulos, LMA Crane, NJ Harlaar, JS De Jong, V Ntziachristos, and GM Van Dam. Near-infrared fluorescence (nirf) imaging in breast-conserving surgery: assessing intraoperative techniques in tissue-simulating breast phantoms. *European Journal of Surgical Oncology (EJSO)*, 37(1):32–39, 2011.

[40] FJ Fleming, ADK Hill, EW Mc Dermott, A O'Doherty, NJ O'Higgins, and CM Quinn. Intraoperative margin assessment and re-excision rate in breast conserving surgery. *European Journal of Surgical Oncology (EJSO)*, 30(3):233–237, 2004.

[41] V Suzanne Klimberg. Advances in the diagnosis and excision of breast cancer. *The American Surgeon*, 69(1):11–14, 2003.

[42] N Biglia, VE Bounous, L Martincich, E Panuccio, V Liberale, L Ottino, R Ponzone, and P Sismondi. Role of mri (magnetic resonance imaging) versus conventional imaging for breast cancer presurgical staging in young women or with dense breast. *European Journal of Surgical Oncology (EJSO)*, 37(3):199–204, 2011.

[43] Matthias Benndorf, Pascal AT Baltzer, Tibor Vag, Mieczyslaw Gajda, Ingo B Runnebaum, and Werner A Kaiser. Breast mri as an adjunct to mammography: Does it really suffer from low specificity? a retrospective analysis stratified by mammographic bi-rads classes. *Acta Radiologica*, 51(7):715–721, 2010.

[44] Paul C Stomper, Janet S Winston, Steven Herman, Donald L Klippenstein, Mark A Arredondo, and Leslie E Blumenson. Angiogenesis and dynamic mr imaging gadolinium enhancement of malignant and benign breast lesions. *Breast cancer research and treatment*, 45(1):39–46, 1997.

[45] Melissa A Mallory, Yasuaki Sagara, Fatih Aydogan, Stephen DeSantis, Jagadeesan Jayender, Diana Caragacianu, Eva Gombos, Kirby G Vosburgh, Ferenc A Jolesz, and Mehra Golshan. Feasibility of intraoperative breast mri and the role of prone versus supine positioning in surgical planning for breast-conserving surgery. *The Breast Journal*, 2017.

[46] Matthew J Pallone, Steven P Poplack, Hima Bindu R Avutu, Keith D Paulsen, and Richard J Barth Jr. Supine breast mri and 3d optical scanning: A novel approach to improve tumor localization for breast conserving surgery. *Annals of surgical oncology*, pages 1–6, 2014.

[47] Hiroko Satake, Satoko Ishigaki, Mariko Kitano, and Shinji Naganawa. Prediction of prone-to-supine tumor displacement in the breast using patient position change: investigation with prone mri and supine ct. *Breast Cancer*, pages 1–10, 2014.

[48] Luca Alessandro Carbonaro, Penampai Tannaphai, Rubina Manuela Trimboli, Nicola Verardi, Maria Paola Fedeli, and Francesco Sardanelli. Contrast enhanced breast mri: spatial displacement from prone to supine patient's position. preliminary results. *European journal of radiology*, 81(6):e771–e774, 2012.

[49] Mitsuhiro Tozaki and Kunihiko Fukuda. Supine mr mammography using vibe with parallel acquisition technique for the planning of breast-conserving surgery: clinical feasibility. *The Breast*, 15(1):137–140, 2006.

[50] Masahiro Sakakibara, Takeshi Nagashima, Takafumi Sangai, Rikiya Nakamura, Hiroshi Fujimoto, Manabu Arai, Toshiki Kazama, Hideyuki Hashimoto, Yukio Nakatani, and Masaru Miyazaki. Breast-conserving surgery using projection and reproduction techniques of surgical-position breast mri in patients with ductal carcinoma in situ of the breast. *Journal of the American College of Surgeons*, 207(1):62–68, 2008.

[51] Norie Yamashiro, Mitsuhiro Tozaki, Tomoko Ogawa, Naoko Kawano, Takako Suzuki, Shinji Ozaki, Naomi Sakamoto, Satoko Abe, and Eisuke Fukuma. Preoperative mri marking technique for the planning of breast-conserving surgery. *Breast Cancer*, 16(3):223–228, 2009.

[52] M Abe, T Kiryu, K Sonoda, and Y Kashiki. Magnetic resonance imaging-guided navigation with a thermoplastic shell for breast-conserving surgery. *European Journal of Surgical Oncology (EJSO)*, 37(11):950–955, 2011.

[53] Timothy Carter, Christine Tanner, Nicolas Beechey-Newman, Dean Barratt, and David Hawkes. Mr navigated breast surgery: method and initial clinical experience. In *Medical Image Computing and Computer-Assisted Intervention–MICCAI 2008*, pages 356–363. Springer, 2008.

[54] Tanja Alderliesten, Claudette Loo, Anita Paape, Sara Muller, Emiel Rutgers, Marie-Jeanne Vrancken Peeters, and Kenneth Gilhuijs. On the feasibility of mri-guided navigation to demarcate breast cancer for breast-conserving surgery. *Medical physics*, 37(6):2617–2626, 2010.

[55] Mehran Ebrahimi, Peter Siegler, Amen Modhafar, Claire MB Holloway, Donald B Plewes, and Anne L Martel. Using surface markers for mri guided breast conserving surgery: a feasibility survey. *Physics in medicine and biology*, 59(7):1589, 2014.

[56] M.D. Barber, J.S.J. Thomas, and J.M. Dixon. *Breast Cancer: An Atlas of Investigation and Management*. Atlases of Investigation and Management. Clinical Publishing Services, 2008. ISBN 9781904392958.

[57] Robert A Smith, Deana Manassaram-Baptiste, Durado Brooks, Vilma Cokkinides, Mary Doroshenk, Debbie Saslow, Richard C Wender, and Otis W Brawley. Cancer screening in the united states, 2014: a review of current american cancer society guidelines and current issues in cancer screening. *CA: a cancer journal for clinicians*, 64(1):30–51, 2014.

[58] Therese B Bevers, Benjamin O Anderson, Ermelinda Bonaccio, Sandra Buys, Mary B Daly, Peter J Dempsey, William B Farrar, Irving Fleming, Judy E Garber, Randall E Harris, et al. Breast cancer screening and diagnosis. *Journal of the National Comprehensive Cancer Network*, 7(10):1060–1096, 2009.

[59] Carol H Lee, D David Dershaw, Daniel Kopans, Phil Evans, Barbara Monsees, Debra Monticciolo, R James Brenner, Lawrence Bassett, Wendie Berg, Stephen Feig, et al. Breast cancer screening with imaging: recommendations from the society of breast imaging and the acr on the use of mammography, breast mri, breast ultrasound, and other technologies for the detection of clinically occult breast cancer. *Journal of the American college of radiology*, 7(1):18–27, 2010.

[60] JA Pain, SR Ebbs, RP Hern, S Lowe, and JW Bradbeer. Assessment of breast cancer size: a comparison of methods. *European journal of surgical oncology: the journal of the European Society of Surgical Oncology and the British Association of Surgical Oncology*, 18(1):44–48, 1992.

[61] Christiane K Kuhl, Simone Schrading, Claudia C Leutner, Nuschin Morakkabati-Spitz, Eva Wardelmann, Rolf Fimmers, Walther Kuhn, and Hans H Schild. Mammography, breast ultrasound, and magnetic resonance imaging for surveillance of women at high familial risk for breast cancer. *Journal of clinical oncology*, 23(33):8469–8476, 2005.

[62] MARIBS Study Group et al. Screening with magnetic resonance imaging and mammography of a uk population at high familial risk of breast cancer: a prospective multicentre cohort study (maribs). *The Lancet*, 365(9473):1769–1778, 2005.

[63] C Kuhl, W Kuhn, M Braun, and H Schild. Pre-operative staging of breast cancer with breast mri: one step forward, two steps back? *The breast*, 16:34–44, 2007.

[64] Nehmat Houssami, Stefano Ciatto, Petra Macaskill, Sarah J Lord, Ruth M Warren, J Michael Dixon, and Les Irwig. Accuracy and surgical impact of magnetic resonance imaging in breast cancer staging: systematic review and meta-analysis in detection of multifocal and multicentric cancer. *Journal of Clinical Oncology*, 26(19):3248–3258, 2008.

[65] Riham H El Khouli, Michael A Jacobs, and Katarzyna J Macura. Breast mri for diagnosis and staging of breast cancer. In *Breast Cancer Screening and Diagnosis*, pages 181–200. Springer, 2015.

[66] Christiane Katharina Kuhl, Peter Mielcareck, Sven Klaschik, Claudia Leutner, Eva Wardelmann, Jurgen Gieseke, and Hans H Schild. Dynamic breast mr imaging: Are signal intensity time course data useful for differential diagnosis of enhancing lesions? 1. *Radiology*, 211(1):101–110, 1999.

[67] Alan Jackson, James PB O'Connor, Geoff JM Parker, and Gordon C Jayson. Imaging tumor vascular heterogeneity and angiogenesis using dynamic contrast-enhanced magnetic resonance imaging. *Clinical Cancer Research*, 13(12):3449–3459, 2007.

[68] James PB O'Connor, Alan Jackson, Geoff JM Parker, and Gordon C Jayson. Dce-mri biomarkers in the clinical evaluation of antiangiogenic and vascular disrupting agents. *British journal of cancer*, 96(2):189–195, 2007.

[69] Gunnar Brix, Wolfhard Semmler, Rüdiger Port, Lothar R Schad, Günter Layer, and Walter J Lorenz. Pharmacokinetic parameters in cns gd-dtpa enhanced mr imaging. *Journal of computer assisted tomography*, 15(4):621–628, 1991.

[70] Thomas E Yankeelov, Jeffrey J Luci, Martin Lepage, Rui Li, Laura Debusk, P Charles Lin, Ronald R Price, and John C Gore. Quantitative pharmacokinetic analysis of dce-mri data without an arterial input function: a reference region model. *Magnetic resonance imaging*, 23(4):519–529, 2005.

[71] Sarah A Englander, Aziz M Ulug, Rachel Brem, Jerry D Glickson, and Peter van Zilj. Diffusion imaging of human breast. *NMR in Biomedicine*, 10(7):348–352, 1997.

[72] Yong Guo, You-Quan Cai, Zu-Long Cai, Yuan-Gui Gao, Ning-Yu An, Lin Ma, Srikanth Mahankali, and Jia-Hong Gao. Differentiation of clinically benign and malignant breast lesions using diffusion-weighted imaging. *Journal of magnetic resonance imaging*, 16(2):172–178, 2002.

[73] Reiko Woodhams, Keiji Matsunaga, Shinichi Kan, Hirofumi Hata, Masanori OZAKI, Keiichi IWABUCHI, Masaru KURANAMI, Masahiko WATANABE, and Kazushige HAYAKAWA. Adc mapping of benign and malignant breast tumors. *Magnetic resonance in medical sciences*, 4(1): 35–42, 2005.

[74] Mi Jung Park, Eun Suk Cha, Bong Joo Kang, Yon Kwon Ihn, and Jun Hyun Baik. The role of diffusion-weighted imaging and the apparent diffusion coefficient (adc) values for breast tumors. *Korean journal of radiology*, 8(5):390–396, 2007.

[75] Riham H EI Khouli, Michael A Jacobs, Sarah D Mezban, Peng Huang, Ihab R Kamel, Katarzyna J Macura, and David A Bluemke. Diffusion-weighted imaging improves the diagnostic accuracy of conventional 3.0-t breast mr imaging 1. *Radiology*, 256(1):64–73, 2010.

[76] Lisa A Newman and Eleftherios P Mamounas. Review of breast cancer clinical trials conducted by the national surgical adjuvant breast project. *Surgical Clinics of North America*, 87(2):279–305, 2007.

[77] William S Halsted. I. a clinical and histological study of certain adenocarcinomata of the breast: and a brief consideration of the supraclavicular operation and of the results of operations for cancer of the breast from 1889 to 1898 at the johns hopkins hospital. *Annals of surgery*, 28(5): 557, 1898.

[78] Dalliah M Black and Elizabeth A Mittendorf. Landmark trials affecting the surgical management of invasive breast cancer. *Surgical Clinics of North America*, 93(2):501–518, 2013.

[79] Umberto Veronesi, Natale Cascinelli, Luigi Mariani, Marco Greco, Roberto Saccozzi, Alberto Luini, Marisel Aguilar, and Ettore Marubini. Twenty-year follow-up of a randomized study comparing breast-conserving surgery with radical mastectomy for early breast cancer. *New England Journal of Medicine*, 347(16):1227–1232, 2002.

[80] Bernard Fisher, Stewart Anderson, John Bryant, Richard G Margolese, Melvin Deutsch, Edwin R Fisher, Jong-Hyeon Jeong, and Norman Wolmark. Twenty-year follow-up of a randomized trial comparing total mastectomy, lumpectomy, and lumpectomy plus irradiation for the treatment of invasive breast cancer. *New England Journal of Medicine*, 347(16):1233–1241, 2002.

[81] Edwin R Fisher, James Dignam, Elizabeth Tan-Chiu, Joseph Costantino, Bernard Fisher, Soonmyung Paik, and Norman Wolmark. Pathologic findings from the national surgical adjuvant breast project (nsabp) eight-year update of protocol b-17. *Cancer*, 86(3):429–438, 1999.

[82] Nina Bijker, Philip Meijnen, Johannes L Peterse, Jan Bogaerts, Irène Van Hoorebeeck, Jean-Pierre Julien, Massimiliano Gennaro, Philippe Rouanet, Antoine Avril, Ian S Fentiman, et al. Breast-conserving treatment with or without radiotherapy in ductal carcinoma-in-situ: ten-year results of european organisation for research and treatment of cancer randomized phase iii trial 10853a study by the eortc breast cancer cooperative group and eortc radiotherapy group. *Journal of Clinical Oncology*, 24(21):3381–3387, 2006.

[83] Charles E Cox, Adela Fernandez, Evan Tummel, Richard Betzold, Wei Wei Zhang, Vanessa Prowler, John Chipko, Michelle Jung, Michelle Vice, and Steven C Shivers. Breast-conserving therapy for breast cancer. In *Breast Disease*, pages 199–214. Springer, 2015.

[84] CF Margaret, HH Alden, CM Townsend, RD Beauchamp, BM Evers, and KL Mattox. Sabiston textbook of surgery: the biological basis of modern surgical practice. 2012.

[85] Monica Morrow, Julia White, Jennifer Moughan, Jean Owen, Thomas Pajack, JoAnne Sylvester, J Frank Wilson, and David Winchester. Factors predicting the use of breast-conserving therapy in stage i and ii breast carcinoma. *Journal of Clinical Oncology*, 19(8):2254–2262, 2001.

[86] Maryam Parviz, Jay Brian Cassel, Brian J Kaplan, Stephen E Karp, James P Neifeld, Lynne T Penberthy, and Harry D Bear. Breast conservation therapy rates are no different in medically indigent versus insured patients with early stage breast cancer. *Journal of surgical oncology*, 84 (2):57–62, 2003.

[87] Donald J Lucas, Jennifer Sabino, Craig D Shriver, Timothy M Pawlik, Devinder P Singh, and Amy E Vertrees. Doing more: Trends in breast cancer surgery, 2005 to 2011. *The American Surgeon*, 81(1):74–80, 2015.

[88] Carla S Fisher, Tonya Martin-Dunlap, Megan Baker Ruppel, Feng Gao, Jordan Atkins, and Julie A Margenthaler. Fear of recurrence and perceived survival benefit are primary motivators for choosing mastectomy over breast-conservation therapy regardless of age. *Annals of surgical oncology*, 19(10):3246–3250, 2012.

[89] R Joseph Nold, R Larry Beamer, Stephen D Helmer, and Marilee F McBoyle. Factors influencing a womans choice to undergo breast-conserving surgery versus modified radical mastectomy. *The American journal of surgery*, 180(6):413–418, 2000.

[90] E Dale Collins, Caroline P Moore, Kate F Clay, Stephen A Kearing, Annette M O'Connor, Hilary A Llewellyn-Thomas, Richard J Barth, and Karen R Sepucha. Can women with early-stage breast cancer make an informed decision for mastectomy? *Journal of Clinical Oncology*, 27(4):519–525, 2009.

[91] Cameron D Adkisson, Laura A Vallow, Kristin Kowalchik, Rebecca McNeil, Stephanie Hines, Elizabeth Deperi, Alvaro Moreno, Vivek Roy, Edith A Perez, and Sarah A McLaughlin. Patient age and preoperative breast mri in women with breast cancer: biopsy and surgical implications. *Annals of surgical oncology*, 18(6):1678–1683, 2011.

[92] Elizabeth Lokich, Ashley Stuckey, Christina Raker, Jennifer Scalia Wilbur, Jessica Laprise, and Jennifer Gass. Preoperative genetic testing affects surgical decision making in breast cancer patients. *Gynecologic oncology*, 134(2):326–330, 2014.

[93] Rajini Katipamula, Amy C Degnim, Tanya Hoskin, Judy C Boughey, Charles Loprinzi, Clive S Grant, Kathleen R Brandt, Sandhya Pruthi, Christopher G Chute, Janet E Olson, et al. Trends in mastectomy rates at the mayo clinic rochester: effect of surgical year and preoperative magnetic resonance imaging. *Journal of Clinical Oncology*, 27(25):4082–4088, 2009.

[94] Elizabeth B Habermann, Andrea Abbott, Helen M Parsons, Beth A Virnig, Waddah B Al-Refaie, and Todd M Tuttle. Are mastectomy rates really increasing in the united states? *Journal of Clinical Oncology*, 28(21):3437–3441, 2010.

[95] Colleen M O'Kelly Priddy, Victoria A Forte, and Julie E Lang. The importance of surgical margins in breast cancer. *Journal of surgical oncology*, 2015.

[96] Oriana Petruolo and Monica Morrow. New guidelines on the adequacy of lumpectomy margin width in patients with ductal carcinoma in situ. *Current Breast Cancer Reports*, pages 1–7.

[97] TP Olson, J Harter, A Munoz, DM Mahvi, and TM Breslin. Frozen section analysis for intraoperative margin assessment during breast-conserving surgery results in low rates of re-excision and local recurrence. *Annals of Surgical Oncology*, 14(10):2953–2960, 2007.

[98] K Motomura, H Inaji, Y Komoike, T Kasugai, S Nagumo, S Noguchi, and H Koyama. Intraoperative sentinel lymph node examination by imprint cytology and frozen sectioning during breast surgery. *British journal of surgery*, 87(5):597–601, 2000.

[99] PJ Van Diest, H Torrenga, PJ Borgstein, R Pijpers, RP Bleichrodt, FD Rahusen, and S Meijer. Reliability of intraoperative frozen section and imprint cytological investigation of sentinel lymph nodes in breast cancer. *Histopathology*, 35(1):14–18, 1999.

[100] CH Lee and D Carter. Detecting residual tumor after excisional biopsy of impalpable breast carcinoma: efficacy of comparing preoperative mammograms with radiographs of the biopsy specimen. *AJR. American journal of roentgenology*, 164(1):81–86, 1995.

[101] Fabio Corsi, Luca Sorrentino, Matteo Bonzini, Daniela Bossi, Marta Truffi, Rosella Amadori, Manuela Nebuloni, Barbara Brillat, and Serena Mazzucchelli. Cavity shaving reduces involved margins and reinterventions without increasing costs in breast-conserving surgery: A propensity score-matched study. *Annals of surgical oncology*, pages 1–9, 2017.

[102] Lorraine Tafra, Richard Fine, Pat Whitworth, Michael Berry, James Woods, Gregory Ekbom, Jennifer Gass, Peter Beitsch, Daleela Dodge, Linda Han, et al. Prospective randomized study comparing cryo-assisted and needle-wire localization of ultrasound-visible breast tumors. *The American journal of surgery*, 192(4):462–470, 2006.

[103] Hernan O Altamar, Rowena E Ong, Courtenay L Glisson, Davis P Viprakasit, Michael I Miga, Stanley Duke Herrell, and Robert L Galloway. Kidney deformation and intraprocedural registration: a study of elements of image-guided kidney surgery. *Journal of Endourology*, 25(3): 511–517, 2011.

[104] Timothy J Carter, Maxime Sermesant, David M Cash, Dean C Barratt, Christine Tanner, and David J Hawkes. Application of soft tissue modelling to image-guided surgery. *Medical engineering & physics*, 27(10):893–909, 2005.

[105] William C Chapman and Robert L Galloway. Image-guided liver surgery. In *Intraoperative Imaging and Image-Guided Therapy*, pages 779–788. Springer, 2014.

[106] Michael I Miga, Keith D Paulsen, John M Lemery, Symma D Eisner, Alexander Hartov, Francis E Kennedy, and David W Roberts. Model-updated image guidance: initial clinical experiences with gravity-induced brain deformation. In *Biomedical Imaging, 2002. 5th IEEE EMBS International Summer School on*, pages 9–pp. IEEE, 2002.

[107] Olivier Clatz, Hervé Delingette, I-F Talos, Alexandra J Golby, Ron Kikinis, Ferenc A Jolesz, Nicholas Ayache, and Simon K Warfield. Robust nonrigid registration to capture brain shift from intraoperative mri. *Medical Imaging, IEEE Transactions on*, 24(11):1417–1427, 2005.

[108] David W Roberts, Alexander Hartov, Francis E Kennedy, Michael I Miga, and Keith D Paulsen. Intraoperative brain shift and deformation: a quantitative analysis of cortical displacement in 28 cases. *Neurosurgery*, 43(4):749–758, 1998.

[109] Simon K Warfield, Florin Talos, Alida Tei, Aditya Bharatha, Arya Nabavi, Matthieu Ferrant, Peter McL Black, Ferenc A Jolesz, and Ron Kikinis. Real-time registration of volumetric brain mri by biomechanical simulation of deformation during image guided neurosurgery. *Computing and Visualization in Science*, 5(1):3–11, 2002.

[110] Alan J Herline, James D Stefansic, Jacob P Debelak, Steven L Hartmann, C Wright Pinson, Robert L Galloway, and William C Chapman. Image-guided surgery: preliminary feasibility studies of frameless stereotactic liver surgery. *Archives of Surgery*, 134(6):644–650, 1999.

[111] Peter H Schönemann. A generalized solution of the orthogonal procrustes problem. *Psychometrika*, 31(1):1–10, 1966.

[112] Alan J Herline, Jeannette L Herring, James D Stefansic, William C Chapman, Robert L Galloway, and Benoit M Dawant. Surface registration for use in interactive, image-guided liver surgery. *Computer Aided Surgery*, 5(1):11–17, 2000.

[113] Michael I Miga, Tuhin K Sinha, David M Cash, Robert L Galloway, and Robert J Weil. Cortical surface registration for image-guided neurosurgery using laser-range scanning. *Medical Imaging, IEEE Transactions on*, 22(8):973–985, 2003.

[114] Thomas Lange, Nils Papenberg, Stefan Heldmann, Jan Modersitzki, Bernd Fischer, Hans Lamecker, and Peter M Schlag. 3d ultrasound-ct registration of the liver using combined landmark-intensity information. *International journal of computer assisted radiology and surgery*, 4(1):79–88, 2009.

[115] Ingerid Reinertsen, Maxime Descoteaux, Kaleem Siddiqi, and D Louis Collins. Validation of vessel-based registration for correction of brain shift. *Medical image analysis*, 11(4):374–388, 2007.

[116] Songbai Ji, Ziji Wu, Alex Hartov, David W Roberts, and Keith D Paulsen. Mutual-information-based image to patient re-registration using intraoperative ultrasound in image-guided neurosurgery. *Medical physics*, 35(10):4612–4624, 2008.

[117] Marloes Maria Johanna Letteboer, Peter WA Willems, Max A Viergever, and Wiro J Niessen. Brain shift estimation in image-guided neurosurgery using 3-d ultrasound. *Biomedical Engineering, IEEE Transactions on*, 52(2):268–276, 2005.

[118] Paul J Besl and Neil D McKay. Method for registration of 3-d shapes. In *Robotics-DL tentative*, pages 586–606. International Society for Optics and Photonics, 1992.

[119] Szymon Rusinkiewicz and Marc Levoy. Efficient variants of the icp algorithm. In *3-D Digital Imaging and Modeling, 2001. Proceedings. Third International Conference on*, pages 145–152. IEEE, 2001.

[120] Gregory C Sharp, Sang W Lee, and David K Wehe. Icp registration using invariant features. *Pattern Analysis and Machine Intelligence, IEEE Transactions on*, 24(1):90–102, 2002.

[121] Logan W Clements, William C Chapman, Benoit M Dawant, Robert L Galloway Jr, and Michael I Miga. Robust surface registration using salient anatomical features for image-guided liver surgery: algorithm and validation. *Medical physics*, 35(6):2528–2540, 2008.

[122] Michael I Miga, David W Roberts, Francis E Kennedy, Leah A Platenik, Alex Hartov, Karen E Lunn, and Keith D Paulsen. Modeling of retraction and resection for intraoperative updating of images. *Neurosurgery*, 49(1):75–85, 2001.

[123] David M Cash, Michael I Miga, Sean C Glasgow, Benoit M Dawant, Logan W Clements, Zhujiang Cao, Robert L Galloway, and William C Chapman. Concepts and preliminary data toward the realization of image-guided liver surgery. *Journal of Gastrointestinal Surgery*, 11(7):844–859, 2007.

[124] Aditya Bharatha, Masanori Hirose, Nobuhiko Hata, Simon K Warfield, Matthieu Ferrant, Kelly H Zou, Eduardo Suarez-Santana, Juan Ruiz-Alzola, Anthony D'amico, Robert A Cormack, et al. Evaluation of three-dimensional finite element-based deformable registration of pre-and intraoperative prostate imaging. *Medical physics*, 28(12):2551–2560, 2001.

[125] Daniel R Lynch. *Numerical partial differential equations for environmental scientists and engineers: a first practical course*. Springer Science & Business Media, 2005.

[126] Joachim Georgii and Rüdiger Westermann. Corotated finite elements made fast and stable. *VRIPHYS*, 8:11–19, 2008.

[127] Christian Dick, Joachim Georgii, and Rüdiger Westermann. A real-time multigrid finite hexahedra method for elasticity simulation using cuda. *Simulation Modelling Practice and Theory*, 19 (2):801–816, 2011.

[128] Joachim Georgii, Maximilian Eder, Kai Burger, Sebastian Klotz, Florian Ferstl, Laszlo Kovacs, and Rudiger Westermann. A computational tool for preoperative breast augmentation planning in aesthetic plastic surgery. *IEEE journal of biomedical and health informatics*, 18(3):907–919, 2014.

[129] Fred S Azar, Dimitris N Metaxas, and Mitchell D Schnall. A deformable finite element model of the breast for predicting mechanical deformations under external perturbations. *Academic Radiology*, 8(10):965–975, 2001.

[130] NV Ruiter. Registration of x–ray mammograms and mr–volumes of the female breast based on simulated mammographic deformation. *Universitat Mannheim: Mannheim*, page 153, 2003.

[131] Abbas Samani, Jonathan Bishop, Martin J Yaffe, and Donald B Plewes. Biomechanical 3-d finite element modeling of the human breast using mri data. *Medical Imaging, IEEE Transactions on*, 20(4):271–279, 2001.

[132] Pras Pathmanathan, David Gavaghan, Jonathan Whiteley, Michael Brady, Martyn Nash, Poul Nielsen, and Vijay Rajagopal. Predicting tumour location by simulating large deformations of the breast using a 3d finite element model and nonlinear elasticity. In *Medical Image Computing and Computer-Assisted Intervention–MICCAI 2004*, pages 217–224. Springer, 2004.

[133] Donald B Plewes, Jonathan Bishop, Abbas Samani, and Justin Sciarretta. Visualization and quantification of breast cancer biomechanical properties with magnetic resonance elastography. *Physics in medicine and biology*, 45(6):1591, 2000.

[134] JJ Ou, RE Ong, TE Yankeelov, and MI Miga. Evaluation of 3d modality-independent elastography for breast imaging: a simulation study. *Physics in Medicine and Biology*, 53(1):147, 2008.

[135] Lianghao Han, John H Hipwell, Björn Eiben, Dean Barratt, Marc Modat, Sebastien Ourselin, and David J Hawkes. A nonlinear biomechanical model based registration method for aligning prone and supine mr breast images. *Medical Imaging, IEEE Transactions on*, 33(3):682–694, 2014.

[136] Lianghao Han, John Hipwell, Thomy Mertzanidou, Tim Carter, Marc Modat, Sébastien Ourselin, and David Hawkes. A hybrid fem-based method for aligning prone and supine images for image guided breast surgery. In *Biomedical Imaging: From Nano to Macro, 2011 IEEE International Symposium on*, pages 1239–1242. IEEE, 2011.

[137] Björn Eiben, Lianghao Han, J Hipwell, Thomy Mertzanidou, Sven Kabus, Thomas Bülow, Cristian Lorenz, GM Newstead, Hiroyuki Abe, Mohammed Keshtgar, et al. Biomechanically guided prone-to-supine image registration of breast mri using an estimated reference state. In *Biomedical Imaging (ISBI), 2013 IEEE 10th International Symposium on*, pages 214–217. IEEE, 2013.

[138] Timothy J Carter, Christine Tanner, William R Crum, Nicolas Beechey-Newman, and David J Hawkes. A framework for image-guided breast surgery. In *Medical Imaging and Augmented Reality*, pages 203–210. Springer, 2006.

[139] Vijay Rajagopal, Martyn P Nash, Ralph P Highnam, and Poul MF Nielsen. The breast biomechanics reference state for multi-modal image analysis. In *Digital Mammography*, pages 385–392. Springer, 2008.

[140] TJ Carter, C Tanner, WR Crum, and DJ Hawkes. Biomechanical model initialized non-rigid registration for image-guided breast surgery. *Computational biomechanics for medicine*, page 104, 2006.

[141] Armen Sarvazyan, Timothy J Hall, Matthew W Urban, Mostafa Fatemi, Salavat R Aglyamov, and Brian S Garra. An overview of elastography-an emerging branch of medical imaging. *Current medical imaging reviews*, 7(4):255–282, 2011.

[142] Vinay Swaminathan, Karthikeyan Mythreye, E Tim O'Brien, Andrew Berchuck, Gerard C Blobe, and Richard Superfine. Mechanical stiffness grades metastatic potential in patient tumor cells and in cancer cell lines. *Cancer research*, 71(15):5075–5080, 2011.

[143] Vijay Rajagopal, Angela Lee, Jae-Hoon Chung, Ruth Warren, Ralph P Highnam, Martyn P Nash, and Poul MF Nielsen. Creating individual-specific biomechanical models of the breast for medical image analysis. *Academic Radiology*, 15(11):1425–1436, 2008.

[144] M Kuhlmann, EC Fear, A Ramirez-Serrano, and S Federico. Mechanical model of the breast for the prediction of deformation during imaging. *Medical engineering & physics*, 35(4):470–478, 2013.

[145] JH Chung, V Rajagopal, P MF Nielsen, and MP Nash. A biomechanical model of mammographic compressions. *Biomechanics and modeling in mechanobiology*, 7(1):43–52, 2008.

[146] Jae-Hoon Chung, Vijay Rajagopal, Tod A Laursen, Poul MF Nielsen, and Martyn P Nash. Frictional contact mechanics methods for soft materials: application to tracking breast cancers. *Journal of biomechanics*, 41(1):69–77, 2008.

[147] Julia A Schnabel, Christine Tanner, Andy D Castellano-Smith, Andreas Degenhard, Martin O Leach, D Rodney Hose, Derek LG Hill, and David J Hawkes. Validation of nonrigid image registration using finite-element methods: application to breast mr images. *IEEE transactions on medical imaging*, 22(2):238–247, 2003.

[148] Sarthak Misra, KT Ramesh, and Allison M Okamura. Modeling of tool-tissue interactions for computer-based surgical simulation: A literature review. *Presence: Teleoperators and Virtual Environments*, 17(5):463–491, 2008.

[149] Laurence Vancamberg, Anis Sahbani, Serge Muller, and Guillaume Morel. Needle path planning method for digital breast tomosynthesis biopsy based on probabilistic techniques. *Digital Mammography*, pages 15–22, 2010.

[150] A Pérez Del Palomar, B Calvo, J Herrero, J López, and M Doblaré. A finite element model to accurately predict real deformations of the breast. *Medical engineering & physics*, 30(9): 1089–1097, 2008.

[151] Pablo de Heras Ciechomski, Mihai Constantinescu, Jaime Garcia, Radu Olariu, Irving Dindoyal, Serge Le Huu, and Mauricio Reyes. Development and implementation of a web-enabled 3d consultation tool for breast augmentation surgery based on 3d-image reconstruction of 2d pictures. *Journal of medical Internet research*, 14(1):e21, 2012.

[152] Liesbet Roose, Wim De Maerteleire, Wouter Mollemans, and Paul Suetens. Validation of different soft tissue simulation methods for breast augmentation. In *International Congress Series*, volume 1281, pages 485–490. Elsevier, 2005.

[153] Björn Eiben, Vasileios Vavourakis, John H Hipwell, Sven Kabus, Thomas Buelow, Cristian Lorenz, Thomy Mertzanidou, Sara Reis, Norman R Williams, Mohammed Keshtgar, et al. Symmetric biomechanically guided prone-to-supine breast image registration. *Annals of biomedical engineering*, 44(1):154–173, 2016.

[154] Rebekah H Conley, Ingrid M Meszoely, Jared A Weis, Thomas S Pheiffer, Lori R Arlinghaus, Thomas E Yankeelov, and Michael I Miga. Realization of a biomechanical model-assisted image guidance system for breast cancer surgery using supine mri. *International journal of computer assisted radiology and surgery*, 10(12):1985–1996, 2015.

[155] Meng Yin, Jayant A Talwalkar, Kevin J Glaser, Armando Manduca, Roger C Grimm, Phillip J Rossman, Jeff L Fidler, and Richard L Ehman. Assessment of hepatic fibrosis with magnetic resonance elastography. *Clinical Gastroenterology and Hepatology*, 5(10):1207–1213, 2007.

[156] Sudhakar K Venkatesh, Meng Yin, James F Glockner, Naoki Takahashi, Philip A Araoz, Jayant A Talwalkar, and Richard L Ehman. Mr elastography of liver tumors: preliminary results. *American Journal of Roentgenology*, 190(6):1534–1540, 2008.

[157] Jeffrey R Basford, Thomas R Jenkyn, Kai-Nan An, Richard L Ehman, Guido Heers, and Kenton R Kaufman. Evaluation of healthy and diseased muscle with magnetic resonance elastography. *Archives of physical medicine and rehabilitation*, 83(11):1530–1536, 2002.

[158] L Xu, Y Lin, JC Han, ZN Xi, H Shen, and PY Gao. Magnetic resonance elastography of brain tumors: preliminary results. *Acta radiologica*, 48(3):327–330, 2007.

[159] Arunark Kolipaka, Philip A Araoz, Kiaran P McGee, Armando Manduca, and Richard L Ehman. Magnetic resonance elastography as a method for the assessment of effective myocardial stiffness throughout the cardiac cycle. *Magnetic resonance in medicine*, 64(3):862–870, 2010.

[160] Yogesh K Mariappan, Kevin J Glaser, and Richard L Ehman. Magnetic resonance elastography: a review. *Clinical anatomy*, 23(5):497–511, 2010.

[161] Nilza G Ramião, Pedro S Martins, Rita Rynkevic, António A Fernandes, Maria Barroso, and Diana C Santos. Biomechanical properties of breast tissue, a state-of-the-art review. *Biomechanics and modeling in mechanobiology*, 15(5):1307–1323, 2016.

[162] Nancy A Lee, Henry Rusinek, Jeffrey Weinreb, Ramesh Chandra, Hildegard Toth, Cory Singer, and Gillian Newstead. Fatty and fibroglandular tissue volumes in the breasts of women 20-83 years old: comparison of x-ray mammography and computer-assisted mr imaging. *AJR. American journal of roentgenology*, 168(2):501–506, 1997.

[163] JÖRN LORENZEN, Ralph Sinkus, Maike Biesterfeldt, and Gerhard Adam. Menstrual-cycle dependence of breast parenchyma elasticity: estimation with magnetic resonance elastography of breast tissue during the menstrual cycle. *Investigative radiology*, 38(4):236–240, 2003.

[164] Baoxian Liu, Yanling Zheng, Guangliang Huang, Manxia Lin, Quanyuan Shan, Ying Lu, Wenshuo Tian, and Xiaoyan Xie. Breast lesions: Quantitative diagnosis using ultrasound shear wave elastographya systematic review and meta-analysis. *Ultrasound in medicine & biology*, 42(4): 835–847, 2016.

[165] Yi Qiu, Yahui Wang, Yiqing Xu, Namas Chandra, James Haorah, Basil Hubbi, Bryan J Pfister, and Xuan Liu. Quantitative optical coherence elastography based on fiber-optic probe for in situ measurement of tissue mechanical properties. *Biomedical optics express*, 7(2):688–700, 2016.

[166] JJ Ou, RE Ong, TE Yankeelov, and MI Miga. Evaluation of 3d modality-independent elastography for breast imaging: a simulation study. *Physics in medicine and biology*, 53(1):147, 2007.

[167] Michael I Miga. A new approach to elastography using mutual information and finite elements. *Physics in Medicine and Biology*, 48(4):467, 2003.

[168] Emre Turgay, Septimiu Salcudean, and Robert Rohling. Identifying the mechanical properties of tissue by ultrasound strain imaging. *Ultrasound in medicine & biology*, 32(2):221–235, 2006.

[169] Marvin M Doyley and Kevin J Parker. Elastography: general principles and clinical applications. *Ultrasound clinics*, 9(1):1–11, 2014.

[170] Douglas M Dumont, Kristy M Walsh, and Brett C Byram. Improving displacement signal-to-noise ratio for low-signal radiation force elasticity imaging using bayesian techniques. *Ultrasound in medicine & biology*, 42(8):1986–1997, 2016.

[171] I Cespedes, J Ophir, H Ponnekanti, and N Maklad. Elastography: elasticity imaging using ultrasound with application to muscle and breast in vivo. *Ultrasonic Imaging*, 15(2):73–88, 1993.

[172] Wei Meng, Guangchen Zhang, Changjun Wu, Guozhu Wu, Yan Song, and Zhaoling Lu. Preliminary results of acoustic radiation force impulse (arfi) ultrasound imaging of breast lesions. *Ultrasound in medicine & biology*, 37(9):1436–1443, 2011.

[173] Liang Zhai, Mark L Palmeri, Richard R Bouchard, Roger W Nightingale, and Kathryn R Nightingale. An integrated indenter-arfi imaging system for tissue stiffness quantification. *Ultrasonic imaging*, 30(2):95–111, 2008.

[174] Richard G Barr and Zheng Zhang. Effects of precompression on elasticity imaging of the breast development of a clinically useful semiquantitative method of precompression assessment. *Journal of Ultrasound in Medicine*, 31(6):895–902, 2012.

[175] Michael I Miga. New approach to elastrograph imaging: modality-independent elastography. In *Medical Imaging 2002*, pages 604–611. International Society for Optics and Photonics, 2002.

[176] Thomas S Pheiffer, Jao J Ou, Rowena E Ong, and Michael I Miga. Automatic generation of boundary conditions using demons nonrigid image registration for use in 3-d modality-independent elastography. *Biomedical Engineering, IEEE Transactions on*, 58(9):2607–2616, 2011.

[177] Chad W Washington and Michael I Miga. Modality independent elastography (mie): A new approach to elasticity imaging. *Medical Imaging, IEEE Transactions on*, 23(9):1117–1128, 2004.

[178] Jao J Ou, Stephanie L Barnes, and Michael I Miga. Application of multi-resolution modality independent elastography for detection of multiple anomalous objects. In *Medical Imaging*, pages 614310–614310. International Society for Optics and Photonics, 2006.

[179] Jared A Weis, Dong K Kim, Thomas E Yankeelov, and Michael I Miga. Validation and reproducibility assessment of modality independent elastography in a pre-clinical model of breast cancer. In *SPIE Medical Imaging*, pages 90381I–90381I. International Society for Optics and Photonics, 2014.

[180] Richard G Abramson, Lori R Arlinghaus, Adrienne N Dula, C Chad Quarles, Ashley M Stokes, Jared A Weis, Jennifer G Whisenant, Eduard Y Chekmenev, Igor Zhukov, Jason M Williams, et al. Mr imaging biomarkers in oncology clinical trials. *Magnetic resonance imaging clinics of North America*, 24(1):11–29, 2016.

[181] Richard G Abramson, Lori R Arlinghaus, Jared A Weis, Xia Li, Adrienne N Dula, Eduard Y Chekmenev, Seth A Smith, Michael I Miga, Vandana G Abramson, and Thomas E Yankeelov. Current and emerging quantitative magnetic resonance imaging methods for assessing and predicting the response of breast cancer to neoadjuvant therapy. *Breast cancer: targets and therapy*, 4:139, 2012.

[182] Jared A Weis, Thomas E Yankeelov, Samantha A Munoz, Rahul A Sastry, Stephanie L Barnes, Lori R Arlinghaus, Xia Li, and Michael I Miga. A consistent pre-clinical/clinical elastography approach for assessing tumor mechanical properties in therapeutic systems. In *SPIE Medical Imaging*, pages 86721F–86721F. International Society for Optics and Photonics, 2013.

[183] Jared A Weis, Allison M Johnsen, Geoffrey E Wile, Thomas E Yankeelov, Richard G Abramson, and Michael I Miga. Development of a diaphragmatic motion-based elastography framework for assessment of liver stiffness. In *SPIE Medical Imaging*, pages 941703–941703. International Society for Optics and Photonics, 2015.

[184] Michael I Miga, Megan P Rothney, and Jao J Ou. Modality independent elastography (mie): Potential applications in dermoscopy. *Medical physics*, 32(5):1308–1320, 2005.

[185] Lianghao Han, John H Hipwell, Christine Tanner, Zeike Taylor, Thomy Mertzanidou, Jorge Cardoso, Sebastien Ourselin, and David J Hawkes. Development of patient-specific biomechanical models for predicting large breast deformation. *Physics in Medicine and Biology*, 57(2):455, 2011.

[186] NHGM Peters, S Van Esser, MAAJ van den Bosch, RK Storm, PW Plaisier, T Van Dalen, SCE Diepstraten, T Weits, PJ Westenend, G Stapper, et al. Preoperative mri and surgical management in patients with nonpalpable breast cancer: the monet–randomised controlled trial. *European journal of cancer*, 47(6):879–886, 2011.

[187] Nicholas Hwang, Dan E Schiller, Pavel Crystal, Ellen Maki, and David R McCready. Magnetic resonance imaging in the planning of initial lumpectomy for invasive breast carcinoma: its effect on ipsilateral breast tumor recurrence after breast-conservation therapy. *Annals of surgical oncology*, 16(11):3000–3009, 2009.

[188] Lindsay Turnbull, Sarah Brown, Ian Harvey, Catherine Olivier, Phil Drew, Vicky Napp, Andrew Hanby, and Julia Brown. Comparative effectiveness of mri in breast cancer (comice) trial: a randomised controlled trial. *The Lancet*, 375(9714):563–571, 2010.

[189] Sheenu Chandwani, Prethibha A George, Michelle Azu, Elisa V Bandera, Christine B Ambrosone, George G Rhoads, and Kitaw Demissie. Role of preoperative magnetic resonance imaging in the surgical management of early-stage breast cancer. *Annals of surgical oncology*, 21(11):3473–3480, 2014.

[190] Lee J McGhan, Nabil Wasif, Richard J Gray, Marina E Giurescu, Victor J Pizzitola, Roxanne Lorans, Idris T Ocal, Chee-Chee H Stucky, and Barbara A Pockaj. Use of preoperative magnetic resonance imaging for invasive lobular cancer: good, better, but maybe not the best? *Annals of surgical oncology*, 17(3):255–262, 2010.

[191] Richard J Bleicher, Robin M Ciocca, Brian L Egleston, Linda Sesa, Kathryn Evers, Elin R Sigurdson, and Monica Morrow. Association of routine pretreatment magnetic resonance imaging with time to surgery, mastectomy rate, and margin status. *Journal of the American College of Surgeons*, 209(2):180–187, 2009.

[192] Virginia Gonzalez, Kerstin Sandelin, Anders Karlsson, Wiveca Åberg, Lars Löfgren, Gabriela Iliescu, Staffan Eriksson, and Brita Arver. Preoperative mri of the breast (pomb) influences primary treatment in breast cancer: A prospective, randomized, multicenter study. *World journal of surgery*, 38(7):1685–1693, 2014.

[193] Janice S Sung, Jie Li, Glenys Da Costa, Sujata Patil, Kimberly J Van Zee, D David Dershaw, and Elizabeth A Morris. Preoperative breast mri for early-stage breast cancer: effect on surgical and long-term outcomes. *American Journal of Roentgenology*, 202(6):1376–1382, 2014.

[194] Laura Esserman, Nola Hylton, Leila Yassa, John Barclay, Steven Frankel, and Edward Sickles. Utility of magnetic resonance imaging in the management of breast cancer: evidence for improved preoperative staging. *Journal of clinical oncology*, 17(1):110–110, 1999.

[195] Uwe Fischer, Olivier Zachariae, Friedemann Baum, Dorit von Heyden, Matthias Funke, and Torsten Liersch. The influence of preoperative mri of the breasts on recurrence rate in patients with breast cancer. *European radiology*, 14(10):1725–1731, 2004.

[196] Michael Braun, Martin Pölcher, Simone Schrading, Oliver Zivanovic, Theresa Kowalski, Uta Flucke, Claudia Leutner, Tong-Wong Park-Simon, Christian Rudlowski, Walther Kuhn, et al. Influence of preoperative mri on the surgical management of patients with operable breast cancer. *Breast cancer research and treatment*, 111(1):179–187, 2008.

[197] Mehra Golshan, Yasuaki Sagara, Barbara Wexelman, Fatih Aydogan, Stephen Desantis, H Elise Min, Kirby Vosburgh, Jayender Jagadeesan, Diana Caragacianu, Eva Gombos, et al. Pilot study to evaluate feasibility of image-guided breast-conserving therapy in the advanced multimodal image-guided operating (amigo) suite. *Annals of surgical oncology*, 21(10):3356–3357, 2014.

[198] Eva C Gombos, Jagadeesan Jayender, Danielle M Richman, Diana L Caragacianu, Melissa A Mallory, Ferenc A Jolesz, and Mehra Golshan. Intraoperative supine breast mr imaging to quantify tumor deformation and detection of residual breast cancer: preliminary results. *Radiology*, 281(3):720–729, 2016.

[199] Paul A Yushkevich, Joseph Piven, Heather Cody Hazlett, Rachel Gimpel Smith, Sean Ho, James C Gee, and Guido Gerig. User-guided 3d active contour segmentation of anatomical structures: significantly improved efficiency and reliability. *Neuroimage*, 31(3):1116–1128, 2006.

[200] William E Lorensen and Harvey E Cline. Marching cubes: A high resolution 3d surface construction algorithm. In *ACM siggraph computer graphics*, volume 21, pages 163–169. ACM, 1987.

[201] WJ Scheroeder and Hoffman WA Auilals. The visualization toolkit user's guide, 2006.

[202] John M Sullivan Jr, Geoffrey Charron, and Keith D Paulsen. A three-dimensional mesh generator for arbitrary multiple material domains. *Finite Elements in Analysis and Design*, 25(3):219–241, 1997.

[203] Thomas S Pheiffer, Amber L Simpson, Brian Lennon, Reid C Thompson, and Michael I Miga. Design and evaluation of an optically-tracked single-ccd laser range scanner. *Medical physics*, 39(2):636–642, 2012.

[204] Diane M Muratore and Robert L Galloway Jr. Beam calibration without a phantom for creating a 3-d freehand ultrasound system. *Ultrasound in medicine & biology*, 27(11):1557–1566, 2001.

[205] Eric N Mortensen and William A Barrett. Intelligent scissors for image composition. In *Proceedings of the 22nd annual conference on Computer graphics and interactive techniques*, pages 191–198, 1995.

[206] Thomas S Pheiffer, Reid C Thompson, Daniel C Rucker, Amber L Simpson, and Michael I Miga. Model-based correction of tissue compression for tracked ultrasound in soft tissue image-guided surgery. *Ultrasound in medicine & biology*, 40(4):788–803, 2014.

[207] Michael Kass, Andrew Witkin, and Demetri Terzopoulos. Snakes: Active contour models. *International journal of computer vision*, 1(4):321–331, 1988.

[208] Paul Viola and William M Wells III. Alignment by maximization of mutual information. *International journal of computer vision*, 24(2):137–154, 1997.

[209] M-P Dubuisson and Anil K Jain. A modified hausdorff distance for object matching. In *Pattern Recognition, 1994. Vol. 1-Conference A: Computer Vision & Image Processing., Proceedings of the 12th IAPR International Conference on*, volume 1, pages 566–568. IEEE, 1994.

[210] Lee R Dice. Measures of the amount of ecologic association between species. *Ecology*, 26(3): 297–302, 1945.

[211] Bernard Fisher, Eleanor Montague, Carol Redmond, Bruce Barton, Donna Borland, Edwin R Fisher, Melvin Deutsch, George Schwarz, Richard Margolese, William Donegan, et al. Comparison of radical mastectomy with alternative treatments for primary breast cancer: a first report of results from a prospective randomized clinical trial. *Cancer*, 39(6):2827–2839, 1977.

[212] Bernard Fisher, Carol Redmond, Roger Poisson, Richard Margolese, Norman Wolmark, Lawrence Wickerham, Edwin Fisher, Melvin Deutsch, Richard Caplan, Yosef Pilch, et al. Eight-year results of a randomized clinical trial comparing total mastectomy and lumpectomy with or without irradiation in the treatment of breast cancer. *New England Journal of Medicine*, 320 (13):822–828, 1989.

[213] Kandace P McGuire, Alfredo A Santillan, Paramjeet Kaur, Tammi Meade, Jateen Parbhoo, Morgan Mathias, Corinne Shamehdi, Michelle Davis, Daniel Ramos, and Charles E Cox. Are mastectomies on the rise? a 13-year trend analysis of the selection of mastectomy versus breast conservation therapy in 5865 patients. *Annals of surgical oncology*, 16(10):2682–2690, 2009.

[214] E Shelley Hwang, Daphne Y Lichtensztajn, Scarlett Lin Gomez, Barbara Fowble, and Christina A Clarke. Survival after lumpectomy and mastectomy for early stage invasive breast cancer. *Cancer*, 119(7):1402–1411, 2013.

[215] Rick G Pleijhuis, Maurits Graafland, Jakob de Vries, Joost Bart, Johannes S de Jong, and Gooitzen M van Dam. Obtaining adequate surgical margins in breast-conserving therapy for patients with early-stage breast cancer: current modalities and future directions. *Annals of surgical oncology*, 16(10):2717–2730, 2009.

[216] CP Behrenbruch, Kostas Marias, Paul Armitage, Niall Moore, Jane Clarke, and JM Brady. Prone-supine breast mri registration for surgical visualisation. In *Medical Image Understanding and Analysis*, 2001.

[217] Milan Sonka and J Michael Fitzpatrick. Handbook of medical imaging(volume 2, medical image processing and analysis). SPIE- The international society for optical engineering, 2000.

[218] Ahmedin Jemal, Freddie Bray, Melissa M Center, Jacques Ferlay, Elizabeth Ward, and David Forman. Global cancer statistics. *CA: a cancer journal for clinicians*, 61(2):69–90, 2011.

[219] Tiffany T Fancher, J Alexander Palesty, Reney Thomas, Tami Healy, Jennifer M Fancher, Chonn Ng, and Stanley J Dudrick. A woman's influence to choose mastectomy as treatment for breast cancer. *Journal of Surgical Research*, 153(1):128–131, 2009.

[220] Cameron D Adkisson, Sanjay P Bagaria, Alexander S Parker, Jillian M Bray, Tammeza Gibson, Colleen S Thomas, Michael G Heckman, and Sarah A McLaughlin. Which eligible breast conservation patients choose mastectomy in the setting of newly diagnosed breast cancer? *Annals of surgical oncology*, 19(4):1129–1136, 2012.

[221] Frédéric Buxant, F Scuotto, Nathalie Hottat, Jean Christophe Noël, and Philippe Simon. Does preoperative magnetic resonance imaging modify breast cancer surgery? *Acta chirurgica Belgica*, 107(3):288, 2007.

[222] Lianghao Han, J.H. Hipwell, B. Eiben, D. Barratt, M. Modat, S. Ourselin, and D.J. Hawkes. A nonlinear biomechanical model based registration method for aligning prone and supine mr breast images. *Medical Imaging, IEEE Transactions on*, 33(3):682–694, March 2014.

[223] Peter Siegler, Claire Holloway, Petrina Causer, Gilbert Thevathasan, and Donald B Plewes. Supine breast mri. *Journal of Magnetic Resonance Imaging*, 34(5):1212–1217, 2011.

[224] Rebekah H Conley, Ingrid M Meszoely, Thomas S Pheiffer, Jared A Weis, Thomas E Yankeelov, and Michael I Miga. Image to physical space registration of supine breast mri for image guided breast surgery. In *SPIE Medical Imaging*, pages 90362N–90362N. International Society for Optics and Photonics, 2014.

[225] Neil D Glossop. Advantages of optical compared with electromagnetic tracking. *The Journal of Bone & Joint Surgery*, 91(Supplement_1):23–28, 2009.

[226] D.C. Rucker, Yifei Wu, L.W. Clements, J.E. Ondrake, T.S. Pheiffer, A.L. Simpson, W.R. Jarnagin, and M.I. Miga. A mechanics-based nonrigid registration method for liver surgery using sparse intraoperative data. *Medical Imaging, IEEE Transactions on*, 33(1):147–158, Jan 2014.

[227] Solveig Hofvind, Barbro F Iversen, Liv Eriksen, Bodil M Styr, Kjell Kjellevold, and Kathinka D Kurz. Mammographic morphology and distribution of calcifications in ductal carcinoma in situ diagnosed in organized screening. *Acta radiologica*, 52(5):481–487, 2011.

[228] Laurence Vancamberg, Anis Sahbani, Serge Muller, and Guillaume Morel. Needle path planning for digital breast tomosynthesis biopsy using a heterogeneous model. In *Robotics and Automation (ICRA), 2011 IEEE International Conference on*, pages 5749–5755. IEEE, 2011.

[229] Fred S Azar, Dimitris N Metaxas, and Mitchell D Schnall. Methods for modeling and predicting mechanical deformations of the breast under external perturbations. *Medical Image Analysis*, 6 (1):1–27, 2002.

[230] Babarenda Gamage, P Thiranja, Vijayaraghavan Rajagopal, Matthias Ehrgott, Martyn P Nash, and Poul MF Nielsen. Identification of mechanical properties of heterogeneous soft bodies using gravity loading. *International journal for numerical methods in biomedical engineering*, 27(3): 391–407, 2011.

[231] Timothy J Carter, Christine Tanner, and David J Hawkes. Determining material properties of the breast for image-guided surgery. In *SPIE Medical Imaging*, pages 726124–726124. International Society for Optics and Photonics, 2009.

[232] Jared A Weis, Katelyn M Flint, Violeta Sanchez, Thomas E Yankeelov, and Michael I Miga. Assessing the accuracy and reproducibility of modality independent elastography in a murine model of breast cancer. *Journal of Medical Imaging*, 2(3):036001–036001, 2015.

[233] Terry S Yoo, Michael J Ackerman, William E Lorensen, Will Schroeder, Vikram Chalana, Stephen Aylward, Dimitris Metaxas, and Ross Whitaker. Engineering and algorithm design for an image processing api: a technical report on itk-the insight toolkit. *Studies in health technology and informatics*, pages 586–592, 2002.

[234] Bin Zheng, Jules H Sumkin, Margarita L Zuley, Xingwei Wang, Amy H Klym, and David Gur. Bilateral mammographic density asymmetry and breast cancer risk: a preliminary assessment. *European journal of radiology*, 81(11):3222–3228, 2012.

[235] S Hennessey, E Huszti, A Gunasekura, A Salleh, L Martin, S Minkin, S Chavez, and NF Boyd. Bilateral symmetry of breast tissue composition by magnetic resonance in young women and adults. *Cancer Causes & Control*, 25(4):491–497, 2014.

[236] Norman F Boyd, Qing Li, Olga Melnichouk, Ella Huszti, Lisa J Martin, Anoma Gunasekara, Gord Mawdsley, Martin J Yaffe, and Salomon Minkin. Evidence that breast tissue stiffness is associated with risk of breast cancer. *PloS one*, 9(7):e100937, 2014.

[237] Jun Chen, KR Brandt, Karthik Ghosh, RC Grimm, KJ Glaser, JL Kugel, and Richard Ehman. Non compressive mr elastography of breasts. *Proceedings of the international society for magnetic resonance in medicine. International Society for Magnetic Resonance in Medicine, Salt Lake City, USA*, 2013.

[238] R Sinkus, J Lorenzen, D Schrader, M Lorenzen, M Dargatz, and D Holz. High-resolution tensor mr elastography for breast tumour detection. *Physics in medicine and biology*, 45(6):1649, 2000.

[239] J Lorenzen, R Sinkus, M Lorenzen, M Dargatz, C Leussler, P Röschmann, and G Adam. Mr elastography of the breast: preliminary clinical results. In *RöFo-Fortschritte auf dem Gebiet der Röntgenstrahlen und der bildgebenden Verfahren*, volume 174, pages 830–834. © Georg Thieme Verlag Stuttgart· New York, 2002.

[240] Ramin V Parsey, Mark Slifstein, Dah-Ren Hwang, Anissa Abi-Dargham, Norman Simpson, Osama Mawlawi, Ning-Ning Guo, Ronald Van Heertum, J John Mann, and Marc Laruelle. Validation and reproducibility of measurement of 5-ht1a receptor parameters with [carbonyl-11c] way-100635 in humans: comparison of arterial and reference tissue input functions. *Journal of Cerebral Blood Flow & Metabolism*, 20(7):1111–1133, 2000.

[241] Anissa Abi-Dargham, Diana Martinez, Osama Mawlawi, Norman Simpson, Dah-Ren Hwang, Mark Slifstein, Satish Anjilvel, Justine Pidcock, Ning-Ning Guo, Ilise Lombardo, et al. Measurement of striatal and extrastriatal dopamine d1 receptor binding potential with [11c] nnc 112 in humans: validation and reproducibility. *Journal of Cerebral Blood Flow & Metabolism*, 20 (2):225–243, 2000.

[242] J Martin Bland and Douglas G Altman. Measuring agreement in method comparison studies. *Statistical methods in medical research*, 8(2):135–160, 1999.

[243] JW Bartlett and C Frost. Reliability, repeatability and reproducibility: analysis of measurement errors in continuous variables. *Ultrasound in obstetrics & gynecology*, 31(4):466–475, 2008.

[244] Xia Li, Richard G Abramson, Lori R Arlinghaus, Hakmook Kang, Anuradha Bapsi Chakravarthy, Vandana G Abramson, Jaime Farley, Ingrid A Mayer, Mark C Kelley, Ingrid M Meszoely, et al. Multiparametric magnetic resonance imaging for predicting pathological response after the first cycle of neoadjuvant chemotherapy in breast cancer. *Investigative radiology*, 50(4):195–204, 2015.

[245] Natasja NY Janssen, Leon C ter Beek, Claudette E Loo, Gonneke Winter-Warnars, Charlotte AH Lange, Marjolein van Loveren, Tanja Alderliesten, Jan-Jakob Sonke, and Jasper Nijkamp. Supine breast mri using respiratory triggering. *Academic Radiology*, 2017.

[246] Rebekah H Griesenauer, Jared A Weis, Lori R Arlinghaus, Ingrid M Meszoely, and Michael I Miga. Breast tissue stiffness estimation for surgical guidance using gravity-induced excitation. *Physics in Medicine and Biology*, 62(12):4756, 2017.

[247] Kristin A Skinner, Howard Silberman, Richard Sposto, and Melvin J Silverstein. Palpable breast cancers are inherently different from nonpalpable breast cancers. *Annals of surgical oncology*, 8 (9):705–710, 2001.

[248] Nicole MA Krekel, Max H Haloua, Alexander MF Lopes Cardozo, Roos H de Wit, Anne Marie Bosch, Louise M de Widt-Levert, Sandra Muller, Henk van der Veen, Elisabeth Bergers, Elly SM de Lange de Klerk, et al. Intraoperative ultrasound guidance for palpable breast cancer excision (cobalt trial): a multicentre, randomised controlled trial. *The lancet oncology*, 14(1): 48–54, 2013.

[249] Jennifer Tseng, Alexandra Kyrillos, Erik Liederbach, Georgia G Spear, Jacob Ecanow, Chi-Hsiung Wang, Tom Czechura, Olga Kantor, Megan Miller, David J Winchester, et al. Clinical accuracy of preoperative breast mri for breast cancer. *Journal of Surgical Oncology*, 2017.

[250] Christiane K Kuhl, Simone Schrading, Heribert B Bieling, Eva Wardelmann, Claudia C Leutner, Roy Koenig, Walther Kuhn, and Hans H Schild. Mri for diagnosis of pure ductal carcinoma in situ: a prospective observational study. *The Lancet*, 370(9586):485–492, 2007.

[251] Martin D Pickles, Peter Gibbs, Anne Hubbard, Ayesha Rahman, Joanna Wieczorek, and Lindsay W Turnbull. Comparison of 3.0 t magnetic resonance imaging and x-ray mammography in the measurement of ductal carcinoma in situ: A comparison with histopathology. *European journal of radiology*, 84(4):603–610, 2015.

[252] TH Kim, DK Kang, and YS Jung. Mr-navigated ultrasound with supine breast mri for suspicious enhancing lesions not identified on second-look ultrasound in breast cancer patients. *Ultraschall in der Medizin-European Journal of Ultrasound*, 37(S 01):SL16_3, 2016.

[253] Doo Kyoung Kang, Yongsik Jung, Sehwan Han, Ji Young Kim, and Tae Hee Kim. Clinical utility of real-time mr-navigated ultrasound with supine breast mri for suspicious enhancing lesions not identified on second-look ultrasound. *Ultrasound in Medicine & Biology*, 43(2):412–420, 2017.

[254] Elijah Polak and Gerard Ribiere. Note sur la convergence de méthodes de directions conjuguées. *Revue française d'informatique et de recherche opérationnelle, série rouge*, 3(1):35–43, 1969.

[255] Reeves Fletcher and Colin M Reeves. Function minimization by conjugate gradients. *The computer journal*, 7(2):149–154, 1964.

[256] Kenneth Levenberg. A method for the solution of certain non-linear problems in least squares. *Quarterly of applied mathematics*, 2(2):164–168, 1944.

[257] Donald W Marquardt. An algorithm for least-squares estimation of nonlinear parameters. *Journal of the society for Industrial and Applied Mathematics*, 11(2):431–441, 1963.

[258] Richard G Abramson, Ayse Mavi, Tevfik Cermik, Sandip Basu, Natasha E Wehrli, Mohamed Houseni, Shipra Mishra, Jay Udupa, Paras Lakhani, Andrew DA Maidment, et al. Age-related structural and functional changes in the breast: multimodality correlation with digital mammography, computed tomography, magnetic resonance imaging, and positron emission tomography. In *Seminars in nuclear medicine*, volume 37, pages 146–153. Elsevier, 2007.

[259] Jeremy C Hebden, Ben D Price, Adam P Gibson, and Gary Royle. A soft deformable tissue-equivalent phantom for diffuse optical tomography. *Physics in medicine and biology*, 51(21): 5581, 2006.

[260] Jared A Weisa, Thomas E Yankeelova, Samantha A Munozc, Rahul A Sastryg, Stephanie L Barnesa, Lori R Arlinghausa, Xia Lia, and Michael I Migaa. A consistent pre-clinical/clinical elastography approach for assessing tumor mechanical properties in therapeutic systems. In *SPIE Medical Imaging*, pages 86721F–86721F. International Society for Optics and Photonics, 2013.

[261] Martin O Culjat, David Goldenberg, Priyamvada Tewari, and Rahul S Singh. A review of tissue substitutes for ultrasound imaging. *Ultrasound in medicine & biology*, 36(6):861–873, 2010.

[262] John Garrett and Elise Fear. A new breast phantom with a durable skin layer for microwave breast imaging. *IEEE Transactions on Antennas and Propagation*, 63(4):1693–1700, 2015.

[263] Matthew J Burfeindt, Timothy J Colgan, R Owen Mays, Jacob D Shea, Nader Behdad, Barry D Van Veen, and Susan C Hagness. Mri-derived 3-d-printed breast phantom for microwave breast imaging validation. *IEEE antennas and wireless propagation letters*, 11:1610–1613, 2012.

[264] Sara M Salvador and Giuseppe Vecchi. Experimental tests of microwave breast cancer detection on phantoms. *IEEE Transactions on Antennas and Propagation*, 57(6):1705–1712, 2009.

[265] David W Winters, Jacob D Shea, Ernest L Madsen, Gary R Frank, Barry D Van Veen, and Susan C Hagness. Estimating the breast surface using uwb microwave monostatic backscatter measurements. *IEEE Transactions on Biomedical Engineering*, 55(1):247–256, 2008.